PhD in
Physics and Astronomy

CYCLE XXXV

COORDINATOR Prof. Giovanni Modugno

Dwarf satellite galaxies at high-redshift: physical understanding and JWST predictions

Academic Discipline (SSD) FIS/05

Doctoral Candidate
Dr. Viola Gelli

Supervisor
Prof. Stefania Salvadori

Coordinator
Prof. Giovanni Modugno

Years 2019/2023

Contents

Introduction

Dwarf galaxies are the most numerous type of galaxies in the Universe at all times and they have played a key role in cosmic history, from the Big Bang to the present day. They are among the *first galaxies* to form, hosting the first generations of stars born from a primordial gas composed of H and He only, marking the end of the "Dark Ages" of the Universe. They constitute the *building blocks* that, coalescing through continuous merger events, gave birth to the massive galaxies we see today. The role of dwarf galaxies during the first billion years after the Big Bang, the so called Epoch of Reionization (EoR, redshift $z \gtrsim 6$), is also essential because they are believed to be the main contributors to the processes of reionization and metal enrichment of the primordial gas. The stellar evolution taking place within these first low-mass galaxies drastically impacted all subsequent structure formation through feedback processes (e.g. Bromm & Yoshida, 2011a; Ciardi & Ferrara, 2005): these key mechanisms shape the properties of galaxies through complex baryonic physics, like supernovae explosions capable of both heating and evacuating the gas, and polluting it with heavy elements. Due to their small masses, dwarf galaxies are very sensitive to such feedback processes, and thus they represent the ideal laboratories in which to study their effects during early galaxy formation.

Dwarf galaxies have been extensively observed in the Local Group, where more than 70 of them have been detected as satellites orbiting around the more massive Milky Way and Andromeda (e.g. McConnachie, 2012); but detecting them at high-redshift poses instead a great challenge due to their extremely low luminosities. However, we can finally explore the rest-frame UV-optical emission of these sources thanks to unprecedented facilities like the James Webb Space Telescope (JWST).

The main purpose of this Thesis is to tackle the many open issues regarding dwarf galaxies evolution in the first billion years of the Universe, and to understand how to unveil their properties at high-z for the first time with JWST. We reach these goals by using state-of-art cosmological simulations of typical massive

galaxies forming in the EoR (Pallottini et al., 2017b, 2022), and focusing on the study of their *satellite dwarf galaxies*, fundamental for several reasons. First of all, they allow us to investigate galaxy assembly taking place in dense environments of the cosmic web. Second, through their study we can unveil the role of feedback processes in driving their evolution and in quenching their star formation, leading to the emergence of the first passive galaxies. Moreover, they can be easily identified in upcoming high-z observations thanks to their proximity to more massive galaxies. Since JWST is now finally starting to shed light on these early cosmic epochs, we make accurate predictions and provide tools to help interpret upcoming data to uncover the properties of the first dwarf galaxies. Indeed, while writing this Thesis, the surprising JWST discovery of the first low-mass passive galaxy at $z > 7$ was reported: we take advantage of our simulations and the new tools I developed to rapidly interpret its emission, seizing this unique opportunity to study the imprint of feedback processes on early galaxy evolution.

The results illustrated in this Thesis appear in the following publications in peer reviewed journals:

- **Gelli V.**, Salvadori S., Pallottini A., and Ferrara A., *The stellar populations of high-redshift dwarf galaxies*, **2020** MNRAS, 498, 41

- **Gelli V.**, Salvadori S., Ferrara A., Pallottini A. and Carniani S. *Dwarf satellites of high-z Lyman Break Galaxies: a free lunch for JWST*, **2021** ApJ Letters, 913, L2

- **Gelli V.**, Salvadori S., Pallottini A., Ferrara A. and Carniani S., *Quiescent low-mass galaxies observed by JWST in the Epoch of Reionization*, **2023**, arXiv:2303.13574, submitted to ApJ Letters

- **Gelli V.**, Salvadori S., Pallottini A., Ferrara A., Carniani S. and Ginolfi M. *Active or passive? Hunting quenched dwarf galaxies at high-z with JWST*, **2023** to be submitted to ApJ

- Pallottini A., Ferrara A., Gallerani S., Behrens C., Kohandel M., Carniani S., Vallini L., Salvadori S., **Gelli V.**, Sommovigo L., D'Odorico V., Di Mascia F., Pizzati E., *A survey of high-z galaxies: SERRA simulations*, **2022** MNRAS, 513, 562

- Aguado D., Skúladóttir A., Caffau E., Bonifacio P., Vanni I., **Gelli V.**, Koutsouridou I., Amarsi A. M., *PISN-explorer: hunting the descendants of very massive first stars*, **2023** MNRAS, 520, 866

and in seminar proceedings:

- **Gelli V.**, *high-z Lyman Break Galaxies with JWST: parallel observations of dwarf satellites*, Proceedings of Hypatia Colloquium 2021: Early Career Astronomer series at ESO.

CHAPTER 1

The first billion years

The first galaxies are thought to be low mass dwarf galaxies that act as the key drivers of early cosmic evolution, marking the transformation of the Universe from a simple state to a very complex one. This is why it is extremely important to understand how these small systems came into existence, how they constituted the building blocks for the formation of massive galaxies, and which physical processes shape them. Their characterization needs to involve cosmology since galaxy evolution inevitably depends on the overall properties of the Universe. We here firstly describe how structure formation happens, highlighting the important role of dwarf galaxies both from a cosmological perspective, both regarding the main physical processes involved. We then focus on current observational probes and knowledge, pointing out to the major improvements expected in the very near feature thanks to the James Webb Space Telescope.

1.1 The standard model of cosmology

Modern cosmology is based on two main hypothesis: the cosmological principle, stating that the Universe is uniform and isotropic on sufficiently large scales, and Einstein's general relativity, which allow us to infer the structure of space-time based on the mass distribution contained in it. We hereafter use the most popular cosmological model, i.e. the so-called ΛCDM model. It consists of a flat Universe in which dark matter is composed of non-relativistic, weakly interacting massive particles (e.g. Longair, 2007). Within such Universe about 70% of the energy is due to the cosmological constant Λ, responsible for the accelerated expansion of the Universe, 25% is due to cold dark matter, and the remaining 5% is due to the

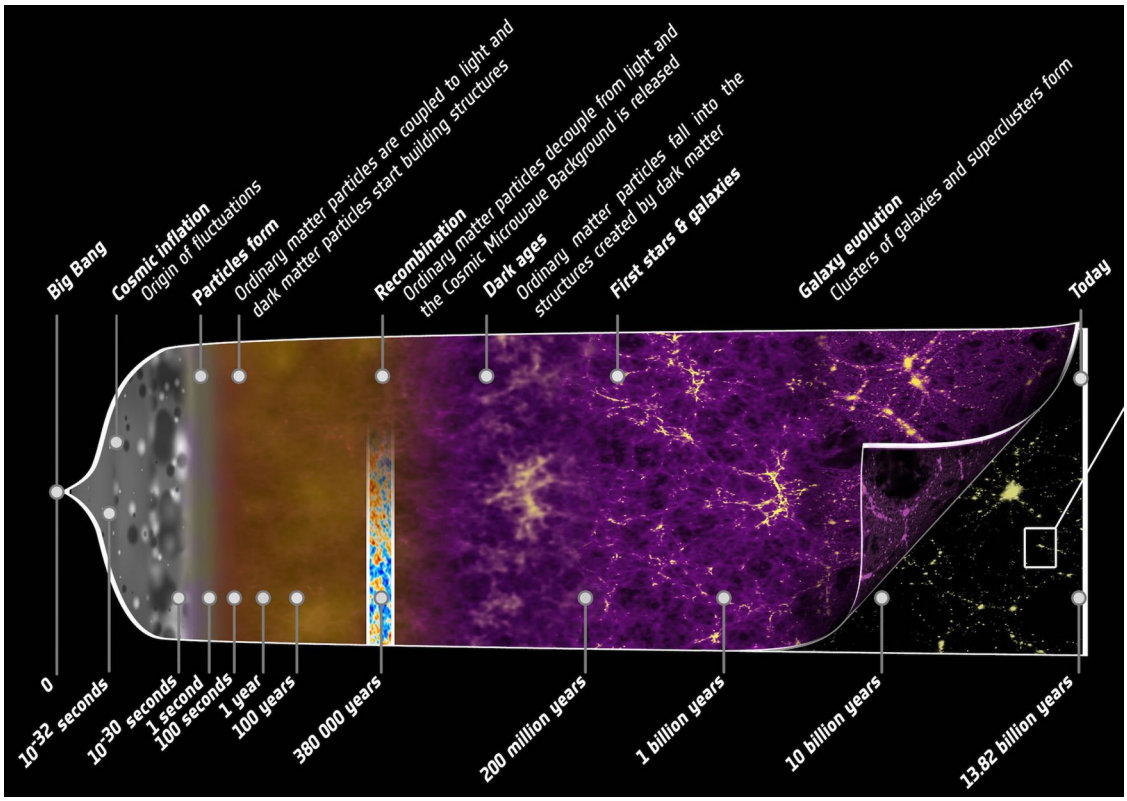

Figure 1.1: The illustration summarises the almost 14 Gyr history of our Universe, showing the main events that occurred from the initial phases of simplicity to the rich variety of cosmic structure that we observe today. From https://www.nasa.gov .

baryonic matter that all the stars and galaxies are made of. The highly homogeneous Universe from which the first structures are believed to form is predicted as a consequence of the very early evolutionary stages right after the Big Bang, $\simeq$ 13.8 Gyr ago. The main phases marking cosmic evolution are represented in Fig.1.1. Starting from very high temperatures and densities, the Universe expands and cools down in time as $T = T_0(1 + z)$, where z is the cosmological redshift, denoting the relative change in the wavelength of emitted and observed light from a distant object due to cosmic expansion: $z = \frac{\lambda_{observed} - \lambda_{emitted}}{\lambda_{emitted}}$. After 5 minutes from the Big Bang (when $T \sim 10^9$K) the first light nuclei are created during the so called primordial nucleosynthesis. After about 50 000 years the density of matter exceeds that of the radiation, marking the beginning of the "matter-dominated era", and the Universe is still hot enough for the gas to be ionized and thermally coupled to radiation through Compton scattering. Only when the temperature decreases to values of $T \sim 10^3$K, at $\sim$ 400 000 yr, protons and electrons start to recombine forming neutral hydrogen and eventually producing the Cosmic Microwave Background (CMB), the last scattering surface of photons interacting with baryons. The CMB

can be observed today as an almost perfect black body background radiation at temperature $T_0 \simeq 2.7\,\mathrm{K}$, which has been redshifted since its emission at $z \sim 1100$. After recombination, the initial conditions that bring to the arising of first stars, galaxies and structures are set. At this point the gas is mainly composed of neutral hydrogen and helium, with a small fraction of free electrons and other elements like ^{3}He, ^{2}D, ^{7}Li and ^{7}Be.

During the immediately following epoch no sources of light are present yet, hence deserving the name "Dark Ages". Yet small dark matter structures start to form through gravitational collapse of perturbation in the density field. The first stars are born in these small dark matter haloes around $z \sim 30$, marking the end of the Dark Ages and opening the way to the creation of the first galaxies. The ΛCDM model predicts in fact the first galaxies to be small dwarf galaxies ($\mathrm{M}_\star \lesssim 10^9 \mathrm{M}_\odot$) constituting the majority of the objects in this early Universe. They form bigger galaxies only at later times in a "bottom up" scenario where structures assemble hierarchically through mergers of smaller ones. The end result after ~ 14 billion years is the Universe as we can observe it today in our neighbourhood, where we see massive galaxies like our Milky Way ($\mathrm{M}_\star \simeq 10^{11} \mathrm{M}_\odot$) that are surrounded by many smaller satellite dwarf galaxies subjected to their gravitational influence.

1.2 Perturbation theory and structure formation

At early times the matter distribution in the Universe is thought to be highly homogeneous. In order to have the formation of structures we need some deviations from perfect uniformity. A possible explanation for the presence of perturbations in the density field is given by the inflation theory, that predicts quantistic fluctuations to be amplified in the very early evolutionary phases just after the Big Bang. CMB observations shows us that small temperature fluctuations of $\Delta T/T = 10^{-5}$ where indeed present at $z \sim 1100$ (e.g. Planck Collaboration et al., 2014). Such small fluctuations grow over time due to gravitational instability, and eventually lead to the formation of galaxies and the large scale structure observed in the present Universe. Let us now see how these perturbations of the density field evolve in an expanding Universe dominated by non-relativistic matter.

1.2.1 Linear regime

We consider the Universe as composed of baryons, treated as an ideal gas, and dark matter, treated as a collision-less fluid. We describe the growth of ini-

tially infinitesimal perturbations of density $\rho(\mathbf{x}, t)$ in terms of the density contrast $\delta(\mathbf{x}, \mathrm{t}) = \frac{\rho(\mathbf{x},\mathrm{t})-\bar{\rho}(\mathrm{t})}{\bar{\rho}(\mathrm{t})}$, where $\bar{\rho}(t)$ is the background density of the expanding Universe. In the linear regime (i.e. $\delta \ll 1$), perturbing the fluid equations we find:

$$\ddot{\delta} + 2\left(\frac{\dot{a}}{a}\right)\dot{\delta} = (4\pi G\rho - k^2 c_s^2)\delta \tag{1.1}$$

where $a = 1/(1+z)$ is the scale factor describing the expansion of the space-time, k is the wave number and c_s the sound speed. The second term on the left hand side is a drag term which tends to suppress perturbation growth due to the expansion of the Universe. The first term on the right hand side is the gravitational one, which causes perturbations to grow via gravitational instability. The last term on the right hand side represents the contribution of the pressure force which opposes gravity. By equating the two terms in parenthesis we can define a characteristic scale, i.e. the so called Jeans length: $\lambda_J = c_s(\frac{\pi}{G\rho})^{1/2}$. If $\lambda = 2\pi/k \gg \lambda_J$ we can neglect the pressure term and find the solution in an Einstein - de Sitter Universe[1]:

$$\delta_{lin} \propto a \propto t^{2/3} \tag{1.2}$$

clearly showing how the amplitude of perturbation grows in time. The general solution for the linear growth factor $\delta_{lin} \propto D(z)$ may be expressed as a function of the cosmological parameters[2]as (Carroll et al., 1992):

$$D(z) = \frac{5}{2}\frac{\Omega_m(z)}{1+z}\left\{\Omega_m^{4/7}(z) - \Omega_\Lambda(z) + \left[1 + \frac{\Omega_m(z)}{2}\right]\left[1 + \frac{\Omega_\Lambda(z)}{70}\right]\right\}^{-1}. \tag{1.3}$$

The dark matter perturbations component is the one that is able to grow the most starting from the earliest epochs, since it interacts very weakly with all the other particles. Nevertheless, after recombination ($z \sim 1100$), baryons inevitably fall into the potential wells of DM perturbations due to gravitational interaction, and rapidly reach their same amplitude.

[1]The Einstein - de Sitter model consists in a flat matter dominated Universe, which is a good approximation to our Universe at very high-redshifts, during the early epochs of structure formation.

[2]Cosmological parameters are used to describe the content of the Universe at different times. They are defined as $\Omega_x(z) = 8\pi G\rho_x(z)/3H^2(z)$, where $H(z) = \dot{a}/a$ and x is Λ for dark energy and m for non-relativistic matter (e.g. Longair (2007) for more details).

1.2.2 Non-linear regime

We have seen that a DM density perturbation will keep growing in an expanding Universe, but as soon as the density contrast δ exceeds the unity ($\delta \gtrsim 1$), perturbation theory is no longer valid and the full non-linear gravitational problem must be considered. The gravitational potential of a given perturbation becomes in fact more and more dominant until the region collapses under its own self gravity.
The simplest approach used to describe non-linear evolution is the idealized case of a spherical top-hat collapse (e.g. Padmanabhan, 1993). It considers perfectly spherical dark matter perturbations with uniform density δ where shells evolve independently, contracting and collapsing ideally into a point. This allows us to define a critical overdensity $\delta_c = 1.686$, corresponding to the overdensity predicted by linear theory at the moment when the top-hat collapses into a point. Such value represents a density threshold guaranteeing that every region whose linearly extrapolated density value excess the critical one ($\delta_{lin} > \delta_c$) will collapse under their gravity. More realistically we can infer that perturbations are never perfectly spherical, and even a slight violation of this symmetry prevents the collapse to a point. What likely happens is that individual collapsing shells start to interact, and dark matter undergoes a violent relaxation process resulting in a *virialized dark matter halo*. The system finally reaches virial equilibrium (where potential energy U and kinetic energy K are related by $U = -2K$) and the end result consists in a virialized halo with density on average about 200 times grater than the background ($\delta_{vir} \sim 200$).
Computing the virial radius and circular velocity ($V_c = \sqrt{GM/r_{vir}}$) for any given dark matter halo of mass M that virializes at redshift z, one obtains (Barkana & Loeb, 2001):

$$r_{vir} = 0.784 \left(\frac{\mathrm{M}}{10^8 h^{-1} \mathrm{M}_\odot} \right)^{1/3} \left(\frac{\Omega_m}{\Omega_m(z)} \frac{\delta_{vir}}{18\pi^2} \right)^{-1/3} \left(\frac{1+z}{10} \right)^{-1} h^{-1}\,\mathrm{kpc} \tag{1.4}$$

$$V_c = 23.4 \left(\frac{\mathrm{M}}{10^8 h^{-1} \mathrm{M}_\odot} \right)^{1/3} \left(\frac{\Omega_m}{\Omega_m(z)} \frac{\delta_{vir}}{18\pi^2} \right)^{1/6} \left(\frac{1+z}{10} \right)^{1/2} \mathrm{km\,s^{-1}} \tag{1.5}$$

where $h = H_0/(100 \mathrm{kms^{-1}Mpc^{-1}})$, with H_0 being the Hubble constant.

1.2.3 Halo mass distribution and hierarchical clustering

We now want to find a way to associate a mass to the collapsed haloes. This is a crucial step toward inferring the abundances of galaxies of different mass that populate the Universe. In order to derive a halo mass function we need to know the statistical properties of the fluctuations. More specifically we need to know the power spectrum of density perturbations $P(k)$, in which the properties of perturbation growth on different scales and times are enclosed. The initial spectrum is predicted to be $P_{in}(k) \propto k^n$ with $n \sim 1$ according to the inflationary theory, and perturbations are given by a gaussian random field. The present day power spectrum can be inferred from observations of the CMB temperature fluctuations and from measurements of the local large scale structure (e.g. Longair, 2007).
To determine the formation of objects of given size and mass, we should consider the statistical distribution of a smoothed density field. The mass variance will be given by:

$$\sigma^2(\mathrm{M}) = \delta^2_{\mathrm{M}} = \frac{1}{2\pi}\int_0^\infty k^3 P(k)\tilde{W}^2(kR)\frac{dk}{k} \tag{1.6}$$

where R is the comoving radius of a sphere of mass M, and $\tilde{W}^2(kR)$ is the top-hat window function, equal to 1 in a sphere of radius R and zero outside. We underline that most of the power is concentrated on small scales, a primary hint to the fact that small low massive objects are the first to collapse.
In order to infer the halo mass function starting from these statistical properties, we exploit an analytical model developed by Press & Schechter (1974), and later refined by Bond et al. (1991). Their approach is based on the assumption that at a given time t the probability that $\delta_{\mathrm{M}} > \delta_c$ is the same as the mass fraction contained in haloes with mass greater than M. The resulting number density of haloes n with mass M at redshift z is:

$$n(\mathrm{M}, z)\mathrm{dM} = \sqrt{\frac{2}{\pi}}\frac{\bar{\rho}_0}{\mathrm{M}}\frac{\mathrm{d}\nu}{\mathrm{dM}}\exp\left(-\frac{\nu^2}{2}\right)\mathrm{dM} \tag{1.7}$$

where $\bar{\rho}_0$ is the present day average mass density, and $\nu \equiv \delta_c/(D(z)\sigma(\mathrm{M}))$. Fig.1.2 shows the number density of haloes with different mass as a function of the redshift. The relation clearly shows how massive haloes become more and more abundant in time, i.e. with lower z. This peculiar behaviour is characteristic of models involving cold dark matter (CDM), where structure formation happens *hierarchically* through continuous merger of smaller dark matter haloes. We stress the fact that low-mass

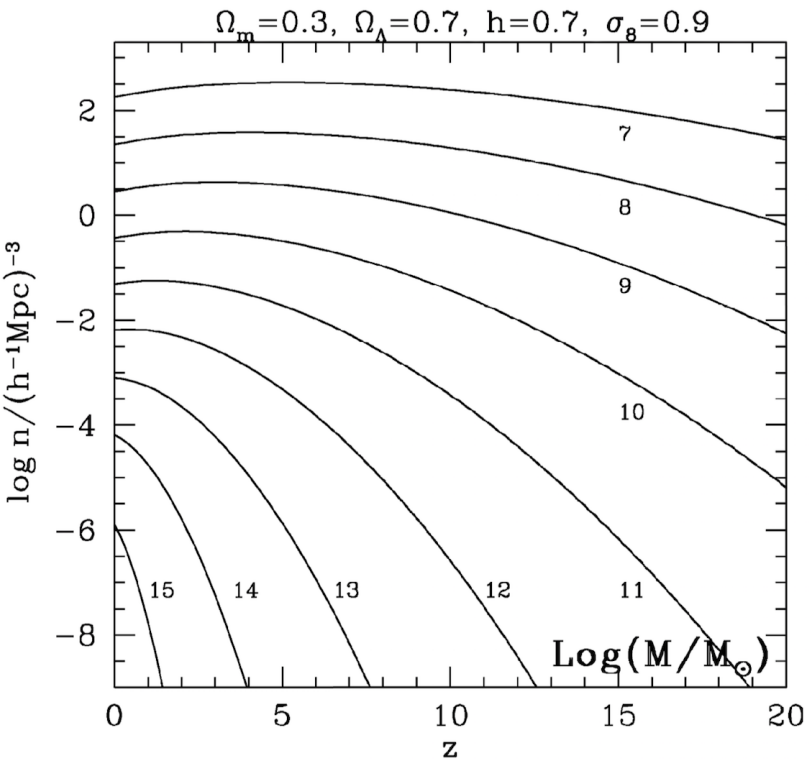

Figure 1.2: Comoving number density of dark matter haloes as a function of redshift. A standard ΛCDM model has been assumed, with parameters indicated above the panel. The label on each curve indicates the halo mass log(M/M$_\odot$)). From Mo & White (2002).

objects, that will likely host dwarf galaxies, are always the most numerous at all epochs. Their abundance has in fact a very weak dependence on the redshift, always maintaining high number density values, as we clearly see in Fig. 1.2.

So far we have dealt with the gravitational dark matter component of structures only, but some of these haloes will at some point form stars. Actually, only some of the low-mass halos, i.e. the building blocks of more massive systems, will be able to form stars, become galaxies (through the complex physical processes regulating gas cooling involved) and experience *merger events* giving birth to progressively more massive galaxies. While studying galaxies properties, it is extremely important to take into account the hierarchical picture and the fact that galaxies do not evolve in an isolated fashion but they are continuously interacting with each other.

Fig.1.3 illustrates a schematic "merger tree" tracing the formation history of an halo through the coalescences of its progenitors. During a single merger event, if two haloes have very different mass, the dynamical process leading to a new final state of equilibrium will be slow. The smaller system will likely end up orbiting

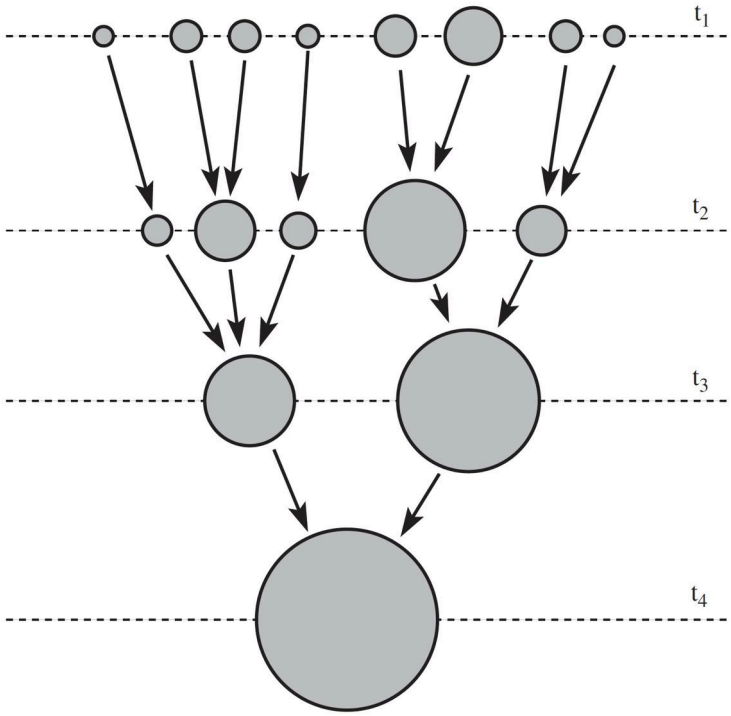

Figure 1.3: A schematic merger tree, illustrating the merger history of a dark matter halo. It shows, at three different epochs, the progenitor halos that at time t4 have merged to form a single halo. The size of each circle represents the mass of the halo. Mo et al. (2010).

within the bigger halo over an extended period of time (e.g. Mo et al., 2010). Keeping in mind that small haloes are indeed the most abundant at all times, it is easy to understand the typical situation encountered in galaxy clusters and groups where a central massive galaxy is surrounded by many smaller *satellite* galaxies orbiting around it. For instance our own Milky Way, considered a typical massive galaxy with its $M_{tot} \simeq 10^{12} M_{\odot}$, is surrounded by dozens dwarf satellite galaxies subjected to its gravitational potential.

1.3 Gas cooling and the formation of the first stars

We now need to take a step back to understand how we pass from a virialized dark matter halo to a halo hosting a galaxy full of stars, gas and heavy elements.[3] After recombination baryonic perturbations, constituted by neutral gas, grow alongside dark matter ones, dragged into their potential wells. During the virialization pro-

[3]By "metals", or "heavy elements", we mean all the elements heavier than helium.

cess within the first haloes, gas undergoes virialization similarly to dark matter. While collapsing it develops shocks and gets heated to virial temperature T_{vir}, at which gravity is balanced by pressure in hydrostatic equilibrium:

$$T_{vir} = \frac{\mu m_p V_c^2}{2k_B} = \\ = 1.98 \times 10^4 \left(\frac{\mu}{0.6}\right) \left(\frac{\mathrm{M}}{10^8 h^{-1} \mathrm{M}_\odot}\right)^{2/3} \left(\frac{\Omega_m}{\Omega_m(z)} \frac{\delta_{vir}}{18\pi^2}\right)^{1/3} \left(\frac{1+z}{10}\right) \mathrm{K} \tag{1.8}$$

where μ is the mean molecular weight of the gas, m_p the proton mass, and k_B the Boltzmann constant (Barkana & Loeb, 2001). In order for a gaseous halo to further collapse forming stars, so that a galaxy might eventually form, certain conditions must be satisfied. First of all the mass must exceed the Jeans Mass, the maximum mass for which gravity is still counteracted by pressure (e.g. Ciardi & Ferrara, 2005):

$$\mathrm{M_J} = 3.08 \times 10^3 \left(\frac{\Omega_m h^2}{0.13}\right)^{-1/2} \left(\frac{\Omega_b h^2}{0.022}\right)^{-3/5} \left(\frac{1+z}{10}\right)^{3/2} \mathrm{M}_\odot. \tag{1.9}$$

$\mathrm{M} \gg \mathrm{M_J}$ is a necessary condition for the gas to form stars, but it is not sufficient. In fact the gas needs also to cool down efficiently, thus breaking hydrostatic equilibrium and allowing the cloud to collapse. In particular the gas cooling time must be shorter than the free-fall time: $t_{cool} \ll t_{ff} = (3\pi/32G\rho)^{1/2}$. The cooling timescale for the gas is defined as (e.g. Ciardi & Ferrara, 2005):

$$t_{cool} = \frac{3}{2} \frac{n\, k_b T}{\Lambda(Z,T)} \tag{1.10}$$

where n is the number density and $\Lambda(Z,T)$ the cooling function. The latter, shown in Fig.1.4, defines the cooling rate of the radiative processes that take place within the gas cloud, based on its temperature T and metallicity $Z = \mathrm{M}_Z/\mathrm{M}_{\mathrm{gas}}$, i.e. the relative amount of elements heavier than helium with respect to the gas mass.

The first dark matter haloes that are able to form stars are very low mass objects, the so called *mini-haloes*, that have total dark matter mass $\mathrm{M} \sim 10^6 \mathrm{M}_\odot$, gas virial temperature $T_{vir} < 10^4$ K (Tegmark et al., 1997), and virializing at $z \sim 30$. At these very early stages of cosmic history, the primordial environment is completely lacking of metals and at such low temperatures gas cooling can only happen through inefficient H_2 roto-vibrational transitions. These peculiar conditions lead

to the birth of the very first stars inhabiting the Universe: the so called Population III (PopIII) stars. These unique primordial metal-free objects have never been directly observed. Even thought their exact mass distribution is unknown, they are thought to have high characteristic masses and hence very short lifetimes (e.g. Bromm, 2013). The mini-haloes hosting them form only a small amount of stars each, and therefore they cannot be directly observed at high-redshifts (e.g. O'Shea et al., 2015).

1.4 Feedback processes

As soon as the first stellar generations form and evolve within mini-haloes, the state of the gas in the Universe is drastically changed. The first stars are born and their light marks the end of the Dark Ages that followed recombination. All subsequent star and structure formation is strongly influenced by their presence through the very different and complex physical processes involved which are often

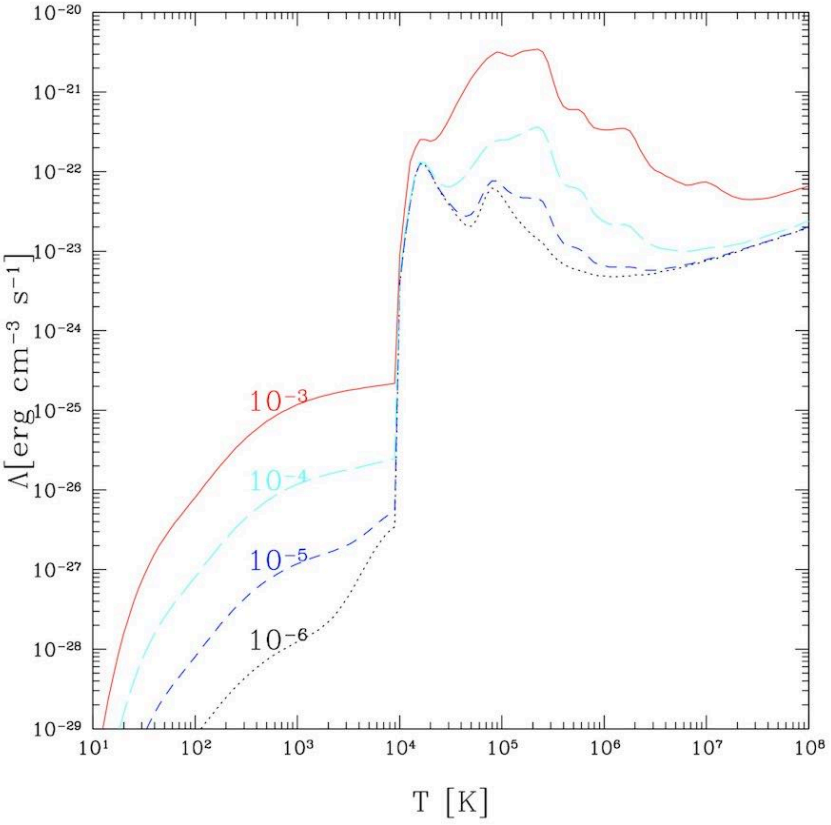

Figure 1.4: Total cooling function due to hydrogen, helium, metals, H_2 and HD molecules as function of temperature, for gas having a hydrogen number density of 1 cm^{-3}. The labels on each curve indicate the metal number fractions Z. From Maio et al. (2007).

tightly coupled to each other. For this reason they are called "*feedback processes*" (e.g. Ciardi & Ferrara, 2005). To determine the properties of the first galaxies forming and evolving at high-redshift it is of fundamental importance to take into account all of these physical processes and to understand their interplay. Feedback processes are often referred to as either positive or negative depending on whether they boost or suppress star formation.

We highlight that dwarf galaxies, due to their shallow potential wells, are the ones that are affected the most by these processes. For instance in such small structures negative feedback can in some cases have drastic consequences and completely *quench* star formation. For the same reason, dwarf galaxies are the perfect candidates in which to study these physical processes, whose effect is so considerable and extremely important in shaping their evolution and final properties.

1.4.1 Radiative feedback and Reionization

Radiative feedback consists in the ionizing and photo-dissociating radiation produced by massive stars. It can have both a local effect within the galaxy in which the radiation was emitted, and a long-range effect, affecting gas in the surrounding intergalactic environment and nearby objects.
Massive stars, like those of type O and B, have high effective temperatures and they are therefore characterised by an emitted spectrum peaked at high energies, with significant amounts of UV radiation. The photons contributing to radiative feedback belong to two energetic bands:

- Photo-dissociating photons are those in the so called Lyman-Werner (LW) band: $11.2\text{eV} < h\nu < 13.6\,\text{eV}$. This radiation is able to dissociate H_2 molecules through the two step Salomon process.

- Photo-ionizing radiation is constituted by photons with $h\nu > 13.6\,\text{eV}$.

This kind of emission may inhibit star formation within galaxies for two main reasons. The UV radiation heats up the gas, that can reach temperatures above T_{vir}, being consequently ejected out of the gravitational potential of the halo. Since $T_{vir} \propto M^{2/3}$, this so called photo-evaporation may have a crucial impact on the smallest structures, like minihaloes, that may be completely disrupted by it, reason why they are not often considered as the first galaxies. On the other hand, the predominant effect of LW radiation is to significantly destroy H_2 from the halo. Since molecular gas represents the primary fuel for star formation, its deprivation

can be drastic for a galaxy, leading to a reduced star formation or even to a complete quenching. In addition, since dwarf galaxies are typically found in dense environments as satellites of more massive galaxies, they may heavily suffer from the feedback effect due to the emission of such luminous neighbours.

The other fundamental consequence of the stellar emission at early times is the *reionization* of the Universe. Their UV radiation ionizes the interstellar medium mainly composed of hydrogen, creating ionized regions (HII regions) surrounding the emitting stars. These HII bubbles grow in volume and expand into the intergalactic medium (IGM). When many haloes are able to form stars, neighbouring bubbles begin to overlap in large numbers, while a background ionizing radiation is created. Eventually the entire IGM will be filled by HII regions and hence ionized. Current theoretical models and observations of luminous high-redshift sources agree that the reionization of the whole IGM is completed in the first billion years after the Big Bang, i.e. by $z \sim 6$ (e.g. Fan et al., 2006; Planck Collaboration et al., 2016). In Fig.1.5 we see a representation of the state of hydrogen intergalactic gas during this so called Epoch of Reionization (EoR).
We may ask ourselves which are the main sources that contribute to this process,

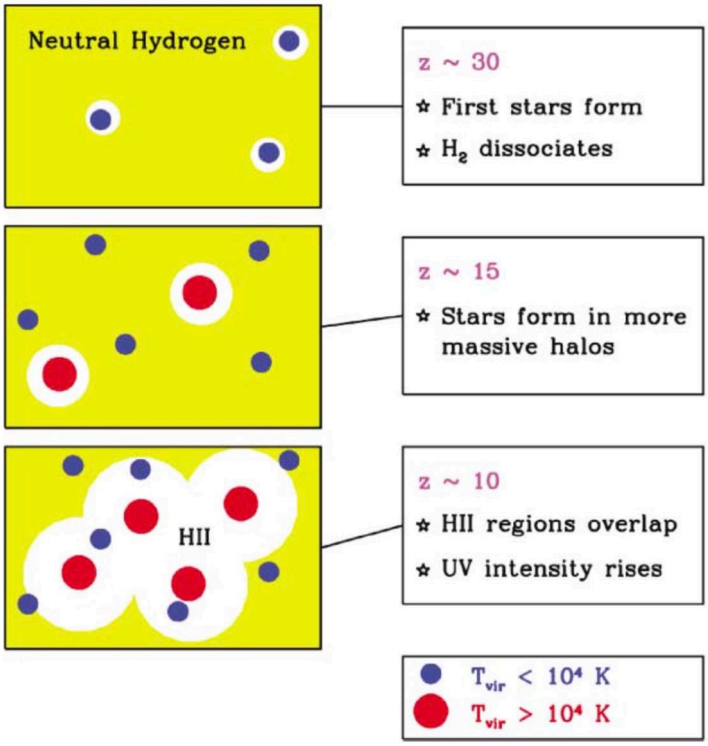

Figure 1.5: Schematic illustration of the stages of the process of reionization of hydrogen in the intergalactic medium. Barkana & Loeb (2001).

and the answer lies once again in the presence of the abundant population of dwarf galaxies at high redshifts. Many studies based on both semi-analitical models (e.g. Salvadori et al., 2014; Yue et al., 2016), numerical simulations (e.g. Wise et al., 2014; Rosdahl et al., 2018), and observations (e.g. Bouwens et al., 2012; Finkelstein, 2016) show that low luminosity dwarf galaxies hosted by atomic cooling halos with masses $M < 10^9 M_\odot$ are most likely the primary reionazation sources.

1.4.2 Chemical feedback

From a chemical point of view we have seen that the primordial Universe, just after recombination, is composed of H and He only, almost completely lacking of metals. In the present-day Universe the environment is much more complex, characterised by the presence of many heavy elements, dust and molecules. To understand how this transition happens we need to know how metals come into existence and spread in the medium. Metals are mainly produced in the interiors of stars, where nuclear reactions happen and elements like C, O, N, Si, Fe are produced. Subsequently they are released into the medium via two main channels: stellar winds and supernovae (SN) explosions. Stellar winds consist in the ejection of matter from the star's atmosphere. They typically characterise massive O/B stars and luminous stars in the latest phase of their evolution, the asymptotic giant branch (AGB). However, at earlier times the main contribution to the amount of metals released into the interstellar and intergalactic medium is due to SNe. Such energetic explosions mark the end of the lives of massive stars with $M > 8\ M_\odot$. During the blast, the interior of the star is violently disrupted and a large amount of metals is injected in the surrounding medium.

The consequences of chemical feedback are manifested in the fact that stars that form in sites that have been polluted by SN events born from a gas enriched in metals, very different with respect to the primordial one. The metallicity of a star ($Z_\star$) reflects the metallicity of the gaseous environment in which it forms, and therefore stars that form in such enriched gas will be more and more metal rich.

In our cosmological scenario, the first metals are produced within the first PopIII stars, the first objects to then exert chemical feedback at very high redshifts. Their SNe pollute the interstellar and intergalactic medium for the first time, the most massive stars $140 < M_\star/M_\odot < 260$ ending their lives as Pair Instability Supernovae (PISN) (e.g. Salvadori et al., 2019). These energetic explosions leave no remnant and release back into the surrounding gas all the PopIII star stellar mass, with 50% in the form of heavy elements, polluting in metals both the host and

neighbouring haloes. Fig. 1.6, from Wise et al. (2012b), shows the overall expected enrichment in metals in haloes of different mass due to previous PopIII SNe: low-mass haloes present a wide spread of possible metallicities due to inhomogenuous enrichment, while all haloes more massive than $M_h > 3 \times 10^7 M_\odot$ are enriched to a metallicity floor of $Z \sim 10^{-3} Z_\odot$.

In terms of efficiency of star formation, chemical feedback is a positive feedback because gas with higher metallicities (Z) cools down more rapidly, as we can see from Fig.1.4. Thus stars can form more efficiently.

1.4.3 Mechanical feedback

During a single supernovae explosion event a great amount of energy is released, of the order of 10^{51} erg, and up to 10^{53} in the case of PISN. This mechanical energy is deposited in the surrounding regions and can cause gas removal from the galaxy itself, locally suppressing star formation. Again, this effect is of extreme importance for dwarf galaxies, that may experience a total evacuation of their gas. The ejection efficiency depends in fact on the halo binding energy E_b and on the kinetic energy E_{kin} released during the explosions, defined respectively as (e.g. Barkana & Loeb, 2001):

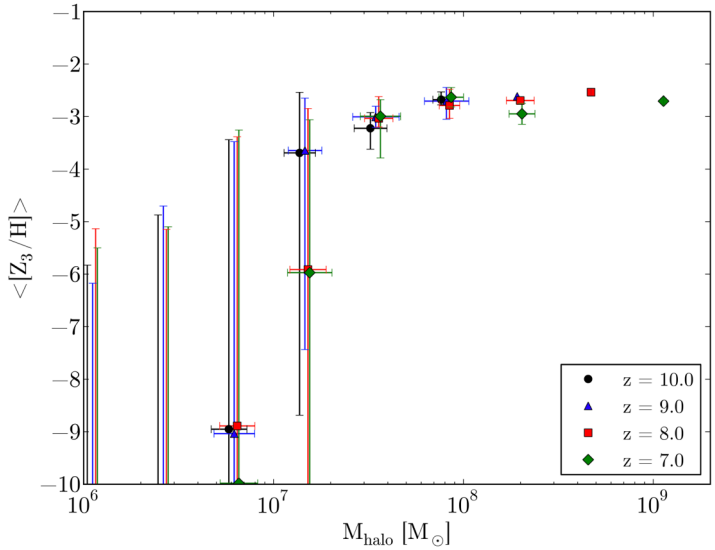

Figure 1.6: From Wise et al. (2012b). Chemical enrichment from the first PopIII stars SNe. All haloes with $M_h > 10^7$ $M_\odot$ reach a metallicity floor of $Z \sim 10^{-3} Z_\odot$ after the rapid evolution of the first massive stars.

$$E_b = \frac{GM_h^2}{2r_{vir}} \tag{1.11}$$

$$E_{kin} = f_{kin}\, N_{SN}\, \langle E_{SN} \rangle \tag{1.12}$$

where M_h is the total halo mass, f_{kin} is the fraction of kinetic energy deposited, N_{SN} the number of supernovae, and $\langle E_{SN} \rangle$ the average energy released in a single explosion. If $E_b \ll E_{kin}$, the halo is not able to counteract the blast and to retain the gas. Due to their low masses, objects like dwarf galaxies have very low binding energies. This makes them particularly fragile structures in which star formation is reduced the most (e.g. Ferrara & Tolstoy, 2000; Salvadori et al., 2008).

The strong impact of stellar evolution in galaxies is now evident, since it not only affects the surrounding interstellar and intergalactic medium by ionizing it, but it also pollutes it with heavy elements due to SN explosions. Fig.1.7 shows a simulation of the evolution of a protogalaxy during a Gyr (Mori & Umemura, 2006). We see that if at first baryonic matter is agglomerated in small individual

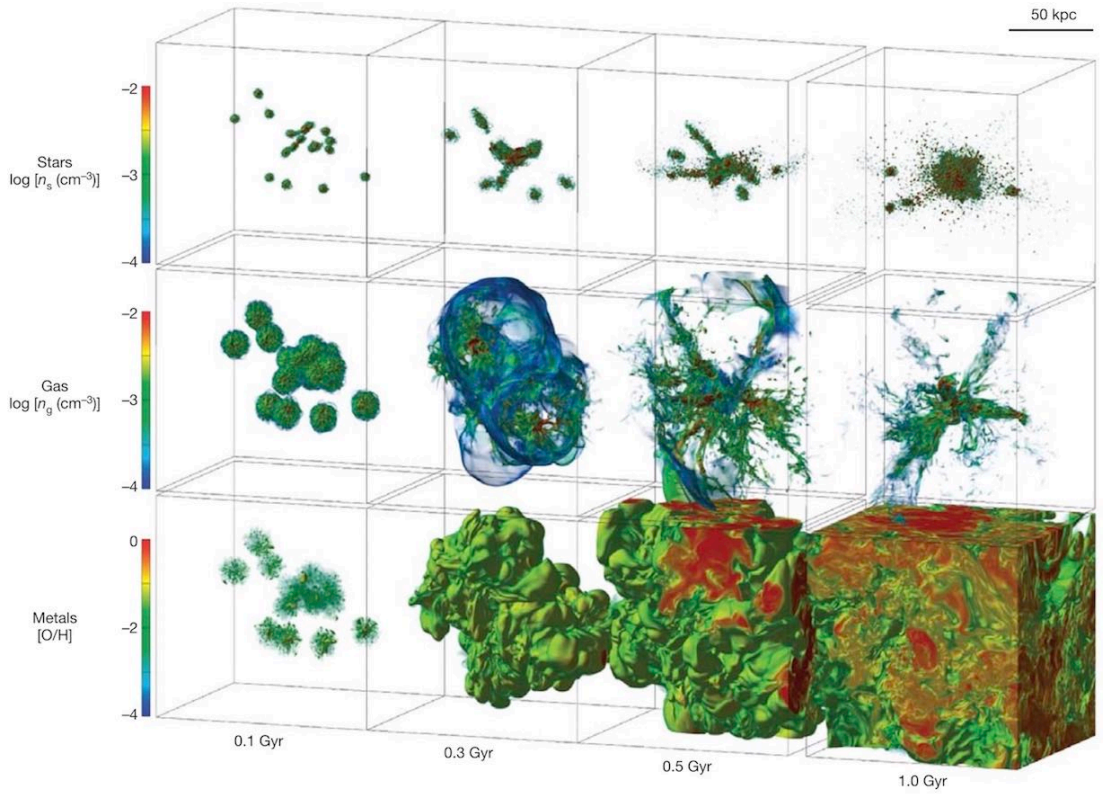

Figure 1.7: Simulation of the first Gyr of evolution of a galaxy with total mass $10^{11}\mathrm{M}_\odot$ (Mori & Umemura, 2006). In the three row are shown the spatial distributions of: stellar density n_s, gas density n_g, and oxygen abundance $[\mathrm{O/H}] = \log(\mathrm{N_O/N_H}) - \log(\mathrm{N_O/N_H})_\odot$.

structures (first column). After ∼300 Myr (second column) gas and metals are largely dispersed due to SN explosions, which create expanding gas bubbles (middle box). Noticeably, in ∼1 Gyr the entire box is filled with heavy elements, with an oxygen to hydrogen abundance ratio that ranges from 1% to solar value.

1.5 The first dwarf galaxies

We have seen that mini-haloes are the first cosmic structures in which PopIII stars can form, heavily influencing subsequent star formation from $z \sim 30$ on. However, at later times we expect more massive haloes to be present, their gas temperature likely exceeds $T_{vir} > 10^4$ K and cooling can efficiently proceed though atomic line emission. We refer to these objects as "atomic-cooling haloes". The first ones able to form are thought to virialize around $z \sim 15$ and to have masses of $\mathrm{M} \sim 5{\times}10^7 \mathrm{M}_\odot$. Since these systems are massive enough to retain gas and sustain star formation for longer times, both observers and theorists agree to consider these low-mass dwarf galaxies as the *first galaxies* (e.g. Bromm & Yoshida, 2011b).

Given the efficiency of chemical feedback by the rapidly evolving first stars, a fast transition also takes place in terms of star formation within the first dwarf galaxies: in those star-forming regions that have been chemically enriched with heavy elements and where the metallicity exceed a critical range ($Z_{\rm crit} = 10^{-6} - 10^{-4}\,\mathrm{Z}_\odot$), gas can collapse through more efficient metal and dust cooling (see Fig. 1.6). This leads to the formation of "normal" lower massive PopII/I stars, that can live for longer times and that dominate the currently observable Universe.

1.6 Observational hints from local dwarf galaxies

Having highlighted the fundamental role of dwarf galaxies in early cosmic evolution and in the study of the physical processes involved, we now illustrate which is our current observational knowledge regarding them. In the last decades, the advances of technology have allowed us to shed light on the physical properties of galaxies both at high-redshift and in the Local Universe. Yet, due to their low luminosity, dwarf galaxies can be accurately observed and their stellar populations studied in details in the Local Group only, even with star by star observations for many of them. The Local Group indeed consists in two massive galaxies, the Milky Way and Andromeda (M31), and their respective *satellite* galaxies, as displayed in Fig. 1.8. These satellite galaxies are mostly small dwarf galaxies, constituting by

far the majority of the objects of the Local Universe. More than 70 of them are located within 3 Mpc from the Milky Way, most of them detected thanks to the Sloan Digital Sky Survey (SDSS, e.g. Belokurov et al., 2007) and studied in details thanks to observatories such as Gaia (Gaia Collaboration et al., 2018). A great variety of dwarf galaxies with different properties are found, with stellar masses ranging from $M_\star \sim 10^3 M_\odot$ to $M_\star \sim 10^9 M_\odot$, and sizes ranging from r $\sim$ 10 pc to r $\sim$ 100 pc. The basic observational parameters that can be derived are distances, velocities, mean metallicities, magnitudes and structural characteristics. Thanks to colours and magnitudes of stars inside a galaxy, we are able to reconstruct star formation histories, thus inferring how and when the galaxy formed its stars throughout past cosmic times.

According to their properties, dwarf galaxies may be divided in a number of different types: early-type dwarf spheroidals, late-type dwarf irregulars, ultra-faint dwarfs and Blue Compact Dwarfs (BCDs) (e.g. Tolstoy et al., 2009). Some of them, like dwarf irregulars and BCDs, are typically gas rich and present *active*

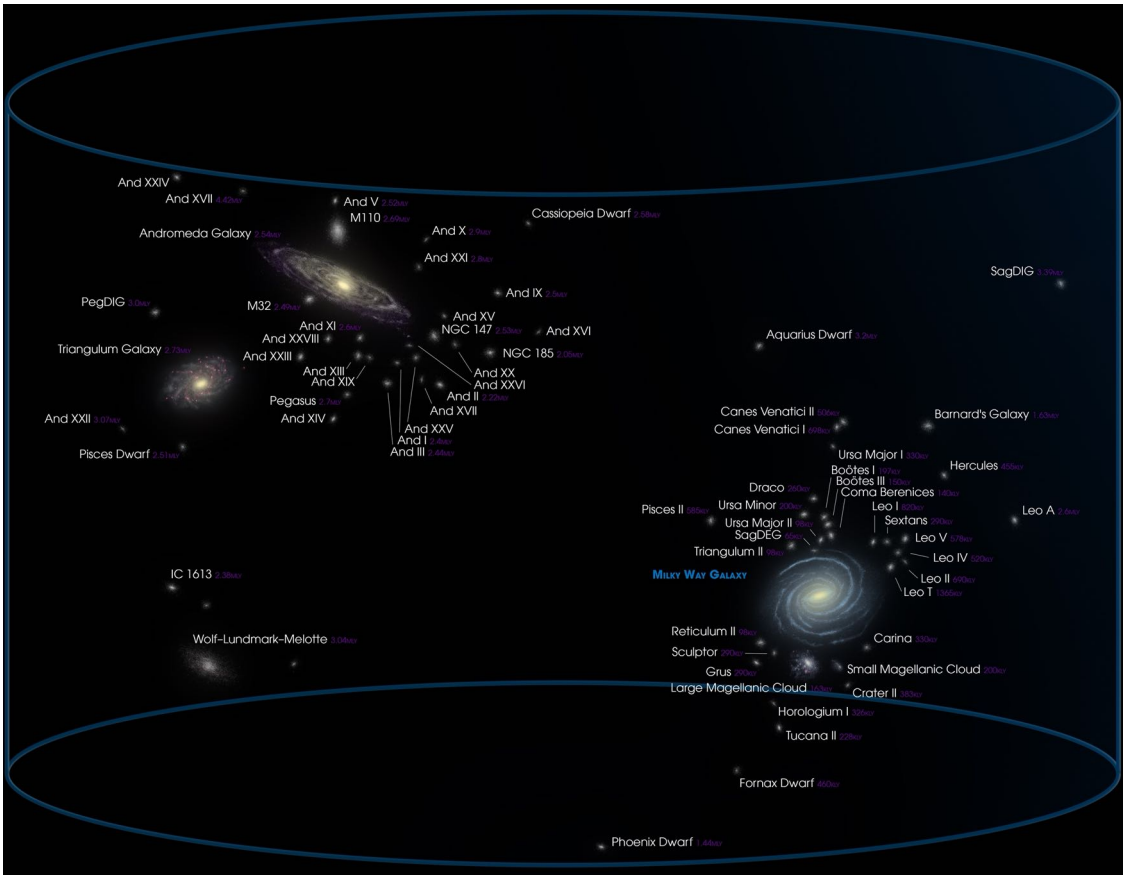

Figure 1.8: Three dimensional representation of our Local Group, with the Milky Way, the Andromeda galaxy (M31) and their satellite galaxies. Credit: ESO.

on-going star formation, while others, like most dwarf spheroidal, are *passive* and characterised by lack of gas and presence of older stellar populations. Whether the presence of a nearby massive galaxy like the MW or M31 may influence the satellites morphology or its composition is not completely understood. Fig. 1.9 (displaying the ratio of HI to luminosity of Local Group satellites vs the distance from the MW or M31) shows that many gas-deficient dwarf spheroidals (orange arrows) are located in close proximity to the massive galaxy, but that some of them can also be found at larger distances up to $\sim$ 900 kpc away (e.g. Cetus and Tucana). Moreover, we notice that star forming satellites are typically more massive, as for instance the Large and Small Magellanic Cloud (LMC and SMC), and can also be found at all distances up to $\sim$ 1500 kpc from the MW/M31. The other fundamental ingredient needed to characterise a galaxy is represented by the stellar metallicities, since these reflect the metallicity of the gas in which star formation took place and hence retain key information on the chemical environment at that time. In the main panel Fig.1.10 we see the stellar mass - metallicity relation found by Kirby et al. (2013): it is an extension at lower masses of the stellar mass - metallicity relation for SDSS galaxies found by Gallazzi et al. (2005) (upper-right

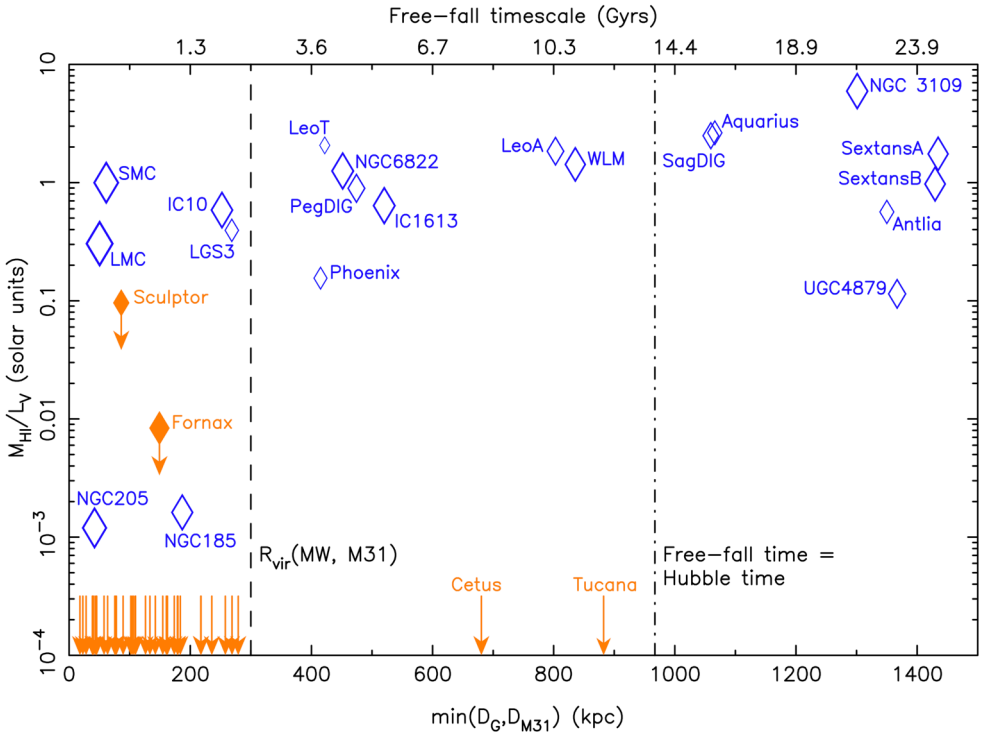

Figure 1.9: HI mass fraction with respect to visual luminosity of Local Group satellite dwarf galaxies as a function of their distance from the closest massive galaxy (either the MW or M31). From McConnachie (2012).

panel), and it reveals how smaller systems appear to be the most metal poor in terms of stellar iron abundance. A similar behaviour is also found for the gas phase (e.g. Mannucci et al., 2010). Indeed, also based on the hierarchical structure evolution theories discussed above, the idea that some of these small galaxies may be the direct descendants of the first galaxies that formed in the Universe is taking hold. The so called "Near-Field cosmology" (e.g. Ricotti & Gnedin, 2005; Salvadori & Ferrara, 2009) consists in the study of primordial stars and galaxies through the search of the signatures they might have left in stars of nearby dwarfs, in order to understand if we may effectively be dealing with survived descendants of the first small galaxies. For instance, by looking for old metal-poor stars in local dwarfs that may retain in their atmospheres the chemical imprint of the primordial environment in which they formed, we can put strong constraints on the origin these systems. Due to the enormous variety of dwarf galaxies characteristics (e.g. Tolstoy et al., 2009), even in the extensively studied Local Group it is not easy to explain their different properties and give a straightforward interpretation of their cosmic role. However, great steps forward will be made in the next few years thanks to surveys like 4DWARFS (*4MOST survey of dwarf galaxies and their stellar*

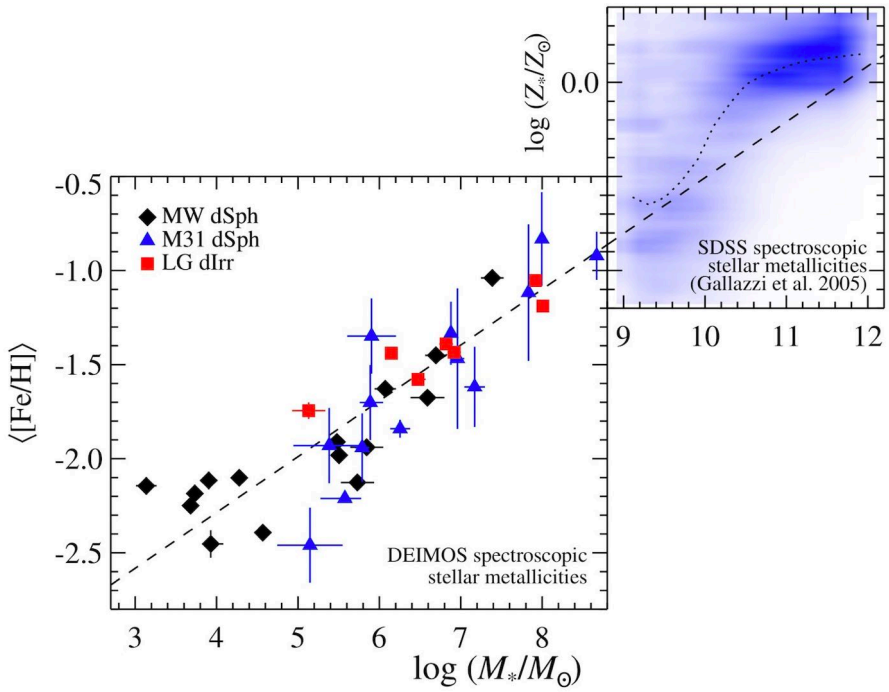

Figure 1.10: Stellar mass - stellar metallicity relation for Local Group dwarf galaxies (left,Kirby et al. (2013)) and more massive Sloan Digital Sky Survey galaxies (right, Gallazzi et al. (2005)). The dashed line is the least-squares fit to the Local Group galaxies, and the dotted line in the right panel is the moving median for the SDSS galaxies.

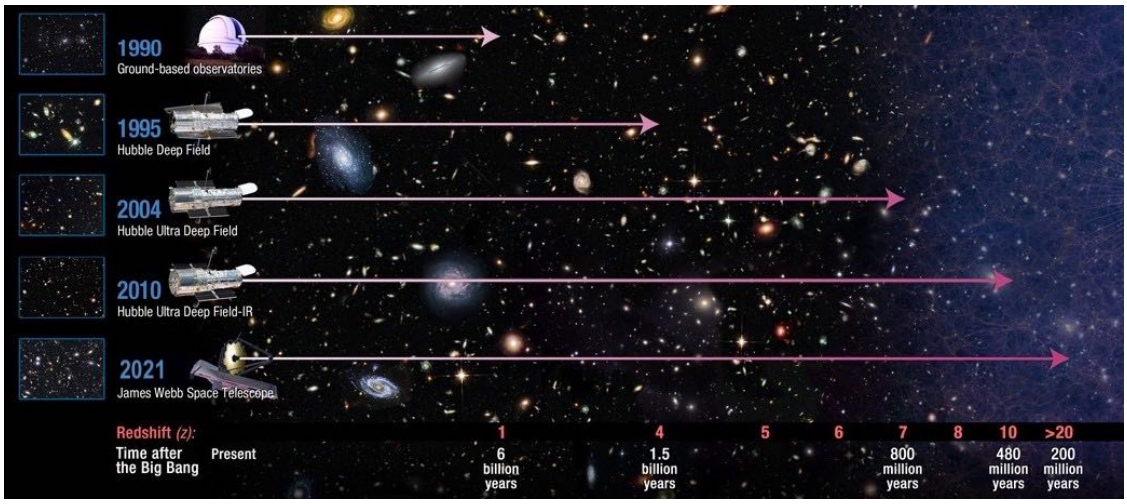

Figure 1.11: The illustration gives an idea of the power of JWST with respect to other telescopes. The farthest very luminous objects reached by HST deep fields are located at $z \sim 10$, while JWST will reach even $z > 20$.

streams, PI: Skuladottir, 28 Co-Is including Gelli). The survey will indeed provide radial velocities, chemical abundances and stellar ages for 140.000 stars in dwarf satellite galaxies of the MW, and thus increase the number of stars with detailed information in such systems by several orders of magnitude. It will provide a new, deeper view of the dwarf satellites and shed light on the chemical evolution and history of star formation in the Local Group environment.

1.7 The JWST era

The most direct approach to study the properties of the galaxies inhabiting primordial Universe during its first billion years is to target them directly at high-z in the Epoch of Reionization ($z > 6$). Thanks to the technological improvements of the past decade, we have been able to get glimpses into the epoch of the first stars and first galaxy. However, it is thanks to the advent of the *James Webb Space Telescope* (JWST, Gardner et al. 2006) that we are now starting to really extend and revolutionize our view of the high-z Universe. This unprecedented 6.5 meters space telescope, launched on the 25th December 2021, is able to detect the faintest dwarf galaxies at high-z, allowing us to investigate *directly* the earliest stages of cosmic evolution. Fig.1.11 illustrates how deep various telescopes are capable of observing, highlighting the power of JWST, that can potentially observe very luminous objects up to $z \sim 20$, with respect to the previous HST deep fields, reaching at most $z \sim 10$.

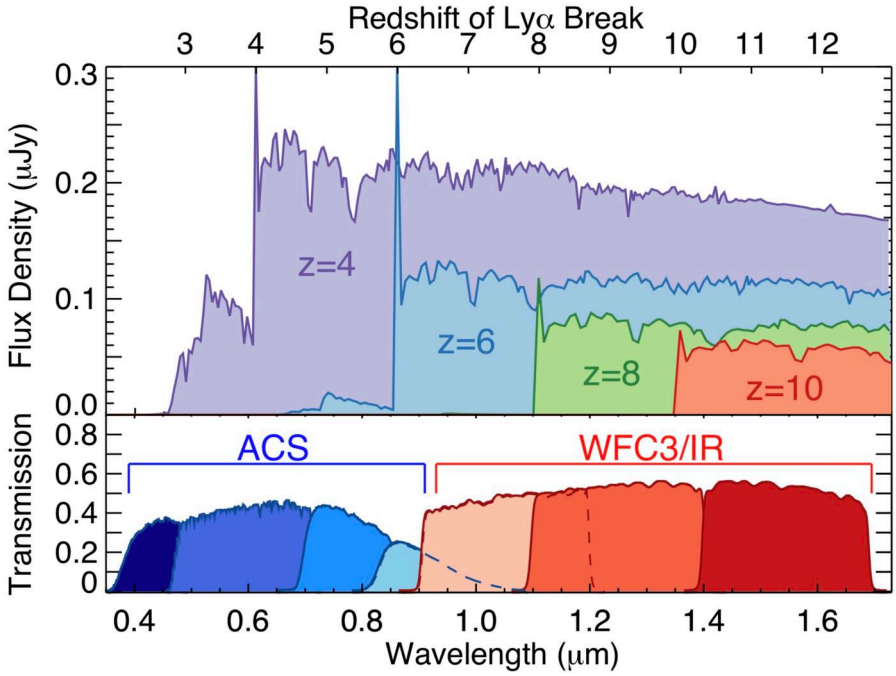

Figure 1.12: Model galaxy spectra at four different redshifts, compared to the Hubble Space Telescope optical (ACS) and near-infrared (WFC3) filters. The models shown have $\log(M/M_{\odot}) = 9$ and age of 10^8 yr. At $z > 6$ the Lyman Break shifts into the near-infrared. From Finkelstein (2016).

1.7.1 Identifying high-z galaxies: the Lyman break technique

Dealing with high-z sources means that all their emission will be redshifted to larger wavelengths due to the expansion of the Universe. For instance at $z > 6$ all the rest-frame UV-optical features of galaxies spectra will be shifted towards the near and mid infrared bands, which is the reason why JWST is optimised for these spectral regions as to thoroughly study such distant objects. Indeed, among the instruments on board we find the JWST Near Infrared Camera (NIRCam Rieke et al., 2005) and the JWST Near Infrared Spectrograph (NIRSpec Jakobsen et al., 2022), that provide imaging, photometry and spectroscopy in the range $0.6 - 5\mu$m.

How can we identify redshifted galaxies at high-z? One of the main features characterising the intrinsic spectra of star-forming galaxies is the "Lyman break": it is found at 912 Å in the rest-frame and it is the result of the hydrogen ionizing radiation from massive stars which is absorbed by neutral gas in the inter-stellar medium. Fig.1.12 shows a model for a galaxy spectrum at four different redshifts, highlighting how the wavelength of the Lyman Break is shifted at higher values for

increasing redshift and how also the total flux gets progressively fainter. The most used photometric techniques used to locate high-z star-forming galaxies are indeed based on the fact that these high-z objects will "disappear" in the bluest broadband filters. All galaxies selected with these methods are referred to as Lyman Break Galaxies (LBG).

Many LBGs have been identified in the past decades, they may have very different properties, but they are usually actively star forming, with typical rates of $\sim 30\,\mathrm{M_\odot yr^{-1}}$ and reaching up to $\sim 100\,\mathrm{M_\odot yr^{-1}}$ (which are extremely high if compared to those of local star forming galaxies like our Milky Way of $\sim 2\,\mathrm{M_\odot yr^{-1}}$), and typical stellar masses around $\sim 10^{10}\mathrm{M_\odot}$, making them amongst the most massive systems that are thought to be present at high-z.

With JWST, unprecedentedly deep and highly resolved observations are being performed. These will allow us not only to identify many new LBGs at much lower masses and higher redshifts, but also to thoroughly inspect already know massive LBGs with deep follow-ups, unveiling and resolving their surrounding regions for the first time.

1.7.2 (Some) preliminary results and ongoing observations

At the time of the writing of this manuscript, JWST has been performing observations since about five months and the first results have already been published. A great effort is currently being made in the search for extremely high-z galaxies to push back the limits of the farthest galaxies known in the Universe. For instance, Donnan et al. (2023) have performed a search for high-z galaxies in JWST deep fields (SMACS0723, CEERS Finkelstein et al. 2017, and GLASS Treu et al. 2022) finding 61 galaxy candidates from $z \sim 8$ up to $z \sim 15$ (47 of which are new). Naidu et al. (2022b) have identified amongst these early observations two remarkably luminous galaxies at $z \sim 10-12$ that should have already built up more than 10^9 $\mathrm{M_\odot}$ in stars in less than $\lesssim 400$ Myr from the Big Bang. On top of imaging and photometry, also spectroscopy is usually needed in order to confirm the effective redshifts of distant galaxies and further investigate their properties through emission lines. For instance Curti et al. (2023) analysed oxygen lines NIRSpec spectra of three $z \sim 8$ galaxies, revealing that the lowest massive of them ($\log M_\star/\,\mathrm{M_\odot} = 7.8$) show a remarkably low metallicity. Thanks to the joint use of NIRCam and NIRSpec in surveys like the JWST Advanced Deep Extragalactic Survey (JADES, Rieke et al. 2019), four metal poor sources have recently been identified by Curtis-Lake et al. (2022) and confirmed to be at $10 \lesssim z \lesssim 13$.

Within the same survey, also the surprising discovery of a low-mass ($\log M_\star/\ \mathrm{M}_\odot = 8.7$) *passive* galaxy at $z \sim 7.3$ was reported by Looser et al. (2023). This passive system, JADES-GS-z7-01-QU, has a Spectral Energy Distribution consistent with not having formed stars (SFR $< 10^{-2.5}\ \mathrm{M}_\odot\mathrm{yr}^{-1}$) during the last ~ 10 Myr. Thus, the unprecedented power of JWST has the potential not only to find the extremely young systems forming at the remotest epochs, but to also to unveil the physical mechanisms shaping the evolution of galaxies at the edge of cosmic Reionization, when the Universe was ~ 1 billion years old. Furthermore, observations like those that will be carried out in the Cycle 1 Proposal 1893 (PI: Carniani, 17 Co-Is including Gelli) will shed light on the galaxy assembly process taking place by accurately investigating known star-forming $z \sim 6-8$ galaxies and possibly unveiling the presence of smaller *satellites* on their surroundings. Indeed, as explained in Sec. 1.2.3 we do expect low-mass dwarf galaxies to be the most abundant type of galaxies at all cosmic times for the hierarchical clustering model, hence we do expect typical massive high-z LBGs to be surrounded by lower massive dwarfs just as our MW is surrounded by its orbiting satellite dwarf galaxies. JWST deep observations can provide an unprecedented opportunity to unveil the faintest amongst them. Some hints of possible systems of massive galaxies with nearby dwarf companions have been reported in preliminary results: Tacchella et al. (2023), Labbe et al. (2022) and Naidu et al. (2022a) detected high-z galaxies within the JADES and CEERS programs that present possible nearby companions at $z \sim 11$, $z \sim 7.5$ and $z \sim 5$ respectively; Hsiao et al. (2023) reported the observation of a lensed system at $z \sim 10.5$; and Matthee et al. (2022) detected multiple groups of galaxies within ~ 10 kpc of each other at $z \sim 6$. These somewhat serendipitous signatures of galaxy assembly in the EoR could soon be greatly enhanced by the statistics provided by wide deep surveys like JADES, that is indeed expected to detect tens of typical $M_\star \sim 10^{10}\ \mathrm{M}_\odot$ LBGs (Williams et al., 2018), possibly unveiling also their lower massive satellites.

1.8 Thesis purpose and plan

The main purpose of this Thesis is to understand the properties and role of dwarf galaxies during the Epoch of Reionization, focusing on the satellites of the most massive LBGs present at that time. The evolution of dwarfs living in the dense regions surrounding massive galaxies are indeed the perfect laboratories to help us understand both galaxy assembly and feedback processes in extreme environments. In view of the vast amount of upcoming JWST data that are now starting to shed

light on these cosmic epochs, it is important to address the following key questions: which physical mechanisms drive the evolution of high-z low-mass galaxies? How do they assemble to form massive galaxies? What is the role of feedback processes and can they quench star formation at high-z? Which among the galaxies populating the faint-end slope of the UV luminosity function can we detect with JWST?

To answer these questions we need cosmological high-resolution simulations, that allow us to investigate the physical properties and evolution of massive high-z galaxies and their companion satellites. In Chapter 2, I illustrate how high-z cosmological zoom-in simulations are developed and describe the simulation by Pallottini et al. (2017b) that reproduces the observed properties of a typical LBG at $z \sim 6$. In Chapter 3, I present an analysis of the simulation, focusing on the stellar properties and evolution of the satellites dwelling within the virial halo of the LBG (Gelli, Salvadori, Pallottini & Ferrara, 2020). Performing SED modeling for the satellites spectra, I present accurate predictions for how they would appear in typical deep observations with the JWST in Chapter 4, also identifying the best observable quantities to infer their key properties (Gelli, Salvadori, Ferrara, Pallottini & Carniani, 2021). We then perform a statistical analysis using a new set of simulations called SERRA (Pallottini et al., 2022, including Gelli) that take into account physical prescriptions for the radiative transfer and reproduces the evolution of a large and diversified set of LBGs in the range $6 < z < 8$, described in Chapter 5. In Chapter 6, I study the unprecedentedly large sample of satellite galaxies of the SERRA simulations, focusing on the distinction between the two main populations: actively star forming and passive satellites. By analysing their star formation histories we investigate the physical mechanisms leading to their quenching and the possibility of unveiling with JWST this population of non-star forming dwarfs at high-z for the first time (Gelli et al. 2021, to be submitted). Chapter 7 presents the interpretation of the first passive low-mass galaxy observed with JWST at $z \sim 7$ (Gelli et al., 2023). In Chapter 8 we move back to the Near-Field cosmology approach by presenting the PISN-EXPLORER: a new tool combining theoretical models with stellar spectral analysis to discover the local descendants of PopIII stars that have been polluted by PISN (Aguado et al., 2023, including Gelli). Ultimately, in Chapter 9 I summarize the results and discuss both implications and possible future plans.

CHAPTER 2

Simulating high-z galaxies

Numerical simulations represent an invaluable tool to study the formation and evolution of structures in the Universe in a full cosmological framework. They allow us to investigate the Universe at all length and mass scales, from large web-like structures of filaments, to small dwarf galaxies. In the first part of this Thesis we analyse indeed dwarf galaxies properties by taking advantage of an already available state-of-the-art cosmological simulation developed by Pallottini et al. (2017b) (hereafter P17), that targets a typical Lyman break galaxy at $z \sim 6$. The simulation is carried out using a customised version of the adaptive mesh refinement (AMR) code RAMSES (Teyssier, 2002) and it is performed with a zoom-in technique. As typically done in cosmological simulations, the initial conditions are set based on the initial gaussian random field of density perturbations, dark matter and stars are treated as non-collisional particles, and the gas as a collisional fluid. In this Chapter we describe firstly how the evolution of these components is solved numerically, then how the simulation run is performed in P17 and how additional physics and feedback processes are taken into account.

2.1 Numerical methods

In order to reproduce the evolution of the different matter components of the Universe in a large simulation box, we need a code that efficiently couples N-body evolution (DM and stars) with hydrodynamics (gas). The code RAMSES, adopted by P17, uses eulerian methods, that discretise the space using a fixed grid. These methods describe the gas dynamics very accurately, but the spatial resolution is limited to the cell size of the grid. To improve the resolution, the so called Adaptive

Mesh Refinement (AMR) technique is used: the spatial grid is continuously refined in smaller cells when certain conditions are satisfied, e.g. if the region is sufficiently dense. In the following we highlight the general features of the main methods used in the simulation.

2.1.1 N-body evolution

Collisionless fluid, like cold dark matter or stars, is represented through a collection of particles of a certain mass. For a simulation to correctly reproduce both the large scale structure with a large number of haloes, and the detailed internal structures of haloes, it needs to have: (i) a very large volume, and (ii) a small minimum particle mass, the so called mass-resolution $\mathrm{M_{res}}$. For instance, if we want to study dwarf galaxies with masses as low as $\mathrm{M_\star} \sim 10^7 \mathrm{M_\odot}$, we need the mass resolution to be smaller than such values, typically $\mathrm{M_{res}} \sim 10^{5-6} \mathrm{M_\odot}$, depending on the precision required to study the problem. As a consequence of the above two requirements, a detailed simulation will necessarily consist in a very large number of particles N. The evolution of a N-body collisionless system is described by the Vlasov-Poisson equations, which read[1]:

$$\frac{\mathrm{d}\mathbf{x}_\mathrm{i}}{\mathrm{d}t} = \mathbf{v}_\mathrm{i} \tag{2.1}$$

$$\frac{\mathrm{d}\mathbf{v}_\mathrm{i}}{\mathrm{d}t} = -\nabla\Phi(\mathbf{x}_\mathrm{i}) \tag{2.2}$$

$$\nabla^2\Phi = 4\pi\mathrm{G}\rho \tag{2.3}$$

where $\mathbf{x}_\mathrm{i}$ and $\mathbf{v}_\mathrm{i}$ are the position and velocity of the particle i, Φ is the gravitational potential and ρ the mass density. RAMSES uses one of the most common methods to numerically solve these equation, i.e. through so called Particle-Mesh codes (Hockney & Eastwood, 1988), based on numerical integration on a grid (or "mesh"). Grid-based N-body schemes are solved in three main steps:

1) compute the mass density ρ on the grid from particle location,

2) solve the Poisson equation on the grid,

3) interpolate the force back to the particle position.

[1]To account for the cosmological environment, the so called "super-moving coordinates" depending on cosmological parameters and the scale factor a are used (e.g. Martel & Shapiro, 1998)

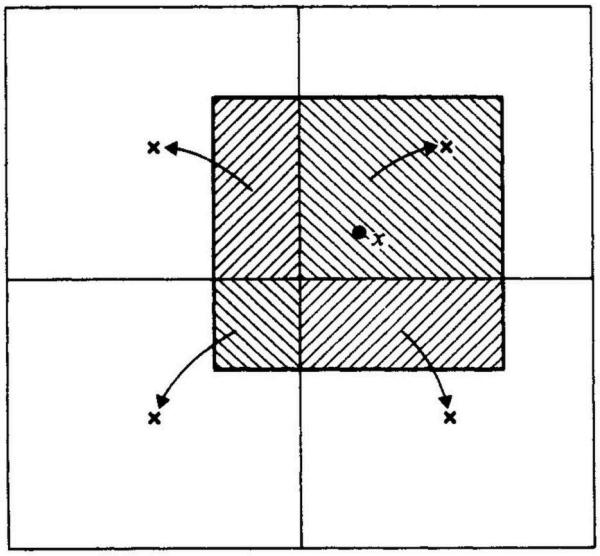

Figure 2.1: Two dimensional Cloud-In-Cell. The particle is located at position x and in two dimensions it has a quadratic shape (shaded ares). The fraction of mass assigned to the four neighbour mesh cells (the four squares with the central x) is given by the area of overlap of the particle shape with the cells. From Hockney & Eastwood (1988).

Step 1 is performed using a "Cloud-In-Cell" interpolation scheme. Each particle is assumed to have a cubical shape, and a fraction of its mass is assigned to each neighbour mesh cell according to the overlapping area, as schematically shown in Fig. 2.1.

Once the density field $\rho(\mathbf{x})$ is known, Poisson equation 2.3 can be solved on the grid (step 2) through Fast Fourier Transform techniques. The force can then be computed by differentiating the potential and finally it can be interpolated back to update particle velocities and then positions (step 3).

For the time integration, a kick-drift-kick leapfrog method is used, in which velocity is updated twice during a single time step when solving the equations of motion. The procedure determining the evolution from t to $t + \Delta t$ is:

$$\mathbf{v}_{\mathrm{i}}(t + \Delta t/2) = \mathbf{v}_i(t) - \nabla_i \Phi(t) \Delta t/2 \tag{2.4}$$

$$\mathbf{x}_i(t + \Delta t) = \mathbf{x}_i(t) - \mathbf{v}_i(t + \Delta t/2) \Delta t \tag{2.5}$$

$$\mathbf{v}_i(t + \Delta t) = \mathbf{v}_i(t + \Delta t/2) - \Delta t \, \nabla_i \Phi(t + \Delta t/2)/2. \tag{2.6}$$

The method is second order in time and the operators are symplectic, i.e. explicitly energy conserving, thus typically preferred in cosmological codes (e.g Springel, 2005; Wadsley et al., 2004; Bryan et al., 2013).

2.1.2 Gas dynamics

The evolution of the gas is described by Euler equations, which are solved on the grid in their conservative form:

$$\frac{\partial \rho}{\partial t} + \nabla \cdot (\rho \mathbf{u}) = 0 \tag{2.7}$$

$$\frac{\partial}{\partial t}(\rho \mathbf{u}) + \nabla \cdot (\rho \mathbf{u}\mathbf{u}) + \nabla P = -\rho \nabla \Phi \tag{2.8}$$

$$\frac{\partial}{\partial t}(\rho e) + \nabla \cdot [\rho \mathbf{u}(e + P/\rho)] = -\rho \mathbf{u} \cdot \nabla \Phi + \mathcal{H} + \mathcal{L} \tag{2.9}$$

where ρ is the mass density, $\mathbf{u}$ is the fluid velocity, e is the specific total energy, $\mathcal{H}$ and $\mathcal{L}$ are the heating and cooling terms, and P is the thermal pressure such that $P = (\gamma - 1)\rho(e - \frac{1}{2}\rho^2)$, with γ being the adiabatic index.
In each grid point, the system is solved using a second order Godunov approach based on Riemann solvers (e.g. Toro, 2013).

2.1.3 Time step

As an explicit time evolution scheme is used for both particles and gas, the time step is carefully determined using stability constraints for both N-body and hydrodynamical solvers. Physical processes must be evolved with the proper timescale, therefore many different constraints due to different physical conditions must be considered. The actual time step will be equal to the minimum of four different values:

$$\min \begin{cases} \Delta t_1 = C_1 \min(t_{ff}) \\ \Delta t_2 = C_2 \frac{\Delta x}{\max(\mathbf{v}_i)} \\ \Delta t_3 = C_3 a/\dot{a} \\ \Delta t_4 = C_4 \frac{\Delta x}{(\max(\mathbf{u}) + c_s)} \end{cases} \tag{2.10}$$

where Δx is the spatial resolution of the grid, $\mathbf{v}_i$ is the particle velocity, $\mathbf{u}$ the gas velocity, a the scale factor of the expanding Universe, c_s the sound speed, and C_1, C_2, C_3, C_4 constants < 1. The first condition ensures that the time step is smaller than the free fall time (t_{ff}) of the gas. The second one imposes that during the time step particles should move by only a fraction of the cell size. The third specifies that the expansion factor should not vary excessively over a time step. The fourth condition is the so called Courant-Friedrich-Levy condition, stating that the time step has to be smaller than the local gas dynamical timescale.

The important role of the choice of the grid is now evident, since it limits the mass, spatial and time resolution, thus determining the nature of physical processes that can be accounted for.

2.1.4 Adaptive Mesh Refinement

The basic grid element in RAMSES is an oct, which is a cube composed of eight cells in the three-dimensional space of the simulation. The cells store the local properties of the gas like density, momentum and metallicity, and the gravitational force. The Adaptive Mesh Refinement method is based on the fact that each cell can be recursively refined to contain sub-octs (see Fig. 2.2). Each oct is labeled with a given level of refinement l. The base of the grid structure is a regular cartesian grid, called the coarse grid, with refinement level $l = 0$. The time step as seen in Sec. 2.1.3 is determined for each level l independently. An important rule is that the resolution should never change by more than one level across shell boundaries. The refinement happens automatically during the simulation run based on the criterion chosen. For cosmological simulations the refinement strategy is usually based on a Lagrangian approach: the idea is to obtain a constant number of particles per cell (Kravtsov et al., 1997), so that two-body effects are minimised. According to this approach, a cell at level l is refined when the density exceeds a level dependent density threshold defined as:

$$\rho_l = M_c \times (\Delta x^l)^{-3} \tag{2.11}$$

where Δx^l is the cell size at level l, and M_c is the maximum mass per cell. As an example we show in Fig. 2.3 the simulation (Pallottini et al., 2017a) density contrast (left panel) and the consequent level of refinement obtained (right panel). Note that the time evolution is treated with a multigrid-tecnique, i.e. on each level l more operations are combined: restriction (to correct quantities based on the time evolution of the coarser level $l - 1$), solution of the Euler equation at the current level l, and prolongation (propagation of the solution to the finer level $l + 1$). See

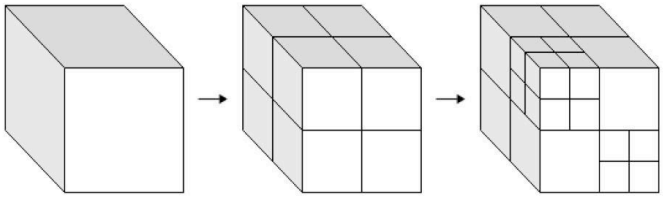

Figure 2.2: An oct refined in sub-octs.

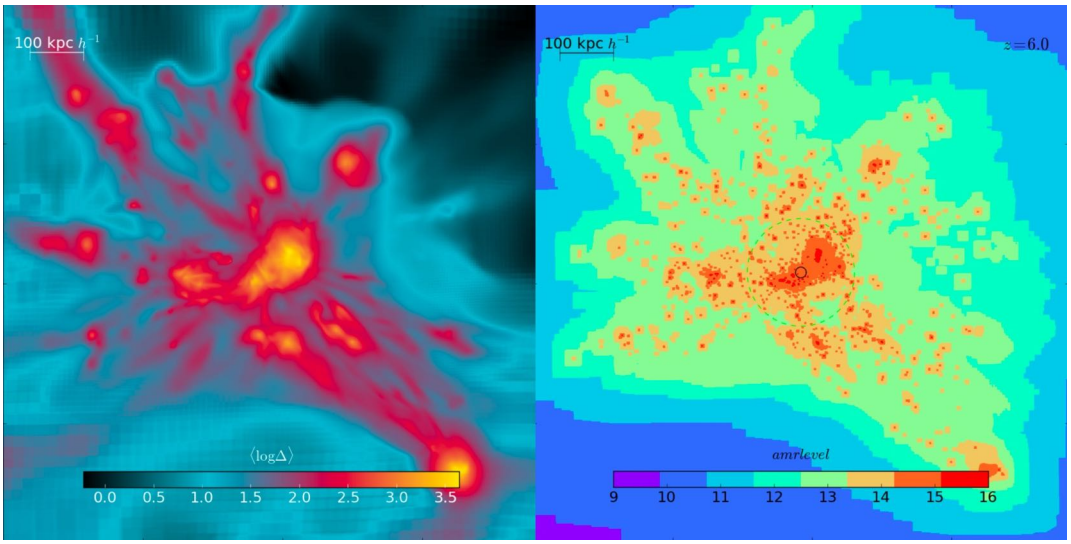

Figure 2.3: A simulation box of size ∼1 Mpc is shown. The colormaps show the density contrast (left panel) and adaptive mesh refinement level (right panel).

Khokhlov (1998) and Teyssier (2002) for details.

2.2 The zoom-in simulation

We now focus on the simulation that we will use for our dwarf satellite galaxies analysis in the next chapters, i.e. Pallottini et al. (2017b). The simulation uses the so called zoom-in technique. The main idea behind it resides in identifying interesting objects in the simulation and focusing the computational resources in sub-volumes containing them. The smaller region encapsulating the formation history of the object of interest is studied with much higher resolution. The sub-volume will be located inside of a lower resolution representation of the larger-scale cosmic environment interacting with the target object through long-range gravitational forces.

The procedure to set-up the zoom-in simulation consists in multiple steps. Firstly, initial conditions (IC) are needed at the starting time of the simulation, set at redshift $z_{start} = 100$. At this epoch density perturbations are still in the linear regime and thus described by a gaussian random field. In P17 ICs[2] are generated with MUSIC (Hahn & Abel, 2011).

The first run performed is a dark matter only run, where a volume of $V^{cosmo} =$

[2] A ΛCDM model with parameters compatible with *Planck* results is assumed (Planck Collaboration et al., 2014): dark energy, matter and baryons density parameters $\Omega_\Lambda = 0.692$, $\Omega_m = 0.308$, $\Omega_b = 0.0481$, and Hubble constant $H_0 = 100h\,\mathrm{km\,s^{-1}Mpc^{-1}}$ with h=0.678.

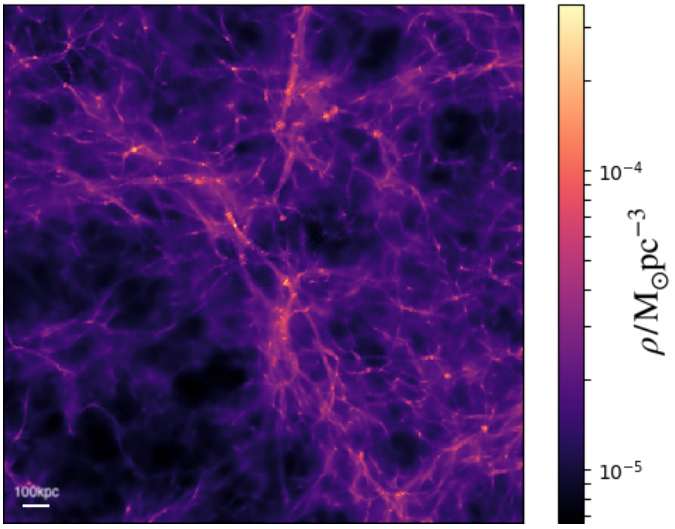

Figure 2.4: Dark matter density large scale distribution at the last snapshot ($z = 6$) of the simulation, in a box of 2 Mpc.

$(20\,\mathrm{Mpc}/h)^3$ evolves from redshift $z = 100$ to $z = 6$. During this run the dark matter mass resolution is $m_{\mathrm{DM}}^{cosmo} = 3.4 \times 10^7/h\,\mathrm{M}_\odot$, and the coarse grid spatial resolution is $\Delta x^{cosmo} = 78.1/h\,\mathrm{kpc}$. No additional levels of refinement are included at this step. The result of this run at $z = 6$ is a the large scale structure in the simulated box, characterised by filaments and a great number of DM haloes, as shown in the snapshot in Fig. 2.4. At this point the target object for the zoom-in high resolution simulation has to be chosen. A catalogue of the dark matter haloes present is obtained using HOP (Eisenstein & Hut, 1998). HOP is an halo-finder, i.e. a method for identifying groups of particles inside N-body simulations. From the catalogue a halo with DM mass $\mathrm{M_h} \simeq 10^{11}/h\,\mathrm{M}_\odot$ is selected. Its virial radius at $z \sim 6$ is $\mathrm{r_{vir}} \simeq 26$ kpc. A selected region surrounding this halo is traced back to $z = 100$, where its dimension determines the zoom-in volume: $V^{zoom} = (2.1\,\mathrm{Mpc}/h)^3$. The ICs are here recalculated, generating 3 additional levels of refinement (while the base grid has 8 levels). The finer dark matter mass resolution is now $m_{\mathrm{DM}}^{zoom} = 6.7 \times 10^4/h\,\mathrm{M}_\odot$, and the coarse grid scale is $\Delta x^{zoom} = 9.7/h\,\mathrm{kpc}$. The simulation is run again, this time including the baryonic matter

	Volume $[(\mathrm{Mpc}/h)^3]$	$m_{\mathrm{DM}}\,[\mathrm{M}_\odot/h]$	$m_{baryons}\,[\mathrm{M}_\odot/h]$	$\Delta x_{z=6}^{min}\,[\mathrm{pc}]$
cosmo	$(20)^3$	3.4×10^7	-	2.5×10^3
zoom-in	$(2.1)^3$	6.7×10^4	1.2×10^4	32.1

Table 2.1: Simulation resolutions for the cosmological run and subsequent zoom-in run.

component. During this zoom-in run, 6 additional levels of refinement are allowed, resulting at $z = 6$ in a final physical resolution of $\Delta x^{min} = 31.9/h\,\mathrm{pc}$ and baryonic mass resolution of $m_{baryons} = 1.8 \times 10^4/h\,\mathrm{M}_\odot$. A summary of the resolutions is reported in Table 2.1. We note that because of the high final spatial resolution, the simulation is expected to probe even the physical properties of the smaller satellite objects in the vicinity of the target halo. For instance the refined cell has mass and size typical of molecular clouds.

2.3 Astrophysical models

Let us now see how physical processes regarding gas cooling and star formation, along with stellar feedback and its effect on the gas component, are taken into account in the zoom-in simulation. The ICs for baryons consist in a primordial gas that at $z = 100$ has a mean molecular weight of $\mu = 0.59$. Moreover the initial gas metallicity is set to a floor value of $Z_{floor} = 10^{-3} Z_\odot$, with the solar value being $Z_\odot = 0.02$. As we have seen in Sec.1.4.2, this value mimics the pre-enrichment of the halo at very high redshifts ($z > 40$), where the simulation do not have enough resolution to accurately follow star formation. We thus highlight that, when performing stellar populations analysis in the next chapters, the most metal poor stars, forming in uncontaminated environment, will be represented by stars with $Z_\star = Z_{floor}$.

2.3.1 Star formation

In the simulation stars, or rather "star particles", form out of gas according to the so called Schmidt-Kennicutt relation (Kennicutt, 1998):

$$\dot{\rho}_\star = \zeta_{\mathrm{SF}} f_{\mathrm{H}_2} \frac{\rho_g}{t_{ff}} \tag{2.12}$$

where $\dot{\rho}_\star$ is the rate of stellar masses formed per unit time and volume, ζ_{SF} is the efficiency of star formation, f_{H_2} is the molecular hydrogen fraction (see Sec.2.3.3 for its calculation), ρ_g is the gas density, and t_{ff} is the free-fall time. ζ_{SF} is set to 0.1, according to observations of molecular clouds (Murray, 2011). We note that cells with number density less than $\sim 15\,\mathrm{cm}^{-3}$ are not allowed to form star particles, since the mass formed would be less than the baryonic mass resolution. The ability of the gas to form stars resides mainly in the amount of molecular gas present, that makes the cooling possible. Once a star particle has formed, it is necessary to assume an initial mass function (IMF, i.e. the mass distribution of

stars that form) for it to represent a realistic stellar population. The IMF chosen is a standard Kroupa IMF, which well reproduces observations of local star forming regions (Kroupa, 2001):

$$\Phi(m) \propto m^{-\alpha_1}\Theta(m_1 - m) + m^{-\alpha_2}\Theta(m - m_1)m_1^{\alpha_2-\alpha_1} \tag{2.13}$$

where m is the stellar mass ranging from $10^{-1}\mathrm{M}_\odot$ to $10^{2}\mathrm{M}_\odot$, $m_1 = 0.5\mathrm{M}_\odot$, $\alpha_1 = 1.3$ and $\alpha_1 = 2.3$. The proportionality constant is chosen such that the IMF is normalised to 1.

2.3.2 Stellar feedback

To understand how stars influence the surrounding interstellar and intergalactic medium, we need to know how stellar evolution has been taken into account in the simulation. In fact stars produce different amounts of radiation, mechanical energy and metals based on their mass, age and metallicity. Heavy elements and mechanical energy injection are due to both SN explosions and stellar winds by O/B or AGB stars.

Chemical feedback is described through the so called return fractions (R) and yields (Y), i.e. respectively the amount of mass returned into the ISM and of metals produced and injected into it. Both these quantities depend on the age $t_\star$ of the stellar population, and on the IMF $\Phi(m)$:

$$R(t_\star) = \int_{m(t_\star)}^{100\mathrm{M}_\odot} [m - w(m, Z_\star)]\Phi(m)\,\mathrm{d}m \tag{2.14}$$

$$Y(t_\star) = \int_{m(t_\star)}^{100\mathrm{M}_\odot} m_Z(m, Z_\star)\Phi(m)\,\mathrm{d}m \tag{2.15}$$

where w is the mass of the remnant and m_Z the metal mass produced by a star of mass m and metallicity $Z_\star$.

Mechanical energy is taken into account separately for stellar winds and SNe, and it is indicated by $\epsilon_\mathrm{w}(t_\star)$ and $\epsilon_\mathrm{SN}(t_\star)$, where only stars with mass $8\mathrm{M}_\odot < m < 40\mathrm{M}_\odot$ are assumed to explode as SNe (e.g. Woosley & Weaver, 1995a). The energy released by a single SN event is 10^{51}erg, independently of the mass of the star. Similarly, the radiative inputs due to stellar emission are taken into account through the quantities ϵ_UV and ϵ_ion, corresponding to the energy associated with the ultraviolet ($912\text{Å} < \lambda < 4000\text{Å}$) and ionizing ($\lambda < 912\text{Å}$) radiation. These two parameters accounts for radiation pressure, but do not include photo-evaporation effects. In order to estimate all of these quantities (R, Y, ϵ_w, ϵ_SN, ϵ_UV, ϵ_ion), a stellar evolutionary model needs to be assumed. In particular the one adopted in P17 has been

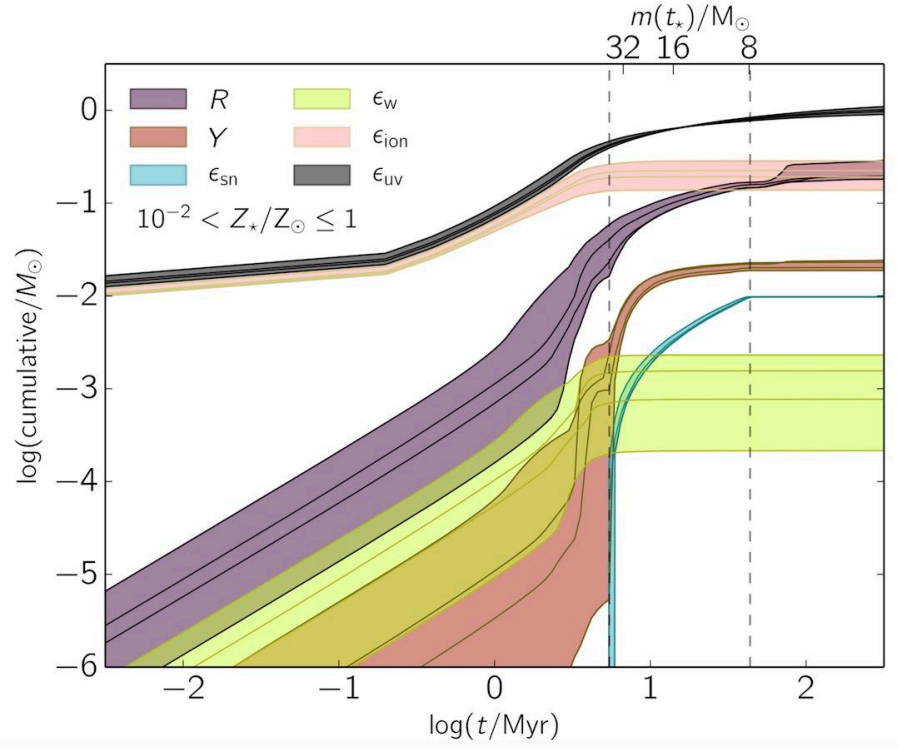

Figure 2.5: From Pallottini et al. (2017a). The cumulative fractions per stellar mass formed of stellar inputs (R, Y, $\epsilon_{\rm w}$, $\epsilon_{\rm SN}$, $\epsilon_{\rm UV}$ and $\epsilon_{\rm ion}$, as labeled in the legend) are shown as a function of stellar lifetime $t_\star$. The upper axis shows the minimum stellar mass with lifetime shorter than $t_\star$. Dark lines denote single metallicity stellar tracks, derived assuming Bertelli et al. (1994) evolutionary model. Vertical dashed lines bracket the time interval in which SNe explode.

computed using STARBURST99 (Leitherer et al., 1999), an online software designed to model spectrometric and physical properties of stellar populations. Stellar evolutionary tracks are taken from Padova model (Bertelli et al., 1994) for four stellar metallicities: $Z_\star/Z_\odot = 0.02$, 0.2, 0.2 and 1. The resulting quantities are shown in Fig. 2.5 as a function of the stellar age $t_\star$. The shaded regions cover the chosen metallicity range, where the four selected $Z_\star$ values are marked by the black lines. Massive O/B stars emission and winds mainly contribute for $\log(t/\mathrm{Myr}) \lesssim 0.8$. The vertical dashed lines enclose the range in which we have SN explosions, i.e. $0.8 \lesssim \log(t/\mathrm{Myr}) \lesssim 1.6$. At late times, $\log(t/\mathrm{Myr}) \gtrsim 1.6$, we find AGB stars contribution, whose effect makes only R and Y increase slightly, meaning that they inject metals and gas into the medium but mechanical energy is negligible.

To better understand the effect of feedback from a stellar population, we can look at the specific luminosity (i.e. energy injection per unit time and mass) from radiation, winds and SNe, shown in Fig. 2.6 (Agertz et al., 2013)[3]. While radiation

[3]Geneva high mass loss stellar tracks are here assumed instead of Padova.

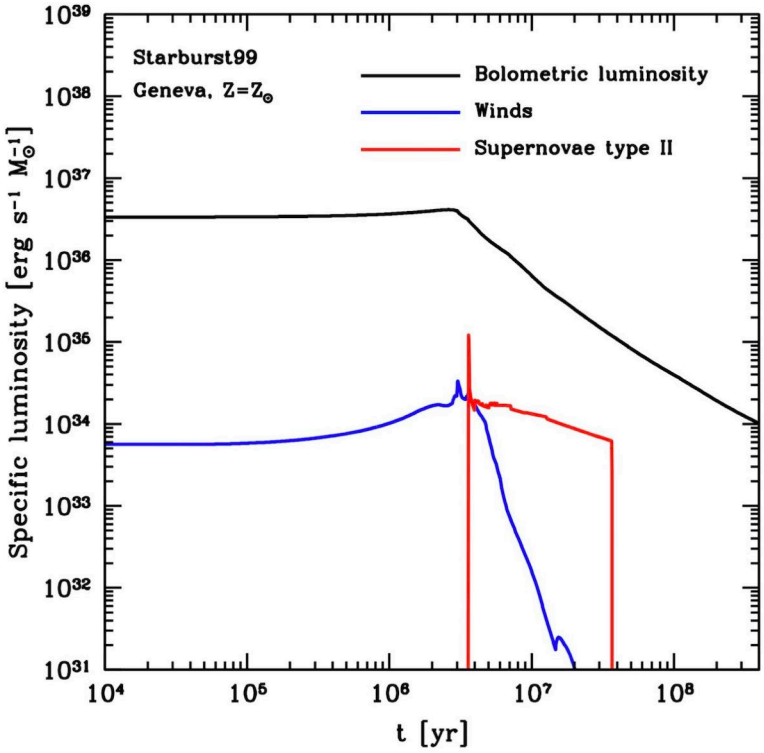

Figure 2.6: Specific luminosity from radiation, stellar winds and supernovae (type II), from Agertz et al. (2013). The energy per unit time and stellar mass is shown as a function of the age of the stellar population, whose evolutionary tracks have been computed with STARBURST99 for Geneva high mass model and stellar metallicity $Z_\star = Z_\odot$.

and stellar winds operate immediately after the birth of the stellar population, the first SNe, due to massive $\sim 40 M_\odot$ stars, explode after ~ 4 Myr. We see that the specific luminosity of the most massive stars, which are the first that are able to explode as SN, is higher by one order of magnitude with respect to those exploding immediately later. This behaviour is due to the fact that the first SN blastwaves dramatically heat the surrounding gas, which had already been pre-heated due to early wind injection and radiation. As a consequence of this efficient coupling between radiation and SNe, the overall effect of negative feedback greatly increases during these first explosions.

2.3.3 Gas chemistry and radiation field

The simulation adopts a non-equilibrium chemical network by KROME (Grassi et al., 2014). It takes into account many elements, ions and molecules (H, H^+, H^-, He^+, H^{++}, H_2, H_2^+), with reactions including photo-chemistry, dust processes and cosmic rays. For metal species evolution, tabulated metal cooling/photo-heating rates

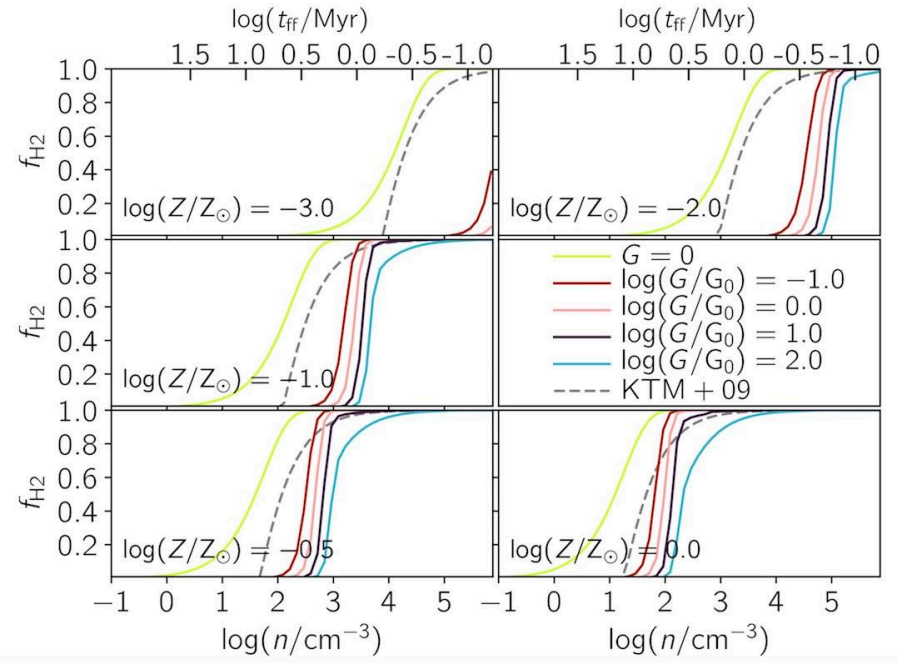

Figure 2.7: From Pallottini et al. (2017b). H_2 mass fractions f_{H_2} as a function of density n are shown, the upper axis indicating the correspondent free-fall times. Different panels show the results for different metallicities Z of the gas, while colors indicate different impinging radiation fields G, varying from $G = 0$ to $G = 10^2 G_0$. For comparison, a model where abundance is derived by modelling the radiative transfer on an idealized molecular could (Krumholz et al., 2009) is reported in the grey dashed lines.

from CLOUDY (Ferland et al., 2013) are assumed. The initial conditions for the various species are calculated following Galli & Palla (1998) and account for the primordial chemistry at very high redshifts $z \gtrsim 100$.

A key feature is the interstellar radiation field (ISRF). It is approximated as *spatially uniform* and its intensity is proportional to the global star formation rate (SFR), i.e. the stellar mass formed per unit time in the simulation box. Ionizing radiation below 912 Å is not included. The intensity G in the FUV Habing band ($6\,\mathrm{eV} < h\nu < 13.6\,\mathrm{eV}$) of the ISRF is given by:

$$G(t) = G_0 \frac{\mathrm{SFR}(t)}{\mathrm{M_\odot yr^{-1}}} \tag{2.16}$$

where $G_0 = 1.6 \times 10^{-3} \mathrm{erg\,cm^{-3} s^{-1}}$ is the average Milky Way value (Habing, 1968). We note that $G(t)$ will in general grow in time, due to the increasing star formation rate of the simulated high-redshift galaxy, as we will better see in Chapters 3 and 6. As a consequence we expect negative radiative feedback due to the ISRF to be more and more efficient through cosmic time.

Dust is also taken into account in the simulation, by making the simple as-

sumption of the dust mass being proportional to the metal mass: $\mathcal{D} = \mathcal{D}_{\odot}(Z/Z_{\odot})$, with $\mathcal{D}$ the dust-to-gas mass ratio and $\mathcal{D}_{\odot} = 6 \times 10^{-3}$ the solar value (Hirashita & Ferrara, 2002). The role of dust is of fundamental importance since it mediates the formation of molecules, for instance the formation of H_2 happens largely on grains. The production of molecular gas is essential since it represents the key ingredient that allows the gas to cool down emitting radiation and therefore enabling star formation. Indeed, in the formation law of Eq.2.12 the star formation rate density is proportional to the fraction of molecular hydrogen f_{H_2}.
As a result of the model adopted, this fraction f_{H_2} of molecular hydrogen formed will depend on the gas density n, metallicity, the intensity of the radiation field and its past history. An example of the behaviour of f_{H_2} for a static patch of gas is displayed in Fig. 2.7, where different panels indicate gas with different metallicity, Z, and the colors indicate different flux values of the ISRF. One can conclude that, for example, at $Z = Z_{\odot}$ and $G = 10^2 G_0$ (cyan curve in the bottom right panel), star formation can happen if $n \gtrsim 260\,\mathrm{cm}^{-3}$.

2.4 A typical high-z Lyman Break Galaxy

The end result at the final snapshot of the simulation (at $z \simeq 6$, i.e. $t \approx 950$ Myr) in the zoom-in region consists in about 10 haloes that host galaxies. Among them, the most massive one represents the central target and it hosts a massive galaxy called "Althæa". It has a stellar mass of $M_{\star} \sim 10^{10} M_{\odot}$ and SFR $\sim 100\,M_{\odot}\mathrm{yr}^{-1}$, and is therefore representative of a typical Lyman break galaxy at $z = 6$. The results for density and temperature on different scales at $z = 6$ are shown in Fig. 2.8.[4] Althæa is located in the centre of a cosmic web knot, and it accretes material from the intergalactic medium mainly through three long filaments. Such filaments are slightly denser ($n \sim 10^{-2}\mathrm{cm}^{-3}$) and colder ($T \simeq 10^{3.5}\mathrm{K}$) than the IGM ($n \simeq 10^{-3}\mathrm{cm}^{-3}$ and $T \simeq 10^{4.5}\mathrm{K}$) and they extend for over ~ 100 kpc, also confirming previous findings (Dekel et al., 2009). On smaller scales, one can appreciate the presence of many smaller structures (of seizes $\lesssim 1$ kpc), much denser than the filaments and hosting galaxies. Some of these reside in the virial volume of Althæa (the virial radius being $r_{vir} \simeq 26$ kpc) and behave as its satellites, subjected to the potential well of the massive host. We can understand this better by looking at Fig. 2.9, showing the spherically-averaged radial density profiles for DM, stars

[4]Note that the snapshots shown are not from the Althæa simulation (P17), but from a previous work by Pallottini et al. (2017a), differing in the chemical prescriptions. However, the final morphological and large-scale properties of the two simulations are consistent.

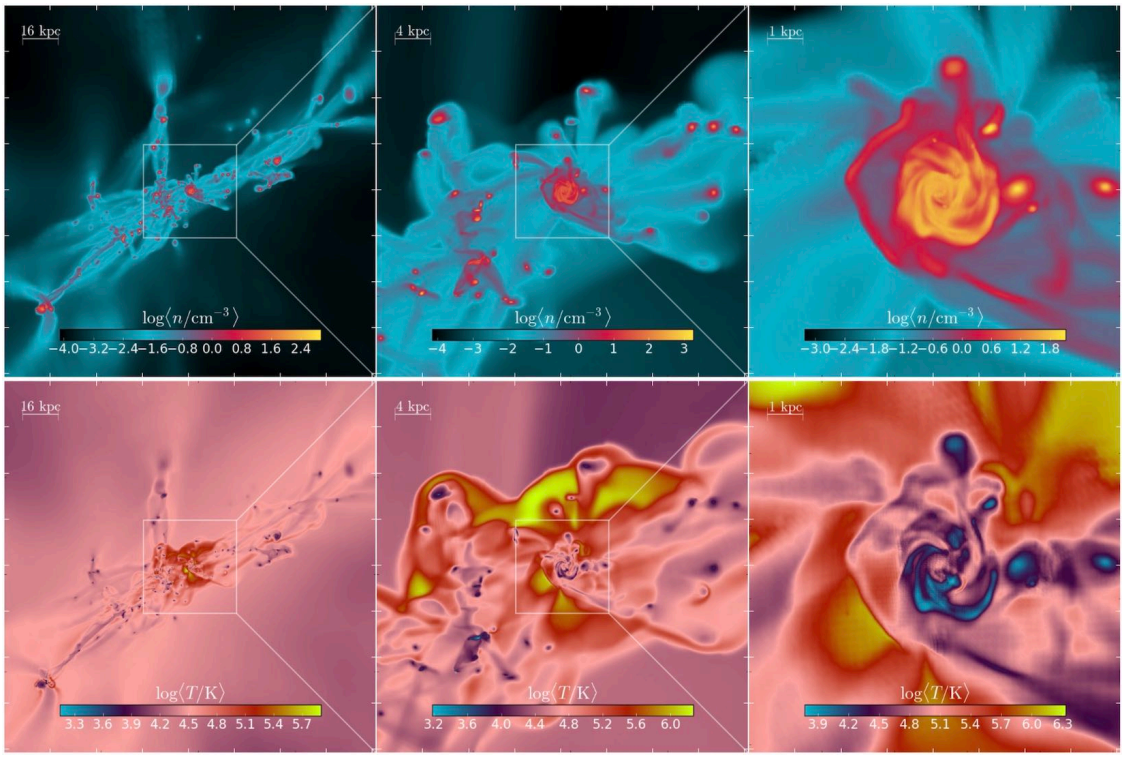

Figure 2.8: From Pallottini et al. (2017a). Maps of density n (top row) and temperature T (bottom row) at $z = 6$, with scales indicated in the insets. From left to right different zooms always centred on the central target galaxy are shown.

and gas in the inner $\simeq 12\,\mathrm{kpc}$ from the centre of Althæa (inner 100 pc in the inset). The stellar contribution dominates in the inner regions where the density reaches $\simeq 10^4\ \mathrm{M_\odot pc^{-3}}$. The gas density smoothly decreases from the central peak of $\simeq 100\ \mathrm{M_\odot pc^{-3}}$, but it exceeds the stellar density for $r \gtrsim 2\,\mathrm{kpc}$. At distances $\gtrsim 500\,\mathrm{pc}$ the DM becomes the dominant component. The grey curve represents the Navarro-Frenk-White (NFW) density profile (Navarro et al., 1997), obtained assuming a concentration parameter of $c = 4$ (e.g. Angel et al., 2016). Comparing it with the DM, we see that the two profiles are consistent at the scale radius $r_s = r_{vir}/c \simeq 6.5\,\mathrm{kpc}$ while in the inner regions the NFW features the classical cusp, which however is not present in the simulated halo. The absence of a cusp is actually in agreement with observations of DM profiles in local dwarf galaxies (e.g. Moore, 1994; Walker & Peñarrubia, 2011). While the absence of a cusp might have a physical origin (e.g. SN feedback, Pontzen & Governato, 2012), the spatial resolution of our simulation, although very high, is probably not yet sufficient to draw a firm conclusion on this issue, which in any case is beyond the scope of our study. The prominent peaks of the stellar and gas radial profiles in Fig. 2.9, pinpointed with gray arrows, correspond to our target satellite structures. We

also notice there are peaks in the gas radial profiles in the outer region ($\gtrsim 8$ kpc) that are instead associated with gas-rich, metal-poor, and star-less systems that have not formed stars yet. Not surprisingly, all the density enhancements are not seen in the DM component as Althæa's DM halo preserves a high density value ($\rho_{\rm DM} \gtrsim 10^{-2}$ M$_\odot$pc^{-3}) up to r_{vir}. Although, as we will see in Sec. 3.2.2, the satellites have a central DM density of $10 < \rho_{\rm DM}/$ M$_\odot$pc$^{-3} < 10^2$, their signal is washed away by the spherical average. The zoom-in simulation has an high enough resolution to allow us to study in details the properties of these dwarf satellite galaxies at high redshift. We are in particular interested in their stellar properties since they could enclose important information about how they formed, and how they are affected by the presence of a nearby massive object like Althæa and by the dense environment in which they are located. In the following Chapter 3 we address these questions and present an in-depth analysis of the physical, chemical and evolutionary properties of the simulated dwarf satellite galaxies.

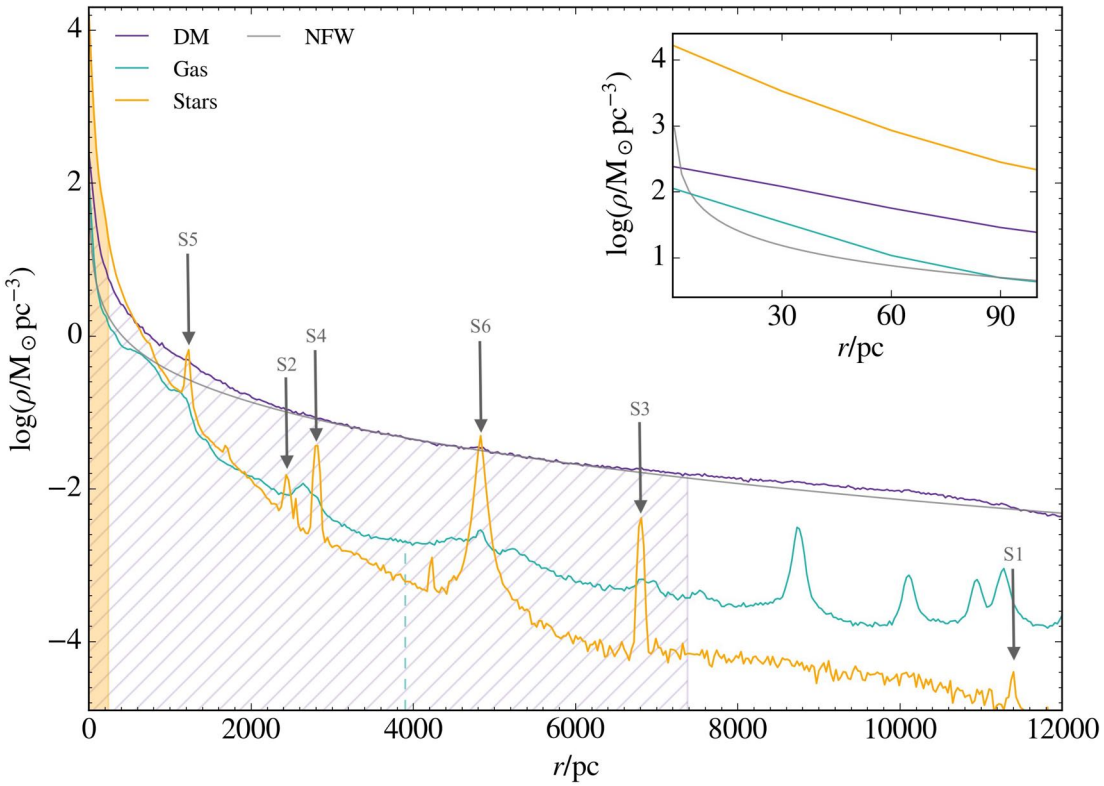

Figure 2.9: From Gelli et al. (2020). Spherically-averaged mass density profiles for DM, stars, and gas in Althæa. The shaded orange area, the dashed green line and the grey hatched area mark regions enclosing 50% of the stellar, gas and DM mass, respectively, contained in a volume of size 20 kpc centred on Aalthæa. The inset is a zoomed view of the inner 100 pc. The arrows locate the stellar overdensities corresponding to satellite galaxies.

CHAPTER 3

Dwarf satellites of high-z LBGs

One of the aims of this Thesis is to study the stellar and evolutionary properties of the faint high-redshift dwarf galaxies that are finally within our reach with the JWST. For this purpose we here present an analysis of the results of the numerical simulation by Pallottini et al. (2017b) presented in the previous Chapter, focusing not only on the massive main target galaxy Althæa, representative of a typical high-z LBG, but also specifically on the dwarf satellites that orbit around it. The results presented in this Chapter are mainly based on the paper Gelli, Salvadori, Pallottini & Ferrara (2020).

3.1 Satellites finder

The first issue we need to solve when aiming at analysing dwarf galaxies in simulations is pinpointing their location. The most used techniques consist in clustering algorithms based on local overdensities or distance-based Friends-of-Friends algorithms (e.g. Springel et al., 2001; Knollmann & Knebe, 2009; Behroozi et al., 2013b; Elahi et al., 2019). However, these methods fail to find the DM sub-haloes hosting dwarf galaxies satellites of a more massive galaxy, especially in the inner regions of the host halo where the DM preserves high density values ($\rho_{\rm DM} \gtrsim 10^{-2}$ M$_\odot$pc^{-3} up to r_{vir}, see Fig. 2.9). I hence developed a dwarf galaxies finder specifically for the satellites, based on the stellar component and with a *a posteriori* check of a DM profile for the identification. The adopted method is the following: we use stellar density maps centered on the central massive galaxy Althæa with size enclosing its virial radius (as the one shown in Fig. 3.1), and look for maxima in the stellar density field, using a threshold of $\simeq 10^{-2}$ M$_\odot$pc^{-3}. This search is performed in two

Table 3.1: Main properties of Althæa's satellites found at $z = 6$. The columns indicate (a) the satellite ID (indexed by increasing stellar mass), (b) distance from Althæa, (c) stellar mass, (d) gas mass, (e) halo mass. The stellar and gas masses are computed within a box of size 1 kpc centred on the satellite. The halo mass is computed as $M_h = (\Omega_m/\Omega_b)(M_\star + M_{gas})$.

Satellite	$D_{\rm Althaea}$ [kpc]	$M_\star$ [$10^8 M_\odot$]	M_{gas} [$10^8 M_\odot$]	M_h [$10^8 M_\odot$]
(a)	(b)	(c)	(d)	(e)
S1	11.42	0.022	2×10^{-4}	0.16
S2	2.45	0.72	0.53	5.36
S3	6.85	1.3	0.16	8.95
S4	2.85	2.2	0.47	16.3
S5	1.23	5.9	0.42	40.3
S6	4.86	11.1	0.53	71.1

maps with line-of-sight perpendicular to each other. We then combine the results to derive the coordinates in the 3D simulated space. The method identifies stellar overdensities but not necessarily *galaxies*, since it does not use any information on the dark matter content, which is then checked *a posteriori*.

We find a total of six satellites hosting stars (white circles of Fig. 3.1). They are numbered from S1 to S6 from the least to the most massive in terms of stellar mass. Tab. 3.1 reports their stellar ($M_\star$), gas ($M_{\rm gas}$) and halo (M_h) mass, along with the distance from the centre of the host galaxy, $D_{\rm Althaea}$. The stellar and gas masses are computed by summing the contribution within a box of size 1 kpc centred on the satellites. While such selected region is chosen as to be large enough to fully include the stellar component, this is not true for the DM component which is likely more extended. Furthermore we recall that the dwarf satellites are embedded in the environment of Althæa. For this reason we compute M_h through the cosmological baryon fraction as $M_h = (\Omega_m/\Omega_b)(M_\star + M_{gas})$, which represents a lower limit of the actual halo-mass. The stellar masses of the six objects range from $2.2 \times 10^6 M_\odot$ of S1 to $1.1 \times 10^9 M_\odot$ of S6; the gas masses are about ten times lower, in the range $\simeq 10^{5-8} M_\odot$. We will hereafter classify the satellites in three categories based on their stellar mass: low-mass (S1 and S2), intermediate (S3 and S4), and high-mass satellites (S5 and S6).

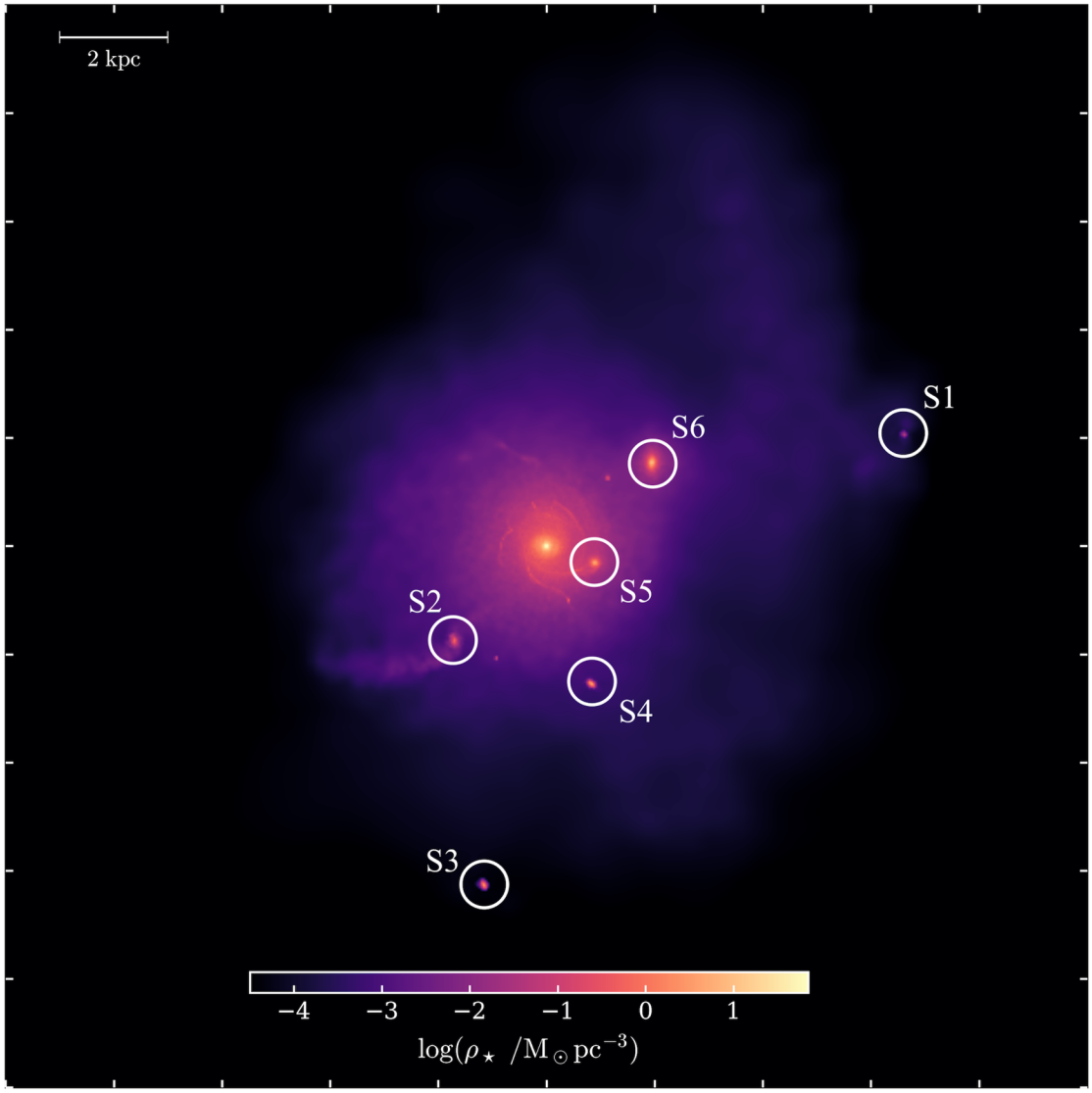

Figure 3.1: From Gelli et al. (2020). Stellar map centred on the simulated galaxy Althæa, at $z = 6$. The field of view is 20 kpc× 20 kpc (corresponding to $3'' \times 3''$ at $z = 6$). The color bar shows the mass-weighted stellar density values. White circles pinpoint the location of the six satellites, S1-S6, whose properties are summarised in Tab. 3.1.

3.2 The physical and stellar properties

3.2.1 Density maps

In Fig. 3.2 the stellar/gas density maps of the six satellites are shown. In low- and intermediate-mass satellites, stars are concentrated in the inner $\simeq 200\,\mathrm{pc}$, where $\rho_\star > 10^{-2}\ \mathrm{M_\odot pc^{-3}}$. More massive objects, i.e. S5 and S6, show a notable diffuse stellar component, with $10^{-2} < \rho_\star/\ \mathrm{M_\odot pc^{-3}} < 1$ in the outer $r > 200\,\mathrm{pc}$

regions. In all satellites, however, the stellar density distribution peaks at the centre ($r < 50\,\mathrm{pc}$), is very close to spherical, and – differently from the main galaxy Althæa – exhibits no hints of a disk (see Fig. 3.1). In most cases the gas distribution tracks the stellar one in the central regions, but it then extends up to larger radii, sometimes filling the entire field of view ($1\,\mathrm{kpc} \times 1\,\mathrm{kpc}$).

We note the peculiar case of the least massive and furthest satellite S1, whose density map indicates a considerable lack of gas. The little gas present ($M_{gas} = 2 \times 10^4$ $\mathrm{M}_\odot$) has an extremely low density, $\rho_{\mathrm{gas}} \simeq 10^{-4}$ $\mathrm{M}_\odot \mathrm{pc}^{-3}$, and a very peculiar distribution. Another quaint feature can be found in S2. In this satellite the gas is concentrated in two well-separated clumps, displaced from the bulk of the stellar population. S2 is located at the edge of Althæa's disk (Fig. 2.9, also seen as a density discontinuity in Fig. 3.1). It is unclear whether the ongoing interaction might be responsible for the displacement. However, this interpretation is possibly supported by the presence of two stellar streams in S2 which might result from tidal forces. Stellar streams are also found in S5, which is the closest

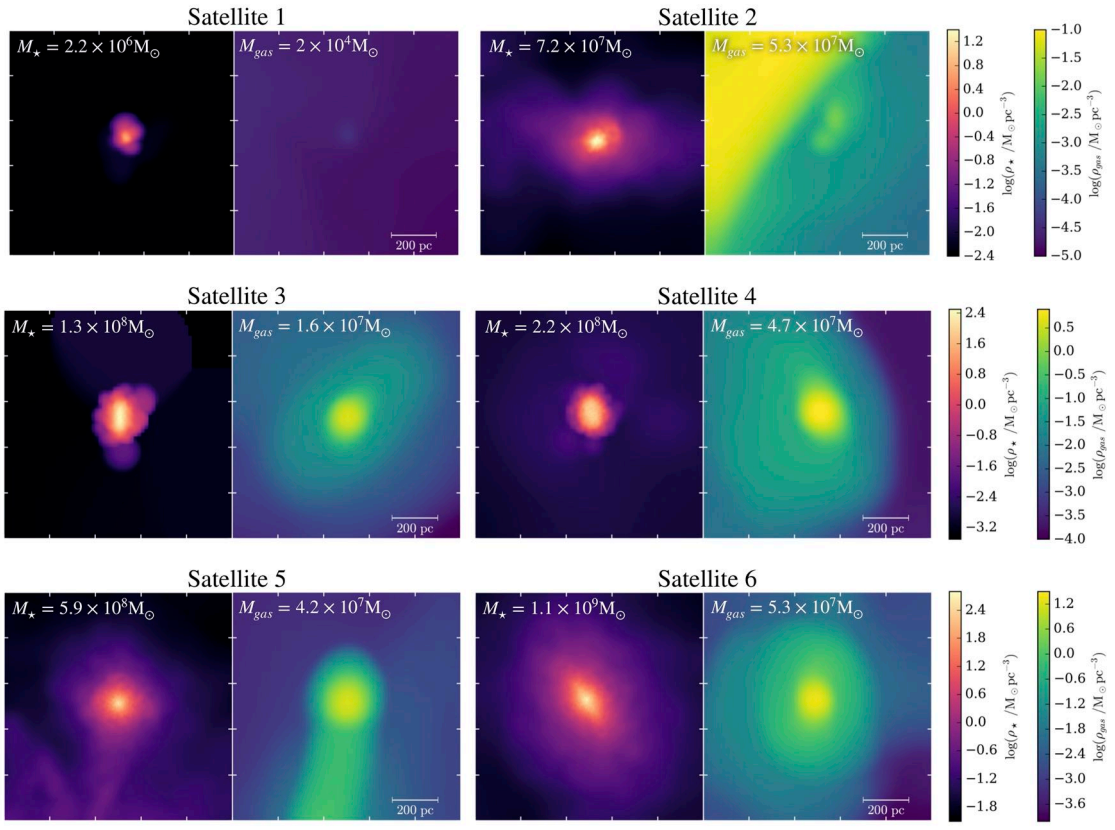

Figure 3.2: From Gelli et al. (2020). Stellar and gas density maps of the six satellites. Each map is obtained by mass averaging the density along the line of sight in a box of size 1 kpc that is centred on the stellar centre of mass of the satellite.

to Althæa ($D_{\text{Althæa}} = 1.23\,\text{kpc}$), while they are not seen in more distant satellites. We later analyse the physical and chemical properties of the streams in Sec. 3.2.4.

3.2.2 Radial profiles

A more quantitative interpretation of the density field properties of gas, stars, and dark matter can be inferred through the spherically-averaged radial density profiles shown in Fig. 3.3. We immediately notice two common features among these systems: (a) stars dominate the total mass in the inner regions ($r < 100\,\text{pc}$); (b) the central density increases with the satellite $M_\star$, from $\rho_\star \simeq 1\ \text{M}_\odot\text{pc}^{-3}$ for S1 ($M_\star = 2.2 \times 10^6\ \text{M}_\odot$) to $\rho_\star \simeq 10^3\ \text{M}_\odot\text{pc}^{-3}$ for S6 ($M_\star = 1.1 \times 10^9\ \text{M}_\odot$).

The low- and intermediate-mass satellites have the entirety of their stars confined in the inner 100 pc. The only exception is represented by satellite S2, whose stellar density flattens after $\simeq 150\,\text{pc}$ due to the presence of the stellar streams visible in the density map (Fig. 3.1). S2 also has a peculiar gas distribution with an independent increase at high radii caused by the diffused gas surrounding Althæa itself.

The dark matter masses range between $5 \times 10^6\ \text{M}_\odot \lesssim M_{\text{DM}}(r < 600\text{pc}) \lesssim 5 \times 10^8\ \text{M}_\odot$ in the displayed inner regions of the satellites. Its profile has typically a central peak as well, but it shows a more uniform distribution throughout the galaxy: it slowly decreases with radius until it reaches the underlying profile of the dark matter halo of Althæa. This is highlighted in each plot by the grey bar on the right axis indicating the DM density range in Althæa (purple curve in Fig. 2.9) in $r = D_{\text{Althæa}} \pm 600\,\text{pc}$.

In all satellites, the gas mass represents $\approx 10\%$ of the stellar mass. This is not unusual for dwarf galaxies since, due to their shallow potential well, they are unable to retain large amounts of gas which is easily evacuated.

We point out the interesting profile of the smallest satellite S1, characterised by the lowest values of stellar, gas, and dark matter densities. Due to the low amount of dark matter particles in the selected volume of $1\,\text{kpc}^3$, in order to obtain a radial profile we averaged over a length of 150 pc, i.e. larger than the spatial resolution. The resulting profile shows the floor value of Althæa dark matter halo, with no evidence of a central dark matter density peak. As a consequence, S1 cannot be considered as a dwarf galaxy. However, the mean velocity of the simulated stellar particles in the satellite centre of mass reference frame is $\langle \text{v} \rangle \simeq 14\ \text{km}\,\text{s}^{-1}$, lower than the escape velocity of $\text{v}_{\text{esc}} \simeq 19\ \text{km}\,\text{s}^{-1}$. This suggest that this object is

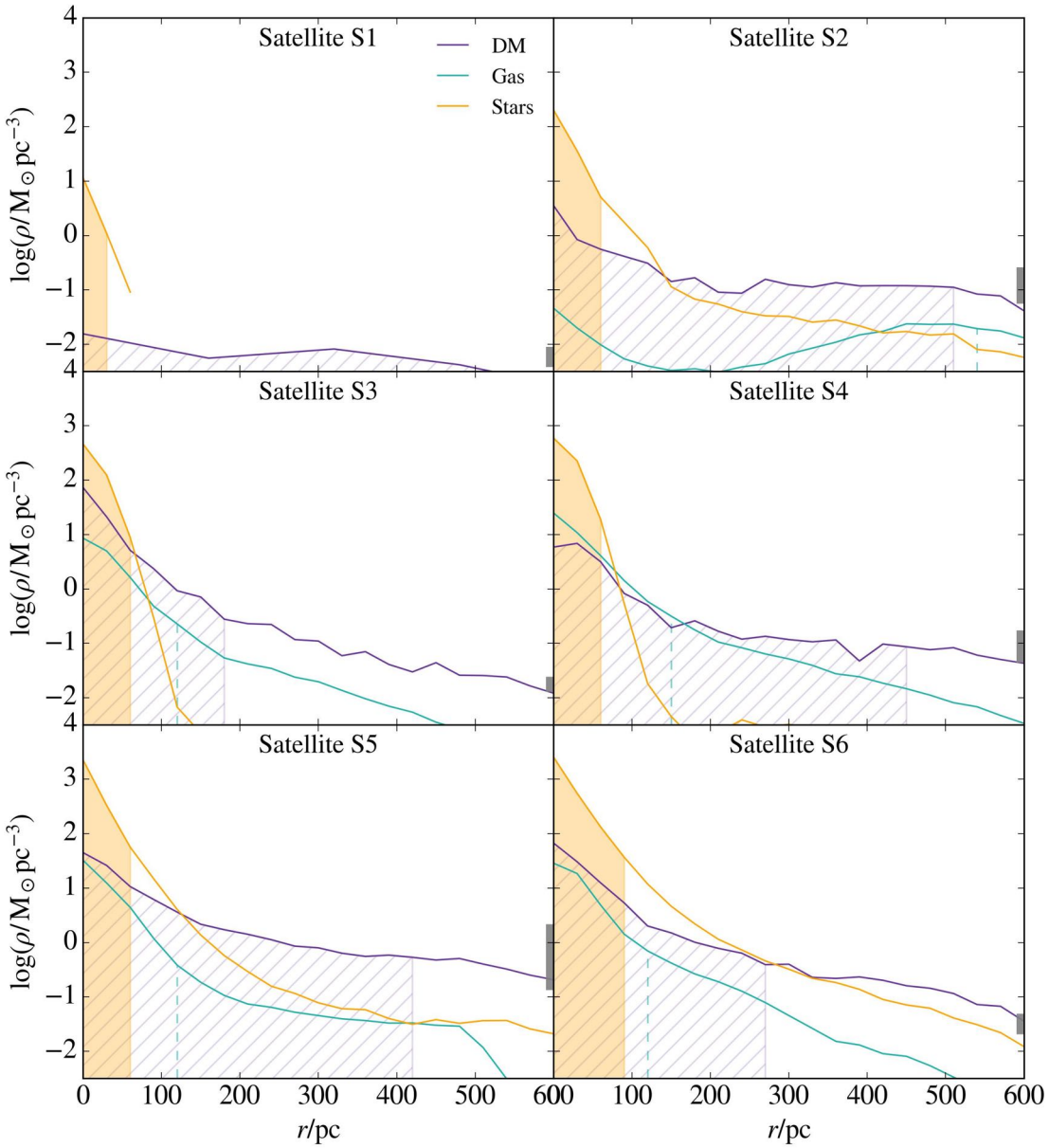

Figure 3.3: From Gelli et al. (2020). Density profiles for the six satellite galaxies. For each satellite, we plot spherically-averaged mass densities for the stellar, gas, and dark matter component. The shaded orange area, the dashed green line and the grey hatched area indicate the regions enclosing 50% of the stellar, gas and DM mass, respectively. The vertical thick line at $r = 600\,\mathrm{pc}$ shows the range of values of the DM profile of Althæa (Fig. 2.9) between $r = D_{\mathrm{Althæa}} \pm 600\,\mathrm{pc}$. See Tab. 3.1 for the total masses of individual satellites.

gravitationally bound, and has virtually no dark matter: a situation akin to what recently measured in (proto-)globular clusters (Vanzella et al., 2017).

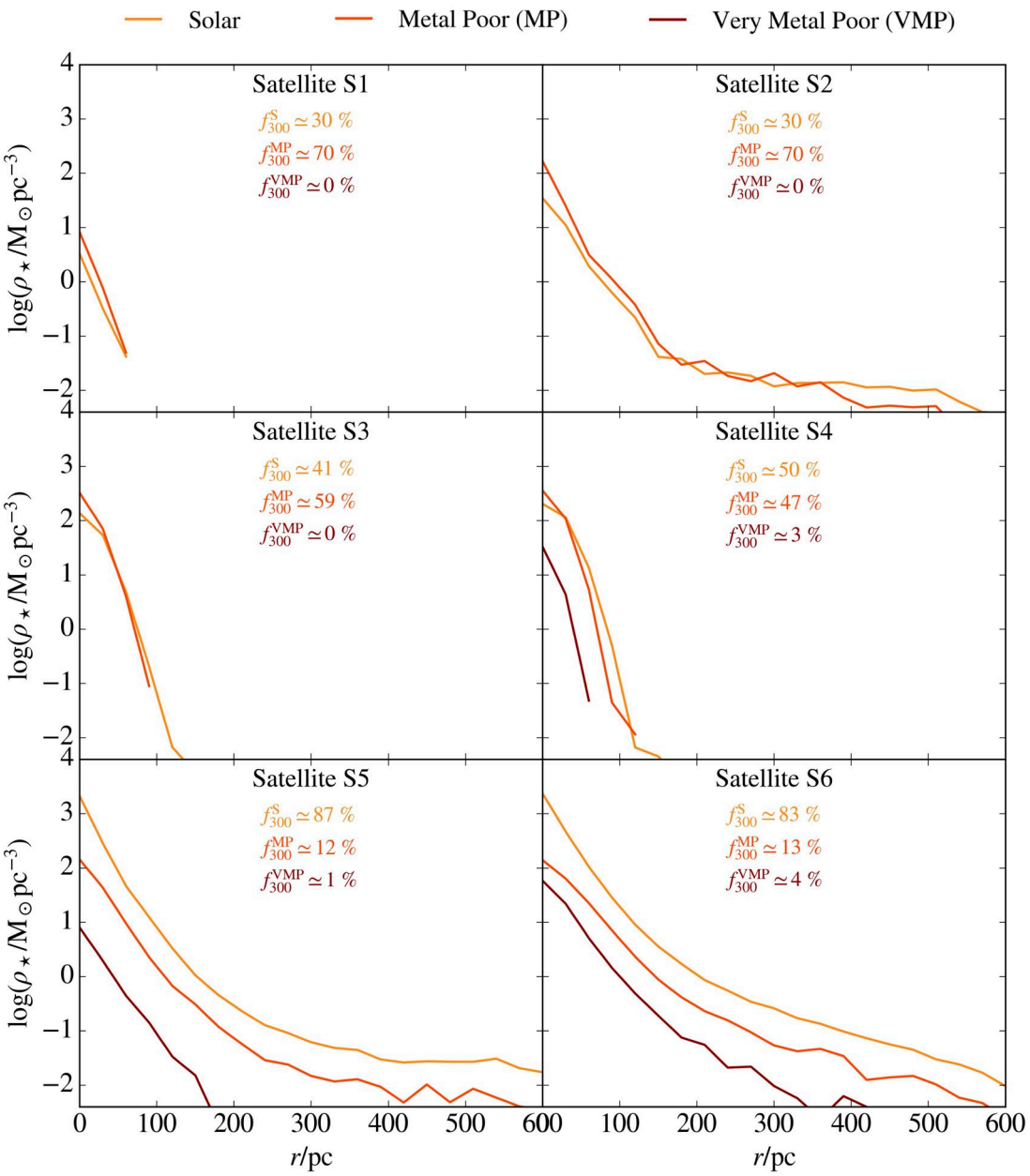

Figure 3.4: From Gelli et al. (2020). Radial profiles of the different stellar populations in each satellite. For each satellites we distinguish different populations based on three metallicity intervals: Solar $\log Z_\star/\,\mathrm{Z}_\odot \geq -0.5$, Metal Poor (MP) $-2 \leq \log Z_\star/\,\mathrm{Z}_\odot < -0.5$ and Very Metal Poor (VMP) $\log Z_\star/\,\mathrm{Z}_\odot < -2$. Similarly to Fig. 3.3, profiles are spherically-averaged and mass weighted. We also indicate the mass fraction of Solar (f_{300}^{S}), MP (f_{300}^{MP}) and VMP (f_{300}^{VMP}) stars in the inner 300 pc of each satellite.

3.2.3 Stellar metallicity

In order to investigate the stellar populations of the satellites, we divided their stars into three categories according to their metallicity. We will hereafter refer

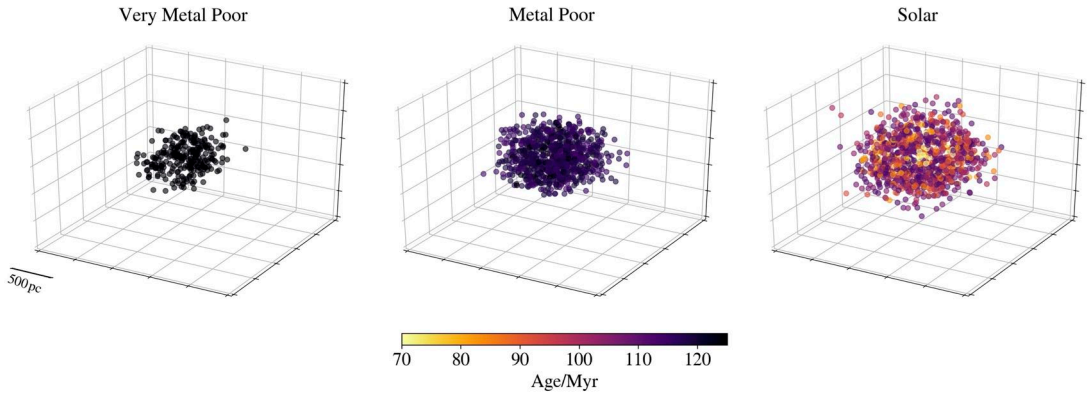

Figure 3.5: From Gelli et al. (2020). 3D spatial maps of an intermediate mass satellite S4 ($M_\star = 2.2 \times 10^8$ $M_\odot$) at $z = 6$. Stars are divided in three metallicity intervals as in Fig. 3.4. In the Metal-Poor and Solar ranges we show 1/6 of the particles, selected randomly, in order to reduce superposition effects. The colorbar indicates the age of each stellar particle.

to *Solar metallicity* stars if $\log(Z_\star/Z_\odot) \geq -0.5$, to *Metal Poor* stars (MP) if $-2 \leq \log(Z_\star/Z_\odot) < -0.5$, and to *Very Metal Poor* stars (VMP) if $\log(Z_\star/Z_\odot) < -2$. Fig. 3.4 shows the spherically-averaged density profiles of these three stellar populations. VMP stars are only present in the most massive satellites S4, S5, and S6 ($M_\star \gtrsim 1.5 \times 10^8$ $M_\odot$); they are always located in the inner regions, and constitute a subdominant stellar population (VMP mass fraction $< 5\%$ at all radii).

MP stars are also a sub-dominant population in the most massive satellites (S5 and S6), which at all radii are dominated by Solar metallicity stars ($80 - 90\%$ of the total stellar mass). Interestingly, in intermediate- (S3 and S4) and low-mass (S1 and S2) satellites MP stars represent on average $60 - 70\%$ of the total stellar mass, and this fraction is even higher in the inner regions.

To understand how different stellar populations are spatially distributed, in Fig. 3.5 we show a rendering of the 3D positions of stellar particles in a typical dwarf satellite (the intermediate-mass S4), color coded with their age at $z \simeq 6$. VMP stars are the oldest, they are more compact and more centrally-concentrated. Conversely, all very young stars have $Z_\star \simeq Z_\odot$ and they are more extended. In spite of these differences, all three stellar populations show a remarkably spherical distribution.

3.2.4 Stellar streams

We now discuss the origin of the stellar streams that are present in the external regions of the two satellites S2 and S5 (see Sec. 3.2.1). The presence of these streams may be expected since they are the two closest satellites to Althæa ($D_{\text{Althæa}} <$

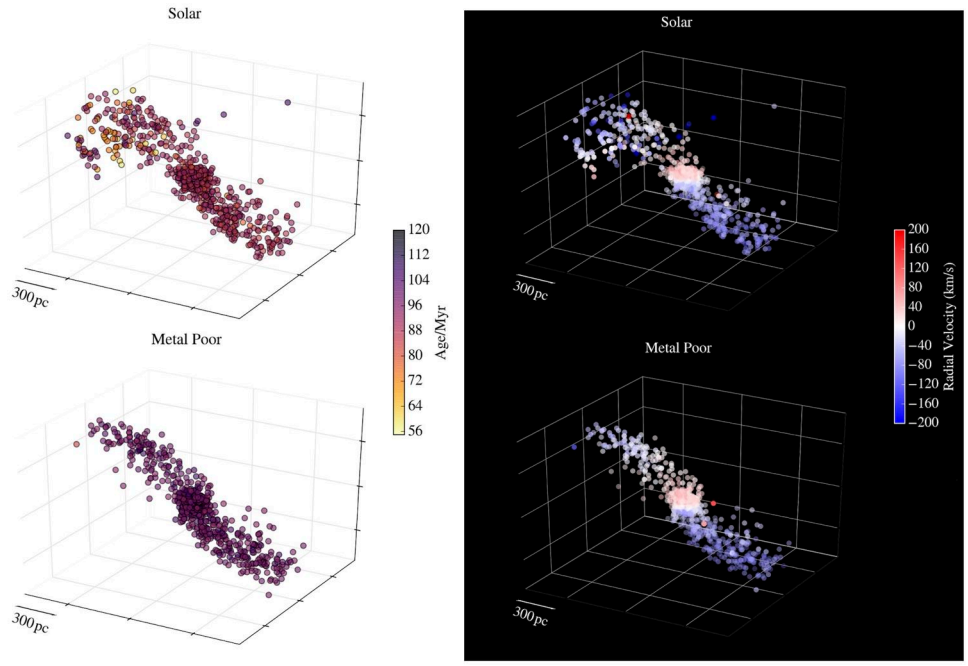

Figure 3.6: From Gelli et al. (2020). 3D spatial maps of stars in satellite S2. The star particles have been divided in metallicity intervals as in Fig. 3.4. The colorbar in the left column shows the stellar ages, while the one in the right column shows the radial velocities of stars with respect to the centre of mass of the satellite.

2.5 kpc), and therefore are most likely affected by tidal interactions. We here study the stellar kinematics in these two satellites to interpret the origin of these structures.

In Fig. 3.6 and 3.7 we display the spatial distribution of the stellar populations of S2 and S5 respectively (using the same metallicity bins as in Sec. 3.2.3). The colours in the left column indicate the stellar age and those in the right indicate the stellar radial velocity with respect to the centre of mass of the satellite.

We find that in S2 the streams are moving toward the centre of the satellite at high velocities, v $\simeq$ 100 km/s, which is greater than the mean velocity of the stars into the bulge, $\langle$v$\rangle \simeq$ 50 km/s. We observe that the stellar streams are composed by both Solar and MP stars, reflecting the same chemical composition of the stellar populations found in the central spherical bulge. This implies that all these stars, both in the streams and in the bulge, are most likely born in the same dwarf galaxy (over a relatively brief period of time $\simeq$ 50 Myr), and that the formation of the streams was caused by a subsequent tidal interaction with Althæa. The most plausible scenario is the one in which the satellite have interacted with the disk of the nearby massive LBG while rotating. Indeed, the rotation likely caused two arms to detach, and at redshift $z \simeq 6$ the stars inside them are falling back onto

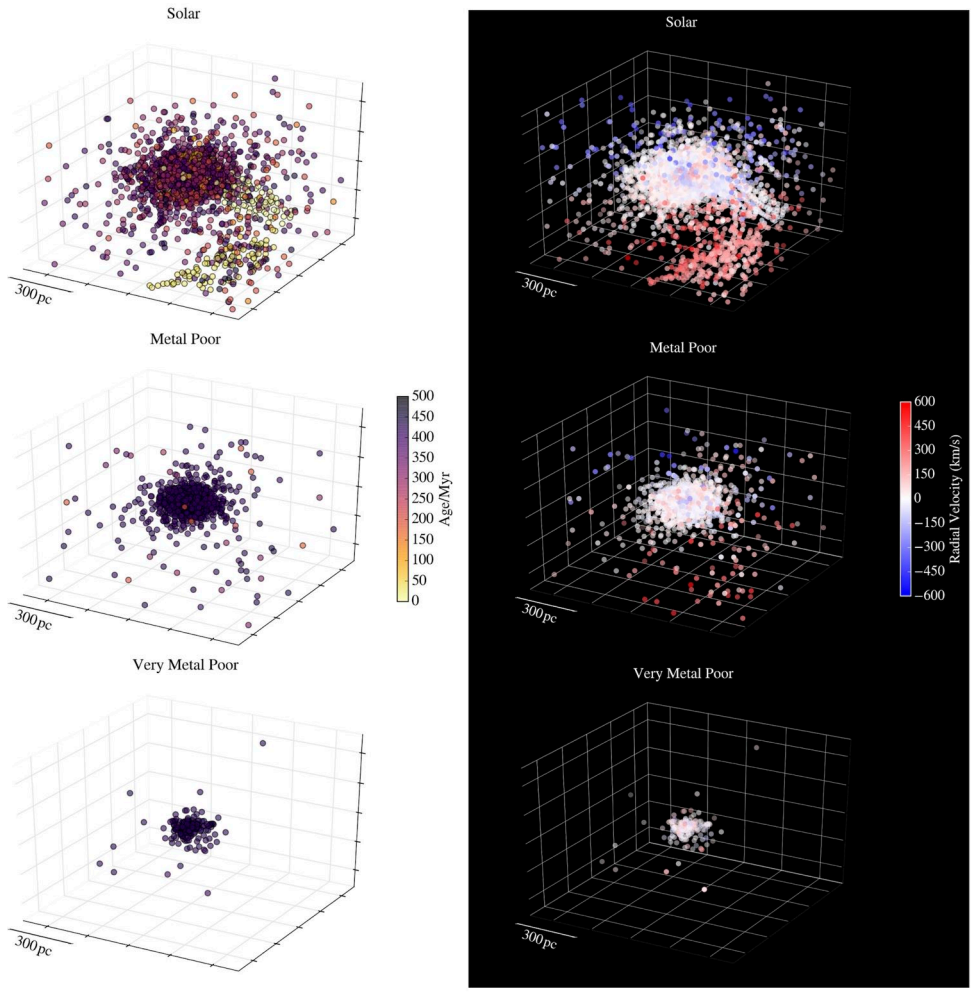

Figure 3.7: From Gelli et al. (2020). 3D maps of satellite S5, as in Fig. 3.6.

the bulge.

In S5 the stellar particles forming the single stream are found in the Solar metallicity population only. These stars are all very young and they are moving away from the satellite at velocity higher than the escape velocity, $v_{esc} \simeq 220$km/s. They are thus falling directly onto Althæa, subjected to its strong gravitational pull. Recalling Fig. 3.2, we notice that also the gas follows a similar spatial distribution as stars, and an analogous infalling stream can in fact be found. This suggests that, since the stellar stream is composed by very young stars, these stars may have formed within the gas rich stream itself while infalling onto Althæa.

We conclude that the streams found in the two satellites, even though caused in both cases by the presence of the nearby Althæa, have a different nature: in S2 we are witnessing a perturbation of the spatial distribution of stars pertaining to a already formed dwarf galaxy; in S5 with a population of newly formed stars

moving from the dwarf satellite to the central LBG Althæa.

3.3 Formation and evolution

We now turn to the analysis of the star formation and metal enrichment histories of individual satellites. These are shown in Fig. 3.8 for three illustrative satellites, one for each of the different mass range categories: S2 (low-mass), S4 (intermediate-mass) and S6 (high-mass). The main panel for each satellite shows the stellar age-metallicity relation, i.e. the metallicity of stellar particles as a function of their age. The colours represent the mass weighted probability distribution function (PDF) in this $Age - Z_\star$ plane. The right and top insets show the integrated quantities for each satellite: the stellar metallicity distribution functions (MDF) at $z \simeq 6$ and the star formation histories (SFH), i.e. the star-formation rate $\mathrm{SFR}(t) = dM_\star/dt\,[\,\mathrm{M_\odot yr^{-1}}]$ as a function of stellar age (or formation redshift).

3.3.1 Low-mass satellites

In low-mass systems (S2, top panel in Fig. 3.8), the SFH is remarkably simple and short, lasting $\simeq 30$ Myr only. All stars are formed in two bursts, separated by a short period of inactivity, and characterised by a SFR that reaches values of 7 $\mathrm{M_\odot yr^{-1}}$. This kind of intermittent SF behaviour represents a common feature of low- and intermediate-mass systems; it can be understood as follows. The first burst of SF lasts for $\simeq 5$ Myr, after which the SF is inhibited. This is the typical timescale for the evolution of massive stars (40 $\mathrm{M_\odot}$) that end their lives as energetic SNe, strongly heating up the gas because of their high specific luminosity.[1] The SF starts again after this transitory quenching phase of ~ 5 Myr, which is of the order of the cooling time computed in the typical conditions of the ISM after a SN event ($T \sim 10^6$ K, $n \sim 10^{-2}\mathrm{cm^{-3}}$ and $Z_{\rm ISM} \sim 10^{-2}\,\mathrm{Z_\odot}$). Afterward in few Myr the SFR reaches the second peak of 8 $\mathrm{M_\odot yr^{-1}}$. The rate is damped again after ~ 5 Myr, and then it continues to decrease until the SF is eventually quenched completely (after ~ 25 Myr).

The $Age - Z_\star$ relation shows us that the first stellar generation formed in S2, at $z \sim 6.4$, has high metallicity: $Z_{\star,in} \simeq 10^{-1.7}\,\mathrm{Z_\odot}$. Dwarf satellites are indeed born from the gaseous environment surrounding the central LBG Althæa, which started

[1] This is a consequence of the fact that the interstellar medium (ISM) where they act has already been pre-heated by stellar radiation and winds (Agertz et al., 2013).

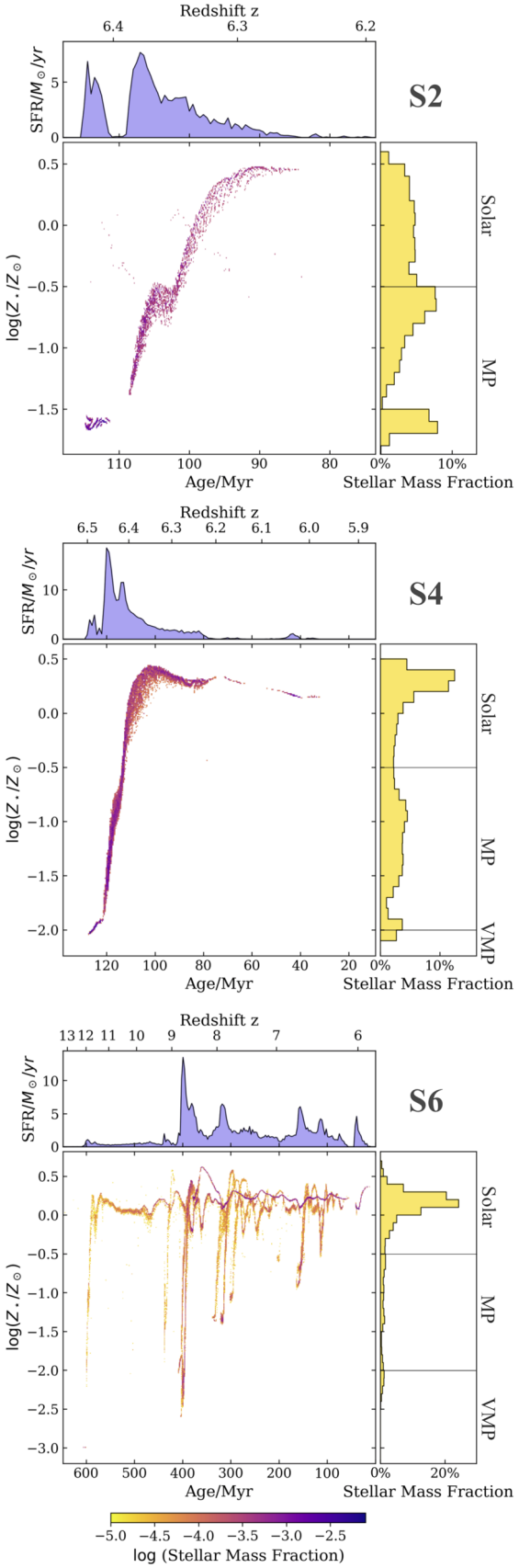

Figure 3.8: (Caption in the next page.)

Figure 3.8: From Gelli et al. (2020). From top to bottom, the three panels show the results for a low-mass (S2), an intermediate-mass (S4), and a high-mass (S6) satellites at $z \simeq 6$. *Main panel*: Metallicity of star particles inside a box of 1 kpc vs their age. The colorbar is the mass-weighted probability distribution function. *Upper inset*: Star formation rate (SFR) as a function of stellar age (lower axis) and redshift z (upper axis). *Right inset*: Metallicity Distribution Function averaged in intervals of $\Delta(\log Z/Z_\odot) = 0.1$.

forming stars at $z \sim 15$ and since then has been polluting its surrounding medium with metals injected via SN-driven outflows.

After the quenching period, stars produced by the second burst in S2 have higher metallicity, as they are born from an ISM polluted by the previous population. The formation then proceeds in a more regular fashion, and stars forming at later times are progressively more metal-rich, rapidly reaching super-solar values. We also notice a brief and slight decrease of $Z_\star$ (age $\simeq 105$ Myr) caused by metal loss via SN-driven winds.

The stellar MDF of S2 at $z \simeq 6$ reflects its SF and chemical enrichment history. It shows two maxima in correspondence of the two main SFR peaks; the fraction of MP stars is 65% of the total.

3.3.2 Intermediate-mass satellites

The history of the intermediate-mass satellite S4 (middle panel in Fig. 3.8) overall resembles that of S2, but a few differences are worth noticing: (i) the SF activity in S4 starts earlier ($z \sim 6.5$) and hence its first stellar population is slightly less enriched ($Z_{\star,in} \simeq 10^{-2}\,\mathrm{Z}_\odot$), (ii) the overall SFH lasts longer (~ 100 Myr) and, (iii) the SFR reaches a higher peak value ($\sim 15\ \mathrm{M}_\odot\mathrm{yr}^{-1}$). As a consequence the MDF is rather evenly distributed in the metallicity range $10^{-2}\,\mathrm{Z}_\odot - 10^{0.5}\,\mathrm{Z}_\odot$ but the peak appears at higher metallicities, i.e. in correspondence with the longer, final SF phase. Thus, the fraction of MP stars is somewhat lower, now representing 47% of the total.

3.3.3 High-mass satellites

The high-mass satellite, S6, has the most complex SF/metal enrichment history (bottom panel of Fig. 3.8). Its first stellar generations are formed at $z \simeq 13$; afterwards the satellite undergoes a continuous SF activity up to $z \simeq 6$, i.e. for ≈ 600 Myr. Contrary to lower-mass satellites, the initial phases of SF in S6 (and S5) are characterised by a moderate SFR $\approx 1-2\ \mathrm{M}_\odot\mathrm{yr}^{-1}$, which suddenly increases

at $z \approx 9$ with a first and highest peak of SFR ≈ 15 $M_{\odot}yr^{-1}$, followed by many other weaker bursts, with the latest one occurring at $z \approx 6$.

The $Age - Z_{\star}$ relation shows that the first stellar generations, formed at $z \approx 13$, have the lowest metallicity, $Z_{\star} = Z_{floor} = 10^{-3}\,Z_{\odot}$, meaning that their formation happened in an almost pristine[2] chemical environment. However, following the first SF events, the enrichment proceeds rapidly, and the ISM metallicity reaches solar values in < 100 Myr. Interestingly, the $Age - Z_{\star}$ plane is characterised by many vertical tracks. They indicate that stars with very low metallicities are continuing to form in the galaxy in spite of the global, average solar metallicity of the satellite. This can be attributed to two types of events: (i) infalling, quasi-pristine gas inducing a new burst of star formation, or (ii) acquisition of low-Z stars due to a dry merger with a smaller, older system. In the latter case, a $Z_{\star} - Age$ relation similar to S2 and S4 should be found for the infalling stars, i.e. a short first burst followed by a longer and more intense one. Some of the vertical tracks in S6 indeed show this behaviour, but others do not. We are led to conclude that both processes are acting at the same time, as expected from the theoretical understanding of galaxy assembling through cosmic times.

The resulting MDF shows that S6 is the only satellite hosting VMP stars at the metallicity floor (and perhaps PopIII stars). These VMP stars only represent $\simeq 4\%$ of S6 total stellar population, which is therefore largely dominated by Solar metallicity stars.

3.4 Global properties

Our analysis indicates that many of the observed properties of dwarf satellites are related to their stellar (hence, halo) mass. The halo mass sets the potential well and therefore determines the ability of the galaxy to retain its gas and survive dynamical interactions. In Fig. 3.9 we summarise the main properties of the dwarf satellites stellar populations showing the following quantities as a function of baryonic mass (lower axis) and halo mass (upper axis): the periapsis potions of the satellites orbits $r_{\rm min}$ (computed by reconstructing their trajectories around the main galaxy as we will later detail in Chapter 6.2.1); the formation time, t_{in}, and metallicity, Z_{in}, of their first stellar generation; the mass-weighted mean stellar metallicity at $z \simeq 6$, $\langle Z_{\star} \rangle$; the fraction of metal poor (MP) stars present, $f_{\rm MP}$; the duration of the SF

[2]We remind that, as we cannot resolve mini-halos, we have set an artificial metallicity floor to mimic their enrichment. Thus, we cannot exclude that the first stellar generation in S6 is indeed made of metal-free, PopIII stars.

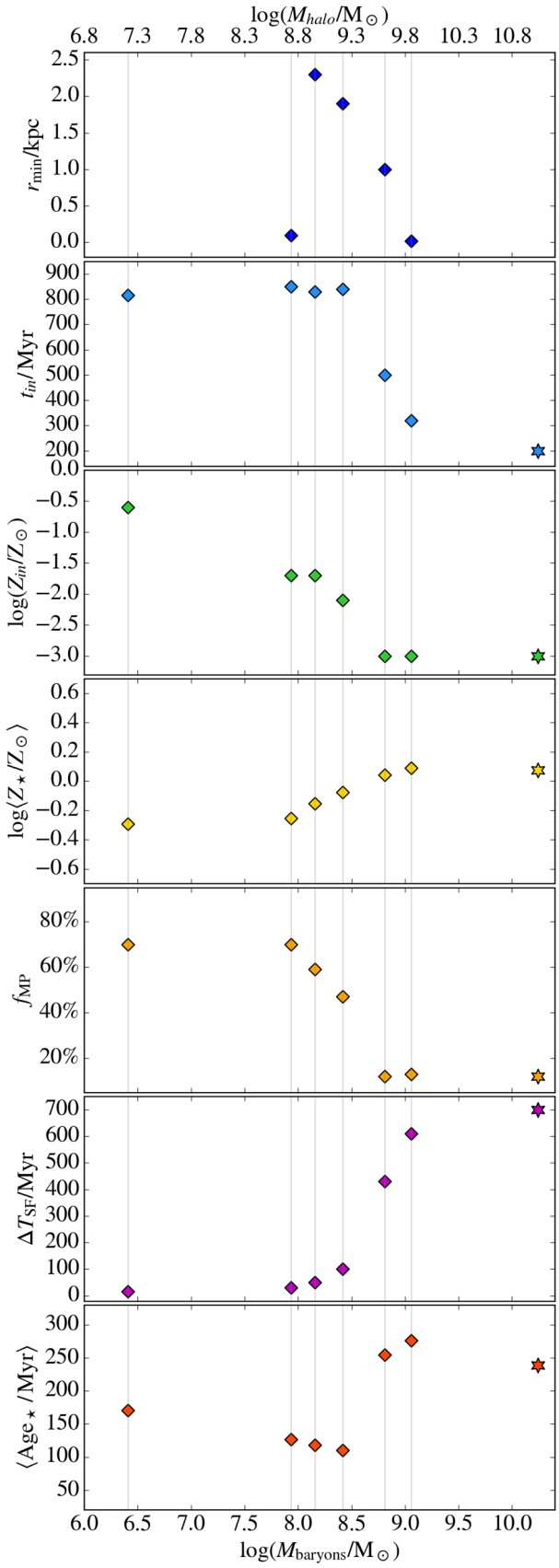

Figure 3.9: (Caption in the next page.)

Figure 3.9: From Gelli et al. (2020). Stellar properties of the six analysed dwarf satellites as a function of their stellar mass (lower axis) and sub-halo mass (upper axis). The star indicates the values for Althæa. From top to bottom we plot: the periapsis potions of the satellites orbits ($r_{\rm min}$); the age of the Universe when the satellite formed (t_{in}); the metallicity of the oldest stellar population in the satellite (Z_{in}); the mass-weighted mean stellar metallicity at $z \simeq 6$ ($\langle Z_\star \rangle$); the mass fraction of metal poor stars ($f_{\rm MP}$); the duration of the SFH ($\Delta T_{\rm SF}$); the mass-weighted mean stellar age $\langle {\rm Age}_\star \rangle$.

activity, ΔT_{SF}; and the mass-weighted mean stellar age $\langle {\rm Age}_\star \rangle$.

From the top panel we see that high-mass satellites have lowest $r_{\rm min}$, allowing them to acquire mass while orbiting through the densest inner regions of Althæa. Also S2 has a small periapsis of 0.1 kpc: this close interaction with the central disk manifests itself with the creation of two stellar streams (see Sec. 3.2.4).

Star formation activity starts relatively late for low- and intermediate-mass satellites ($800 \lesssim t_{in}/{\rm Myr} \lesssim 850$); instead, the two most massive dwarfs formed the first stars much earlier (300 Myr after the Big Bang for S6). Consistently with this picture $t_{in} = 200$ Myr for Althæa. As a consequence the initial metallicity (i.e. at formation) of the galaxies decreases with mass (third panel). Low- and intermediate-mass satellites have $Z_{in} = [10^{-2.5} - 10^{-0.7}]\,{\rm Z}_\odot > Z_{\rm floor}$, while the most massive S5 and S6 have $Z_{in} = Z_{\rm floor} = 10^{-3}\,{\rm Z}_\odot$ like Althæa.

Even though only the most massive dwarfs contain a VMP stellar component, they also have the highest mean stellar metallicity (fourth panel). While all systems are dominated by metal rich stars $\langle Z_\star \rangle > 0.3\ {\rm Z}_\odot$, low-mass satellites contain a higher fraction of MP stars (fifth panel), similar to what observed in the Local Group (Kirby et al., 2013).

The duration of the SF activity ΔT_{SF} (sixth panel) strongly depends on stellar mass. Lower mass satellites have short SFHs and form stars in a few, short bursts without experiencing any merger events (see Sec. 3.3). Higher mass systems are instead active for much longer periods during which fresh fuel is also brought in by merger episodes, allowing SF to proceed uninterruptedly for over 400 Myr.

As low- and intermediate- mass satellites formed at similar times t_{in}, the increase of ΔT_{SF} parallels the decreasing trend of $\langle {\rm Age}_\star \rangle = 100 - 150$ Myr (bottom panel); high-mass satellites present instead older populations, i.e. $\simeq 250$ Myr. Note that – despite the earlier onset of the SF process – the stellar population of Althæa is slightly younger than 250 Myr as a result of its increasing SFH (see Fig. 3.10). Overall, the $\langle {\rm Age}_\star \rangle$ trend is broadly in agreement with that found by other theoretical works (Tacchella et al., 2018, in particular see Fig. 10 therein).

In summary, our findings are consistent with a scenario in which high-mass systems are the oldest and form out of an virtually unpolluted gas. Still, because of their high-mass and complex assembly history, they continue to form stars for a longer period of time, and hence are more metal-rich and host a smaller fraction of metal-poor stars. On the other hand, low-mass satellites are the youngest systems and form in environments that have been already pre-enriched by SN-driven outflows exploding in the central LBG. Yet, since they form stars for a short period of time, their metallicity is lower and thus they host a larger fraction of metal-poor stars. Such behaviour is similar to that found by statistical models that study Local Group dwarf galaxies in a cosmological context (Salvadori et al., 2015) implying that this is a general outcome of ΛCDM hierachical structure formation.

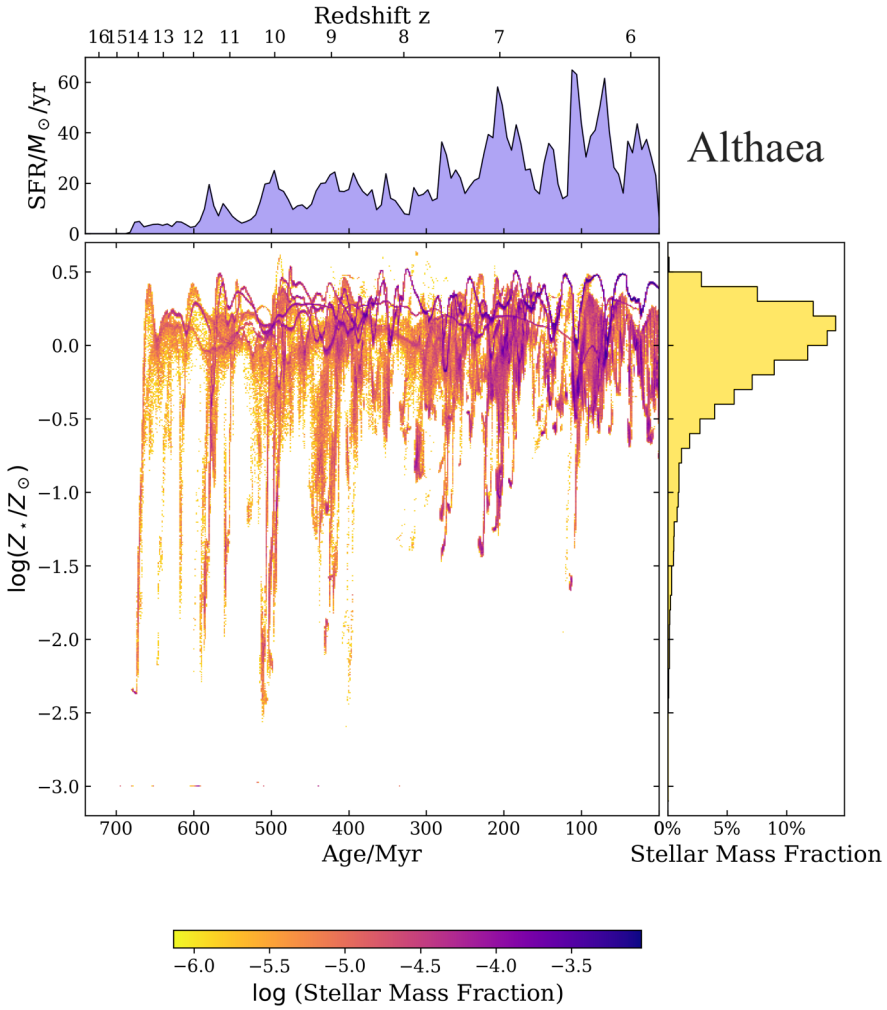

Figure 3.10: From Gelli et al. (2020). *Age* − $Z_\star$, Star Formation History and Metallicity Distribution Function of Althæa, as in Fig. 3.8.

3.5 Comparing with Althæa

The properties of the central LBG Althæa fit nicely in the global trends in Fig. 3.9, as confirmed by the stellar age-metallicity relation, SFH, and MDF, all shown in Fig. 3.10. The effect of merger events (vertical stripes) fuelling SF over long periods of time is visually remarkable. Althæa has formed stars for ≃700 Myr and, despite forming its first stars in a virtually unpolluted environment, its stellar population by $z \simeq 6$ is dominated by solar metallicity stars. The radial profiles of the different stellar populations (Fig. 3.11) confirm that the more massive the system considered is, the more negligible the fraction of VMP stars present, which indeed represent only the 1% of stars in Althæa.

3.6 Discussion and conclusions

We investigated the properties of dwarf satellites of a typical high-z LBG. These small systems have not been directly observed yet, but they will be one of the most exciting targets at reach of JWST. To this aim we have analysed cosmological zoom-in simulations presented in (Pallottini et al., 2017b). These simulations have sufficiently high mass ($\Delta m \simeq 10^4\,\mathrm{M}_\odot$), and spatial resolution ($\Delta x \simeq 30\,\mathrm{pc}$) to examine the inner structure of the smallest systems surrounding the central LBG called Althæa.

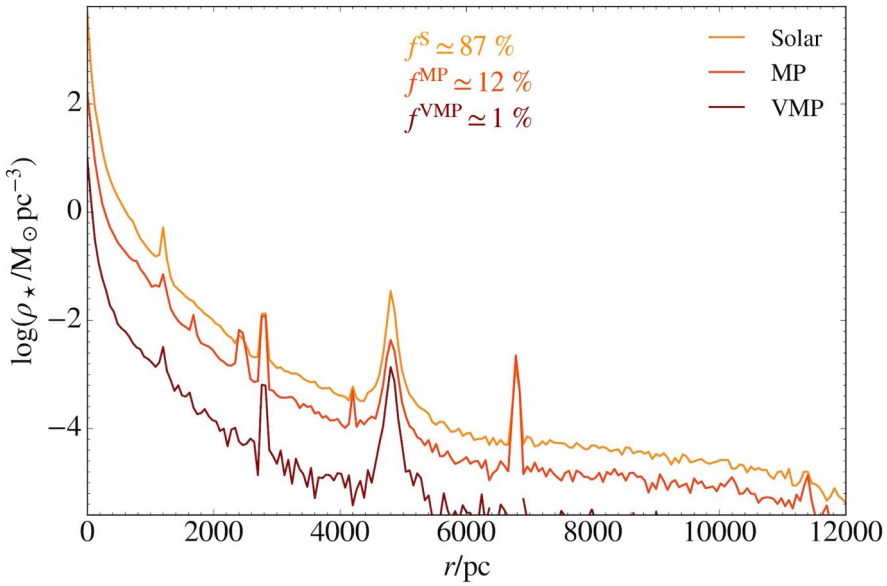

Figure 3.11: From Gelli et al. (2020). Radial profiles of the different stellar populations of Althæa as in Fig. 3.4.

We identified six dwarf satellites within $\lesssim 12$ kpc from Althæa's centre, whose stellar [gas] masses are in the range $\log(M_\star/\ \mathrm{M}_\odot) \simeq 6-9$ [$\log(M_{gas}/\ \mathrm{M}_\odot) \simeq 4.3-7.75$]. We analysed the properties of their stellar populations in terms of spatial distributions, formation history and kinematics. The main results are:

- All satellites experience periods of high star formation rates, SFR $\gtrsim 5\,\mathrm{M}_\odot\mathrm{yr}^{-1}$, hence they are expected to produce emission lines such as the H_α with high luminosities (e.g. see L_α − SFR relation from Kennicutt & Evans (2012)). With the high sensitive NIRSpec instrument (Giardino et al., 2016), JWST will be able to detect in 10 ks emission lines of sources at $z \simeq 6$ with SFR $\sim 2\ \mathrm{M}_\odot\mathrm{yr}^{-1}$, implying that our satellites will indeed be observable.

- The evolution of the satellites strongly depends on their total mass. Low-mass systems ($\mathrm{M}_\star \lesssim 5\times10^8\mathrm{M}_\odot$) have short ($\simeq$ 50Myr) and simple SFHs, which become increasingly complex and long ($>$ 500Myr) in more massive systems experiencing frequent merger events.

- The chemical properties of the stellar populations of dwarf satellites also depend on their mass. High-mass systems ($M_\star > 5\times10^8\ \mathrm{M}_\odot$) form their first stars at $z > 9$ from nearly pristine gas. Lower-mass satellites form later ($z < 7$), and in a circumgalactic medium already enriched by SN-driven outflows from Althæa and its progenitors.

- In all satellites, the most metal-poor stars are concentrated towards their center ($r \lesssim 200$ pc) while metal-rich stars extend up to larger radii. Both components show a remarkably spherical shape. Stellar streams/arms caused by tidal effects are only observed in two closest satellites (S2 and S5).

- The least massive satellite S1 has very low gas content and completely lacks of DM. We speculate that it might be a possible high z proto-globular cluster candidate (e.g. Vanzella et al., 2017).

How do our findings compare with the data available for Local Group satellites? First, we find characteristic behaviours of stars with different metallicities in galaxies of all masses, which are encountered at all epochs independently from

the redshift: (i) the fraction of MP stars decreases with increasing mass of the galaxy; (ii) metal-poor (-rich) stars tend to dwell in the inner regions (to spread out), as also reported by semi-analytical models and numerical simulations for the formation of the the Milky Way and its dwarf satellites (Salvadori et al., 2010; Starkenburg et al., 2017b).

Second, we have pointed out that high-z dwarfs may form stars at a sustained rate (> 5 $M_\odot yr^{-1}$). There is a marked difference with the local dwarf spheroidal galaxy population orbiting around the Milky Way. These objects are characterised by low SFR (< 0.01 $M_\odot yr^{-1}$) and metallicities (< 0.01 $Z_\odot$). Hence, LBG satellites may be more similar to Blue Compact Dwarfs found at the edge of the Local Group: these are gas-rich systems characterised by ongoing SF at very high-rates, SFR $\simeq 1 - 10$ $M_\odot yr^{-1}$ (e.g. Tolstoy et al., 2009), or possibly (i.e. S1) tidal dwarf galaxies (Bournaud & Duc, 2006; Fensch et al., 2019).

A limitation of our study is represented by the finite mass resolution of stellar (DM) particles of $\simeq 10^4$ $M_\odot$ ($\simeq 10^5$ $M_\odot$). As a consequence, we cannot resolve minihaloes hosting the first stars, which in principle could influence the results for the population of low-mass satellites. However, since we are focusing our study in a biased high-density region of the cosmic web, we expect to be here in the presence of a high UV background (e.g Pallottini et al., 2019): an UV flux of $G = G_0$ roughly corresponds to a background in the Lyman-Werner band of intensity $J_{LW} \simeq 40\, J_{21}$ (with $J_{21} = 10^{-21} \mathrm{erg\,s^{-1}cm^{-2}\,Hz^{-1}\,sr^{-1}}$). Considering that a critical flux of $J_{LW} \sim 10^{-2} J_{21}$ should suppress minihalo formation (Johnson et al., 2013), the central LGB is expected to suppress star formation in such small objects already at $z \sim 10$ (e.g. Graziani et al., 2015, for the MW environment). Therefore accounting for the presence of minihaloes would not change significantly the properties of the simulated low-mass satellites, which formed at $z < 7$. Consistently with the absence of minihaloes hosting PopIII stars (e.g. Wise et al., 2012a; O'Shea et al., 2015), we had to introduce a metallicity floor of $Z_{\rm floor} = 10^{-3} Z_\odot$ to mimic the expected gas pre-enrichment (Davé et al., 2011; Wise et al., 2012a; Pallottini et al., 2014). This metallicity floor however only marginally affects our results, since stars with $Z_\star < 10^{-2} Z_\odot$ represent only a tiny ($< 1\%$) contribution to the stellar mass budget of the satellites. We also note that stars with $Z_\star < 10^{-3} Z_\odot$ are an extremely rare stellar population even in smallest local dwarf galaxies with $M_\star < 10^7 M_\odot$ (e.g. Salvadori et al., 2015).

The simulations also predict the existence of additional eight *starless, gas-rich, and metal-poor* satellites. In these interesting systems, located at $D_{\rm Althæa} = 8 - 12$ kpc, the SF was likely inhibited by UV photo-dissociation of H_2, as predicted by

(Salvadori & Ferrara, 2012). Because of their high and dense gas content, these small satellites might be observed as Damped Ly-α systems (D'Odorico et al., 2018), and retain in their metal-poor gas the chemical signature of very massive first stars (Salvadori et al., 2019). It is however worth recalling that the treatment of the UV radiation field, and hence of radiative feedback, is rather coarse in the currently used simulation. We improve this aspect in the implemented SERRA suite of simulations (described and analyzed in Chapters 5 and 6), with on-the-fly multi-frequency radiative transfer and hydrogen ionizing radiation, which could lead to additional photo-evaporation effects (e.g. Decataldo et al., 2019).

In the following Chapter 4 we derive the emission of the six satellites and Althæa, and investigate if and how can they be observed with JWST.

CHAPTER 4

A free lunch for JWST

JWST is expected to detect many LBGs: the emission of dozens of them will most likely appear already within the deep fields of high priority surveys like JADES (Rieke et al., 2019), that will reach exposure times of $\sim$ 20 hrs for imaging with the NIRCam instrument. This provides the remarkable opportunity to exploit planned JWST surveys to detect *for the first time* and *for free* their dwarf satellites population.

Will JWST be able to effectively detect dwarf satellites of massive LBGs through imaging and photometry? Will such observations shed light on the star formation rates, stellar metallicity and presence of young/metal-poor stars in these systems?

We address these issues by using once again the Althæa cosmological zoom-in simulation (Chapter 2 and Pallottini et al. 2017b), and by modeling the emission and dust attenuation of the satellite galaxies, focusing on the stellar continuum. The results are based on the paper Gelli et al. (2021).

4.1 SED modeling

To derive the intrinsic spectral energy distributions (SED) of the dwarf satellites based on their simulated stellar populations, we use STARBURST99 (Leitherer et al., 1999), also consistent with the simulation prescriptions. We proceed as follows: considering the total SFH of the selected galaxy (up to $z \sim 6$, final snapshot of the simulation), we sample it in timesteps of $\Delta t = 5$ Myr, which assure a good convergence for the spectra. At each time step we consider a single burst of star formation: the stellar mass, metallicity and formation time are given as an input to STARBURST99. The final output consists in the rest frame intrinsic spectrum of

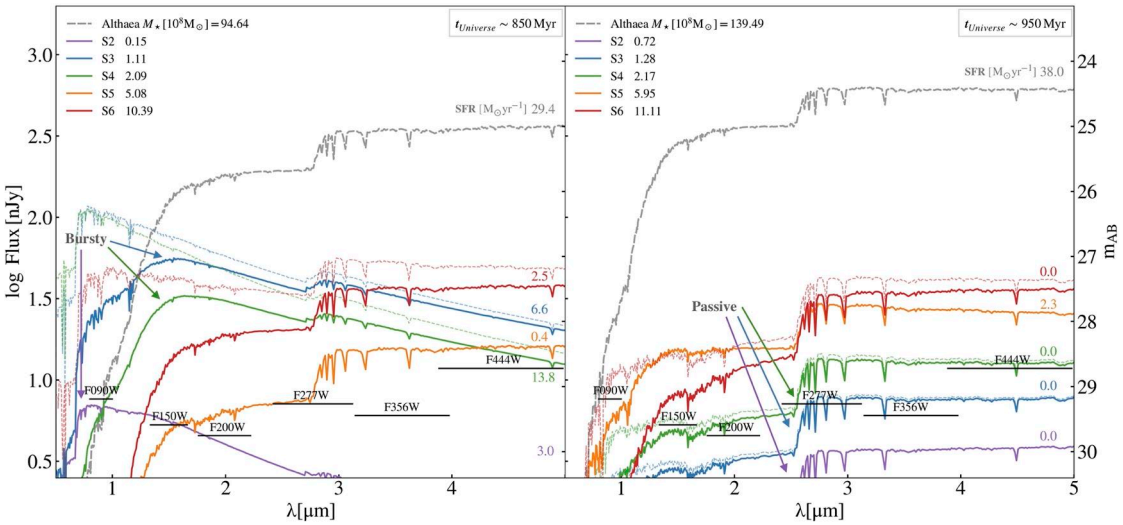

Figure 4.1: From Gelli et al. (2021). Spectral Energy Distributions for the five high-z satellites (coloured continuous curves) and the central LBG Althæa (gray dashed) shown at two different times. *Left: Bursty phase* ($z \simeq 6.5$), in which the three smallest satellites are experiencing a star formation burst. *Right: Passive phase* about 100 Myr later ($z \simeq 6$), when star formation has been quenched. The black horizontal lines show the sensitivities of JWST/NIRCam filters for point sources with S/N=5 and exposure time of ~ 3 hrs. The dashed curves show the intrinsic (i.e. unattenuated) stellar emission for three satellites.

the galaxy at all times from its formation up to $z \sim 6$.

The intrinsic spectrum can be attenuated by dust, for which we adopt the SMC synthetic extinction curve by Weingartner & Draine (2001). This is the natural choice for dwarf galaxies and a good approximation for high-z sources at $\lambda > 0.3\,\mu m$ (Gallerani et al., 2010). We compute the optical depth as: $\tau = C_{\rm ext} \times N_{\rm H}[{\rm cm}^{-2}] \times Z[\,{\rm Z}_\odot]$, where $C_{\rm ext}$ is the tabulated cross section per H nucleon, and $N_{\rm H}$ and Z are the gas hydrogen column density and metallicity averaged on different line-of-sights. The latter two are retrieved directly from the simulation, considering the gas composition in the selected satellite galaxy at the snapshots available (i.e. every 18 Myr), and interpolating at intermediate times. The final spectra are obtained by reprocessing the intrinsic stellar spectra with the derived dust transmission curves. We note that we do not take into account the subsequent absorption of the inter-galactic medium (IGM): for galaxies at $z \sim 6$ it is expected to attenuate the flux observed at $\lambda \lesssim 1\mu$m, therefore affecting the flux in the filter F090W.

The resulting SEDs of the satellites and the central LBG Althæa are shown in Fig. 4.1, in the NIRCam wavelength range, $0.6 - 5\,\mu m$, and for two different redshifts: $z \simeq 6.5$ (left panel) and $z \simeq 6$ (right panel). We adopt the same notation

as in Chapter 3 and Gelli et al. (2020) to indicate the satellites, i.e. they are named from S1 to S6 with increasing stellar mass. S1 is the proto-globular cluster: its flux is more than 2 order of magnitudes below that of the other satellites, hence invisible even for JWST deep surveys. We notice that the flux of the central LBG (gray dashed) always exceeds that of the satellites by more than an order of magnitude at $\lambda > 2\mu m$, because of the larger stellar mass. The two displayed redshifts pin-point two relevant evolutionary stages of the 3 smallest satellites (S2, S3, S4, $M_\star \lesssim 5 \times 10^8$ M$_\odot$):

– *Bursty phase* ($z \simeq 6.5$, left panel): in this epoch the least massive satellites are all experiencing the brief ($\lesssim$ 50 Myr) burst of star formation in which they form all of their stars. At this stage they are characterised by relatively high star formation rates, up to SFR ~ 14 M$_\odot$yr^{-1}. Their stellar populations are hence dominated by young newly formed stars, resulting in spectra with an intense rest-frame UV flux at $\lambda \lesssim 2.5\mu m$.

– *Passive phase* ($z \simeq 6$, right panel): this stage takes places ~ 100 Myr later, when the star formation in the least massive satellites has been completely suppressed by SN feedback. The older stars and lack of ongoing star formation result in redder spectra. Note that at $\lambda \lesssim 2.5\mu m$ the flux has decreased by a factor ~ 10.

SEDs of the two most massive satellites (S5 and S6, $M_\star \gtrsim 5 \times 10^8$ M$_\odot$) are dominated by old stellar populations in both epochs, since they are older than 300 Myr. The SFH of these systems is characterised by a low-level, continuous activity fuelled by merger events which produce peaks with SFR < 5 M$_\odot$yr^{-1} (see Fig. 3.8). By $z \sim 6.5$ these high-mass systems can be therefore considered as "stabilised" since the bulk of their stellar population is already in place. As a result, their SED is almost unchanged between the two stages. Also, in the first stage they are fainter than S2, S3, S4 due to the lower SFR, and to their more dusty nature; as lower systems fade, massive systems are the brightest ones in the passive phase[1].

To highlight dust effects on the final spectra, we compare the intrinsic stellar emission for S3, S4 and S6. As the dust content broadly scales with galaxy stellar mass, massive systems suffer a larger attenuation. For instance, even though S3 and

[1]The SFR of the most massive satellite (red curve) is temporarily zero during the second stage at $z \simeq 6$ because of a recent (~ 10 Myr before) burst of star formation and the subsequent SN feedback effect.

S4 have similar intrinsic fluxes at wavelengths $\lambda \sim 1\mu m$ during the bursty phase, the more massive S4 is more attenuated. Low-mass systems are, however, particularly affected by dust extinction during their starburst phase, which is characterized by higher gas column density in the star forming regions. Interestingly, the predicted fluxes are in most cases well above the sensitivity of NIRCam in different filters, shown for a S/N = 5 in $\sim$ 3 hrs by horizontal black lines. However, these estimates are valid for point sources. To draw solid conclusions on their observability, we need to assess whether the satellites can be spatially resolved by JWST.

4.2 Identifying dwarf satellites

To enable a detailed spatial/morphological analysis, we have produced sysnthetic images of the central LBG and its dwarf satellites at $z \sim 6$ (Fig. 4.2). The images are built from stellar density maps of the simulated, face-on LBG disk (e.g. see Fig. 3.1), and using the proportionality between stellar mass and observed magnitude in the selected bands. The high-resolution images are then convolved with a gaussian with the FWHM of the selected NIRCam filter, and rebinned to match the instrument pixel size.

Fig. 4.2 shows the synthetic images of the LBG system at $z \sim 6$ over an area of $2.5'' \times 2.5''$ (well within the field of view of NIRCam of $2.2' \times 2.2'$) in two wide filters (F200W and F356W). The coloured pixels within the images show the flux at S/N$\sim$ 3, with exposure times of $\sim$ 20 hrs (top) and $\sim$ 3 hrs (bottom). The white contours indicate the areas with a signal-to-noise ratio[2] of S/N$\sim$ 10. The image shows the system at $z \sim 6$, i.e. the last snapshot available during the passive phase, when the three low-mass satellites are at their faintest level. This conservative choice reveals how, even in this worst case of detectability conditions during their evolution, many satellites do exceed the flux sensitivity thresholds. Namely, the flux of the S5 and S6 reach S/N=10 in both filters and they are detectable in just 3 hrs of observations. All 5 dwarf galaxy satellites are well detected in the wide filter F356W in 20 hrs. In F200W, S2 and S3 remain undetected at $z \sim 6$, but they are detectable in $\sim$ 17 hrs at previous stages when their flux is higher

[2]Flux limits for $\sim$ 3 hrs are retrieved from Table1 of *https://jwst-docs.stsci.edu/near-infrared-camera/nircam-predicted-performance/nircam-sensitivity*, which assumes circular photometric apertures 2.5 pixels in radius and 1.2 $\times$ minimum zodiacal light background. We rescale these values for 20 hrs, consistently with the values reported in Rieke et al. (2019). The used results were downloaded as of June 2021, but we note that the effective sensitivity limits re-estimated after the first JWST observations have proved to be even lower (see Chapter 6).

($6.5 \lesssim z \lesssim 6.2$). Fig. 4.2 shows that to distinguish the dwarf galaxy satellites from the central LBG, a separation of $\gtrsim 0.25''$ is required. Noticeably, this requirement is achieved for all dwarf satellites with the exception of S5, which is located in the inner regions (1.2 kpc from the centre of Althæa) and whose emission is likely confused with that of the central LBG.

In conclusion, dwarf satellites of high-z LBGs can be actually observed with

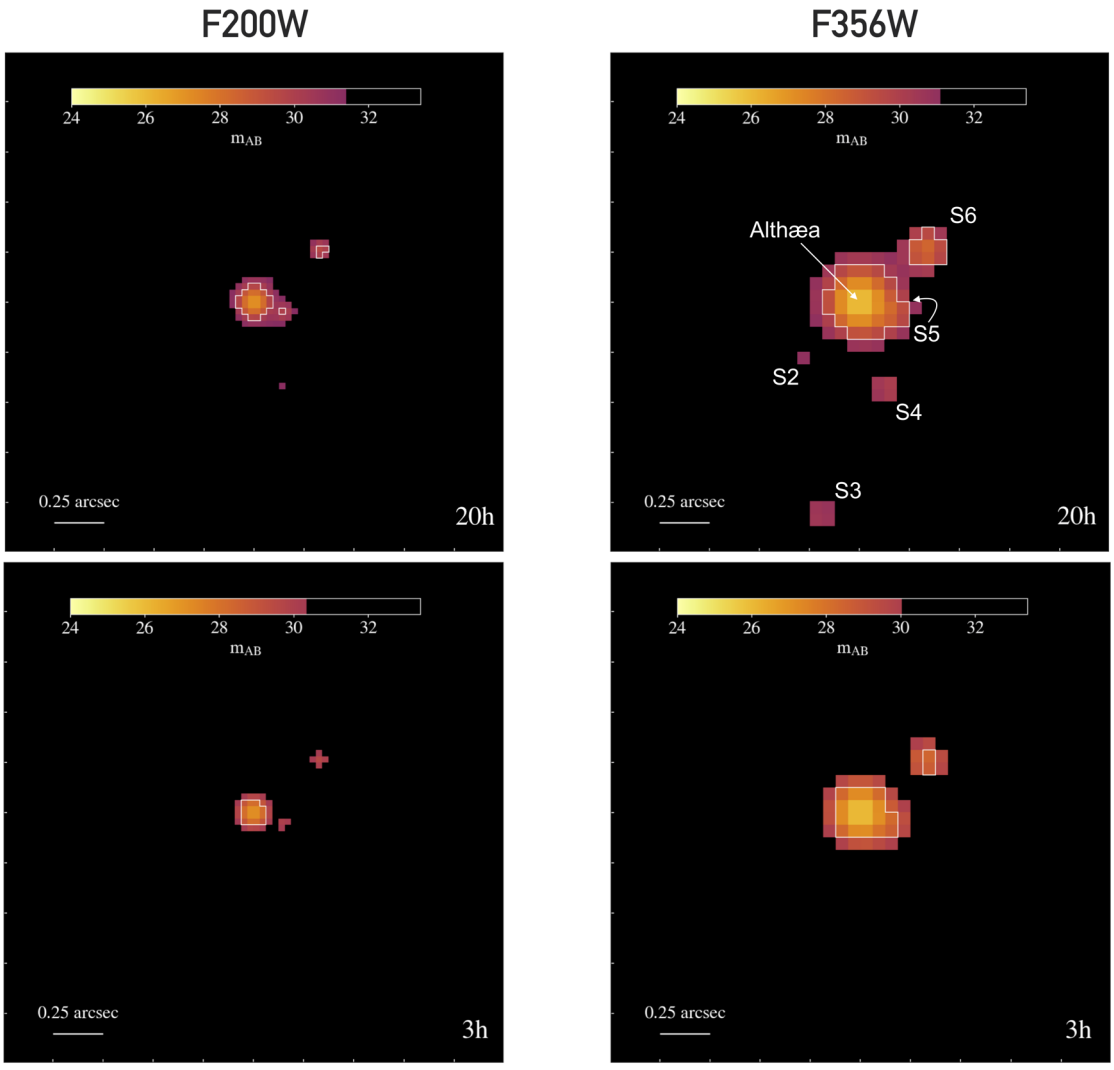

Figure 4.2: From Gelli et al. (2021). Synthetic images centred on the LBG at $z = 6$ in a field of view of size 2.5×2.5 arcsec, corresponding to 15×15 kpc. The maps are displayed in two NIRCam filters: F200W (left, short-wavelength channel with pixel scale of $0.032''$) and F356W (right, long-wavelength channel with pixel scale of $0.065''$), and for exposure times of 20 hours (top) and 3 hours (bottom). The images are shown for S/N=3 and the white contours identify the pixels with S/N=10. The location of the satellites are pinpointed by the labels S2,...,S6 from the least to the most massive system.

JWST within the planned deep surveys exceeding ~ 20 hrs of exposure time.

4.3 Key observables

What information can be inferred from their photometry, in particular through colour-magnitude diagrams (CMDs)? While retrieving colours and magnitudes, we checked the possible contamination by nebular emission lines (e.g. H_α, H_β, [OIII]λ5007 and [OII]λ3727), post-processing the simulation outputs with CLOUDY (Ferland et al., 2017), with the caveat of not having a consistent modeling of the interstellar radiation field with radiative transfer (later implemented in Chapters 5 and 6). Our estimates show that emission lines are expected to produce negligible variation in both colour and magnitude (< 0.1dex) for the three satellites farther from Althæa (S3, S4, S6), while the two located in its proximity ($\lesssim 0.4''$) suffer heavier line contamination due to the nearby LBG disk. Fig. 4.3 shows the CMDs from $z \sim 6.5$ ($t_{Uni} \sim 850$ Myr) to $z \sim 6$ ($t_{Uni} \sim 950$ Myr) of the 3 best-target satellites which (i) are located farther from the central LBG, and (ii) can be identified in only 7 hrs observations in F356W at $z \sim 6$ (the faintest evolutionary stage).

In the upper four panels (a-b-c-d) we plot the color F200W-F356W as a function of the AB magnitude in the filter F200W, and the symbols are color-coded according to SFR, stellar metallicity, $Z_\star$, fraction of young, $f_\star$(Age < 5 Myr), and metal-poor $f_\star(\mathrm{Z}_\star < 10^{-0.5}\,\mathrm{Z}_\odot)$ stars. The path of each satellite in the CMD helps clarify how its SED evolves with time. We notice two trends: (i) a complex one characterising "active" low-mass satellites (S3 and S4), which first (*bursty phase*) become brighter (from $\mathrm{m_{AB}} \approx 29$ to $\mathrm{m_{AB}} \approx 27$) with roughly constant colour (F200W-F356W ≈ -0.5), and then (*passive phase*) become progressively dimmer and redder as they age; (ii) the simpler one of the high-mass S6, which by $z \approx 6.5$ is already "stabilized", i.e. old/red (F200W-F356W$\gtrsim 0.5$), and therefore only shows a modest variation ($\lesssim 1$ dex) in both magnitude and colour.

Since the high-mass satellite forms only $\sim 6\%$ of its stellar mass during the time considered, no significant variation takes place in terms of both $Z_\star$ (always super-solar, panel b) and $f_\star(\mathrm{Z}_\star < 10^{-0.5}\,\mathrm{Z}_\odot)$ ($\lesssim 15\%$, panel d). Conversely, its SFR varies due to a short bursts of star formation (SFR ~ 5 $\mathrm{M_\odot yr^{-1}}$, panel a) which is however too weak to significantly affect the fraction of young stars (panel c). On the other hand, low-mass satellites, during the first ~ 10 Myr displayed, experience the peak of their bursty star formation period in which they form the bulk of their stellar mass. The SFR reaches its peak ($\gtrsim 10$ $\mathrm{M_\odot yr^{-1}}$, panel a),

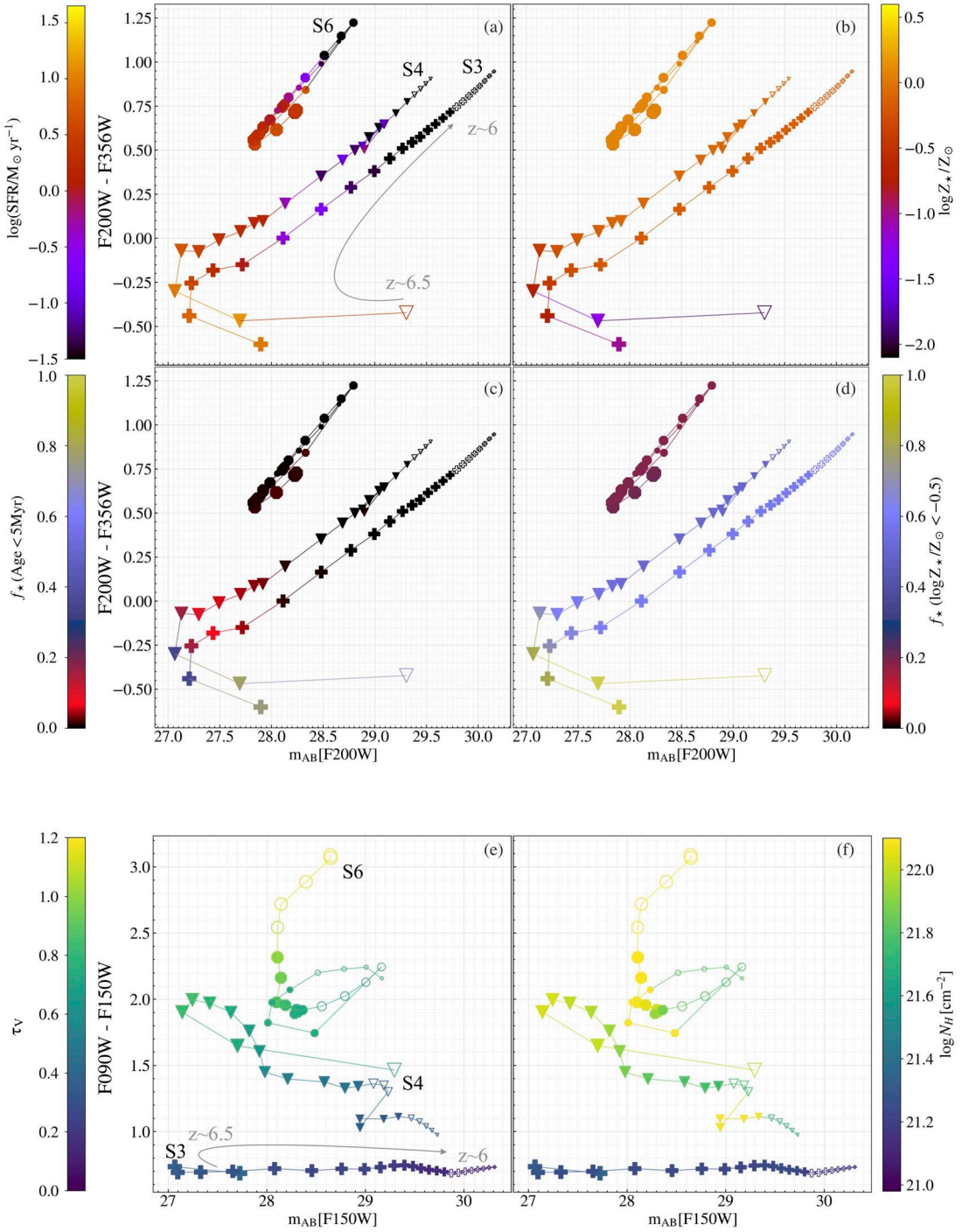

Figure 4.3: From Gelli et al. (2021). Color-magnitude diagrams of three satellites using different NIRCam filters. A line traces the evolution of each satellite in the diagram, the size of the markers decreasing in cosmic time from $t_{\sim}850$ Myr (in correspondence of the bursty phase of low-mass satellites) to ~ 950 Myr (passive phase), in steps of 5 Myr. Empty markers pinpoint the stages at which the satellite do not exceed the S/N=3 sensitivity threshold in 20 hrs in the selected filters. In each panel the markers are colour-coded according to different quantities. The first four characterise stellar populations: SFR, stellar metallicity, fraction of young stars (Age < 5 Myr), and fraction of metal poor stars [$\log Z_{\star}/\mathrm{Z}_{\odot} < -0.5$]. The last two refer to the ISM, i.e the dust optical depth τ_{V}, and hydrogen column density N_{H}.

and the SED is mostly determined by newly formed young ($\gtrsim 50\%$, panel c), and metal-poor stars ($\gtrsim 80\%$, panel d). The stellar metallicity shows a rapid increase during the bursty phase ($Z_\star \gtrsim 10^{-1}\,Z_\odot$, panel b). Over the ~ 100 Myr shown, these low-mass systems spend only ~ 20 Myr in the initial bursty phase, implying that in principle, when observing a high-z low-mass satellite, it will be more likely to detect it during the longer passive phase when their SFR has decreased and $Z_\star$, $f_\star(\mathrm{Age} < 5$ Myr), and $f_\star(Z_\star < 10^{-0.5}\,Z_\odot)$ settle to their final, constant values.

The two bottom panels (e-f) show the color F090W-F150W as a function of the F150W magnitude[3], and are colour-coded according to the V-band dust optical depth, τ_V, and N_H. The SED shape in this spectral range is determined by two competing factors: young stellar populations, enhancing the flux at short wavelengths, and dust drastically reducing it. The trends in the CMD show that in general more massive satellites, which are dustier and denser, have higher F090W-F150W. The smallest object displayed (S3) shows a simple constant trend of the F090W-F150W, reflecting its simple SFH in which it settles to constant values of metallicity and column density. More massive satellites show a more complex behaviour, in which the color becomes bluer at each small burst episode. The trends of the optical depth (e) and column density (f) are associated with the color: for instance, objects with F090W-F150W $\gtrsim 2.5$ have $\tau_V \gtrsim 1$ and $N_H \gtrsim 10^{22}\mathrm{cm}^{-2}$.

4.4 Discussion and conclusions

Based on our high-resolution cosmological simulations, we show that JWST will be able to detect for the first time faint dwarfs satellite galaxies of typical LBGs at the end of the Epoch of Reionization. Remarkably, this should happen already during the first planned observations. The JADES survey, for instance, will reach exposure times of ~ 20 hrs, sufficient for observing most satellites even during the faintest stages of their evolution. The survey will detect ~ 50 LBGs with stellar mass $M_\star \sim 10^{10}\,M_\odot$ (Williams et al., 2018), i.e similar to Althæa. According to our simulations, we then expect to detect a total of $\sim 100 - 250$ companion dwarf satellites, ~ 40 of which will be most likely star bursting and dominated by young and metal-poor stars. The simulation used in this work (Pallottini et al., 2017b) is ideal to study this kind of high-z sources as it reproduces key observed properties of known LBGs, from $L_{[CII]}$ luminosities (Carniani et al., 2018) to the

[3]We remind that the colors shown are retrieved from IGM-corrected SEDs and therefore the actual observed value of the flux in the F090W filter could be lower.

Schmidt-Kennicutt relation (Krumholz et al., 2009). In the following Chapters 5 and 6, we will investigate the expected statistics of high-z dwarf satellite galaxies and probability of observing them in different phases, using a larger sample of LBG targets from the SERRA suite (Pallottini et al., 2022).

Once candidate dwarf satellites are individuated based on the proximity to a massive LBGs, a measurement of their photometric redshift is needed to infer if they do belong to the LBG system, or if we are rather dealing with independent foreground or background sources. NIRCam will be able to retreive $z \sim 6$ galaxies redshifts with a percentage of misidentifications as lower z galaxies of 9% (Bisigello et al., 2016), hence allowing a successful identification of the target LBG satellites.

An additional interesting finding of the simulation analysis (see Chapter 3 and Gelli et al., 2020) is the presence of a proto-globular cluster among the satellite population of the LBG at $z \sim 6$. This is characterised by a stellar mass $M_\star \sim 10^6$ M$_\odot$, formed in an single burst of star-formation (< 15 Myr), and completely lacking both gas and dark matter. In this study, we find that such objects, despite their predicted existence in the vicinity of LBGs, are not bright enough to be observed with JWST/NIRCam: more than $\sim$ 1000 hrs would be required to detect their light at S/N$\sim$ 3. Since within the JADES survey we do not expect the presence of gravitationally lensed sources, the hundreds of expected observed satellites around LBGs will be indeed dwarf galaxies, and not globular clusters (e.g. Vanzella et al., 2017). Among them, some will be most likely detected while experiencing their burst of star formation.

We showed how photometric observations will be most relevant to shed the first light on high-z satellite galaxies and, provided that many of these sources will be discovered in the surroundings of LBGs, we suggested that the F200W-F356W color is a powerful diagnostic tool to understand their properties. For example, F200W-F356W $\lesssim -0.25$ characterises star-bursting (SFR $\sim$ 5 M$_\odot$yr^{-1}), low-mass ($M_\star \lesssim 5 \times 10^8$ M$_\odot$), low stellar metallicity systems, with $\sim$ 80% of their stellar population made of young and metal-poor [$\log(Z_\star/Z_\odot) < -0.5$] stars.

CHAPTER 5

The SERRA simulations: building up statistics

Cosmological high-resolution simulations have proven to be an invaluable tool to study and understand the processes regulating the formation and evolution of galaxies as observed, also allowing to make theoretical predictions for upcoming observations. In the previous Chapters, the Althæa simulation (Pallottini et al., 2017b) allowed us to deeply investigate the physical properties of a typical $z \sim 6$ LBG along with its six satellites. Now, in order to understand the general global trends and properties of the ever increasing number of high-z galaxies targeted by observations, we need to extend our study and use a statistical significant number of simulated systems. In this Chapter, based on the results of the paper by Pallottini et al. (2022) including Gelli, we present SERRA: a set of multiple zoom-in high-resolution (1.2×10^4 $M_\odot$, $\simeq 25$ pc at $z = 7.7$) simulations targeting $M_\star \sim 10^8 - 10^{10}$ $M_\odot$ galaxies at $z \sim 6$. Each simulation follows the evolution of $10 - 30$ galaxies in a cosmological environment, and here we analyse the results from 10 simulations focusing at $z = 7.7$, for a total of 202 galaxies.

5.1 Numerical simulations

Most of the assumptions and techniques adopted in SERRA are the same that have been used in previous simulations (Pallottini et al., 2017a,b) and the models adopted have been described in Chapter 2.3 (e.g. the stellar feedback and non-equilibrium chemistry prescriptions). In the following we describe the implementations for the radiative transfer prescriptions that have been included in SERRA,

and two relevant post processing phases, i.e. the computation of emission lines and the identification and selection of the sample of galaxies.

5.1.1 Radiation

While not as critical as for simulations that aim at studying the reionization process (e.g. CROC Gnedin & Kaurov 2014, CODA II Ocvirk et al. 2020, SPHINX Rosdahl et al. 2018), the interstellar radiation field (ISRF) is an important physical ingredient for early galaxy evolution (e.g. Katz et al., 2017; Trebitsch et al., 2017; Pallottini et al., 2019). Thus, radiative transfer should be consistently implemented. This has been done using, on top of the AMR code RAMSES, the RAMSES-RT module (Rosdahl et al., 2018) through which radiative transfer is solved on-the-fly. Photons are treated as a fluid sharing the same AMR structure of the gas and they are divided into energy bins, whose density and velocity fields are tracked separately. We follow 5 photon bins (see also Pallottini et al., 2019) in the $6.0 - 24.59$ eV range. The first two energy bins cover the Habing (1968) band, $6.0 - 13.6$ eV, which regulates the temperature of the ISM and photo-dissociation regions (PDR); of the two, the higher energy bin is specific for the Lyman-Werner radiation ($11.2 - 13.6$ eV), which photo-dissociates H2 via the two-step Solomon process (Stecher & Williams, 1967). The last three energy bins cover the H-ionising photons up to the first ionisation level of He, $13.6 - 24.59$ eV. Gas and dust represent sinks for the radiation while stars act as sources. We neglect the cosmic UV background contribution, since the typical ISM densities are sufficiently large to ensure an efficient self-shielding (Gnedin, 2010).

5.1.2 Line emission

Line emission is calculated on a cell by cell basis by using CLOUDY models (Ferland et al., 2017). We use grids of CLOUDY models for density, metallicity, radiation field intensity, as a function of the column density, which is used as a stopping criterion for the calculation. We account for the turbulent and clumpy structure of the interstellar medium (ISM), by parameterising the underlying distribution as a function of the gas Mach number (Vallini et al., 2017, 2018), expressing the thermal to turbulent energy ratio. We have two grids of CLOUDY models, in which the impinging SED includes – does not include – ionising radiation ($h\nu > 13.6$eV). We consider radiation to be ionising in those cells that i) contain young ($t_\star \leqslant 10$ Myr) stars or ii) have a ionisation parameter larger then $\geq 10^{-3}$. Every grid is composed of 17 density bins ($10^{-2} \leqslant n/\mathrm{cm}^{-3} \leqslant 10^{6.5}$), 8 metallicity bins ($10^{-3} \leqslant Z/\,\mathrm{Z}_\odot \leqslant$

$10^{0.5}$), and 12 ISRF intensity bins ($10^{-1} \leqslant G/G_0 \leqslant 10^{4.5}$), for a total of 1632 distinct models per grid. For the SED of the impinging radiation field on the slab of gas of interest in CLOUDY, we use our fiducial SED with stellar age of 10 Myr and solar metallicity, since the stellar population is the primary contributor to the interstellar radiation field in our simulated galaxies.

5.1.3 Outputs and identification

After each individual zoom-in simulation is completed, we identify galaxies and compute their emission properties. Each simulation outputs multiple snapshots equispaced in redshift $\Delta z \simeq 0.5$ for $9 \leqslant z \leqslant 15$, and equispaced in time ($\Delta t \simeq 10$ Myr) for $6 \leqslant z \leqslant 9$; this setup gives a total of about 70 snapshots per simulation. In each snapshot, apart from the central target, there are about $10 - 30$ galaxies in the zoom-in region, depending on environment and redshift. To identify the target DM halos and galaxies we use ROCKSTAR-GALAXIES (Behroozi et al., 2013b), a clustering algorithm that performs a phase-space identification for multi-mass simulations. It uses a friend-of-friend algorithm that adopts a metric accounting for both spatial and velocity separations. We treat separately DM and stellar particles, and allow ROCKSTAR-GALAXIES to identify groups with a minimum number of 100 (20) DM (stars) particles. ROCKSTAR-GALAXIES provides the linking relations between halo (central) and sub-halo (non-central), but we note that the latter category do not encompass the *satellite* galaxies residing in the inner parts of host DM haloes. Their search and analysis will be performed in Chapter 6 with the method described in Chapter 3.1 and Gelli et al. (2020). Finally, we label each galaxy by the name of the simulation, number of the snapshot, and stellar halo ID.

5.2 Results

5.2.1 Overview and morphology

What do SERRA galaxies look like? To have a visual representation, we select 9 different $M_\star \sim 10^9$ $M_\odot$ galaxies in the redshift interval $6 \lesssim z \lesssim 8$, chosen as a showcase of the different evolutionary stages. In Fig. 5.1 we plot maps of the gas surface density Σ_g of these galaxies, oriented face-on[1]. In a cosmological structure formation scenario, gas starts to condense in overdensities generated by dark matter halos. Via filamentary accretion in the inter-galactic and circum-galactic medium,

[1]We define the face-on orientation by using the total stellar angular momentum.

gas flows to the centre of the potential DM well, where it can cool and reach densities high enough that H_2 and thus star formation is possible (upper panels in Fig. 6.4). Mergers represent landmarks of galaxy evolution, as per the hierarchical build-up scenario, and objects can often be seen in different phases of the merging process (middle panels). If the galaxy mass is high enough and it is not disturbed by mergers, a spiral structure (e.g. Ceverino et al., 2015; Pallottini et al., 2017a) forms within a rotating and pressure supported disk (e.g. Inoue et al., 2016; Leung

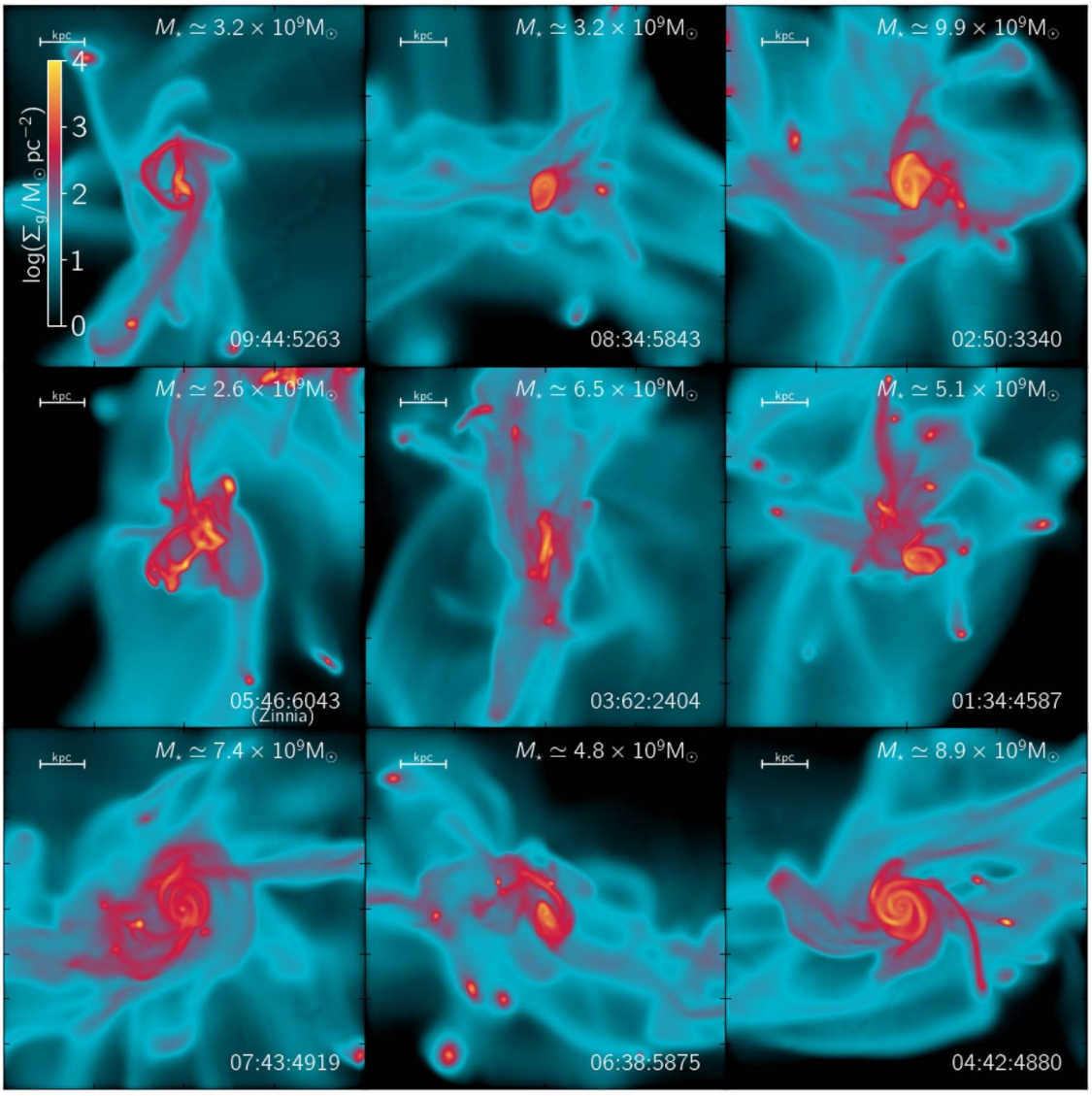

Figure 5.1: Overview of SERRA galaxies. Each panel shows the gas surface density of a galaxy with $M_\star \gtrsim 10^9$ $M_\odot$. To give a qualitative overview of the different morphologies found in SERRA, each galaxy is taken from a different simulation in the suite. For each panel, the galaxy stellar mass and identifier and name when present are shown in the upper right and lower right parts, respectively. From Pallottini et al. (2022).

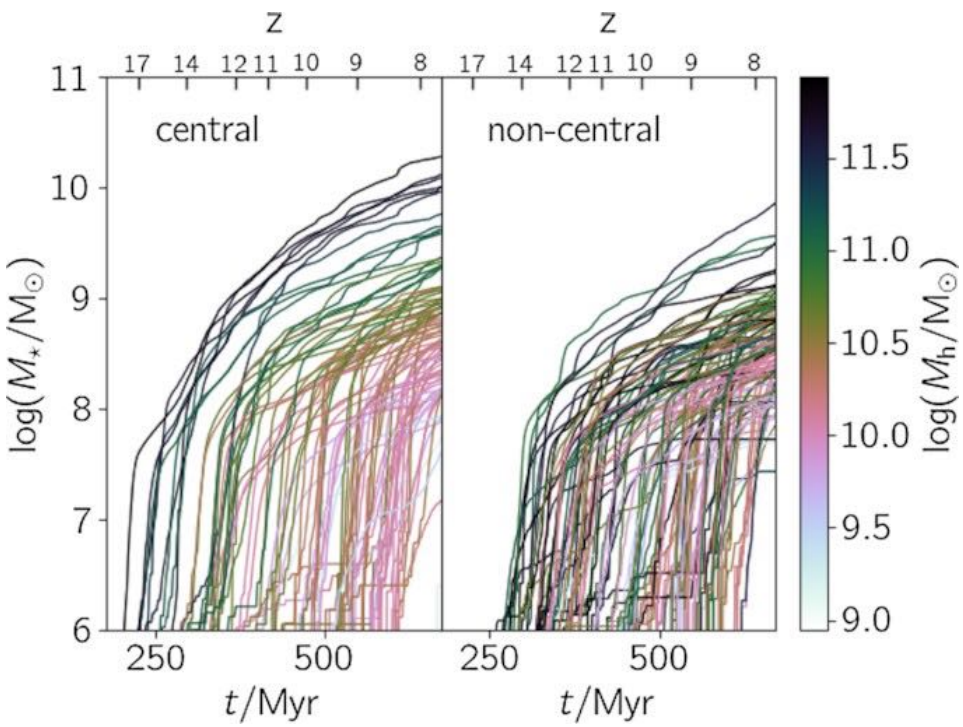

Figure 5.2: Cumulative stellar mass as a function of cosmic time (and z in the upper axis) in the SERRA simulation. Galaxies are divided into central (89 objects, left panel) and non-central (113 objects, right panel), depending on whether they are the most massive galaxy in the host dark matter halo. For each of the 202 galaxies, the evolutionary track is coloured according to the host halo mass at $z = 7.7$. From Pallottini et al. (2022).

et al., 2020), while it continues to accrete gas and forming stars (lower panels). The morphological evolution is particularly rapid at high-z, as the rate of mergers per unit time and fresh gas accretion is an increasing function of redshift (e.g. Fakhouri et al., 2010; Correa et al., 2015). Furthermore, the stellar feedback is particularly violent because of the episodic and bursty nature of the star formation history. Thus the same galaxy can dramatically change its morphology in a relatively short time lapse, i.e. ~ 25 Myr (e.g. Kohandel et al., 2019).

5.2.2 Stellar build-up

The stellar mass build-up of galaxies in SERRA is plotted in Fig. 5.2. The evolution is shown up to $z = 7.7$ for 202 individual galaxies, each one of them being coloured according to the host halo mass[2]. Galaxies start to form from $z \sim 18$, when the

[2]Here as halo mass we adopt 'M200c', i.e. integrating the DM mass contained in a sphere centred around the stellar centre of mass up to the radius where the density is 200 times higher then critical density δ_c, i.e. $M_h = \int \rho_{DM} \mathrm{d}^3 r = 200 \delta_c \int \mathrm{d}^3 r$.

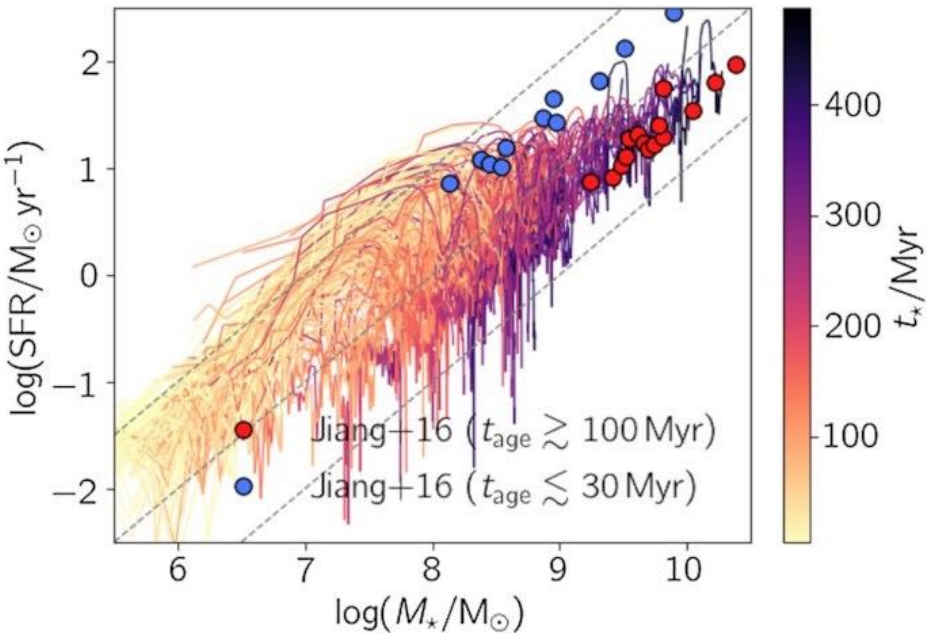

Figure 5.3: Evolution of SFR vs $M_\star$. Each galaxy is coloured with its age as it increases with $M_\star$. Crosses are the observations from Jiang et al. (2013) with the sample divided in young and old galaxies. The three dashed lines indicate a constant value of sSFR = SFR/M$_\star$ = 1, 10, 100 Gyr^{-1}. From Pallottini et al. (2022).

Universe is $t \sim 200$ Myr old. In the plotted redshift range the stellar masses span from 10^6 to 5×10^{10} M$_\odot$. Since the suite is surveying biased regions of the Universe, relatively rare galaxies $M_\star \gtrsim 10^{10}$ M$_\odot$ are present since $z \lesssim 9$; in particular, 37 targets have $M_\star \geqslant 10^9$ M$_\odot$ at $z = 7.7$. Regardless of the distinction, almost all the galaxies experience a rapid increase of their stellar mass in their first ~ 100 Myr, followed by a less intense growth phase. To have a closer look, in Fig. 5.3 we can check so called "main sequence", i.e. the star formation rate as a function of galaxy stellar mass, that we colored with the galaxy age[3] ($t_\star$). Galaxies in SERRA start their life with a specific star formation rate sSFR = SFR/M$_\star$ = 100 Gyr^{-1} and gradually move to sSFR = 10 Gyr^{-1} as they grow older (around $t_\star \simeq 200$ Myr). As expected from the sSFR evolution (see Madau & Dickinson, 2014, and reference within), galaxies in the EoR have extreme values with respect to what observed locally ($z = 0$, sSFR $\simeq 0.1$ Gyr^{-1}) and at low redshift ($z = 1$, sSFR $\simeq 1$ Gyr^{-1}). The values reported for $M_\star \simeq 10^9$ M$_\odot$ galaxies in SERRA are in good agreement with those observed at $z \sim 7$ (González et al., 2010; Stark et al., 2013). Moreover, $z \sim 6$ observations by Jiang et al. (2013) show that young (old) galaxies have

[3]Here the galaxy age $t_\star$ is defined as the time from the first star formation event; we stress it should be interpreted as time reference more then a galaxy physical property

sSFR $\simeq$ 39.7 Gyr^{-1} (4.1 Gyr^{-1}), i.e. hinting at a decreasing trend of sSFR with galaxy age. Direct comparison with the data from Jiang et al. (2013), reveals that the general trends from the stellar tracks of SERRA galaxies well reproduce the observations of old galaxies.

The halo to stellar mass relation, often used as a benchmark for the efficiency of star formation, is shown in Fig. 5.4 for central galaxies at $z = 7.7$ in SERRA. The halo (stellar) mass range from about 10^9 to 5×10^{11} $\mathrm{M}_\odot$ (10^6 to 5×10^{10} $\mathrm{M}_\odot$). These central galaxies have an average trend that is in broad agreement with the $M_\star - M_h$ from Behroozi et al. (2013c). Notably, the redshift-dependent turnover at $M_h \sim 10^{11}$ $\mathrm{M}_\odot$ is well reproduced. The SERRA predictions diverge from the Behroozi et al. (2013c) curve at $M_h \lesssim 5 \times 10^{10}$ $\mathrm{M}_\odot$, where we mind that the curve is extrapolated, and are instead in this range closer to the results of RENAISSANCE Xu et al. (2016).

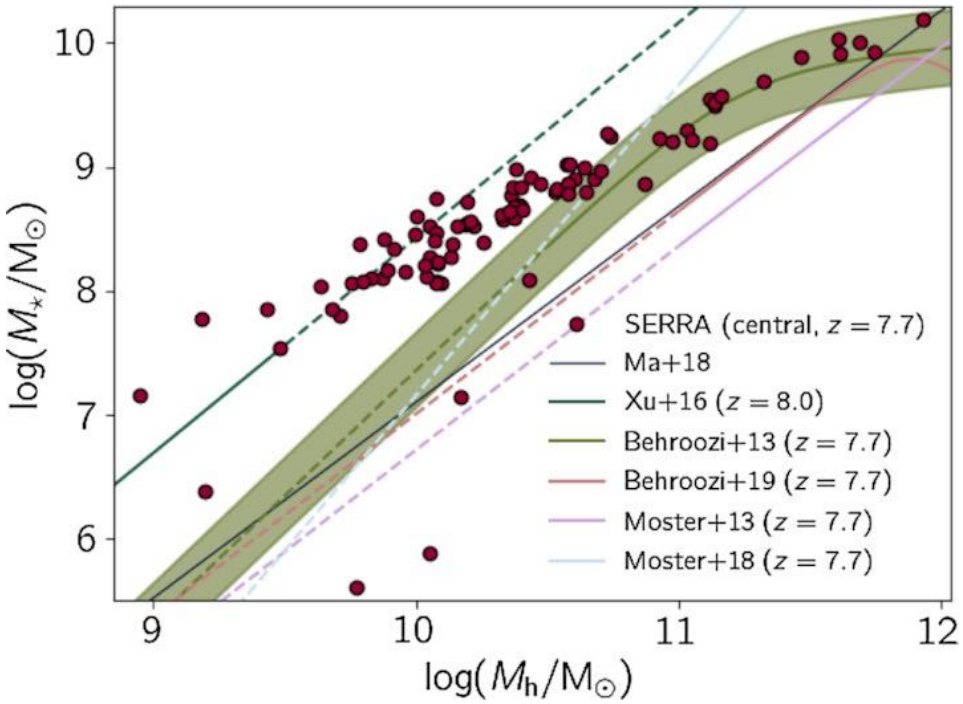

Figure 5.4: Halo - stellar mass ($M_\star - M_h$) relation for 89 simulated central galaxies at $z = 7.7$. We overplot the results from other numerical simulations from REINASSANCE (Xu et al. 2016, at z = 8) and FIRE-2 (Ma et al. 2018, redshift independent fit), along with the results from different abundance matching models (Behroozi et al., 2013c; Moster et al., 2013, 2018) at the same redshift. Dashed lines indicate the M_h ranges where models are extrapolated. From Pallottini et al. (2022).

5.2.3 Comparison with observed relations

The Schmidt-Kennicutt (KS) relation for SERRA galaxies is plotted in Fig. 5.5, where we find that simulated galaxies are typically located above the *local* relation (Heiderman et al., 2010):

$$\Sigma_{\rm SFR}^{\rm KS} = 10^{-12}(\Sigma_{\rm g}/\ {\rm M}_\odot{\rm kpc}^{-2})^{1.4}\ {\rm M}_\odot{\rm yr}^{-1}{\rm kpc}^{-2}, \tag{5.1}$$

which is a fit to the Kennicutt (1998) relation. Observations of both local starbursts (e.g. Kennicutt, 1998; Bothwell et al., 2010) and $1 \lesssim z \lesssim 2$ galaxies (e.g. Bouché et al., 2007; Tacconi et al., 2010; Daddi et al., 2010) match our results quite well. The deviation from the KS can be quantified via the "burstiness" parameter (e.g. Ferrara et al., 2019)

$$k_s \equiv \Sigma_{\rm SFR}/\Sigma_{\rm SFR}^{\rm KS}, \tag{5.2}$$

which also governs the observability of several emission lines (e.g. Vallini et al., 2020, 2021). SERRA galaxies are in general remarkably "bursty", presenting at $z = 7.7$ an average value of $k_s = 3.03^{+4.9}_{-1.8}$.

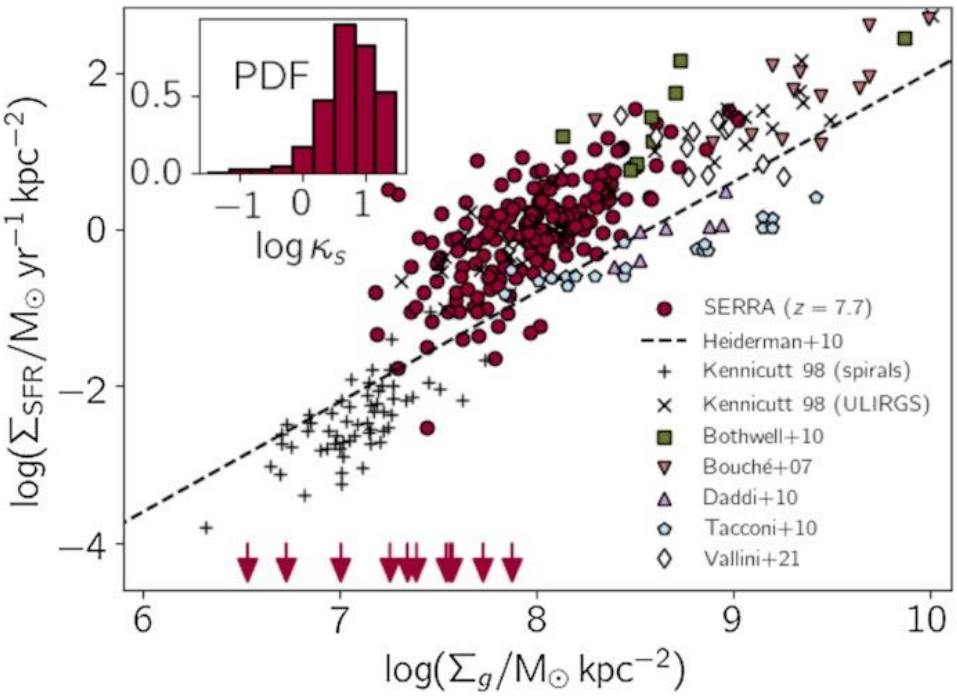

Figure 5.5: Schmidt-Kennicutt relation at $z = 7.7$, i.e. the star formation vs gas surface density. Upper limits (red arrows) are shown for the 11 objects that are temporarily quenched. We also report comparison with different sets of observations (see Sec. 5.2.3) and an inset with the probability distribution function (PDF) of the burstiness parameter k_s, defined in Eq. 5.2 for SERRA galaxies. From Pallottini et al. (2022).

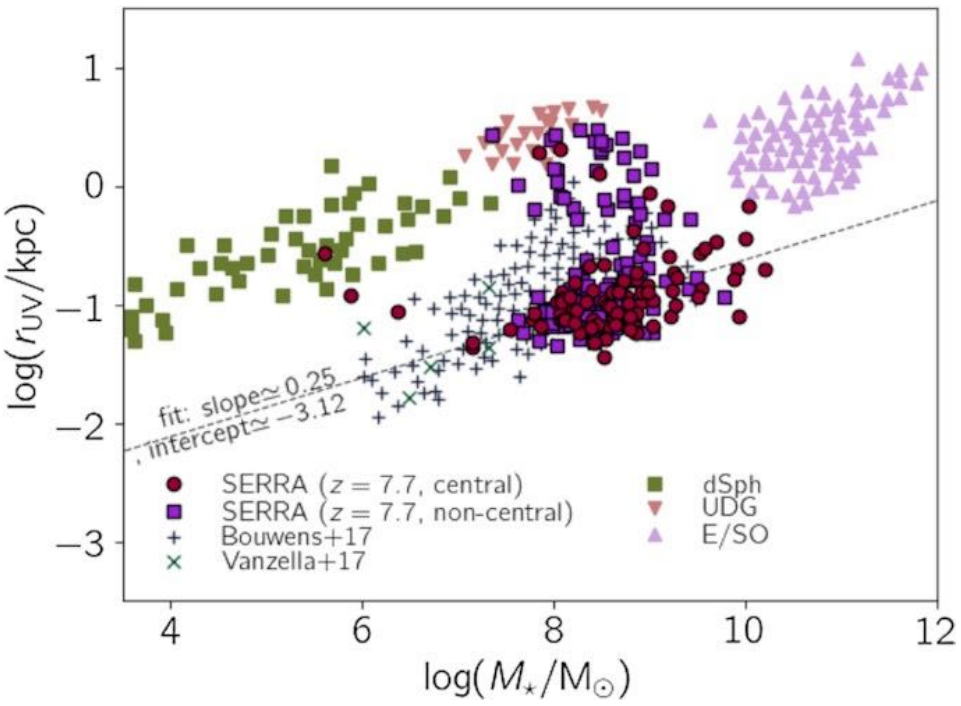

Figure 5.6: Size-stellar mass relation for SERRA galaxies, with the dashed line illustrating the fit for the central galaxies (obtained by excluding the outliers due to mergers). We report comparison with both high-z and local observations. From Pallottini et al. (2022).

CO detections (D'Odorico et al., 2018; Pavesi et al., 2019) in EoR galaxies are rather difficult and rare, making a precise assessment of the gas mass rather uncertain, but indirect methods may overcome such problems. Using an approach based on FIR [CII] and [O III] lines Vallini et al. (2021) finds $k_s = 36.3^{+19.1}_{-18.7}$ for 10 galaxies at $z > 5.5$, and Markov et al. (2022) finds $\log k_s = 1.43^{+0.38}_{-0.53}$. These values are in line with the values found for SERRA galaxies with approximately $\Sigma_g \simeq 10^9$ M$_\odot$kpc^{-2}.

The size-stellar mass relation for our sample is reported in Fig. 5.6. We define the galaxy size, $r_{\rm UV}$, as the radius that contains 50% of the UV luminosity. In our sample, the behaviour is two folded: most of the galaxies have $r_{\rm UV} \simeq 100$pc, while about 10% of the objects have larger sizes ($\simeq$ 1kpc). The latter group is composed by galaxies – mostly non centrals – that have recently experienced or are experiencing a merger. While their size-stellar mass relation resembles that of local Ultra Diffuse Galaxies (UDG, e.g. Brodie et al., 2011; Norris et al., 2014), this might be a transient feature related to the merging phase. Fitting the relation for the central SERRA galaxies excluding the mergers, we obtain:

$$\log r_{\rm UV}/{\rm kpc} = (0.249 \pm 0.002) \log M_\star/\ {\rm M}_\odot - 3.12 \pm 0.13. \tag{5.3}$$

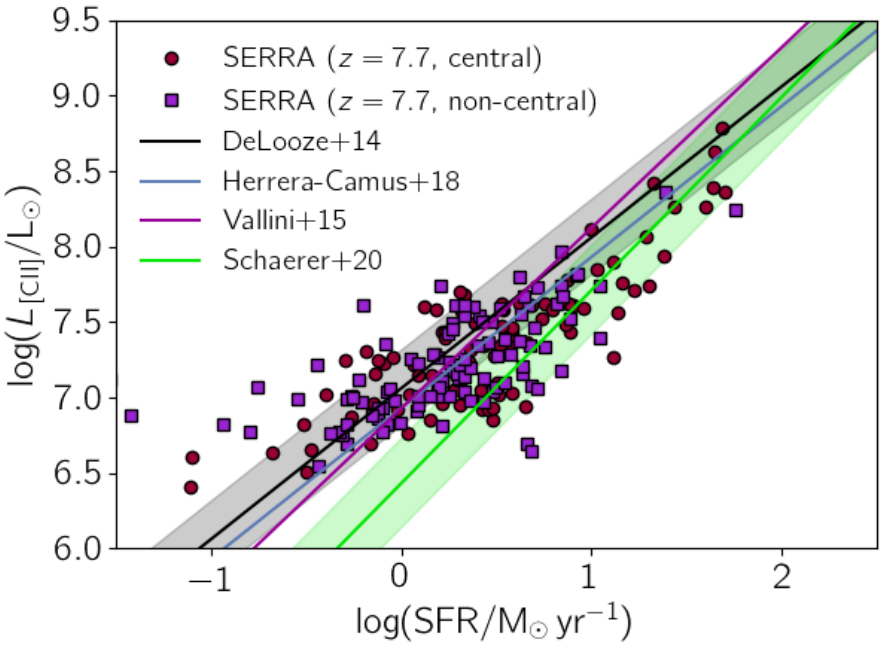

Figure 5.7: The integrated [CII] − SFR relation found in SERRA at $z = 7.7$, along with results from local (De Looze et al., 2014; Herrera-Camus et al., 2018) and $z = 4 - 6$ observations (Schaerer et al., 2020), and results from physical motivated models (Vallini et al., 2015, $Z = 0.5$ $Z_\odot$). From Pallottini et al. (2022).

The size-stellar mass relation from SERRA has a slope consistent with the corresponding one in the local universe en- compassing dwarf spheroidals (dSphs), Ultra Diffuse Galaxies (UDG), and elliptical/lenticular (E/S0); however in SERRA the relation is offsetted by about an order of magnitude, qualitatively as expected from the redshift evolution (Shibuya et al., 2015). Our data is broadly consistent with that derived by Bouwens et al. (2017) for $6 \lesssim z \lesssim 8$ lensed galaxies and by Vanzella et al. (2019) for $z \gtrsim 3$ for "proto-globular" clusters.

Regarding emission lines, the [CII] − SFR relation is presented in Fig. 5.7. The values are consistent with local data (De Looze et al., 2014; Herrera-Camus et al., 2018), albeit with a larger scatter. This is expected on the basis of the early work by Carniani et al. (2018) analysing 20 targets, and of the more recent analysis of the ALPINE sample presented in Schaerer et al. (2020, 118 targets). The scatter in the relation is driven by the larger spread of physical properties (such as n, Z, κ_s) deduced for high-z galaxies (Vallini et al., 2015; Ferrara et al., 2019); further, the scatter appears to be larger for non-central objects, as a consequence of the interactions with their nearby more massive galaxy.

In Fig. 5.8 we analyze how emission lines for SERRA galaxies compare to avail-

able local data. with all the available low-redshift data to assess whether early systems differ substantially from their local counterparts

To conclude, in Fig. 5.8 we show the SFR dependence of different lines ([CII], [OIII] and [OI] 63μm) for simulated galaxies, and compare it with available data of local galaxies to assess possible similarities with starbursts galaxies, dwarfs, $z \sim 0.5$ and Ultra Luminous InfraRed Galaxies (ULIRGs, De Looze et al., 2014). Regarding the [CII] (tracing both cold/warm neutral and ionised ISM) and [OI] (tracing dense atomic and molecular gas), the bulk of SERRA galaxies follows the starbursts and $z \sim 0.5$ relation. We note that at progressively higher SFR $\gtrsim$ 3 $M_{\odot}yr^{-1}$ the simulated galaxies move farther away from the slope characterising the local dwarf galaxy population. The [OIII]-SFR relation is more complex, with a fraction of galaxies having their SFR temporarily quenched, and therefore showing a strongly reduced [OIII] luminosity.

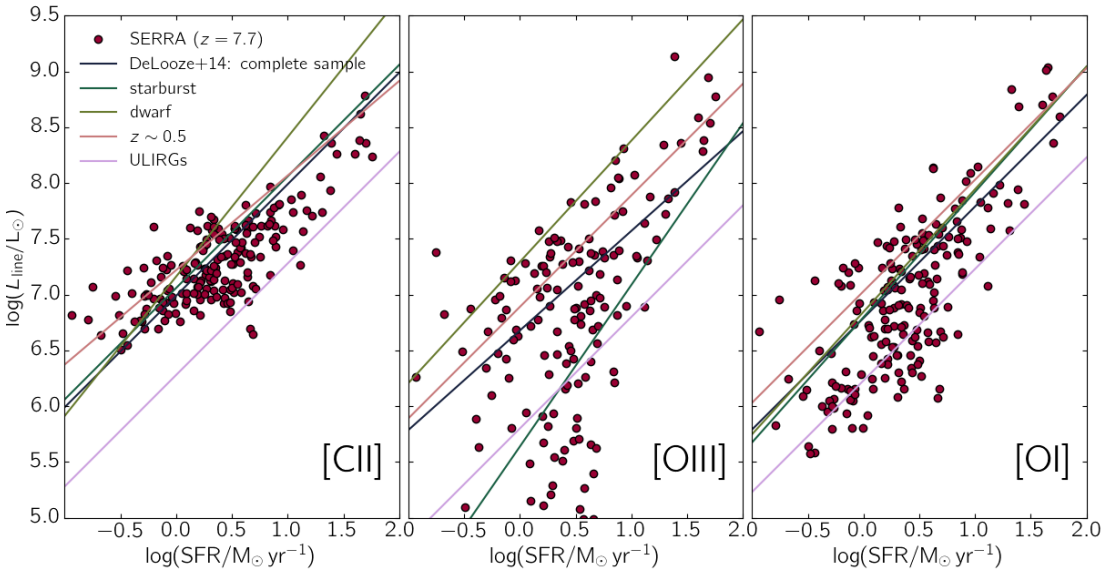

Figure 5.8: SERRA emission line predictions compared to available local data. We show [CII], [OIII] and [OI] as a function of SFR in the left, central, and right panel, respectively. Fits to observed trends for different classes of galaxies in the low-z Universe are shown. The dwarf galaxy observations are taken from De Looze et al. (2014), as well as the classification and the relative fits, which are based on additional data from Brauher et al. (2008); Graciá-Carpio et al. (2011); Sargsyan et al. (2012); Parkin et al. (2013); Díaz-Santos et al. (2013); Farrah et al. (2013).

5.3 Conclusions

The SERRA suite of zoom-in high-resolution cosmological simulations provides a unique set of massive galaxies at high-z along with their physical and emission properties, environments and evolution. The $z = 7.7$ sample, consisting of 202 targets, has proven successful in reproducing the typical properties of observed high-z galaxies, from the Schmidt-Kennicutt to the size-stellar mass and [CII] − SFR relation. The described set of galaxies constitute a biased sample of massive galaxies living in the densest environments of the cosmic web, mimicking a surveys targeting those galaxies luminous enough to be studied with current instruments (HST and ALMA), and that are now being investigated in more details with JWST. But it is only JWST that is able for the first time to unveil and resolve also the populations of satellites expected to dwell within these massive haloes. It is hence timely and essential to derive the properties of the large statistical sample of satellite galaxies provided by the SERRA simulations, analysed in Chapter 6.

CHAPTER 6

Passive satellites: quenching star formation at high-z

The analysis of the histories of star formation of high-z dwarf galaxies in Sec. 3.3 revealed that, while all of them form their stars in intense bursts of star formation as expected from typical high-z systems, some of them later stop forming stars and remain *passive* thereafter. The observations of passive galaxies is essential in order to understand which events drive the transition from a star-forming to a non star-forming state, a key open issue in galaxy evolution. The variety of physical mechanism responsible may involve the complex feedback processes but also environmental interactions. Many passive galaxies have been observed and studied both in the local universe (e.g. dwarf spheroidals and ultra-faint dwarf galaxies Tolstoy et al., 2009; Simon, 2019), and at redshifts up to $z \sim 5$ (Santini et al., 2021). With the upcoming revolutionising JWST observations we can now finally aim at unveiling the presence of passive galaxies beyond $z > 6$: what processes are able to quench star formation in the EoR? How many and in which environments are passive galaxies expected to exist at early times? What strategies are needed in order to unveil them with JWST data?

We assess these questions in this Chapter, based on the results of the paper Gelli et al. 2023, to be submitted. We analyse the outputs of multiple simulations within the SERRA suite, which evolve up to redshifts in the range $6 < z < 8$. Within the last snapshot of each simulation, we use ROCKSTAR (Behroozi et al., 2013a) to select typical massive Lyman break galaxies, obtaining a sample of 14 galaxies with stellar masses of $M_\star \simeq 10^{9.5} - 10^{10.5}$ $M_\odot$ and star formation rates SFR $\simeq 30 - 100$ $M_\odot yr^{-1}$. For each of the 14 selected LBGs, we analyse the region

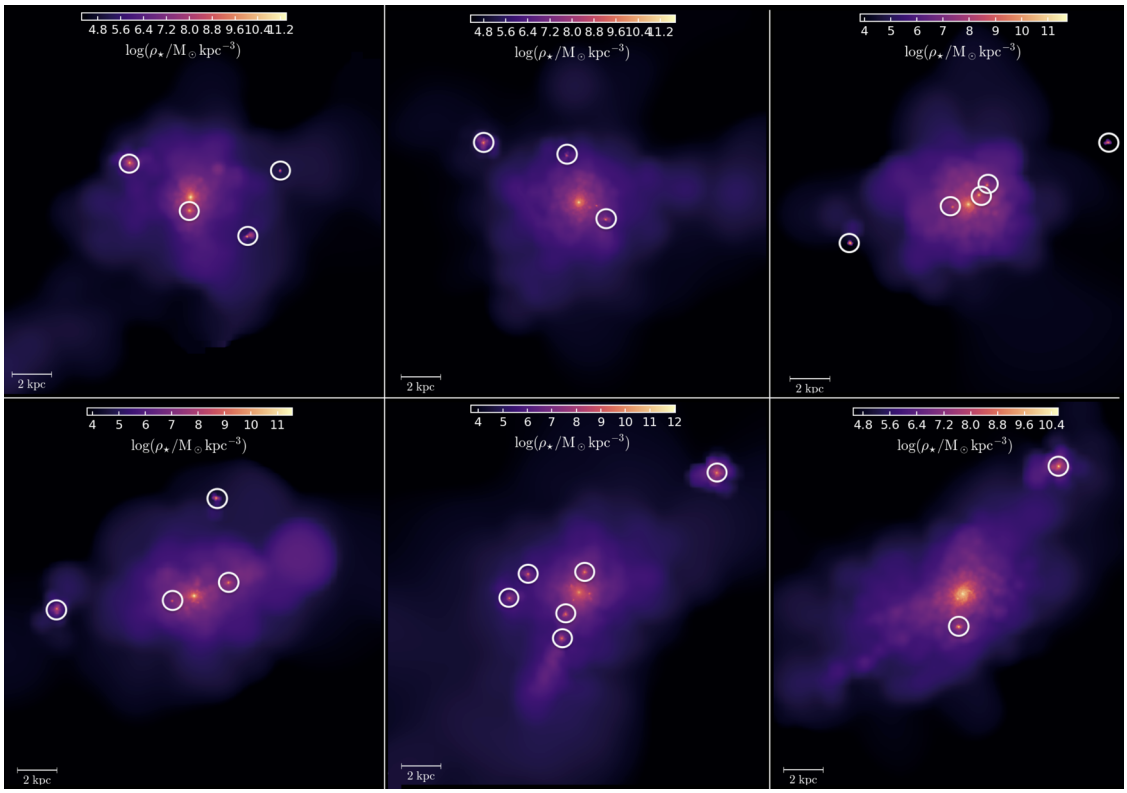

Figure 6.1: Stellar density maps of six simulations of the SERRA suite. The maps are centred on massive LBGs of $M_\star \sim 10^{10}$ $M_\odot$, that are surrounded by smaller satellite galaxies (white circles).

enclosed within its virial radius (typically in the range $R_{\rm vir} = 15-25$kpc) and using the satellites finder (described in Sec. 3.1) we find 60 dwarf satellite galaxies orbiting around the 14 host LBGs. In Fig. 6.1 we show as an example the stellar density maps of six massive galaxies in SERRA, with the located satellites pinpointed with the white circles. In order to take full advantage of the large set of simulations, we can also further enhance the statistics of galaxies of our sample by analysing outputs of the multiple snapshots available for each simulation (see Sec. 5.1.3) and treating each one as an individual system. Tracking the LBGs back in cosmic time in the $6 < z < 8$ range gives a final sample of 42 LBGs systems and 131 dwarf satellites.

6.1 The satellites zoo

The satellites in SERRA have a wide range of stellar masses, varying from 10^7 to $10^{9.5}$ $M_\odot$, and of gas masses, from 10^5 to 10^9 $M_\odot$, which are typically between $0.5-1$ order of magnitudes lower with respect to the stellar component. We now

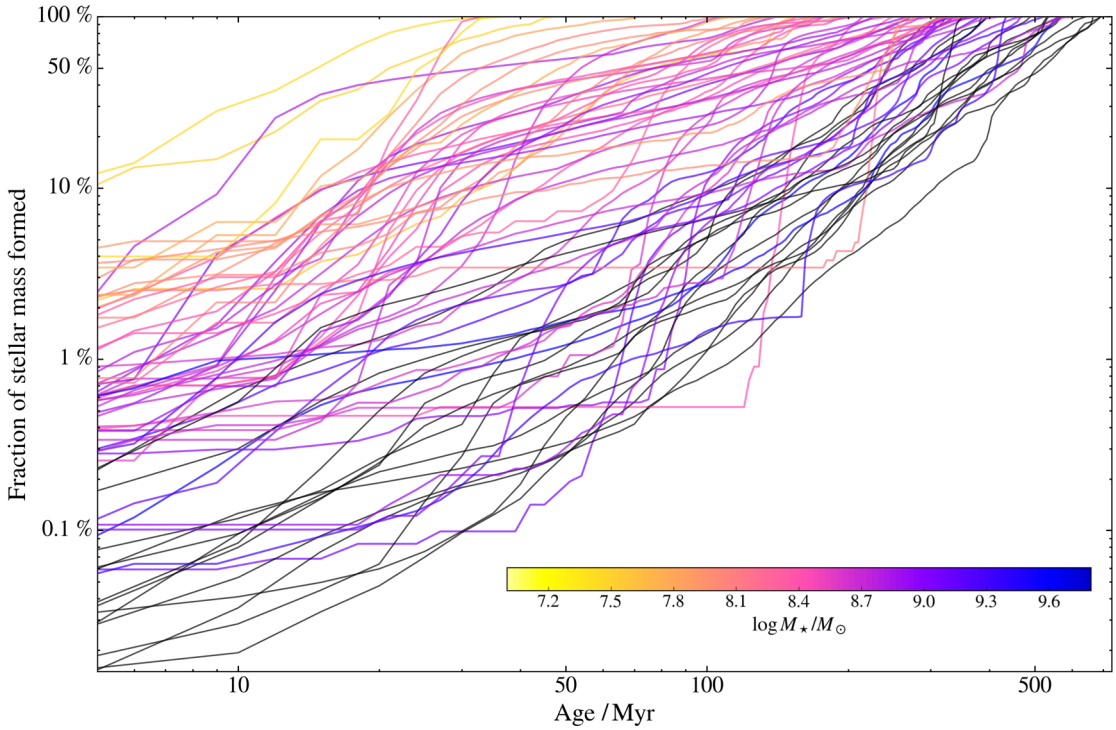

Figure 6.2: Fraction of stellar mass formed with respect to the final stellar mass ($M_\star$) of each galaxy as a function of the time from its first formation event. The colours indicate the final stellar mass for the satellite galaxies, and the central massive hosts ($M_\star \sim 10^{10}$ $M_\odot$) are displayed in in black.

proceed to analyze their star formation histories that can also be very diverse and based on which the satellites can be divided into two main categories: *actively star-forming* satellites, and *passive* satellites.

6.1.1 Evolution

To have a first look at how the satellites form and built-up, in Fig. 6.2 we show the fraction of stellar mass formed as a function of the time since the first event of star formation for each galaxy. The colours correspond to the final stellar mass of each galaxy, with the central LBG hosts represented in black. There is a clear mass-dependent general trend, for which low mass galaxies form all of their stellar content in a few tens of Myr, whereas progressively higher massive ones build up in much longer times (up to $\sim$ 500 Myr). Interestingly, a similar behaviour is witnessed in the SFH of many local dwarf galaxies orbiting around the Milky Way and M31 galaxy (e.g. Weisz et al., 2014), suggesting that this is a general universal trend, independent on the environment and cosmic epoch. Still, a few exceptions from the main trend can be noticed in some of our galaxies whose evolutionary tracks are

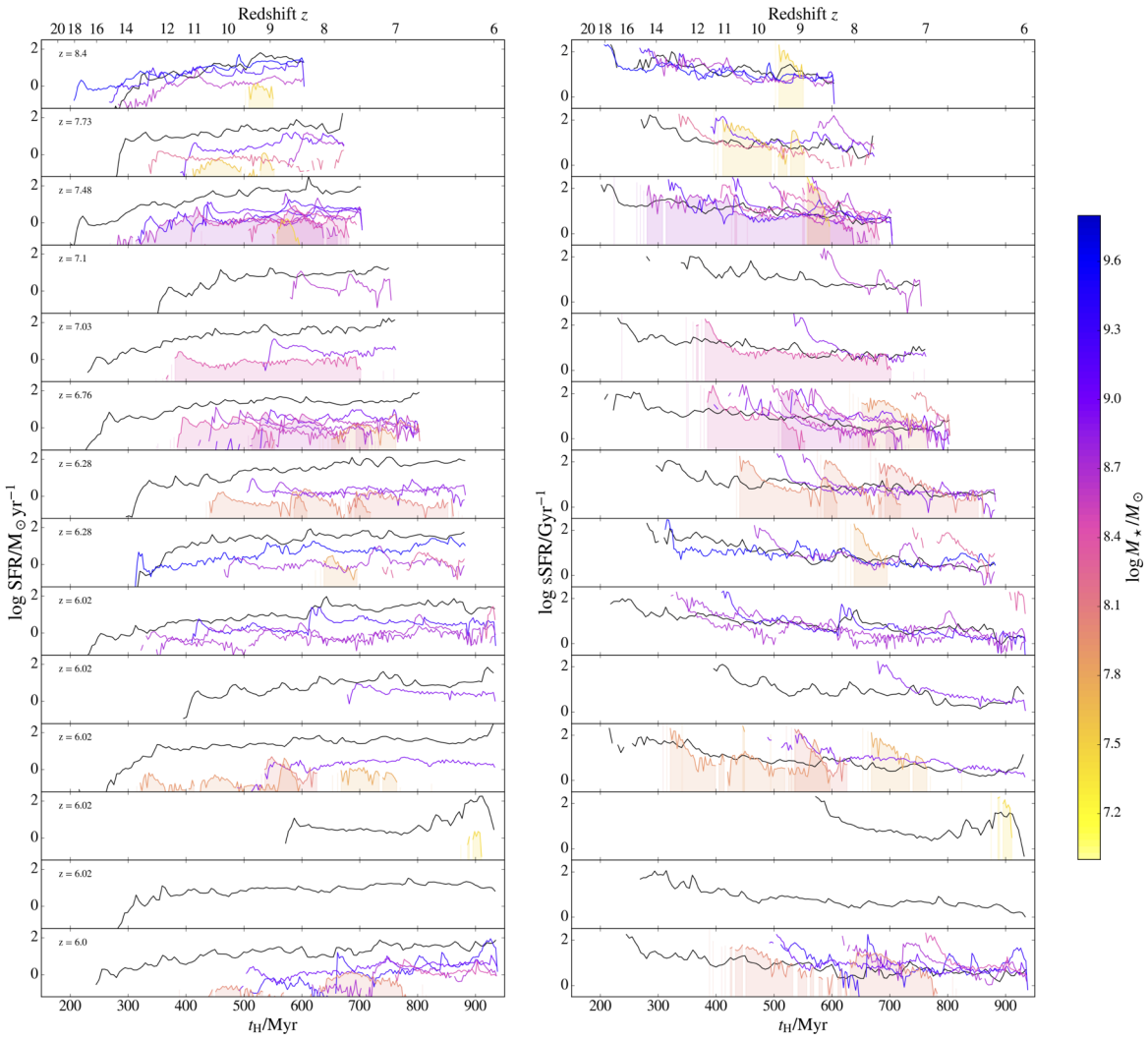

Figure 6.3: Star formation rate (SFR) and specific star formation rate (sSFR) as a function of the age of the Universe (t_H) for the 14 systems of galaxies (central LBGs in black, satellites coloured as in Fig. 6.2). Inside each panel the final redshift for each simulation is reported. Filled curves are used for the satellite galaxies that are passive at the end of the simulation (30% of the sample).

characterised by extended horizontal trends, tracing prolonged phases in which star formation has been temporarily stopped by feedback processes. Similarly, many low mass galaxies ($M_\star < 5 \times 10^8$ M$_\odot$) are permanently quenched, i.e. they stop forming stars and remain passive once they have formed all of their stellar content.

In order to better investigate their evolution, in Fig. 6.3 we show the star formation rates (SFR) and specific star formation rates (sSFR) as a function of the age of the Universe $t_{\rm H}$ (and redshift z, upper axis), averaged over in 3 Myr time bins. Each panel corresponds to a system of central LBG and its satellite dwarf galaxies present in the latest snapshot of each simulation (corresponding redshifts indicated

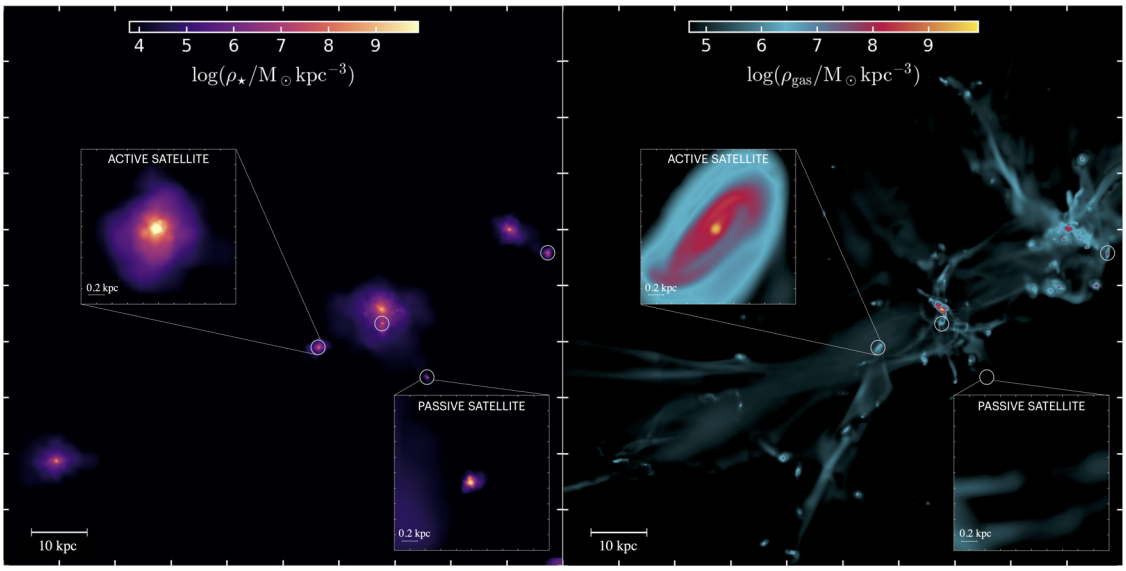

Figure 6.4: Example of stellar ($\rho_\star$) and gas ($\rho_{\rm gas}$) density maps of a system at $z = 6$ within the SERRA simulations. Field of view has a size of 100 kpc and contains 3 massive LBGs ($M_\star \sim 10^{10}$ M$_\odot$) with respectively 1, 3 and 0 satellites dwarf galaxies orbiting around them (pinpointed with white circles). The insets show two zoomed region of size 2 kpc centred on a typical star-forming active satellite ($\log M_\star/$ M$_\odot = 8.97$) and on a typical passive satellite ($\log M_\star/$ M$_\odot = 7.96$).

inside the panels). We notice that the number of satellites orbiting around each LBG does not depend on the central host galaxy properties (e.g. stellar mass or age), nor on the redshift. All the central LBGs have star formation histories (left column) quite similar to one another, and characterized by a steady increase of the SFR with time, always reaching very high values up to ~ 100 M$_\odot$yr^{-1}. The formation of the satellites is instead much more diversified, featuring several bursts, sudden decreases or interruptions of star formation. The reason is to be found in their low masses and thus shallow potential wells, which make these systems very sensitive to all kind of feedback and environmental effects, making their evolution more irregular. Once again, such susceptibility is witnessed and well proven also in Local dwarf galaxies, where detailed observations show how their SFH are heavily shaped by feedback and environmental effects (e.g. Weisz et al., 2014). Specifically, different processes are at play, like the heating and outflows of gas produced by SNe, the radiative feedback from the nearby LBG and the mergers and infall of fresh gas, particularly frequent in these high-density biased environments (Kohandel et al., 2020; Rizzo et al., 2022). The interplay of all these mechanisms lead to a variety of SFHs, that can however be divided into two main categories: the *active* satellites, that are able to sustain star formation for long times ($\gtrsim 200$ Myr), and *passive*

ones, that are completely quenched and not able to form star anymore (similarly to what found for the 3 satellites evolution in Chapter 3.3).

The sSFR(t) reveals that all galaxies, host LBGs and satellites alike, are star-bursting objects. The initial sSFR is typically as high as $\sim 100\,\mathrm{Gyr}^{-1}$, in correspondence of the first burst of star formation, and it then rapidly decreases of ~ 1 order of magnitude in less that ~ 50 Myr. The fact that these high-z galaxies are particularly *bursty*, also in their later evolution, is evident in the sSFR(t) since these are characterised by may bumps and sudden increases whenever subsequent bursts of star-formation take place due to accretion of fresh gas or mergers. Within the overall sample of satellites, the quenched passive ones represent 31% of the total population, and their evolution is shown with filled curves in Fig. 6.3.

In Fig. 6.4 we show as an example density maps of one simulation at $z = 6$, where three massive LBGs are found within a $(200\ \mathrm{kpc})^3$ volume. The stellar density map (left panel) reveals how the two most massive LBGs (central and upper right galaxies in the map, with $\log M_\star/\ \mathrm{M}_\odot = 10.32$ and 9.79) are surrounded by respectively three and one dwarf satellite galaxies. The massive galaxy located in the lower left part of the map (with $\log M_\star/\ \mathrm{M}_\odot = 9.81$) does not instead show the presence of orbiting satellites. Through the large scale gas density map (right panel) we clearly see the presence of the typical dense filaments along which the gas is accreted and where galaxies tend to form. In the two insets of Fig. 6.4 we display the zoomed maps of two of the satellites, pertaining to and representative of the two above mentioned categories. One is *actively* forming stars, large in size (with stars extending up to ~ 500 pc from its centre) and beginning to form a gas disk-like structure, typical of the most massive LBGs. The other one is *passive*, with all its stars concentrated within $\lesssim 200$ pc and almost completely devoid of gas.

6.1.2 Global physical properties

We need to understand the physical properties expected for the stellar populations of high-z passive and active satellites and of their host massive LBGs, and how these depend on their masses. In Fig. 6.5 we show six physical quantities as a function of $M_\star$, distinguishing between the two classes of satellites: *passive* (orange), *active star-forming* (light blue). The massive LBGs are represented through the grey star symbols.

As expected, with increasing stellar mass, we notice an increase in the average $\langle \mathrm{SFR} \rangle$ (top-left panel), where the mean is performed over the time in which the

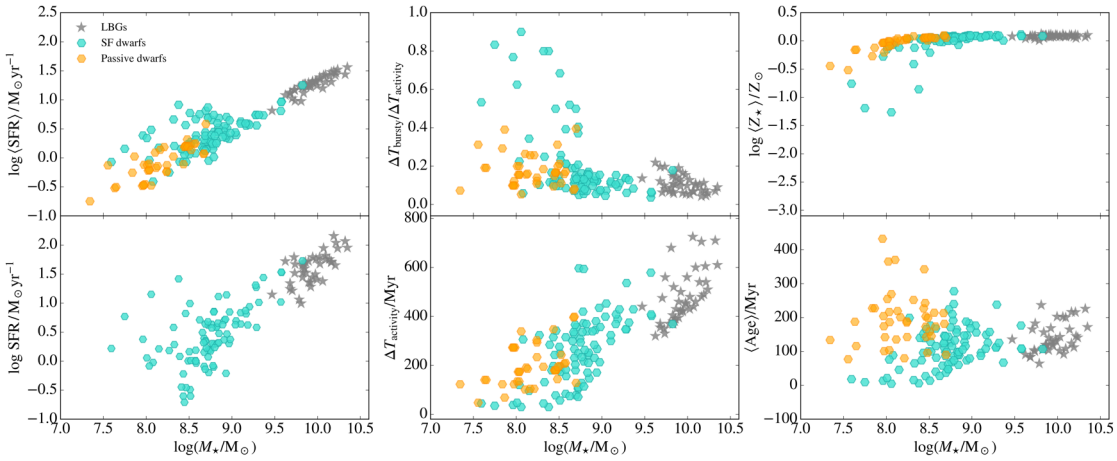

Figure 6.5: For the 131 satellites and 42 LBGs in the redshift range $6 < z < 8$, we show as a function of thier stellar mass: average $\langle \mathrm{SFR} \rangle$; instantaneous SFR; $\Delta T_{\mathrm{bursty}}/\Delta T_{\mathrm{activity}}$ i.e. time span in which a galaxy has sSFR > 50 Gyr^{-1} divided by the time in which it has SFR $\neq 0$; star-forming activity time $\Delta T_{\mathrm{activity}}$; mean stellar metallicities and ages.

galaxy has been forming stars. The plot also shows that passive galaxies may have formed their stellar populations with $\langle \mathrm{SFR} \rangle$ as high as ~ 3 M$_\odot$yr^{-1}.

The instantaneous SFR (bottom-left) presents an even steeper trend with the mass, and more scatter at low masses: in this regime the systems with high SFR of a few ~ 10 M$_\odot$yr^{-1} are very young galaxies ($\lesssim 50$ Myr) that are experiencing their first intense bursts of star formation.

How "bursty" a satellite is can be quantified through the ratio $\Delta T_{\mathrm{bursty}}/\Delta T_{\mathrm{activity}}$ (middle-top). $\Delta T_{\mathrm{bursty}}$ is defined as the time span in which a galaxy has sSFR $>$ 50 Gyr^{-1} and $\Delta T_{\mathrm{activity}}$ as the time in which it has SFR $\neq 0$. We notice that low-mass ($M_\star < 5 \times 10^8$ M$_\odot$) active galaxies are significantly bursty (ratios > 0.5), because in their very active early stages of formation. The ratio of star-forming galaxies, LBGs included, then stabilizes around ~ 0.1 once they have build-up enough stellar mass ($M_\star > 5 \times 10^8$ M$_\odot$). On the other hand, passive galaxies have a range of $\Delta T_{\mathrm{bursty}}/\Delta T_{\mathrm{activity}}$, always < 0.4, depending on for how long they where able to form stars before being quenched.

The increasing trend of $\Delta T_{\mathrm{activity}}$ (middle-bottom) shows that low-mass passive galaxies can form stars for up to ~ 300 Myr before being quenched, whereas more massive satellites and the central LBGs can continuously form stars for up to ~ 700 Myr.

By looking at the average stellar metallicity (top-right) we understand how, despite the very diverse star formation histories experienced by the satellites, metal enrichment proceeds very rapidly through SNe explosions and winds once the star

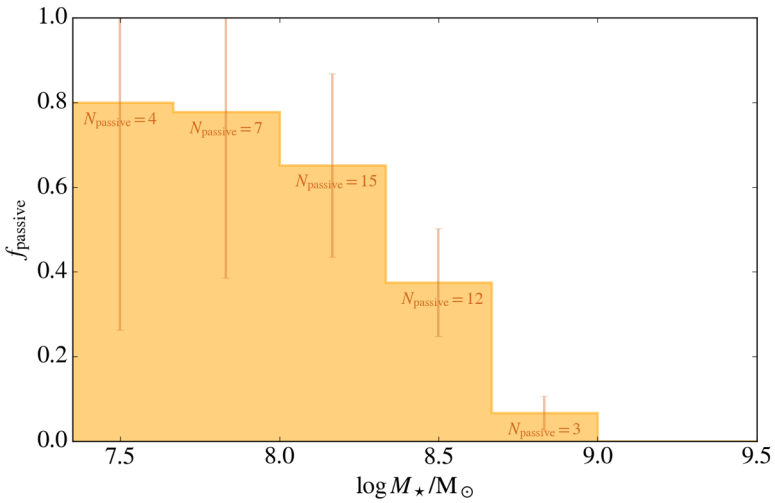

Figure 6.6: Fraction of passive satellites per bin of stellar mass, with errorbars showing the standard deviation of the counts in each bin.

formation starts taking place. The pollution of the ISM with heavy elements by SNe leads to high metallicities ($Z_\star \sim {\rm Z}_\odot$) in typically just a few ~ 10 Myr, thus causing the presence of highly enriched stellar populations in both passive and active satellites. The only few exceptions at $\log(Z_\star/{\rm Z}_\odot) < -1$ are represented by those low-mass young bursty galaxies, more metal-poor since they are in the process of forming their first stellar populations from a gas that has not yet been enriched by metals due to previous star formation.

The average stellar ages (bottom-right) span a wide range of values. We may notice that in the low-mass regime ($< 5 \times 10^8$ ${\rm M}_\odot$) we find either young (a few 10 Myr old) star-forming satellites experiencing their first burst of star formation, or passive systems that can instead be very old up to ~ 400 Myr.

Similarly to what observed in the Local Universe, we notice that the low-mass passive galaxies are expected to exist also in the dense environments of the high-z Universe and to dominate the dwarf satellite galaxies population in the low stellar mass regime. In fact, Fig. 6.6 shows that the fraction of passive satellites per stellar mass bin decreases with increasing stellar mass of the satellite, dropping drastically above $M_\star > 5 \times 10^8$ ${\rm M}_\odot$. We note that similar trends are also expected for quenched satellites at $z \sim 0$ (e.g. Joshi et al., 2021).

In the following Section, we investigate which specific physical processes play a key role in quenching these low-mass dwarfs.

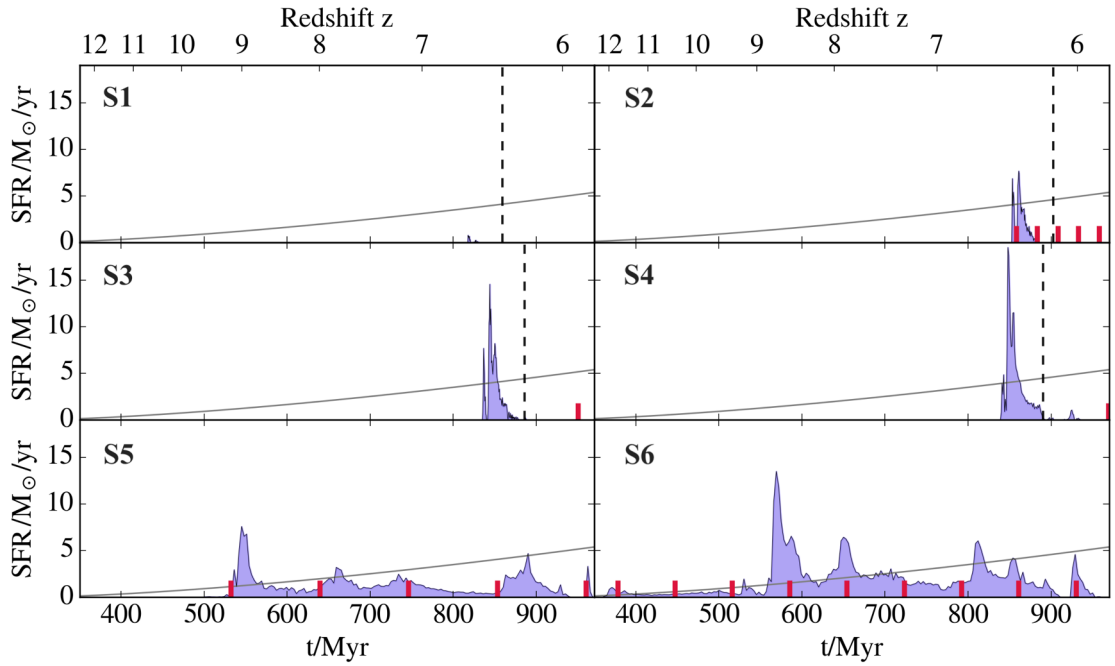

Figure 6.7: Star formation histories of the six dwarf satellites in the Althæa simulation as a function of the cosmic time (lower axis) and redshift (upper axis). Red segments indicate the time at which the satellites were at their orbital periapsis; see Sec. 6.2.1 and Tab. 6.1 for details. The value of the interstellar radiation field, scaled for display purposes, $G(t)/20G_0$, is overplotted as a grey line. For S1,S2,S3 and S4, the vertical dashed line indicates the last SN explosions associated to the peak of star formation.

6.2 What quenches star formation?

We here intend to isolate the physical processes driving the SFH of the satellites, ultimately uncovering what determines their final properties. In order to do this, we analyse in details the histories of star formation of six different satellites evolving up to $z \sim 6$ (Fig. 6.7), using those fron the Althæa simulation (see Chapter 3), that present analogue behaviours as the ones in SERRA[1]. It is evident from Fig. 6.7 that low/intermediate mass satellites (from S1 to S4) form all of their stars in two short bursts ($\sim$ 50 Myr) and are afterwards completely quenched, while the high-mass ones (S5-S6) have remarkably longer SFHs, lasting $400-500$ Myr, i.e. up to $z \simeq 6$.

Does the presence of the nearby central LBG leave an imprint on the SFHs of the smallest satellites via, e.g. dynamical interactions, or is it internal stellar feedback that mostly determines their evolution? In the following, we review these

[1]With respect to SERRA in the Althæa simulation there is no on-the-fly radiative transfer, but its effect doesn't produce remarkable differences on the global star formation and quenching of the satellites, that is indeed found in both cases.

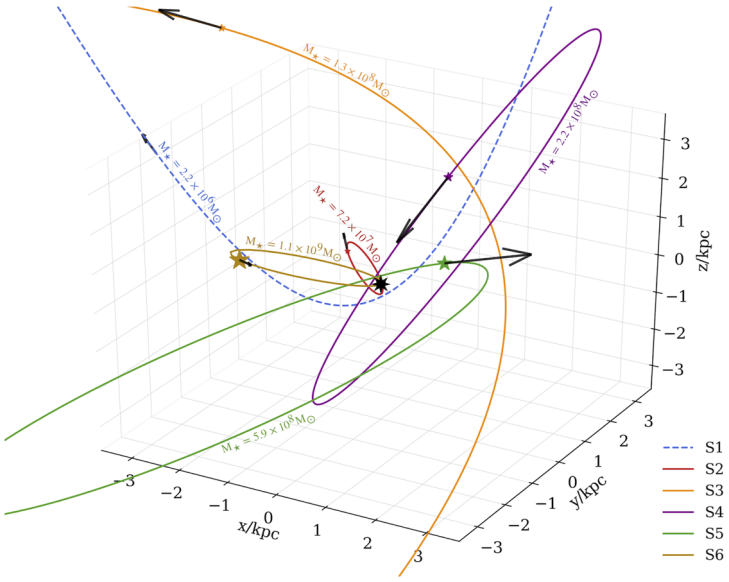

Figure 6.8: Orbits of the six dwarf satellites around the central galaxy Althæa (central black star). The stars and arrows indicate the location and the velocity direction of the satellites at $z \simeq 6$, and their sizes are proportional to the stellar mass and to the velocity respectively. The dashed blue line correspond to the open hyperbolic trajectory of satellite S1.

two possibilities in detail.

6.2.1 Quenching by dynamical interactions

The orbital motion of the dwarf satellites is mainly determined by the gravitational influence of the central massive galaxy Althæa. While forming stars, a satellite may pass through regions of varying density and even near the central galaxy, possibly interacting with it. In order to shed light on the influence that such dynamical interactions have on the satellite properties, we compute the orbits of the satellites adopting a simple approach, similar to those applied to MW satellites (e.g. Simon, 2019), and which can provide a good approximation of their effective motions.

We start by selecting a reference frame in which Althæa is at rest at the origin, and assume that each satellite moves on an elliptical orbit around the central galaxy. Approximating the satellites as point-like masses, the orbital equations for the two-body problem[2]:

$$\ddot{\mathbf{r}} + \frac{GM_{\rm A}}{r^3}\mathbf{r} = 0\,, \tag{6.1}$$

where $M_{\rm A}$ is the mass enclosed within a sphere of radius $D_{\rm Althæa}$ (i.e. the distance of the satellite from the central galaxy at $z \sim 6$) centred on Althæa. Working

[2]This approach neglects mutual interactions with other satellites.

in the plane identified by the satellite velocity vector, $\mathbf{v}_{z\simeq6}$, and the position of Althæa, and further using polar coordinates $r-\theta$, we impose two initial conditions: $r(\theta=0) = D_{\rm Althæa}$ and $\mathbf{v}(\theta=0) = \mathbf{v}_{z\simeq6}$. Then,

$$r(\theta) = \frac{D_{\rm Althæa}}{(1-\beta^2)\cos\theta - (v_r/v_t)\sin\theta + \beta^2}; \tag{6.2}$$

v_r, v_t are the radial and tangential components of $\mathbf{v}_{z\simeq6}$, respectively; $\beta = v_c/v_t$ involves Althæa's circular velocity, $v_c = (GM_A/D_{\rm Althæa})^{1/2}$. In Tab. 6.1 we show the main parameters describing the orbits found: the radius at the periapsis $r_{\rm min}$; the time difference between the current instant ($z \simeq 6$) and the time at which the satellite was at the periapsis $\Delta {\rm T}^{\rm near}$; the orbital period T; the eccentricity e; the modulus of the bulk velocity of the satellite $|\mathbf{v}_{z\simeq6}|$; and the escape velocity $v_{\rm esc}$ from Althæa at the satellite initial location.

In Fig. 6.8 we show the orbits derived for the six dwarf satellites. The least massive satellite, S1, has no closed orbit solution and its bulk velocity (187 km/s) exceeds the local escape velocity (160 km/s). We conclude that not only S1 is not a proper galaxy – given the absence of a dark matter overdensity (see Sec. 3.2.2) – but it is also not gravitationally bound to the halo in which it is located.

The velocities of the other satellites with respect to Althæa vary in the range $\sim (60-360)$ km/s; two of them (S2 and S6) have highly eccentric orbits ($e > 0.9$) and small periapsis ($r_{\rm min} < 1$ kpc). The orbital periods range from $T = 25$ Myr to $T > {\rm t}_{\rm Hubble}$ like in the case of S3, meaning that this dwarf galaxy has not yet completed an orbit at $z = 6$. Despite this, all satellites have $\Delta {\rm T}^{\rm near} < 70$ Myr, which implies that they all crossed the periapsis within the last 70 Myr (see Tab. 6.1).

The time of the periapsis position is a key quantity to interpret the SFHs since at the periapsis the satellites passed across the innermost and densest regions of Althæa and thus it is most likely for the satellite to have directly interacted with it, for example through gas accretion or tidal effects. To interpret the SFHs, we here assume that the dwarf satellites have always moved along the orbits shown in Fig. 6.8. Yet, we should stress that such estimate works successfully only over brief periods of time ($\simeq$ few$\times$10 Myr around $z \sim 6$) since on longer timescales the mass of the two bodies (i.e. the satellite and Althæa) might change significantly due to merger processes; multi-body interactions can also become important.

With this caveat in mind, we can compare in Fig. 6.7 the time of the periapsis position of each satellite (red vertical lines) with their SFHs. For low mass satellites (S2, S3, S4) no connection can be found between the orbital motion and the shape of the SFH. In particular, these small satellites stopped forming stars more than

Table 6.1: Orbital elements of each satellite: distance of the periapsis ($r_{\rm min}$), time of the periapsis ($\Delta T^{\rm near} = t_{z\simeq6} - t_{r_{\rm min}}$), period of the orbit (T), eccentricity (e), modulus of the velocity ($v_{z\simeq6}$), and escape velocity ($v_{\rm esc}$). See the text in Sec. 6.2.1 for the details of the calculation.

Element	S1	S2	S3	S4	S5	S6
$r_{\rm min}$[kpc]	–	0.1	2.3	1.9	1.0	0.02
$\Delta T^{\rm near}$[Myr]	–	12	20	0	10	69
T [Myr]	–	25	3990	505	107	40
e	–	0.92	0.92	0.84	0.69	0.99
$v_{z\simeq6}$[km s^{-1}]	187	63	199	290	360	80
v_{esc}[km s^{-1}]	160	320	208	314	247	247

100 Myr before passing at the periapsis. For the two high-mass satellites (S5 and S6) instead, we see that the periapsis positions roughly correspond to the peaks of the SFR. This suggests that these satellites likely experienced compression and acquired new gas while passing through the densest and innermost regions nearby the LBG.

We conclude that dynamical interactions around the central galaxy Althæa do not represent the key process quenching the SF in the smallest satellites, although they may lead to non-negligible tidal effects and the creation of stellar streams (see Sec. 3.2.4). Dynamical interactions play instead a role in regulating and timing the SF activity of the most massive satellites.

6.2.2 Quenching by feedback processes

Feedback processes are a key factor influencing the evolution of dwarf galaxies. In particular, we can distinguish between two negative feedback effects: (i) mechanical feedback, i.e. SN explosions occurring in the dwarf galaxy heating/removing the gas; (ii) external radiative feedback linked to the presence of the nearby LBG, which produces photons that dissociate H_2 molecules preventing SF in the dwarf. Mechanical feedback starts $\simeq$ 5 Myr after the first SF episode, i.e. as soon as $M \simeq 40$ M$_\odot$ stars end their lives as SNe. It continues for $\simeq$ 40 Myr after the last SF event, i.e. until the explosion of $M \simeq 8$ M$_\odot$ stars. The second effect is instead linked to the SF activity in the main LBG galaxy; massive star there produce large amounts of Lyman-Werner band radiation ($11.2 < h\nu/\mathrm{eV} < 13.6$) capable of photo-dissociating H_2, molecules via the so-called two-step Solomon process.

In the current simulation the average flux of the UV interstellar radiation field

(ISRF) in the Habing band ($6.0 - 13.6\,\mathrm{eV}$; Habing 1968), is evaluated as $G(t) = G_0(\mathrm{SFR}(t)/\ \mathrm{M_\odot yr^{-1}})$, where the SFR is computed by considering all stars within the virial volume of Althæa, and $G_0 = 1.6 \times 10^{-3}\mathrm{erg\,cm^{-2}\,s^{-1}}$ is the MW value.[3] High G values are expected for typical LBGs, as also inferred by observations of high-z LBGs (Carniani et al., 2017) and of local dwarf galaxies, which are often considered as their present-day counterparts (Cormier et al., 2014). The ISRF is largely dominated by Althæa, and assumed to be spatially uniform. Thus, at any time, all dwarf satellites are illuminated by the same UV flux independently of their location (Sec. 2.3.3). This is a fair approximation in the proximity of the central LBG and hence for the six satellites which are all found within 12 kpc from it (Behrens et al., 2018; Pallottini et al., 2019). H_2 self-shielding is taken into account in the simulation on a cell by cell basis through the Richings et al. (2014) prescription, being expressed as a function of the H_2 column density, turbulence, and temperature.

For each satellite in Fig. 6.7 we show both the time of the last SN explosion associated to the peak of SF, and the evolution of the impinging ISRF using the SFR of Althæa, which follows the simple law $\mathrm{SFR}(t) = 1.5\ \log(t_\star/30\ \ \mathrm{Myr})$, with $t_\star$ the time since its first SF event (see Fig. 2 of Pallottini et al. 2017b). Hence, the ISRF steadily increases with time, reaching $G = 100\,G_0$ at $z \approx 6$.

We are now ready to assess the impact of feedback on the SFHs of the satellites. We start our analysis from low- and intermediate-mass satellites. Fig. 6.7 shows that their SF activity is concentrated between $t \sim 800 - 900$ Myr and then they are completely quenched up to $z \simeq 6$. The first decrease and then complete suppression of SF is caused by the energetic SN feedback that heats and ejects the gas. The effect of radiative feedback is to dissociate H_2 molecules in the gas, but we notice that the ISRF does not vary significantly in the last ~ 200 Myr and therefore has no crucial impact in changing the ISM conditions in such time interval. Even more importantly, its contribution is not appreciable due to the low amount of remaining gas after SN explosions took place and the satellites are rendered passive. This is true also in the population of satellites in SERRA, where also the radiation of local stellar population is taken into account through radiative transfer, since the amount of gas typically present in the passive low-mass dwarfs is $M_{\mathrm{gas}} \lesssim 10^7\ \mathrm{M_\odot}$. The low amount of H_2 masses predicted in the simulated satellites ($0 < M_{\mathrm{H_2}}/\ \mathrm{M_\odot} < 8 \times 10^4$) are consistent with measurements from the Dwarf Galaxy Survey (Madden et al., 2013; Cormier et al., 2014), and models of low-z dwarfs (Lupi & Bovino, 2020).

[3] For the MW we can roughly assume $\mathrm{SFR} \approx 1\ \mathrm{M_\odot yr^{-1}}$.

From Fig. 6.7 we see that in all these small systems the last SNe explosions happened $\geq$ 50 Myr before, so that the gas might have had all the time to re-collapse and form stars. Despite this, the satellites remain passive because they experience *starvation*: due to their small masses, and hence low binding energies, these low-mass satellites are not efficient in pulling into their potential wells fresh gas, that is instead preferably drawn onto nearby more massive systems, and are thus unable to trigger SF again.

High-mass satellites (here S5 and S6) are in general characterised by have long and uninterrupted SFHs for two reasons: (i) they better withstand SN explosions, i.e. the feedback is not as efficient in removing gas as in small satellites; (ii) they are massive enough to acquire fresh gas when passing near Althæa (as discussed in Sec. 6.2.1).

We conclude that the main process responsible for quenching star formation in dwarf satellites is the internal mechanical feedback from SN explosions. Combined with the inefficiency in pulling gas from the circum-galactic medium onto these low-mass haloes thus suffering starvation, this lead to the expected presence of a large population of passive dwarf galaxies in the densest regions of the high-z universe.

6.3 Unveiling passive satellites

We have shown that the regions surrounding massive LBGs may represent ideal places where to look for passive galaxies and probe feedback effects taking place at high-z. Due to their typically low stellar masses (see Fig.6.6), the detection of these faint systems is indeed challenging, but finally within reach thanks to the unprecedented sensitivity and resolution provided by JWST. It is therefore time to investigate the expected emission of the overall population of satellite dwarf galaxies in order to understand if and which ones we do expect to detect in JWST surveys (e.g. JADES Rieke et al. 2019, CEERS Finkelstein et al. 2017) and to find the best key photometric observables that could allow the identification of passive systems.

6.3.1 SED modeling

In this pragraph we review the methods used to derive the synthetic SEDs of the galaxies. Firstly, we model their stellar continuum emission using STARBURST99 (Leitherer et al., 1999). We compute the contribution of each stel-

lar particle to the overall galaxy emission, modeling them as individual bursts of star formation considering their masses, ages (interpolated over timesteps of 5 Myr) and metallicities (interpolated over the values available in STARBUSRT99: $Z_\star/\mathrm{Z}_\odot = 0.02, 0.2, 0.4, 1., 2.5$), by adopting the same Kroupa (2001) IMF used in the simulation.

We use CLOUDY (Ferland et al., 2017) to compute nebular line emission within the gas of the simulated galaxies, accounting for the ISM density, metallicity, internal structure, and radiation field (see Sec. 5.1.2, Vallini et al., 2018; Pallottini et al., 2019). We compute the main lines typically contributing to the rest-frame UV-optical spectrum, i.e. hydrogen (Hα, Hβ, Hγ), oxygen ([OII]3726,3729 and [OIII]4959,5007) and carbon (CIII]1909). The contribution to the spectrum of a given emission line at rest-frame wavelength $\bar{\lambda}$ is calculated by summing cell-by-cell luminosities computed via CLOUDY and assuming a Gaussian profile:

$$\frac{L_\lambda}{\mathrm{erg\,s^{-1}\mathring{A}^{-1}}} = \sum_{cell\,i} \frac{L_i(\bar{\lambda})}{\mathrm{erg\,s^{-1}}} \frac{1}{\sqrt{2\pi}\sigma} \exp\left(\frac{\lambda-\bar{\lambda}}{\sqrt{2}\sigma}\right)^2 \tag{6.3a}$$

where

$$\frac{\sigma}{\mathring{\mathrm{A}}} = \frac{\Delta v}{c}\bar{\lambda}\,, \tag{6.3b}$$

and Δv is the broadening of the line due to thermal and turbulent motions (Kohandel et al., 2019).

Finally, the presence of dust in the simulation is taken into account, leading to an attenuation of the overall SED luminosity. Specifically we adopt a dust-to-metal ratio of $f_d = 0.08$ and assume a MW-like dust composition and grain size distribution[4]: we use the extinction curve from Weingartner & Draine 2001 to attenuate the synthetic intrinsic SED of each galaxy[5].

[4]We note that these assumptions are different from the ones made in Chapter 4 and Gelli et al. (2021), where we assumed an SMC-like extinction curve and $f_d = 0.3$. This change of assumptions is driven by ALMA recent measurements of high-z galaxies (Bouwens et al., 2022), that supports a MW-like dust (Ferrara et al., 2022b) and lower dust-to-metal ratios (Behrens et al., 2018; Laporte et al., 2017). However, the main results do not change significantly with respect to the previous assumptions when considering these two changes.

[5]To further test our method for retrieving the galaxies emission, we compared the results for one selected snapshot with those of the complete spatially resolved post processing code SKIRT (Baes & Camps, 2015) with setup used in Behrens et al. (2018) and Pallottini et al. (2022), and obtained consistent results.

6.3.2 JWST predictions

The resulting SEDs of central LBGS, active star-forming and passive satellites are shown in Fig. 6.9, where the flux density is plotted as a function of the wavelength in the range $0.6 < \lambda/\mu m < 5$, covered by the NIRCam and NIRSpec instruments on board JWST. The SEDs of active satellites are characterised by higher flux at all wavelengths with respect to passive ones, due to both their higher stellar masses and star formation rates. The passive satellites' spectra, instead, typically present particularly prominent Balmer jumps, since there are no young stars contributing to the emission. As a consequence, these passive systems are expected to be characterized by redder colours and to predominantly appear in higher wavelength filters at $\lambda \gtrsim 3\mu m$. The higher star formation rates and gas content of active satellites also provokes the presence of strong emission lines in some of the them. On the other hand, most passive dwarfs do not show nebular line emission, even if there are a few exceptions that can be due to the following two reasons: i) the presence of a nearby star-forming galaxy with extended line emission contaminating the flux of the passive dwarf, or ii) the fact the dwarf is undergoing a *temporary* quenching (as witnessed in some satellites SFH, see Fig. 6.3) and its gas is once again cooling and possibly about to reignite star formation. The effect of dust extinction is relevant in some of the star-forming satellites with $M_\star \gtrsim 10^{8.5}$ $M_\odot$, where column densities can reach $N_H \sim 10^{22} cm^{-2}$, but it is instead completely unimportant in low-mass passive dwarfs where the amount of gas and dust is negligible. The horizontal black lines are the expected NIRCam filters sensitivity limits for point

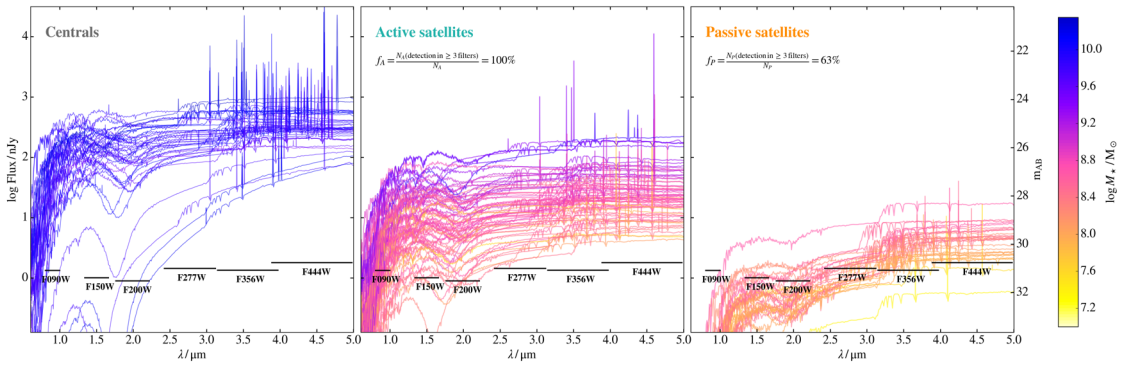

Figure 6.9: Spectral energy distributions, before IGM absorption, of the central galaxies and their active and passive satellites at redshifts $6 < z < 8$ in the wavelength range covered by JWST/NIRCam and NIRSpec. Horizontal lines correspond to the typical expected sensitivity limits for NIRCam imaging for a 20 hrs exposure observation with S/N ~ 3.

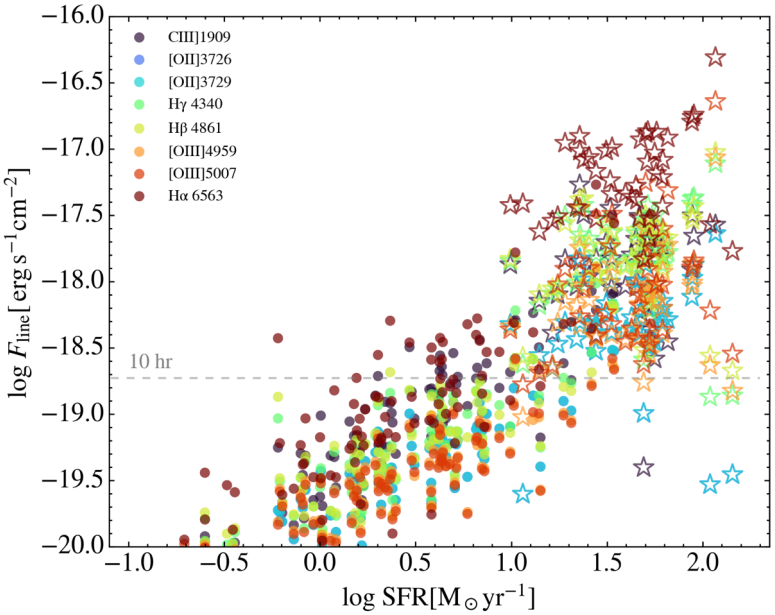

Figure 6.10: Nebular lines fluxes of all the star-forming satellite dwarf galaxies and central LBGs (empty star symbols) as a function of their star formation rate, with the expected sensitivity limit for IFU observations with JWST/NIRSpec (dashed grey line).

sources with signal-to-noise ratio of S/N ~ 3 and exposure time of ~ 20 hrs[6]. These reveal how most satellites are expected to be bright enough to and hence should be detected in deep surveys at least in the long-wavelength channel filters $> 3\mu$m where the flux is strongest.

Regarding emission lines, their presence is witnessed in all the highly star-forming central LBGs, but also in many star-forming satellites of our sample: in Fig. 6.10 we show the flux of all the computed emission lines as a function of the SFR of the star-forming satellites and centrals galaxies, along with the expected NIRSpec sensitivity limit for spectroscopic observations. Note that the Hα line, which is the most prominent one in all our star-forming galaxies, is observable with JWST up to $z < 6.6$ only, while at higher redshifts it falls outside the wavelength range ($\lambda > 5\ \mu m$). Even though very deep observations will be required to detect Balmer lines for many star-forming satellites, interestingly we point out that the field-of-view of the JWST spectrograph NIRSpec in the IFU observing mode is $3'' \times 3''$, that corresponds to ~ 18 kpc $\times$ 18 kpc at $z \sim 6$. Therefore, deep spectroscopic follow-ups of luminous LBG candidates are expected to catch in the same field-of-

[6]Flux limits for a 10 ks integration are retrieved from Table 1 of https://jwst-docs.stsci.edu/jwst-near-infrared-camera/nircam-performance/nircam-sensitivity with last updated done on 25th November 2022

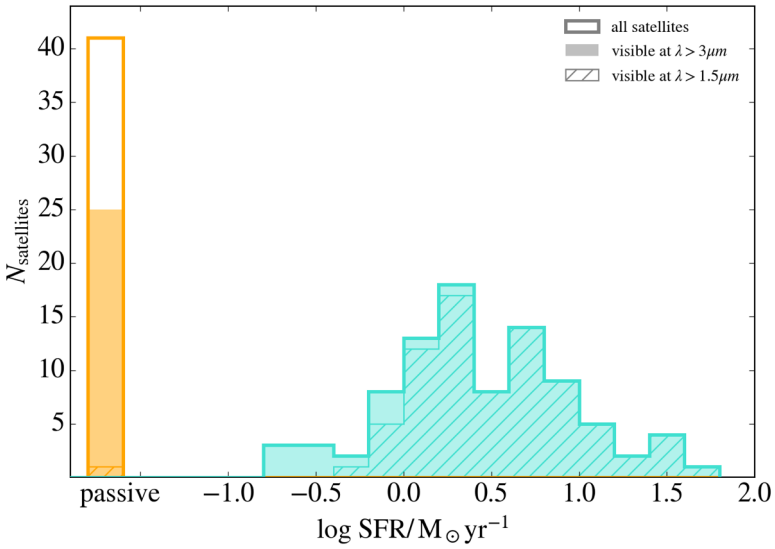

Figure 6.11: Distribution of the star formation rate of the satellite galaxies. The filled and dashed histograms show the distribution of satellites that would be detectable in typical JWST/NIRCam images (in $\sim$ 20 hrs with S/N $>$ 3).

view also their satellites dwarf galaxies, enabling simultaneous measurements of all the galaxies of the systems.

Still, deep images exploiting with the wide field-of-view of NIRCam ($2 \times 2.2' \times 2.2'$) represent the optimal way to locate as many satellite candidates as possible, potentially reaching also the non star-forming passive systems. In fact, considering our complete sample of simulated dwarf satellites, and also taking into account instrumental effects through synthetic images as done in Sec. 4.2 (e.g. see also Fig. 6.14), we can evaluate how many of these systems would be in principle observed if targeted within a deep (20 hrs) observation (e.g. as reached in the JADES survey). The histogram in Fig. 6.11 shows the number of satellites in bins of $\log \mathrm{SFR}/\ \mathrm{M}_\odot \mathrm{yr}^{-1}$, different hatches identifying those systems that are detectable (with S/N $>$ 5) in: i) all filters above $\lambda > 1.5\mu m$, ii) long wavelength filters $\lambda > 3\mu m$. As seen in the previous sections, the majority of the satellites are star-forming (their average SFR $\sim$ 5 $\mathrm{M}_\odot \mathrm{yr}^{-1}$) and 87% of them should be visible at all wavelengths in between $1 < \lambda/\mu\mathrm{m} < 5$. The remaining satellites are passive dwarf galaxies, constituting 31% of the sample (41 out of 131): interestingly, among these, 61% are expected to be luminous enough to be detectable in long wavelength channel filters (i.e. F277W, F356W, F444W) in deep surveys.

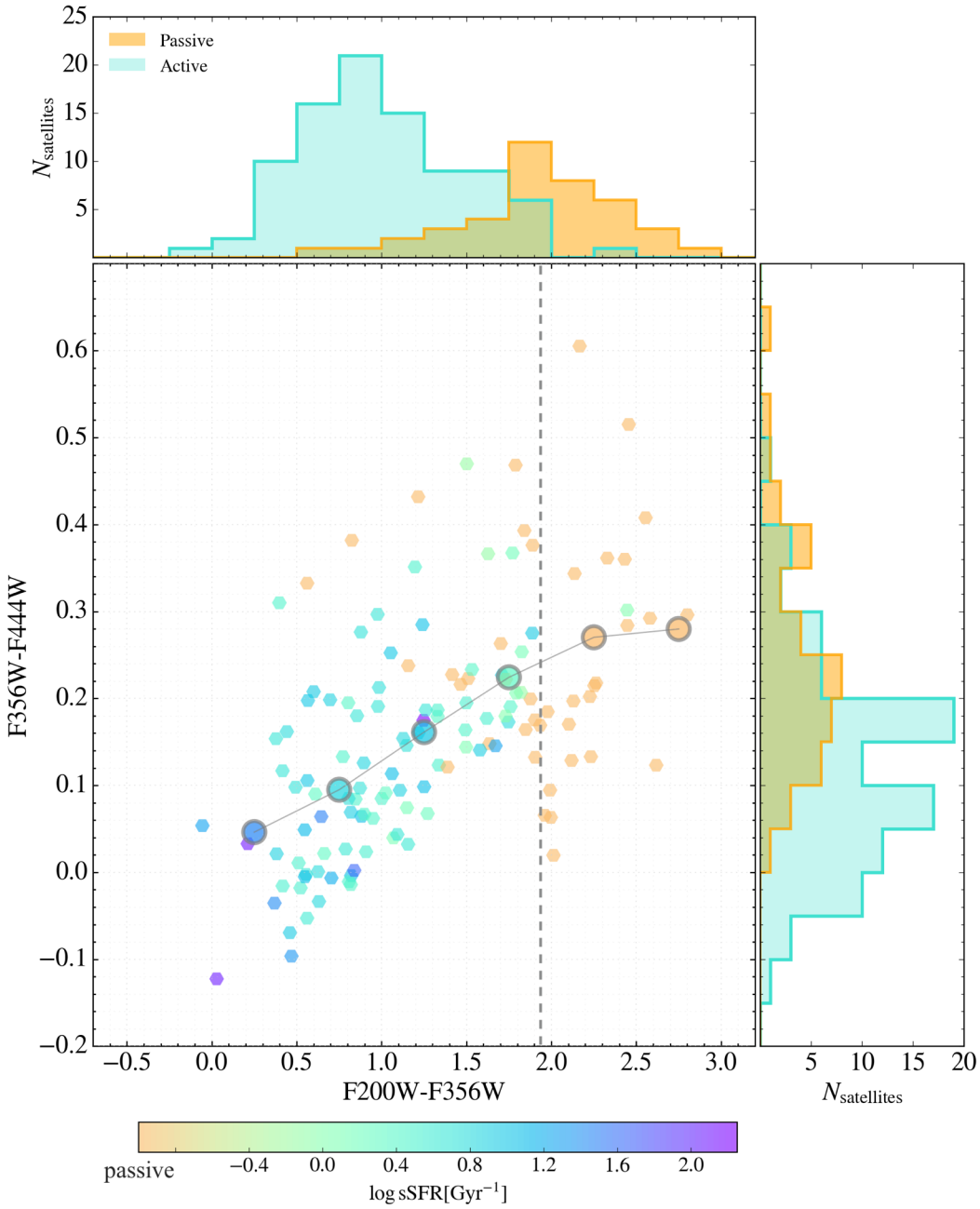

Figure 6.12: Color - color diagram showing F356W-F444W vs F200W-F356W. The small dots are the values for all the sample of satellites, coloured with their sSFR, the orange ones identifying passive systems. The larger points highlight the mean values of F356W-F444W, clearly showing and increasing trend with F200W-F356W and with decreasing sSFR. In the corresponding histograms, the satellites are dived in the two active and passive categories.

6.3.3 Active or passive?

Having shown that the detection of passive dwarf satellites is effectively achievable and expected along with that of star-forming ones around high-z massive LBGs, we now investigate which are the key observable that can allow through photometry to distinguish these sources. Color-color diagrams prove to be an invaluable tool to easily infer the galaxies properties. The one in Fig. 6.12 shows for all the dwarf satellites in our sample the differences in AB magnitude in the filters F356W-F444W, indicative of the SED slope above $\lambda > 3\mu m$, versus F200W-F356W, encompassing the Balmer break for galaxies in the range $6 < z < 8$. Each satellite marker is colored according to its specific SFR, as are the mean values of F356W-F444W per bin of F200W-F356W shown through the larger circles. In the histograms presented in the top and right panels we can see the distribution of the selected colors for the two classes of satellites: active and passive. There is a distinct trend of the average color F356W-F444W, that as expected increases with more prominent Balmer jumps and with decreasing sSFR. In the lower left portion of the diagram (F356W-F444W $\lesssim 0.1$ and F200W-F356W $\lesssim 1.5$) only actively star-forming systems with sSFR $> 5\,\mathrm{Gyr}^{-1}$ can be found. We remind that also nebular lines from the ISM are taken into account and contribute to the emission, but in the hereby used wide (W) filters, the largely dominating contribution to the measured fluxes is given by the continuum stellar emission, especially for passive and low-SFR galaxies, that have low gas fractions.

The substantial scatter in the obtained color-color distribution is primarily due to the large variety of formation histories of the satellites which lead to a wide range of SFRs, ages and stellar masses; to a minor extent, considering systems at redshift in the range $6 < z < 8$ increases the scattering, since different spectral features fall into different wavelength bands. Instead, as we have seen in Sec. 6.1.2, metallicity does not play a key role and does not add a level of degeneracy since, all the stellar populations of the satellites are rapidly reaching solar values, and the metallicity have a relatively low scatter. Ultimately, the main driver of a satellite dwarf galaxy's location in the diagram is its recent star formation, causing passive and active satellites to be situated in two different regions of the diagram, as emphasized also by the histograms. Specifically, in the region F200W-F356W $\gtrsim$ 1.9 (right of the dashed line) we find almost exclusively the presence of passive satellites, with a 4% contamination (one active system only in our sample). Note that many passive galaxies, since they are the lowest massive and faintest dwarf galaxies (see Fig. 6.9), are in most cases not expected to be detectable in the F200W

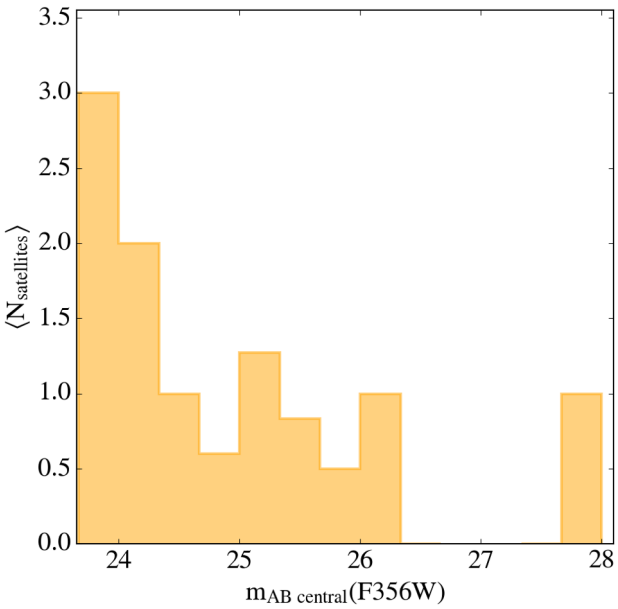

Figure 6.13: Average number of passive galaxies per central host massive galaxy as a function of its magnitude (in AB mag in the JWST wide filter F356W).

filter in planned surveys (see Fig. 6.11). As a consequence only lower limits will be available for F200W-F356W, but this will nonetheless allow to identify the "passive" region within the diagram, successfully discovering them.

6.3.4 Observational strategy

We have demonstrated that the surroundings of high-z massive LBGs may provide unique places to uncover a population of passive dwarf galaxies at high-z. The first step to uncover them within ongoing and upcoming deep surveys with NIRCam should consist in identifying the central LBGs that are most likely expected to host satellite galaxies. These are massive galaxies ($9.5 < \log M_\star/\ \mathrm{M}_\odot < 10.5$) between $6 < z < 8$, and with typical magnitudes in the range $\mathrm{m_{AB}(F356W)} \approx 23.5 - 28$. Fig. 6.13 shows that the expected number of passive satellite per massive LBG vary between 0 and 3, and increases for more luminous systems (e.g. all centrals $\mathrm{m_{AB}(F356W)} < 24.5$ have at least 2 passive satellites). If present, the satellites should be then easily identifiable in NIRCam images within typically $\sim 3''$ from the host LBG. In Fig. 6.14 synthetic images of a $z \sim 6$ group of galaxies from our sample are shown in different NIRCam filters. Pixels are coloured with increasing flux when the signal-to-noise exceeds S/N > 5 (black elsewhere), for an exposure time of 20 hrs. The image of size $5'' \times 5''$, corresponding to 30 kpc × 30 kpc, is centered on the host massive LBG. We can indeed notice within this area the

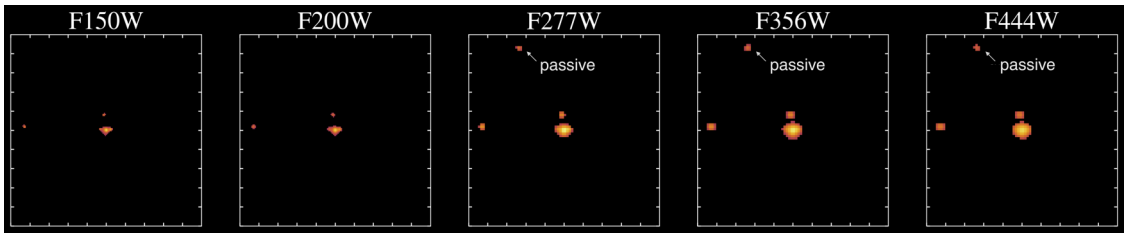

Figure 6.14: Synthetic image of a LBG (in the centre) and its satellite galaxies at $z \sim 6$ as they would appear in different JWST/NIRCam filters. The coloured pixels are those with expected flux at S/N > 5 in a typical 20 hrs observation. The displayed field of view has a side of $5''$. One out of the three satellites is passive, and luminous enough to appear in the long wavelength filters only, as pinpointed by the white arrow.

presence of 3 dwarf satellite galaxies, clearly spatially resolved from the luminous host galaxy whenever located at at least $> 0.25''$ from its center (as already found in Gelli et al. 2020 and Sec. 4.2 for another simulated system). Among the three satellites, one is passive and it appears in the long wavelength filters only (i.e. F277W, F356W, F444W) due to the fact that it is currently not forming stars and is dominated by older stellar populations. Its emission is therefore characterized by a strong Balmer break making the flux drop below $\sim 3\mu m$, where only upper limits would be available in a $\sim$ 20 hrs observation. This example illustrates how it is possible to detect the emission of passive galaxies at high-z in deep images with JWST, and investigating the surroundings of massive LBGs represents the best way to easily uncover many of them. Wide images and photometry hence represent the principal means to both individuate many LBG satellites candidates within large surveys, and to infer their physical properties. We therefore need to assess how reliably can we trust photometric redshift when identifying satellite galaxies.

6.3.5 Identification through photometric redshift

The illustrated method is obviously fully relying on images and photometry and a natural question arises: using photometric information only, with what accuracy can we state that, given a high-z LBG, the surrounding sources are actually its satellites? For a source located in the plane of the sky nearby a LBG to be one of its satellites, and not a background or foreground interloper, it needs to have the exact same redshift as the LBG itself. Spectroscopic follow-ups of satellites candidates would conclusively confirm this, but how accurately can we identify the candidate passive and active satellites relying on photometric redshift only? We can give an answer to this question using a simple probabilistic argument.

First of all, we evaluate the accuracy of the expected typical photometric red-

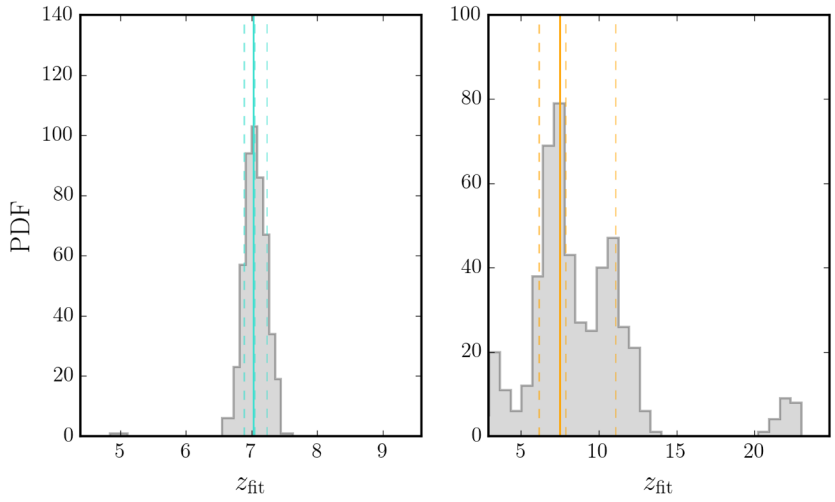

Figure 6.15: BAGPIPES results for the photometric redshift for two typical satellites, active (left) and passive(right).

shifts by fitting our synthetic photometric data with BAGPIPES (Carnall et al., 2018), adopting a general model with constant SFH and initial and final time varying from 1 Myr to the age of the Universe. The results for two typical active and passive satellites are shown in Fig. 6.15. The fit is in general successful for all active satellites, where we typically have flux measurements in at least 5 filters (see Fig. 6.11), leading to photometric redshift errors of $\Delta z_{\rm phot} \sim 0.1$. For the faint passive galaxies we considered instead that the measurements are typically available in just 3 filters, whereas only upper limits can be used at wavelengths below $< 3\,\mu$m. This naturally leads to much larger uncertainties and the errors can reach values of $\Delta z_{\rm phot} \sim 3$. It is also notable that in the fitting results for the passive galaxy at $z_{\rm true} = 7.5$, the probability distribution function shows a secondary peak at $z \sim 21$. In fact, particular care must be taken when fitting potential passive galaxies at the edge of reionization epoch, the Balmer jump may be confused with the Lyman break, and these galaxies could be mistaken for very high-z galaxies.

Such errors, especially for passive satellites, could seem excessively large to draw solid conclusions. However, this is not the case. We can compute the probability for a source detected in the vicinity of a given massive LBG (within R_{vir}), and with a photometric redshift compatible with being a satellite (see a simple illustrative sketch in Fig. 6.16). This probability can be quantified as

$$P(sat) = \frac{\langle N_{sat} \rangle}{\langle N_{sat} \rangle + N_{field}}, \tag{6.4}$$

where $\langle N_{sat} \rangle$ is the average number of expected detectable[7] satellites per LBG system, and N_{field} is the number of the expected detectable field galaxies in the same redshift range. The latter can be evaluated as

$$N_{field} = \int_{M_{min}}^{M_{max}} \int_{z-\Delta z_{phot}}^{z+\Delta z_{phot}} \phi(z, M) \frac{dV}{dz} dz\, dM, \tag{6.5}$$

where $\phi(z, M)$ is the Schechter luminosity function in units $\mathrm{mag}^{-1}\mathrm{Mpc}^{-3}$ (Bouwens et al., 2021), and the comoving volume element per unit redshift is given by

$$\frac{dV}{dz} = \frac{\pi \Delta\theta^2 D_L^2(z)}{(1+z)^2} \frac{1}{H_0 \sqrt{\Omega_0 (1+z)^3 + \Omega_\Lambda}}, \tag{6.6}$$

with $\Delta\theta$ is the angle corresponding to the virial radius (see Fig. 6.16). We fix M_{min} and M_{max} as the magnitude of the most luminous of our simulated satellites, and the magnitude corresponding to the sensitivity limit of JWST/NIRCam, respectively. Considering the "worst case scenario" (i.e. maximising the possible number of interlopers) with: maximum virial radius ($R_{vir} = 25$ kpc), detectability limit of the deepest JWST surveys in the wide filter F200W at S/N=3, and $\Delta z_{phot} \approx 3$ as derived with BAGPIPES for quiescent satellites, we get $N_{field} \simeq 0.18$. Given that $\langle N_{sat} \rangle = 2.95$, we obtain that the probability of a source with compatible photometric redshift to be a satellite dwarf galaxy of the nearby LBG is 94%. Thus, the proposed method is robust against uncertainties in the photometric redshift.

6.4 Discussion and conclusions

Using the SERRA suite of cosmological simulations we have demonstrated how the satellites of massive LBGs at high-z represent a unique class of objects that provide the best opportunity to find low-mass passive galaxies in the EoR. Through a careful analysis of the sample 131 satellites of 42 massive LBGs ($10^{9.5} < M_\star / \mathrm{M}_\odot < 10^{10.5}$) between $6 < z < 8$ and their complex realistic SFHs and emission properties we found that:

- $\sim 70\%$ are actively forming stars with a wide range of $0.2 < \mathrm{SFR} / \mathrm{M}_\odot \mathrm{yr}^{-1} < 50$; the remaining $\sim 30\%$ of satellites are passive (SFR = 0)
- the fraction of passive satellites decreases with the mass, constituting $> 80\%$ of the population below $M_\star < 10^8$ $\mathrm{M}_\odot$;

[7] We assume a deep observation of 20 hrs reached in e.g. JADES as done in Sec. 6.3.2

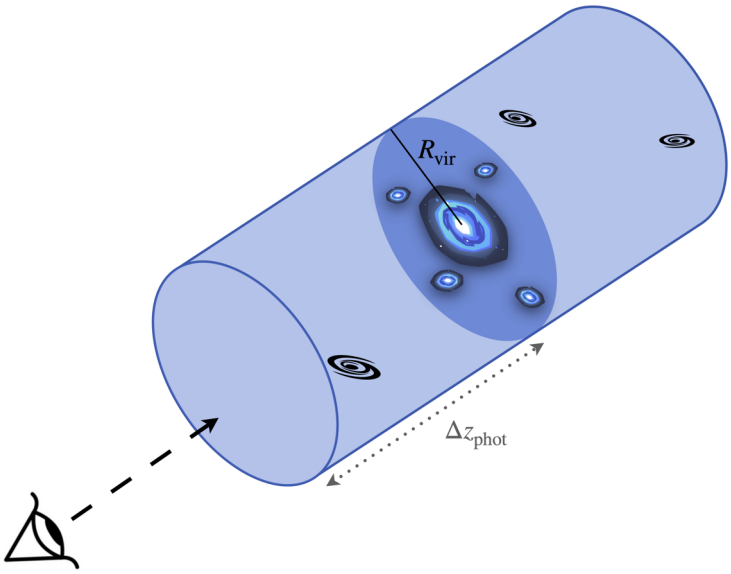

Figure 6.16: Simple sketch illustrating the possible presence of background or foreground contaminant interloper galaxies (black spiral symbols) in the cosmic volume enclosed by the same redshift range measured for the satellites in the observed region around an LBG.

- mechanical feedback from SNe, heating/evacuating the gas, is the key physical process able to quench the star formation in the smallest satellites, that subsequently suffer *starvation* not being able to pull additional gas onto themselves;

- dynamical interactions of the satellites with the central massive galaxy likely played a role in regulating and timing the SF activity of the largest satellites only.

- all satellites, active and passive, share common properties: i) they all were very bursty during their first stages of star formation where sSFR $\sim 100\mathrm{Gyr}^{-1}$, ii) their stellar populations are all rapidly enriched in metals due to internal SN chemical enrichment, reaching $Z_\star \sim \mathrm{Z}_\odot$ in a few 10 Myr.

- in NIRCam images the emission of satellites, that are typically located at angular distance between $0.25'' - 3''$ from the central LBG, can spatially resolved and all *star-forming* satellites are expected to be detectable in $\sim$ 5 hrs exposure time observations.

- most *passive* galaxies, whose spectra are characterised by prominent Balmer jumps, are expected to be detectable in less than < 20 hrs in NIRCam long wavelength filters;

- once satellite candidates are identified, the color - color diagram F356W-F444W vs F200W-F356W, showing a clear trend with the sSFR, allows to distinguish passive from active satellites.

CHAPTER 7

The first passive low-mass galaxy detected by JWST

In Chapter 6 we have seen that we expect JWST to be able to uncover a population of passive galaxies at high-z, especially at low stellar masses. Indeed, interestingly, among the very first JWST results the discovery of a low-mass galaxy at $z = 7.3$ has been reported by Looser et al. (2023) from the JADES program: JADES-GS-z7-01-QU. According to Looser et al. (2023), the spectral energy distribution (SED) of JADES-GS-z7-01-QU is consistent with a metal-poor $M_\star \approx 5 \times 10^8$ $M_\odot$ stellar population formed in a short and intense burst of star formation followed by rapid quenching (star formation rate SFR $< 10^{-2.5}$ $M_\odot yr^{-1}$), about 10–20 Myr before the epoch of observation. In this Chapter, based on Gelli et al. (2023), I aim at interpreting this specific finding. To this end, I first performed an analysis of "field" low-mass ($M_\star \lesssim 5 \times 10^8$ $M_\odot$) galaxies, which has revealed that the evolution of satellite and field dwarf galaxies does not differ at low-masses. This was indeed expected from Chapter 6, where I found that environmental processes, such as interactions with the central galaxy, do not play a role in driving the low-mass dwarf galaxies evolution, which is instead regulated by internal feedback processes.

7.1 The duty cycles of low-mass galaxies

In Fig. 7.1 we show the star formation histories (SFHs) for some SERRA low-mass galaxies up to different observation redshifts, highlighting that all galaxies with final mass $M_\star \lesssim 10^9$ $M_\odot$ have experienced passive phases, or are still quenched at the final snapshot, which is identified as the redshift of observation.

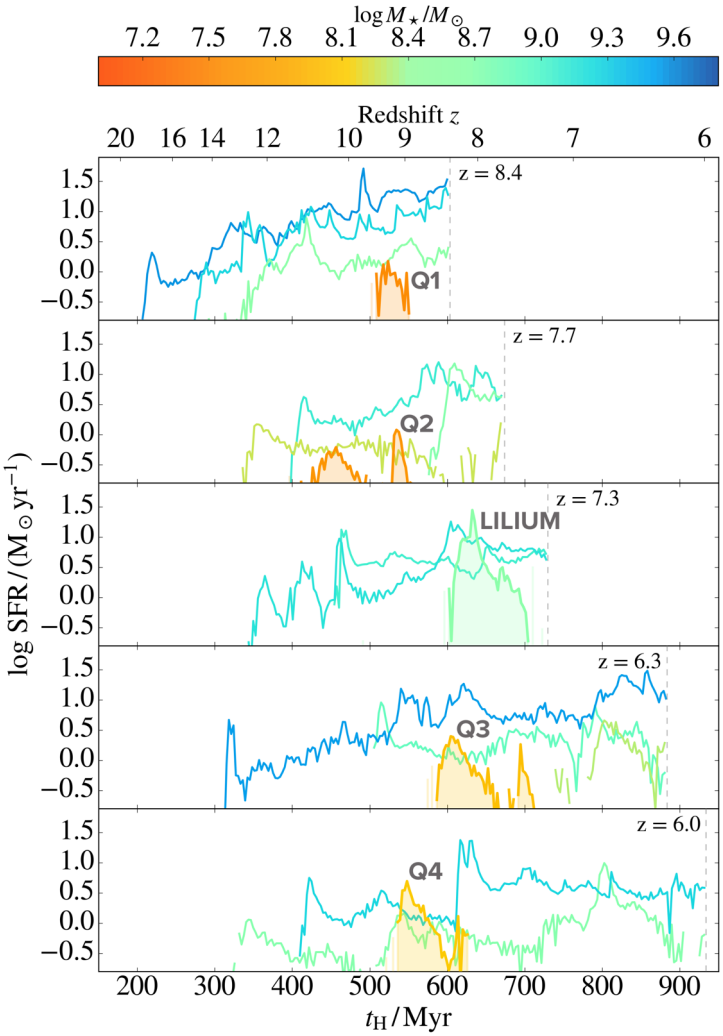

Figure 7.1: Star formation rate (SFR) as a function of the age of the Universe (t_H) for some SERRA galaxies simulated up to different redshifts, color coded with the final stellar mass. Filled curves and names denote galaxies that are passive at the end of the simulations (30% of the sample).

Interestingly, after the SF peak, these low-mass galaxies feature a smooth SFR decrease lasting some tens of Myr until the final quenching. This trend is typical of stellar feedback powered by SNe, as explosions occur with a delay time that increases with a decreasing SN progenitor mass (see also Chapter 6 and Gelli et al. 2020). For low-mass systems, this behaviour is encountered in both field and satellite galaxies, implying that environmental process do not drive their evolution.

In the middle panel of Fig. 7.1 we pinpoint the galaxy *Lilium*, which is passive at $z = 7.3$ and has the same stellar mass of JADES-GS-z7-01-QU.

Fig. 7.2 shows the galaxy SFR duty cycle, i.e. the ratio between the actively star forming (SFR> 0) time interval, $\Delta t_{\rm on}$, and the time elapsed between the first

star formation event, $t_{\rm form}$, and the observation redshift at $t_{\rm obs}$:

$$f_{\rm duty} = \frac{\Delta t_{\rm on}}{t_{\rm obs} - t_{\rm form}} \,. \tag{7.1}$$

Galaxies are color-coded with the mass-averaged age of their stellar populations; passive systems (Q1-Q4) identified in Fig. 7.1 are specifically indicated.

Galaxies with $M_\star < 10^9$ M$_\odot$ can be either passive or active, and the fraction of passive systems increases with decreasing stellar mass, becoming the dominating population for $M_\star < 10^{8.3}$ M$_\odot$ (see histograms in the upper panel of Fig. 7.1). In this mass range passive galaxies (a) are older (average ages > 100 Myr), (b) have lower and more scattered duty cycles ($f_{duty} \approx 0.2 - 0.9$) than active galaxies ($f_{duty} \approx 0.8 - 0.99$). For $M_\star > 10^9$ M$_\odot$, instead, *all* galaxies are active, and they have been forming stars for $\geq 95\%$ of their lifetime.

The average duty cycle of passive and active galaxies clearly reflects these trends with stellar mass, slowly increasing from $f_{duty} \approx 0.6$ for $M_\star \approx 10^{7.5}$ M$_\odot$ to ≈ 0.99 for $M_\star \geq 10^9$ M$_\odot$. Noticeably, the passive galaxy *Lilium* ($\log M_\star/$ M$_\odot = 8.7$) has a duty cycle $f_{\rm duty} \approx 0.84$ that is consistent with the values obtained for JADES-GS-z7-01-QU using different stellar population synthesis tools by Looser et al. (2023, see Table 1 therein).

7.2 Interpreting JADES-GS-z7-01-QU

Lilium was selected among SERRA passive galaxies due to its similarity with JADES-GS-z7-01-QU in terms of stellar mass, duty cyle (Fig. 7.2), and the time elapsed between SF quenching and observation redshift: $\Delta t_{\rm quench} \sim 15$ Myr for *Lilium* vs. $\Delta t_{\rm quench} \sim 10 - 40$ Myr for JADES-GS-z7-01-QU. However, the stellar populations of *Lilium* are more metal-rich ($Z_\star \approx$ Z$_\odot$) than deduced by Looser et al. (2023) for JADES-GS-z7-01-QU, $Z_\star \approx 0.01$ Z$_\odot$. In spite of these similarities, the SED we predict for *Lilium* (Fig. 7.3, left panel) is too faint to match the one observed in JADES-GS-z7-01-QU. What is the origin of such discrepancy?

We first check the role of stellar metallicity by imposing that all the stars in *Lilium* have $Z_\star \approx 0.01$ Z$_\odot$. However, the resulting SED only increases by ~ 0.2 dex (see Fig. 7.3, left panel). The right panel of Fig. 7.3 displays the SFH of *Lilium*. At $z \approx 8.4$, i.e. around 120 million years before observations, *Lilium* started to form stars at a progressively increasing rate. After ≈ 35 Myr it experienced a short and intense burst of star formation (SFR $\gtrsim 25$ M$_\odot$yr^{-1}), after which 80% of the final stellar mass was already in place. Then, the SFR was gradually suppressed by

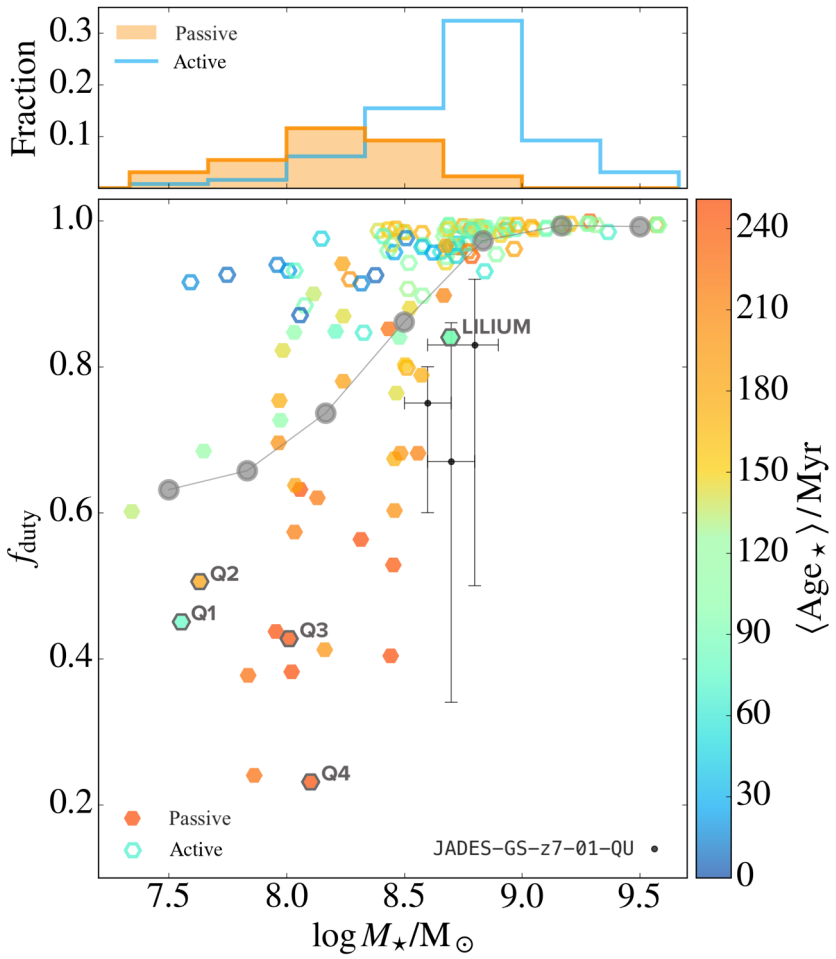

Figure 7.2: Duty cycle $f_{\rm duty}$ as a function of the stellar mass of passive (filled) and active (hollow) galaxies from SERRA, coloured with the average age of the stellar population. The average trend of $f_{\rm duty}$ with the mass is shown through the grey circles. The three points with errorbars are the values inferred for JADES-GS-z7-01-QU using different spectral fitting codes (BAGPIPES by Carnall et al. 2018, PROSPECTOR by Johnson et al. 2021, BEAGLE by Chevallard & Charlot 2016) derived from Table 1 of Looser et al. (2023). The histograms in the upper panels show the stellar mass distribution of active and passive low-mass galaxies.

stellar feedback. Indeed, the galaxy continued to form stars at a much lower rate, $\lesssim 2$ $\mathrm{M_\odot yr^{-1}}$, for ≈ 50 Myr, i.e. up to $z \approx 7.45$ when it was completely quenched. Therefore, at the redshift of observation, $z = 7.3$, the average stellar age of *Lilium* is ≈ 90 Myr old (see Fig. 7.2).

In the same panel, we plot a SFH similar to the one derived by Looser et al. (2023) using BAGPIPES, essentially a top-hat with a SFR $= 15$ $\mathrm{M_\odot yr^{-1}}$ but with the same $\Delta t_{\rm quench}$ and $M_\star$ as *Lilium*. With this SFR, the observed $M_\star$ is produced in only ≈ 30 Myr, resulting in a much younger (≈ 30 Myr) stellar population. As a consequence, the corresponding experimentally-derived SED reaches fluxes

about 10× higher than *Lilium* (Fig. 7.3, left) and matches JADES-GS-z7-01-QU photometry if a metallicity of 0.01 $Z_\odot$ is further assumed.

This result shows that the discrepancy between the SEDs of *Lilium* and JADES-GS-z7-01-QU is largely due to differences in their SFHs, and to a lesser extent, metallicity. The key difference is the fact the SFR decrease in *Lilium* after the SF peak is too prolonged, resulting in a high fraction of old stars at the time of the observation. This suggests the need for an abrupt quenching right after the SF peak.

To test this hypothesis, we artificially impose that SF in *Lilium* was abruptly halted ~ 5 Myr after the peak, and we renormalize it to get the same $M_\star$ value. Assuming to observe the galaxy after $\Delta t_{\rm quench} = 10 - 20$ Myr from the halt, and thus shifting the SFHs to match the redshift of the observations, i.e. $z = 7.3$, we find that the *Lilium* SED now perfectly matches the observed one even by assuming the simulated stellar metallicity, $Z_\star \approx Z_\odot$.

7.3 Discussion

In spite of the fact that *Lilium* is very similar to JADES-GS-z7-01-QU, the simulated SED does not match the observed one. We have shown that this is due to the fact that star formation in JADES-GS-z7-01-QU is quenched on a much shorter time scale than in *Lilium*.

If the quenching has to be produced by SNe, there is an intrinsic timescale on which such feedback acts, which is given by the time over which SNe associated with a given burst explode. This value is $\gtrsim 30$ Myr for a Kroupa IMF (see, e.g. Fig. 2 in Pallottini et al. 2017b). The quenching cannot therefore be significantly shorter than this minimum value, and this is exactly what we see in the SFH of *Lilium* and the other quenched low-mass galaxies (Q1, Q2, Q3, Q4). Basically, the SFR decline under the action of SN feedback is very gradual, resulting in a too large number of stars that are old by the time at which the galaxy is observed. This is a general problem of SF quenching in low-mass galaxies which inherently depends on the delay of SN explosions associated to the deaths of progenitors of different mass (e.g. Rosdahl et al., 2017).

We speculate that the decline could be more abrupt if the mechanical energy is instead provided by a hidden AGN and/or radiation pressure from the stars as soon as the luminous source crosses the Eddington threshold driving an outflow (Carniani et al., 2016; Ferrara et al., 2022a; Ziparo et al., 2023; Fiore et al., 2023). If true, the SFR decline might be a powerful diagnostic of different feedback types.

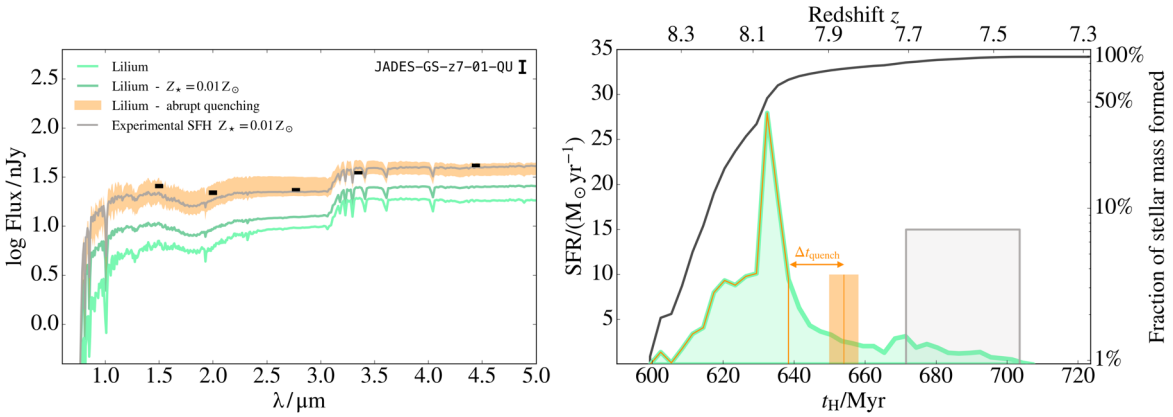

Figure 7.3: Spectral energy distributions of simulated galaxies at $z = 7.3$ (*left panel*), compared with JADES-GS-z7-01-QU, and corresponding SFH and fraction of stellar mass formed (*right*). Shown are the SEDs for: (a) *Lilium* (green), (b) an idealised SFH model with constant SFR + a quenching lookback time $\Delta t_{\rm quench} \sim 15$ Myr with two stellar metallicities as indicated (grey), and (c) *Lilium* with a modified SFH featuring an abrupt quenching at $t_H \approx 640$ Myr, and observed after $\Delta t_{\rm quench}$ varying between $10 - 20$ Myr (orange).

Another puzzle posed by the JADES-GS-z7-01-QU observation is its long latency before the first episode of star formation. This source is observed at $z = 7.3$ and, according to the SED interpretation, has formed all its stars in a short (≈ 30 Myr) burst. This sets the start of its star formation activity at $z \approx 7.8$. From the observed stellar mass $M_\star = 10^{8.7}$ M$_\odot$, and conservatively assuming that all its baryons were turned into stars, we can set a lower limit to the host halo, $M \gtrsim (\Omega_m/\Omega_b) M_\star = 3.2 \times 10^9$ M$_\odot$. Assuming a standard growth history, this halo should have crossed the critical mass $M \approx 10^8$ M$_\odot$, marking the separation between minihalos, in which the SF is easily suppressed, and the star-forming Lyα-cooling halos at $z \gtrsim 11.7$. Thus, in the redshift interval $7.8 < z < 11.7$ (280 Myr), although conditions were in principle favourable to star formation in terms of gas cooling, the galaxy did not form a significant amount of stars. A possibility might be the following: if a galaxy spawns a massive stellar cluster ($M_\star \simeq 10^5$ M$_\odot$) as its first star formation event, its radiation can photo-dissociate molecular hydrogen and prevent further star formation for up to ~ 300Myr (see Alyssum, Pallottini et al., 2022).

As JWST will build a sizeable sample of passive high-z galaxies, we will be able to solve these puzzles and understand the nature of the feedback-regulated evolution of low-mass systems.

CHAPTER 8

PISN explorer

In this Chapter we turn to the approach of Near-Field cosmology, previously introduced in Chapter 1.6, illustrating a novel way to investigate the early Universe by studying the local relics of primordial star formation. In particular, I here introduce the `PISN-explorer`, an innovative tool that I contributed to develop, that is able to uncover the descendants of the very first massive supernovae within large samples of observed local stars. The idea behind the `PISN-explorer` also offers a general methodology that could be applied to unveil even the hidden signatures of the first stars in high-z sources, as I will later illustrate in Chapter 9.2. The following contents are based on the paper by Aguado et al. (2023).

8.1 Introduction: Pair Instability Supernovae

The first (Pop III) stars formed out of primordial composition gas, i.e. in environments where the fragmentation process was less efficient then in local star-forming regions, thus enabling the formation of more massive stars than those that we observe today: from a few tens, up to *thousands* of solar masses (e.g. Susa et al., 2014; Hirano et al., 2015). Their characteristic mass, furthermore, was likely ≥ 10 $M_{\odot}$ (e.g. Bromm, 2013). According to cosmological models, these primitive stars were likely hosted by the bulge and the stellar halo of the Milky Way (see e.g. Salvadori et al., 2010; Starkenburg et al., 2017a; Tumlinson, 2010) and by Local group dwarf galaxies (e.g. Salvadori et al., 2015). Very massive first stars, $140 \leq m_{*}/M_{\odot} \leq 260$, are predicted to end their lives as energetic Pair Instability Supernovae (PISN), which inject 50% of their mass in the form of metals into the interstellar medium (ISM). Thus, a single PISN will strongly enrich the primordial gas with a prob-

ability distribution function peaking at [Fe/H] ≈ -2.0 (Karlsson et al., 2008; de Bennassuti et al., 2017; Salvadori et al., 2019), leaving a unique chemical signature with a strong odd-even effect (e.g. Heger & Woosley, 2002; Takahashi et al., 2018). Unfortunately, pure PISN descendants are predicted to be extremely rare, representing, even at the peak metallicities, $< 0.1\%$ of Milky Way stars (de Bennassuti et al., 2017). The traditional approach of searching only for stars showing 100% PISN enrichment has thus not proven successful. Rather, a large fraction of PISN descendants are expected to also have a significant contribution from normal Pop II stars, which can form early on in the Pop III-enriched ISM and then evolve as core-collapse supernovae (CCSN). The abundances of the so-called *killing* elements Cu and Zn (Salvadori et al., 2019) may be the smoking gun for a true PISN descendant. These elements are barely produced by PISNe, but yielded by all other supernovae (see also Vanni et al. in prep). The extreme sub-solar abundances of Zn and Cu with respect to Fe from PISNe, persist even in environments polluted by other sources up to a 50% level (Salvadori et al., 2019). But given the rarity of such stars, until now, only two descendants of PISN have been reported (Aoki et al., 2014; Salvadori et al., 2019). We are thus in the situation where even a few more identified PISN descendants would greatly advance the field.

In the recent years there has been a breakthrough in large spectroscopic surveys in and around the Milky Way, targeting millions of stars with intermediate- to high-resolution spectra (e.g. Gaia, APOGEE, GALAH, GES) These numbers will further increase with two large upcoming spectroscopic surveys WEAVE (Dalton et al., 2016) and 4MOST (de Jong et al., 2019). For the first time, we have the statistics to identify and characterise rare populations, such as PISN descendants.

Searching through such large databases, however, requires a focused and dedicated effort, and with this goal in mind we here present an innovative methodology, the `PISN-explorer`. With a combination of theoretical models (Salvadori et al., 2019), and the `FERRE` code (Allende Prieto et al., 2006), the `PISN-explorer` exploits all the chemical abundances measured by large surveys to identify stars that have likely been dominantly enriched by PISN ($\gtrsim 50\%$).

8.2 The theoretical models

The models used by the `PISN-explorer` are adopted from the general parametric study presented in Salvadori et al. (2019). This study provides predictions for the chemical properties of an ISM predominantly imprinted by very massive first stars exploding as PISNe, i.e. where the PISNe products account for $\geq 50\%$ of metals in

the ISM. The model is general because it condenses the unknown physical processes related to early cosmic star-formation, metal diffusion, and mixing, into three free parameters: 1) the star formation efficiency, f_*, which provides the fraction of ISM gas condensed into stars; 2) the dilution factor, $f_{\rm dil}$, which parametrises the amounts of metals effectively retained into the ISM; 3) and the mass fraction of ISM metals contributed by PISNe, $f_{\rm PISN}$. Predictions for a PISN-imprinted ISM are provided by exploring the full parameter space. Hence the predictions are general and essentially model independent.

The ansatz of this approach is to assume that a single very massive first star exploding as PISN can form in the primordial star-forming (mini-)haloes. This assumption is strongly supported by the results of hydrodynamical cosmological simulations following the formation of the first stars (e.g. Hirano et al., 2014). The chemical enrichment of the ISM is evaluated after the injection of metals by a single PISN ($f_{\rm PISN} = 100\%$) with different progenitor masses, $m_{\rm PISN} = [140 - 260]{\rm M}_\odot$. It turns out that the final metallicity (or [Fe/H]) of the ISM is settled by the PISN mass and by the ratio between the star-formation efficiency and the dilution factor, $f_*/f_{\rm dil}$. Furthermore, it is always $Z_{\rm ISM} > 10^{-3}\,{\rm Z}_\odot$, which implies that "normal" Pop II stars can form out of this medium and thus contribute to the subsequent ISM enrichment (see Fig. 2 of Salvadori et al. 2019).

The abundance ratios of each element X (from C to Zn) with respect to iron, are computed by varying the relative contribution of PISN and Pop II stars to the chemical enrichment ($f_{\rm PISN} = [50 - 100]\%$) and by assuming that Pop II stars form according to a standard Larson Initial Mass Function (IMF): $\phi(m_\star) = m_\star^{-2.35} exp(-m_{ch}/m_\star)$ with $m_{ch} = 0.35$ M$_\odot$ (Larson, 1998). The calculations are made by adopting the yields by Heger & Woosley (2002) for very massive first stars exploding as PISNe, ${\rm Y_X^{PISN}}(m_{\rm PISN})$, and of Woosley & Weaver (1995b) for Pop II stars with initial masses $m_* = [8-40]{\rm M}_\odot$ and metallicities, $Z_* = [10^{-4}; 1]{\rm Z}_\odot$, which explode as CCSN, ${\rm Y_X^{II}}(m_*, Z_*)$. According to Woosley & Weaver (1995b) we assume that stars between 40 and 140 M$_\odot$ collapse directly into a black hole thus not contributing to the chemical enrichment. Note that since we are integrating over the entire Pop II IMF the derived yields are not so different from those obtained with models assuming that $m_* > 20$ M$_\odot$ stars produce a negligible amount of heavy elements (e.g. Limongi & Chieffi, 2018). Salvadori et al. (2019) demonstrated that the ISM abundance ratios, [X/Fe], or the chemical abundance pattern of the stars formed out of it, depend upon $f_{\rm PISN}$, the yields of PISN and of Pop II stars; but they are not directly affected by $f_*/f_{\rm dil}$ although this ratio controls the metallicity of the Pop II stars contributing to the ISM enrichment.

8.3 Exploited datasets

The goal of this work is to efficiently select candidates for PISN descendants from existing and publicly available data that should provide reliable elemental abundances together with stellar parameters: effective temperature, surface gravity, and metallicity ($T_{\rm eff}$, log g, and [Fe/H]). We perform our selection using different surveys, i.e. APOGEE (Majewski et al., 2017), GALAH (De Silva et al., 2015), Gaia-ESO (Gilmore et al., 2012, 2022), MINCE (Cescutti et al., 2022) survey, and the JINA database (Abohalima & Frebel, 2018).

8.4 Methodology

The `PISN-explorer` consists in a systematic methodology to efficiently select PISN-polluted candidates from the selected datasets using theoretical predictions from Salvadori et al. (2019) (Sec. 8.2) in combination with the `FERRE` code[1], capable of performing fitting to a rectangular grid of theoretical models. The `PISN-explorer` methodology implies several steps:

1. Packaging of models: a grid of theoretical predictions for the chemical abundances of PISN descendants (50-100% PISN pollution) is created with a `FERRE`-friendly header, with key information included in the header (such as label for each free parameter included in the models $f_{\rm PISN}$, $\log_{10}(f_*/f_{\rm dil})$, and $m_{\rm PISN}$), and complete with the chemical abundances predictions ([$X_{i=6,30}$/Fe]).

2. Preparing the data: for each star in our sample we prepared three different files with 25-columns length each: 1) the measured chemical ratios ([$X_{i=6,30}$/Fe]$_{\rm obs}$) from C to Zn; 2) the uncertainties ($\sigma_{[X_{i=6,30}/Fe]_{\rm obs}}$); and 3) the weight we gave to each measurement (i.e. double weight to the the *killing* elements Cu and Zn).

3. Launching the code: `FERRE` look for the best fit by interpolating between the nodes of the grid. In Fig. 8.1a we show an example of a fit with the observed values ([$X_{i=6,30}$/Fe]$_{\rm obs}$, blue dots) for a single APOGEE object, and the best fit (red line) derived with `FERRE`, giving a set of parameters: $f_{\rm PISN} = 66.1\%$;

[1] `FERRE` is available from http://github.com/callendeprieto/ferre

Figure 8.1: From Aguado et al. (2023). Example of the `PISN-explorer` analysis performed on an APOGEE star.

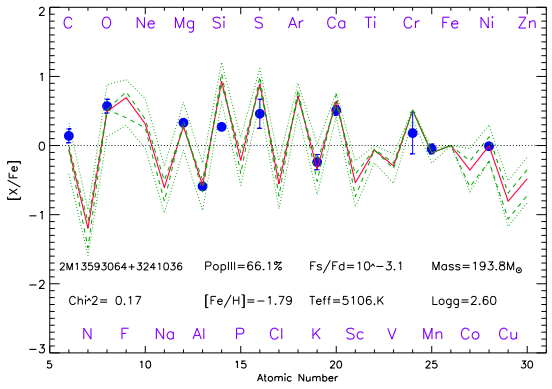

(a) The measured chemical signature of 2M13593064+3241036 from APOGEE (blue dots) together with the best fit to a PISN model computed with the `PISN-explorer` (red line). Derived PISN parameters and main stellar parameters are also shown. Finally, for comparison we show interpolated models with ±20 $M_\odot$ of PISN mass (dotted lines) and ±15% of PISN contamination (dashed lines).

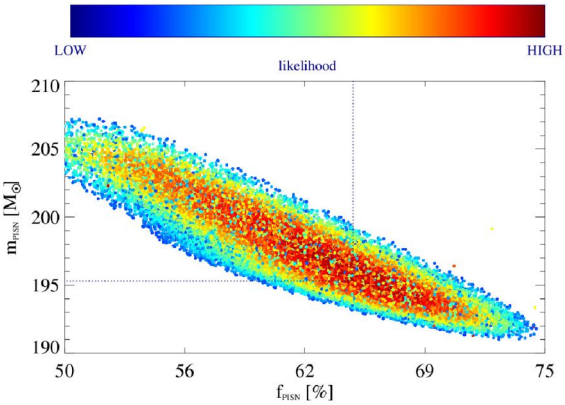

(b) $f_{\rm PISN} - m_{\rm PISN}$ space of solutions when applying and MCMC algorithm computed with `FERRE` over the chemical signature of 2M13593064+3241036 including 10 chains of 50,000 experiments each. Color bar represents the likelihood of each solution.

$f_*/f_{\rm dil} = 10^{-3.1}$; and $m_{\rm PISN} = 193.8$ $M_\odot$.

4. Interpreting the results and caveats: we need to consider that when a star's chemical signature is very far from the theoretical predictions (the vast majority of the cases), the code will not be able to find a good fit and will usually end up on a solution with a high χ^2 at the limit of the grid ($m_{\rm PISN} = 140$ $M_\odot$, for example) that should therefore be discarded. Moreover, corrections due to inhomogeneities in the three-dimensional (3D) stellar atmosphere and the non-local thermodynamic equilibrium (NLTE) state of the matter for elemental abundances will significantly improve the results of the analysis. Finally, since the odd-even contrast is a key signature of PISN yields, but odd-elements are more difficult to detect, the higher is the number of available odd elemental abundances the better performance can be obtained with our methodology.

5. MCMC validation: to ensure that degeneracy in the parameters determination is not affecting our methodology we used a Markov-Chain Monte-Carlo (MCMC) analysis based on self-adaptive randomised subspace sampling (Vrug et al., 2009). In Fig. 8.1b we show the likelihood in the $f_{\rm PISN} -$

$m_{\rm PISN}$ space of solutions. Although the employed algorithm looking for the best solution is different, unsurprisingly the best solution is compatible within the uncertainties with the one shown in Fig. 8.1a ($f_{\rm PISN} = 65\%$; $f_*/f_{\rm dil} = 10^{-3.1}$; and $m_{\rm PISN} = 195.3$ M$_\odot$).

8.5 Target selection

Our sample mainly consists of nearby stars from the disk, the bulge, and the halo of the Milky Way (Sec. 8.3). We analyzed 1,438,497 stars following the methodology explained in Sec. 8.4 with no further cuts applied at this stage and in Fig. 8.2 we show in blue the metallicity distribution function of the whole sample. The target selection based on the `PISN-explorer` analysis is a two step procedure based: first on hard cuts applied blindly over the entire sample, *systematic selection* (e.g. discarding objects with too few chemical abundances or with fits with $\chi^2 > 0.35$); and second, on more specific and survey-dependent selection, *individual selection* (e.g. discarding objects with [Cu, Zn/Fe] > 0). This leads to 166 candidates from all included surveys (Sec. 8.3), shown in red in Fig. 8.2. Finally, with extra criteria such as observability cuts ($V_{mag} \leq 16$) we end up with a 45 objects golden catalogue that contains the most promising candidates to be enriched by PISN pollution. One of the most promising candidates, 2M13593064+3241036 from APOGEE, is shown in Fig. 8.1a. For this object the quality of the fit is remarkable but, unfortunately, APOGEE does not provide measurements for Zn and Cu, the smoking gun of PISN

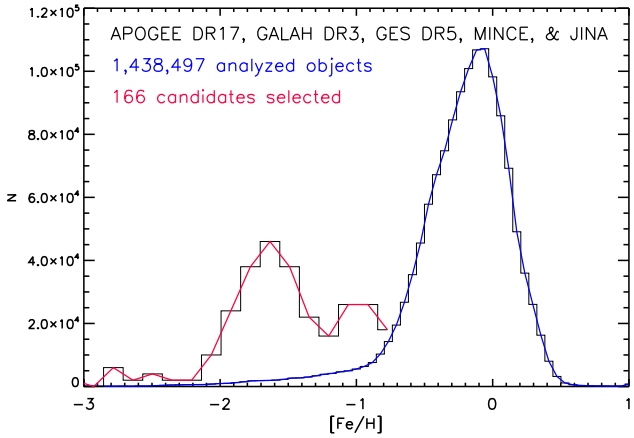

Figure 8.2: From Aguado et al. (2023). Metallicity distribution functions for the 1.4 million stars analysed (blue), and the 166 PISN selected candidates (red). Note that the red distribution has been arbitrarily scaled for easier comparison.

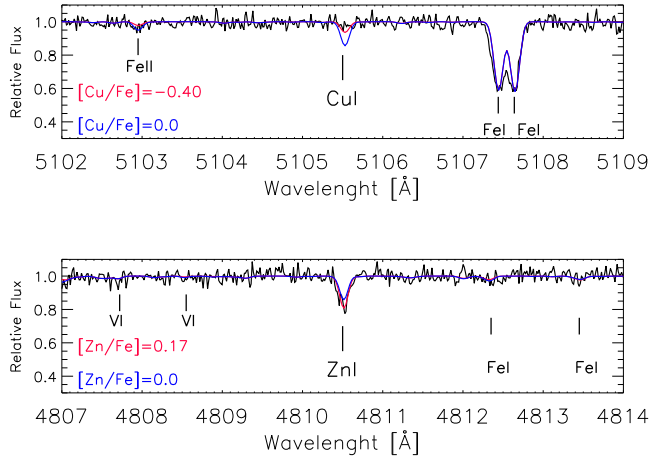

Figure 8.3: From Aguado et al. (2023). UVES spectrum (black lines) of the star 2M13593064+3241036, around the absorption lines: Cu I at 5105 Å (top); and Zn I at 4810 Å (bottom). Two models at different elemental abundances are also shown (blue and red lines). Other metallic absorption lines in the spectra are also labelled.

pollution. Therefore, we applied for an ESO-DDT proposal of one hour to try to accurately measure both *killing* elements, Zn and Cu.

8.6 PISN descendant candidates

8.6.1 Observations and analysis of 2M13593064+3241036

Our target, 2M13593064+3241036, was observed with UVES at the 8.2 m VLT Kueyen Telescope in a single observing block (OB) of one hour in service mode, during the night of the 28th of March 2022.

APOGEE analysis pipeline (ASPCAP; García Pérez et al., 2016) used spectral profile fitting to derive for 2M13593064+3241036: $T_{\rm eff}$=5106 K, log g=2.60, and [Fe/H]= −1.79 (Majewski et al., 2017). We perform a similar analysis for our UVES optical spectrum by fitting the data with the `FERRE` and we derived: $T_{\rm eff}$= 5036 ± 105 K, log g= 2.59 ± 0.20, [Fe/H]= −2.29 ± 0.10, and [C/Fe]= +0.05 ± 0.15. The metallicity discrepancy is reamrkable and unusual, and could be related to a problem to the sky or background subtraction in the APOGEE spectrum. Unfortunately, it significantly impacts elemental abundances, that we have analysed taking advantage of the `FERRE` code. The results are shown in Table 8.1. The fact that the star is more metal-poor than previously published with APOGEE makes the *killing* ratios [Cu/Fe] and [Zn/Fe] higher than expected, with catastrophic conse-

Table 8.1: Stellar parameters, abundances, ratios, errors and number of detected lines for individual species derived in 2M13593064+3241036 from UVES and APOGEE data.

Gaia DR2 id 1457695618046140800
RA(deg) = 209.877547, DEC(deg) = 32.684315
$v_{rad} = -13.45\,\mathrm{km\,s^{-1}}$, $T_{\mathrm{eff}} = 5035\,\mathrm{K}$, $\log g$ =2.59

Species	$\log\epsilon(\mathrm{X})_{\odot}^{1}$	$\log\epsilon(\mathrm{X})$	[X/Fe][2]	$\sigma_{\mathrm{[X/Fe]}}$	N	$\mathrm{[X/Fe]_{NLTE}}$
C (CH)	8.39		0.05	0.11	–	
N (CN)	7.78		<0.10	–	–	
O I	8.66		1.10[3]	0.15	2	
Na I	6.17	4.22	0.36	0.12	2	−0.13
Mg I	7.53	5.77	0.28	0.09	9	0.28
Al I	6.37	3.86	−0.20	0.11	2	0.06
Si I	7.51	5.48	0.40	0.10	1	0.34
K I	5.08	5.08	0.24[3]	0.10	1	
Ca I	6.31	4.53	0.39	0.12	12	0.49
Sc II	3.05	0.87	−0.07	0.08	3	
Ti I	4.90	3.10	−0.19	0.23	4	
Ti II	4.90	3.01	−0.05	0.08	16	−0.12
V I	4.00	1.85	−0.02	0.08	8	
Cr I	5.64	3.23	−0.27	0.11	6	
Mn I	5.39	2.68	−0.25	0.08	3	
Fe I	7.45	5.31	−2.31[4]	0.06	231	−2.27
Fe II	7.45	5.16	−2.38[5]	0.09	7	
Co I	4.92	2.83	0.08	0.12	6	
Ni I	6.23	3.84	−0.37	0.13	5	
Cu I	4.21	–	<−0.40	–	–	
Zn I	4.60	3.84	0.17	0.13	2	
Sr II	2.92	0.12	0.12	0.09	2	
Y II	2.21	0.63	−0.63	0.09	4	
Zr II	2.59	0.24	0.24	0.09	3	
Ba II	2.17	0.13	0.13	0.10	3	
Eu II	0.52	0.55	0.03	0.10	2	

[1] Solar abundances adopted from Asplund et al. (2005)
[2] LTE and NLTE ratios are referred to $\mathrm{[Fe/H]_{LTE}}$ and $\mathrm{[Fe/H]_{NLTE}}$.
[3] Abundance derived from the APOGEE spectrum and not used here.
[4] [Fe/H] from Fe I is given instead of [X/Fe]
[4] [Fe/H] from Fe II is given instead of [X/Fe]

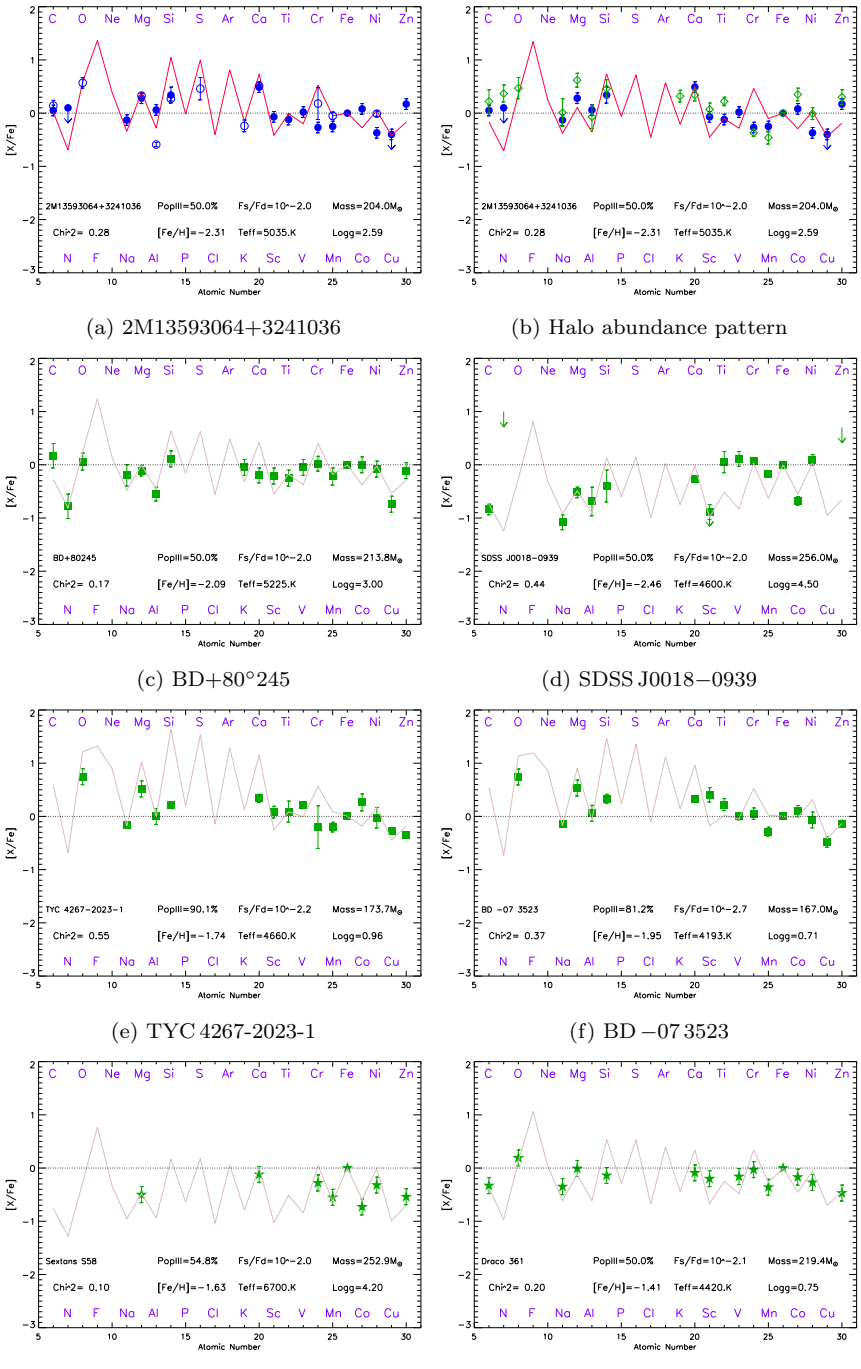

(a) 2M13593064+3241036 (b) Halo abundance pattern

(c) BD+80°245 (d) SDSS J0018−0939

(e) TYC 4267-2023-1 (f) BD −07 3523

(g) Sextans S58 (h) Draco 361

Figure 8.4: From Aguado et al. (2023). Results of the `PISN-explorer` analysis. Points are measured chemical abundances while lines are best fits. Listed on the plot are parameters of the fit, along with $T_{\rm eff}$, $\log g$, and [Fe/H]. *Top row:* Our new analysis is presented (blue filled circles) and compared to the APOGEE results (a, blue open circles); and the average abundance pattern and the best fit of the Cayrel et al. (2004a) sample (b, green open diamonds). *Second row:* Previously published candidates for dominant PISN enrichment (green squares), SDSS J0018−0939 (c; Aoki et al. 2014) and BD+80°245 (d; Salvadori et al. 2019). *Third row:* Candidates selected from the MINCE survey (e and f; Cescutti et al. 2022). *Bottom row:* Promising candidates for PISN descendants (green star symbols) in the Sextans (g; Shetrone et al. 2001) and Draco (h; Cohen & Huang 2009) dwarf spheroidal galaxies.

quences (UVES spectrum and values in Fig. 8.3). Furthermore, the [Mg/Al] ratio has dramatically increased by 0.69 dex which clearly attenuates the odd-even effect. Still some key features remain, such as high [Si/Fe] value, and [Ca/Mg] > 0. In Fig. 8.4a we show the elemental abundances from Table 8.1 together with the best `PISN-explorer` fit and parameters. The best fit gives significantly different results than the original analysis: $m_{\rm PISN} = 204.0$ M$_\odot$ (prev. 193.8 M$_\odot$), and $f_{\rm PISN} = 50\%$ (prev. 66%), and $f_*/f_{\rm dil} = 10^{-2.1}$ (prev. 10^{-2}); and the quality of the fit is now worse (See Fig. 8.1a). Also comparing with a regular giant halo star (see Fig. 8.4b), given their similar fits, we can conclude that 2M13593064+3241036 is likely like other halo stars with no major contribution from PISN pollution.

8.6.2 Previously reported candidates

To verify our methods, we analyse with `PISN-explorer` two stars that have been reported as probable PISN descendants and compare with the published results (our results are shown in Figs 8.4d and 8.4c).

The star BD+80°245 (Carney et al., 1997; Fulbright et al., 2010; Ivans et al., 2003; Roederer et al., 2014), is a low-α halo star (Fig. 8.4c), which was initially proposed as a PISN descendant (Salvadori et al., 2019) based on the low abundance of the *killing* elements (Cu and Zn). Their originally derived PISN parameters were $f_{\rm PISN} = 50\%$; $f_*/f_{\rm dil} = 10^{-4.0}$; and $m_{\rm PISN} = 223$ M$_\odot$. Our analysis, as explained, is based on the same set of models (Heger & Woosley, 2002; Salvadori et al., 2019) but the way we fit the data with `FERRE` is different (see Sec. 8.4). The best solution we get is $f_{\rm PISN} = 50\%$; $f_*/f_{\rm dil} = 10^{-2.0}$; and $m_{\rm PISN} = 213.8$ M$_\odot$ with a $\chi^2 = 0.17$, which is in good agreement with Salvadori et al. (2019). Interestingly, the $f_*/f_{\rm dil}$ factor is significantly different in the two analysis while the quality of the fit is similar. The reason for that is that $f_*/f_{\rm dil}$ is the least sensitive parameter within the models and the `FERRE` code tends to go to the limit of the grid.

SDSS J0018−0939, a possible PISN descendant proposed by Aoki et al. (2014), has remarkably low α-abundances ([Mg/Fe] $= -0.52$, [Ca/Fe] $= -0.26$), see Fig. 8.4d. The authors excluded that the peculiar chemical pattern could not be produced by CCSN or SN Ia. They concluded that the most likely origin is PISN and they attribute a $f_{\rm PISN} = 100\%$ value. Unfortunately, no informative upper limits for Cu and Zn were measured in this star. Analysing it with the `PISN-explorer`, we derived $f_{\rm PISN} = 50\%$; $f_*/f_{\rm dil} = 10^{-2.0}$; and $m_{\rm PISN} = 256$ M$_\odot$ with $\chi^2 = 0.44$. Although the χ^2 is elevated, we are able to reproduce the chemical signature of lighter elements (See Fig. 8.4d), but the models failed for iron-peak elements. The

low α ratios lead to high mass of the progenitor (256 $M_\odot$) in agreement to what was claimed by Aoki et al. (2014). However, the $f_{\rm PISN} = 50\%$ value suggests that this star could be polluted by PISN but a higher contribution should be attributed to normal Pop II stars exploding as CCSN. Further observations in order to detect and measure *killing* elements is highly required to confirm the percentage of PISN contamination we see in this star.

The *Pristine* survey (Starkenburg et al., 2017c) derives metallicities for halo stars based on narrow band filter photometry. In this context, there is also a remarkable observational effort to derive Cu and Zn in metal-poor stars (Caffau et al., 2022). The authors found, among others, three interesting candidates to be polluted by PISN production using also the `PISN-explorer`. In particular, in their Fig. 12, they show the chemical pattern of TYC 1118-595-1, a very metal-poor star with [Fe/H] $= -2.12$, and derived $f_{\rm PISN} = 50\%$; $f_*/f_{\rm dil} = 10^{-2.3}$; and $m_{\rm PISN} = 193$ $M_\odot$. TYC 2207–992–1 and TYC 1194–507–1 are also reported together with a best fit that suggested that they could be enriched by PISN up to $f_{\rm PISN} = 83\%$ and 90%, respectively. However, the probability of such is significantly smaller than for TYC 1118-595-1 due to the lower quality of the fit. According to what is explained in Sec. 8.4, we consider that TYC 1118-595-1 is likely reflecting the theoretical predictions in their chemical pattern in a percentage that could be to the order of $f_{\rm PISN} = 50\%$ or slightly smaller. TYC 2207–992–1 is also a very promising candidate with a progenitor mass $m_{\rm PISN} = 170$ $M_\odot$ while TYC 1194–507–1 has more uncertain origin due to the low quality of the fit.

We also mined the bibliography including high-resolution analysis of halo stars looking for interesting candidates. We found that the vast majority of interesting stars published before 2018 are already included in the JINA database. However, Xing et al. (2019) found an interesting star, J1124+4535, with [Fe/H] $= -1.27$ and [Zn/Fe] $= -0.37$. We also analyzed its chemical signature with the `PISN-explorer` and found $f_{\rm PISN} = 50\%$; $f_*/f_{\rm dil} = 10^{-2.4}$; and $m_{\rm PISN} = 231$ $M_\odot$. The quality of the fit is relatively good ($\chi^2 = 0.29$) but the absence of Cu measurement or upper limit prevents us to conclude that this object is polluted by PISN. We propose to re-observe this interesting object with peculiar chemistry to confirm its origin.

8.6.3 PISN candidates in classical dwarf galaxies

It is commonly accepted that the classical dwarf spheroidal galaxies are massive enough to retain the chemical products of PISN explosions (see e.g. Bromm & Loeb, 2003; Salvadori et al., 2008). However, their total number of stars is much

lower compared to more massive systems. Consequently, the expected fraction of PISN descendants in classical dwarf galaxies is expected to be significantly higher than in the Milky Way. Therefore, classical dwarf galaxies are interesting places to search for PISN descendants. Luckily, within the JINA database there are ~ 50 stars from Fornax, Sextans, Draco, and other dwarf satellites. In Figs. 8.4g and 8.4h two interesting examples of the `FERRE` analysis are shown, Sextans S58 (Shetrone et al., 2001) and Draco 361 (Cohen & Huang, 2009). The quality of both fits are remarkably high with $\chi^2 = 0.10, 0.20$, respectively. Additionally, the *killing* element Zn, is largely subsolar in the atmosphere of the two stars [Zn/Fe] ~ -0.45. Actually, the case of Sextans S58 with $f_{\rm PISN} = 55\%$ suggests that the majority of the material this star formed from was polluted mostly by PISN with a mass of $m_{\rm PISN} = 253$ M$_\odot$.

Finally, we also identified another star from JINA database, Draco 3053 (Cohen & Huang, 2009). This star is also Zn-poor with [Zn/Fe] $= -0.3$ and the best set of parameters derived with the `PISN-explorer` are $f_{\rm PISN} = 50\%$; $f_*/f_{\rm dil} = 10^{-2.0}$; and $m_{\rm PISN} = 218$ M$_\odot$; and $\chi^2 = 0.19$. In this case, the high quality of the fit and the low value of Zn suggest that this star could be indeed polluted by PISN in a percentage close to $f_{\rm PISN} = 50\%$. Further observations of all of the three candidates in Draco and Sextans galaxies are required.

8.7 Discussion

In the previous sections we have validated and applied our proposed `PISN-explorer` methodology to find PISN descendants. Although the 2M13593064+3241036 candidate seems not to be as interesting as expected (mostly due to the initial overestimation of metallicity in APOGEE), its study was useful to understand the capabilities of our methodology. As shown, its chemical signature, and in particular the *killing* elements Cu and Zn, is not significantly different from that of an average *pattern* for regular giant halo stars. Indeed, when the contribution of Pop II stars exploding as normal CCSN becomes $> 50\%$, the peculiar chemical signatures left by different Pop III star progenitors are essentially lost (Vanni et al. in prep.)

A different situation is presented for BD+80°245, shown in Fig. 8.4c. For this star we confirm the result provided by Salvadori et al. (2019) and we conclude that it is at least partially (but genuinely) polluted by PISN. The clearly low value of the *killing* elements that this stars shows is indeed the smoking gun of PISN contamination. On the other hand, the analysis of SDSS J0018−0939 shows that while very different from a regular halo star (see Sec. 8.6.2), the percentage of

material produced by PISN may not be as high as originally suggested by Aoki et al. (2014). In any case, some further high-resolution observations of this interesting star are needed to better constrain the amount of Cu and Zn and shed light over the exact amount of material that effectively come from PISN production. At this point we propose using facilities that will be available in the next generation of 30 m telescopes. Moreover, the agreement of our analysis with previous works suggests that the `PISN-explorer` is efficient in characterising candidates.

A very challenging issue when identifying the descendants of the very massive first stars is how to discriminate between them and a regular halo star (mostly polluted by Pop II exploding as CCSN). By comparing Fig. 8.4b with 8.4c, 8.4d, 8.4g, and 8.4h it is clear that the chemical signatures that correspond to good fits in this work ($\chi^2 \lesssim 0.20$) are very different than the mean abundance pattern for a regular giant halo star (Cayrel et al., 2004b). The much higher CNO abundances together with high α's (i.e. Mg, Ti) led to a significantly higher χ^2. Obviously, this is deeply related with the fact that the regular halo star pattern is not Zn-poor, which is the most robust indicator. Additionally, as shown in Fig. 8.4b, the odd-

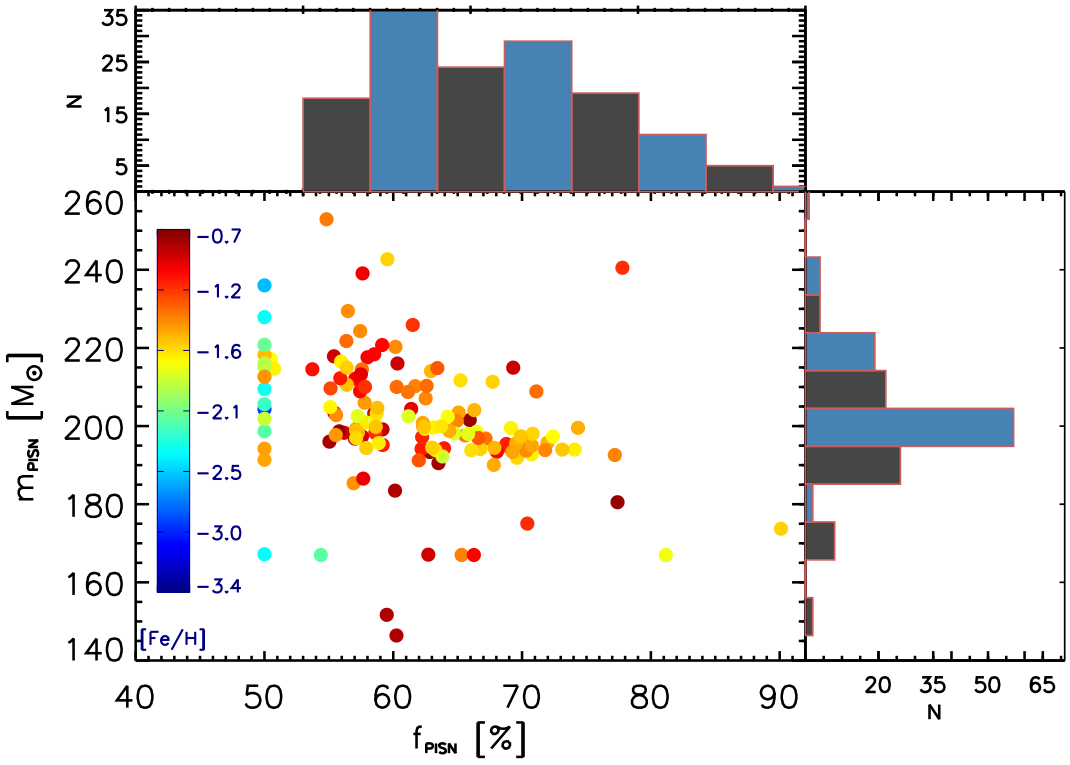

Figure 8.5: From Aguado et al. (2023). Our catalogue of 166 candidate PISN descendants, shown in the $f_{\rm PISN} - m_{\rm PISN}$ plane, colour-coded by metallicity. Histograms of the candidates are also shown on top and right side panels.

even effect is clearly lost for atomic numbers higher than Z=19, i.e. for most of the iron-peak elements. According to our novel `PISN-explorer`, the most efficient way to separate PISN candidates from other halo field stars is a combination of the criteria presented in Sec. 8.5, low values of χ^2, and the killing elements deficiency $[\mathrm{Cu, Zn/Fe}] < 0$. In Figs. 8.4e and 8.4f two interesting examples of promising candidates from MINCE survey with subsolar Cu and Zn abundances are shown.

Moreover, the `PISN-explorer` allowed us to successfully identify very interesting PISN descendants candidates in classical dwarf galaxies (see Fig. 8.2). Note that none of them are found in the less massive ultra-faint dwarf galaxies. These systems, which are smaller and thus have lower binding energy than classical dSph galaxies, are probably not able to retain the chemical products of energetic PISN (Rossi et al. in prep). Unfortunately, since those from classical dwarfs are typically distant and therefore faint, the next generation of 30 m class telescopes will be required to derive systematically their *killing* elements.

A final remark concerns the MDF of our 166 selected candidates shown in Fig. 8.2. It is indeed extremely interesting to see that its main peak is located at $[\mathrm{Fe/H}] = -1.7$, i.e. exactly at the level predicted by the cosmological models for the MW formation of de Bennassuti et al. (2017) (see their Fig. 9) and close to the values provided by the parametric study of Salvadori et al. (2019), $[\mathrm{Fe/H}] \approx -2$, and by the inhomogeneous chemical enrichment model by Karlsson et al. (2008), $[\mathrm{Fe/H}] \approx -2.5$. This result is quite remarkable since the `PISN-explorer` does not use the iron abundance to select PISN candidates, as our selection is solely based on the predicted chemical abundance ratios, [X/Fe]. We should also note that it is very likely that our sample, and thus our selected candidates, are biased towards higher [Fe/H]. In fact, both APOGEE and GALAH rapidly decrease in accuracy in the very metal-poor regime, which is possibly the origin of the second peak at higher $[\mathrm{Fe/H}] \approx -1$. Finally, we recall that the iron abundances of PISN descendants is expected to vary in a broad range, $-5 < [\mathrm{Fe/H}] < 0.5$ (see Fig. 7 of Salvadori et al., 2019). Therefore, it is quite normal that in our MDF we find a second and smaller peak at $[\mathrm{Fe/H}] = -3.0$. This peak is indeed made by PISN candidates selected from the JINA database, which is naturally biased towards Fe-poor stars.

In Fig. 8.5 we display the $f_{\mathrm{PISN}} - m_{\mathrm{PISN}}$ distribution for our 166 selected candidates colour coded by metallicity. While the histograms of f_{PISN} are peaked at lower contribution and monotonically decreases, which is expected, the distribution of m_{PISN} is more condensed around 200 $\mathrm{M}_{\odot}$. We also see a more metal-poor population lying at $f_{\mathrm{PISN}} = 50\%$, values should actually be avoided when selecting

candidates. However, as we pointed out, after visual inspection we could consider them as a candidates whether they show a remarkably good fit and Cu and Zn abundances are subsolar. This population was selected following this approach and some of them (due their visibility and/or special features) are included in our golden sample. However, some others are quite faint and we propose to observe at higher SNR when possible with the future high-resolution spectrographs.

8.8 Conclusions

We have presented a new methodology to identify candidates that have been significantly polluted by PISN in the early Universe. We mined different datasets in order to find chemical patterns that match with what is expected to find if significant PISN production took place. We summarise here the main conclusions:

- Current and upcoming large spectroscopic surveys (APOGEE, GALAH, GES, 4MOST, WEAVE), and existing databases such as JINA, are an invaluable tool to unveil the origin and characteristics of the very massive first stars, which exploded as PISN.

- The `PISN-explorer`, using the `FERRE` code in combination with theoretical predictions (Salvadori et al., 2019) is a very efficient methodology when selecting PISN descendant candidates in large databases.

- The MDF of the selected candidates is a confirmation of the predicted peak in PISN production at [Fe/H] ~ -1.7 (de Bennassuti et al., 2017).

- *killing* elements (Cu and Zn), low values of α-elements (Mg and Ti), and clear odd-even effect (e.g. high [Mg/Na], and/or high [Mg/Al]), are indicators of PISN production. Therefore, they could be used to efficiently select candidates.

- It is possible that 2M13593064+3241036 was mostly polluted by PISN production but the presence of Zn on its atmosphere does not allow us to confirm this hypothesis. BD+80°245 contains significant material that was formed during a PISN event. The $f_{\rm PISN}$ value previously reported for SDSS J0018−0939 (100%) could be significantly lower according to its chemical signature.

- Sextans S58 is the most promising candidate and maybe mostly formed out of PISN material. To confirm this hypothesis further high-resolution follow-up is

needed to complete the chemical signature already reported in the literature. Draco 361 and Draco 3053 are also excellent candidates selected from classical dwarf galaxies.

- From our selected 166 candidates we propose 45 of them as a golden catalogue with the most promising and visible stars for future follow-up.

Future high-resolution facilities mounted in the Extremely Large Telescope such as ANDES (Marconi et al., 2022) and other facilities will provide and unbeatable opportunity to observe stars in dwarf satellites, where it is more likely to find PISN descendants. In addition to it, the next generation of large spectroscopic surveys such as WEAVE (Jin et al., in press) and 4MOST (de Jong et al., 2019) with high resolution observations will be an unbeatable place to test the `PISN-explorer` and finally finding the descendants of the very massive first stars.

CHAPTER 9

Summary and outlook

In this Thesis I have investigated the nature and the manifold properties of the faintest galaxies living in the Epoch of Reionization, which can finally be unveiled in upcoming JWST observations. I explained why faint low-mass dwarf galaxies are of fundamental interest given their importance in a cosmological context, from the build-up of massive galaxies to their contribution in shaping later galaxy evolution through feedback processes. Using state-of-the-art cosmological simulations that reproduce the observed properties of typical massive Lyman break galaxies at $z \sim 6-8$, I uncovered the remarkable population of dwarf satellite galaxies orbiting around them. These small systems living in dense environments represent a unique class of sources for investigating high-z galaxy evolution, since they are easy to identify and can shed light on multiple processes simultaneously, from stellar feedback and quenching to mass assembly. Furthermore, I studied the evolution of more isolated low-mass dwarf galaxies at high-z, to interpret the first JWST observation of a passive low-mass galaxy at $z = 7.3$. I will here go through the foremost results of the works I have carried out as leading author during my Ph.D. and their main implications.

9.1 Results of my work

Mass-driven properties and evolution of high-z dwarfs

To address the key scientific questions of my Thesis, I developed a *satellite finder* that enabled the search of dwarf satellite galaxies in the densest regions surrounding massive galaxies in cosmological simulations (Gelli, Salvadori, Pallottini & Ferrara,

2020). A thorough analysis of the six satellites orbiting around a typical $M_\star \sim 10^{10}$ $M_\odot$ Lyman break galaxy at $z \sim 6$ revealed that, even in such extreme dense environments, their evolutionary and chemical properties are mainly regulated by their mass, ranging from $M_\star \sim 10^6$ $M_\odot$ to 10^9 $M_\odot$. Namely, most low-mass galaxies ($M_\star < 5 \times 10^8$ $M_\odot$) form through short (< 100 Myr) and intense bursts of star formation with rates up to SFR $\gtrsim 10$ $M_\odot yr^{-1}$. In most of them star formation is however rapidly suppressed by SN explosions that heat and evacuate the remaining gas. High-mass satellites ($M_\star > 5 \times 10^8$ $M_\odot$), on the other hand, experience longer and more complex star formation histories, lasting up to ~ 500 Myr. Even though all satellites are rapidly chemically enriched up to solar metallicities ($Z \sim Z_\odot$), in our cosmological scenario high-mass dwarfs typically form at earlier times ($z > 9$) in a still pristine environment, whereas the stars of low-mass systems form later ($z < 9$) within an interstellar medium that has already been significantly polluted with heavy elements produced by the central LBG. However, despite their initial higher metallicities, these low-mass satellites contain a larger amount ($> 50\%$) of metal-poor stars ($\log Z_\star/Z_\odot < -0.5$). Such evolutionary patterns, along with the tendency for the most metal-poor stars to dwell in the inner regions ($r < 200$ pc) of the galaxies, are analogue to what found by models of dwarf galaxies in the Local Group (e.g. Salvadori et al., 2015). *This implies that these behaviours are a general outcome of hierarchical structure formation and a consequence of the universality of the assembly processes in* ΛCDM.

Mass assembly in dense environments

Galaxy evolution in the biased high-density regions surrounding a massive galaxy at high-z are also characterised by numerous *merger events*. In some systems, mergers counteract the negative feedback of SNe and allow star formation to continuously proceed for hundreds of Myr. It is indeed through frequent mergers with smaller satellites that also the central host LBG efficiently builds-up its $\sim 10^{10}$ $M_\odot$ stellar mass in the first billion years of evolution. These continuous direct interactions often lead to the formation of *tidal streams* in the satellites dwelling in the innermost regions. Despite the variegated star formation histories encountered in the dwarf satellites evolving in such dense biased environments, all of them experience a bursty evolution and at some point in their histories reach high SFRs of > 5 $M_\odot yr^{-1}$. *As a consequence, their* Hα *emission is expected to be detectable with JWST and, given the typical satellite distances of* < 15 *kpc from the central host, their light can be resolved within the JWST/NIRSpec field of view when performing spectroscopic follow-ups of* $z \sim 6$ *LBGs.*

A free lunch for JWST

We have demonstrated that star-forming satellites are within reach of JWST in spectroscopic follow-ups of high-z galaxies (e.g. Cycle 1 Proposal 1893, PI: Carniani, 17 Co-Is including Gelli), but the telescope is going to perform also many surveys providing wide and deep images: can we use photometry to investigate the population of high-z dwarf satellites? To answer this question I derived the expected rest-frame UV-optical spectral energy distributions (SED) of the dwarf satellites and took into account the expected performances of JWST/NIRCam in order to make accurate predictions for their observability (Gelli, Salvadori, Ferrara, Pallottini & Carniani, 2021). Specifically, I used STARBURST99 (Leitherer et al., 1999) to model the stellar continuum emission and considered the effect of dust attenuation (Weingartner & Draine, 2001). In addition to the synthetic SEDs, I produced mock images of the systems of galaxies, demonstrating that JWST is capable of detecting also low-mass satellites and spatially resolve their emission from that of the highly luminous central LBG. I produced color-magnitude diagrams that provide simple but powerful diagnostic tools to infer the properties of satellites through photometry: for instance, F200W-F356W < -0.25 can be used to identify low-mass star-bursting metal-poor dwarf galaxies. *With deep surveys* (e.g. JADES Rieke et al., 2019)*, where JWST is expected to observe many LBGs at* $z \sim 6$*, we will hence be able to catch for the first time and "for free" also the stellar emission of their faint satellites dwarf galaxies.*

Passive galaxies and quenching mechanisms at high-z

Thanks to the SERRA suite of simulations (Pallottini et al., 2022, including Gelli), I could perform an in depth study of a large statistical sample of satellites of $M_\star \sim 10^{9.5-10.5}$ $M_\odot$ LBGs at $6 < z < 8$ (Gelli et al., to be submitted). Their analysis revealed that 31% of the dwarf satellites population consists in *passive* galaxies that are currently not forming stars (SFR ~ 0). I investigated the causes of their early quenching by considering stellar evolution timescales and reconstructing their orbits to assess the impact of direct interactions with the nearby massive host: the main process responsible for the quenching is *internal SN feedback* that heats up and easily washes out the remaining gas in low-mass haloes. Moreover, due to their low potentials, most of these galaxies suffer *starvation* and are not efficient in pulling additional gas onto themselves. Interestingly, these passive systems constitute the majority of satellites in the low-mass regime, i.e. $\sim 70\%$ among those at $M_\star < 10^8$ $M_\odot$. A similar trend is witnessed in the Local Group, where passive galaxies

have typically low masses and are dominated by old stellar populations (e.g. dwarf spheroidals), *suggesting once again a universal tendency of structure formation for which smaller systems are more easily quenched.*

How to uncover passive galaxies with JWST

Despite passive satellites being amongst the faintest ones, I demonstrated that their detection is expected to be feasible through JWST/NIRCam imaging in deep observations. Their vicinity to bright LBGs can be used to easily locate them within the large observed areas and photometric information can be used to address their nature. Specifically, I identified a novel and effective method to distinguish passive from active satellites: the F356W−F444W vs F200W−F356W color-color diagram. Indeed at F200W − F356W $\gtrsim 1.9$, we find 96% of the satellites to be passive (25 out of 26, Gelli et al., to be submitted). *Deep photometric surveys are expected to be able to detect them, therefore providing us the opportunity to observe for the first time early passive dwarf galaxies at* $z > 6$.

The impact of the environment on low-mass galaxies

Among the results of the first months of JWST observation, the discovery of a low-mass passive galaxy at $z = 7.3$ (JADES-GS-z7-01-QU) was reported by Looser et al. (2023). The galaxy appears to have a stellar mass of $M_\star = 10^{8.7}$ $M_\odot$ and to be isolated in the field. Driven by the aim to interpret this observation, I compared the properties of isolated and satellites galaxies in the SERRA simulations, finding that for $M_\star \lesssim 5 \times 10^8$ $M_\odot$ no differences in their star formation histories are found: *the evolution of all high-z low-mass galaxies is dominated by internal feedback processes independently of the environment, i.e. for both field and satellites.*

Interpreting JADES-GS-z7-01-QU

Comparing JADES-GS-z7-01-QU with the simulations, we find and select a passive galaxy with same stellar mass, redshift and duty cycle. However, its emission is compatible with JADES-GS-z7-01-QU only if its SFH is artificially truncated a few Myr after the main star formation peak. As SN feedback can only act on a longer timescale (> 30 Myr), this implies that *the observed abrupt quenching in this source must be caused by a faster physical mechanism, such as radiation-driven winds, and that the SFR decline is a powerful diagnostic of different feedback types.*

9.2 A look to the future

The results of this Thesis brought to light the relevant interplay of different processes (e.g. SN feedback, mergers) in driving the evolution of dwarf galaxies dwelling in the peculiar densest high-z environments of the cosmic web around massive Lyman break galaxies and the huge potential of JWST to unveil them all. At this point a natural question arises: how do dwarf galaxies form and evolve in different environments? In fact, given the way that low-mass systems are extremely sensitive to all kind of feedback and environmental processes, we expect a possibly variegated population of dwarf galaxies inhabiting the diverse regions of the high-redshift Universe. In order to interpret upcoming results consistently with the cosmological scenario, it is important to understand how the star formation histories of dwarf galaxies depend on the density of the region in which they develop. How do they evolve in different environments? By processing the outputs of different cosmological simulations (e.g. Illustris TNG Springel et al. 2018, THESAN Garaldi et al. 2022, simulations considering the formation of the first PopIII stars Maio et al. 2010), I will be able to expand the range of analysed density regimes characterising different regions of the Universe and understand how the properties and evolution of dwarf galaxies change in all the different cosmic environments. I will derive the spectra of each analysed dwarf galaxy, producing a large collection of mock SEDs to help interpret upcoming JWST observations. Indeed, currently widely used SED-fitting codes (e.g. PROSPECTOR Leja et al. 2017, CIGALE Boquien et al. 2019) adopt relatively simple models for the evolution of galaxies and do not take into account which systems are expected to exist in a cosmological context and their complex star formation histories. For this reason I plan to also create an online tool where it will be possible to insert the observational parameters (e.g. instruments and filters used, exposure time) and the obtained data, and that will give as output the best fitting galaxies in our sample and their detailed properties (mass, age, metallicity, star formation history, environment). Such tool would allow to interpret the emission of faint high-z sources in light of the numerous possible realistic scenarios predicted by simulations.

We have highlighted in this Thesis the unprecedented potential of JWST in unveiling very low-mass galaxies at very high redshifts and another critical question may be posed: can also the first galaxies hosting PopIII stars be detected directly at high-z? Several attempts to address this point have been made, and some diagnostics that may enable their identification have been found (e.g Nakajima & Maiolino, 2022). However, for how long and how efficiently the first galaxies form stars is

still unknown, as is the mass distribution of the first stars (see Sec. 1.3). Moreover, different cosmological simulations produce different results regarding the star formation rates and redshift up to which PopIII stars can form (e.g. Jaacks et al., 2018; Liu & Bromm, 2020), adding the possibility for pristine regions to be present up to $z \sim 4$ (e.g. Pallottini et al., 2014). All these still numerous uncertainties will make it difficult to reliably interpret the upcoming observations. In addition, many recent observations and also preliminary JWST results (e.g. Naidu et al., 2022b; Donnan et al., 2023) are discovering numerous massive galaxies at high-z, possibly calling into question the most accredited ΛCDM cosmological scenario. It is therefore important to develop simple models, independent of cosmology and capable of describing the variety of galaxies hosting PopIII stars and making us able to constrain the conditions for their detectability.

With this aim in mind, I plan to link the Near- and Far-field cosmology approaches and create a wide set of "pure" PopIII galaxies models obtained by varying the following "unknow" physical quantities: PopIII stellar mass ($M_\star$), gas mass ($M_{\rm gas}$), star formation rate (SFR), redshift of formation ($z_{\rm form}$), and PopIII initial mass function (IMF). For each of them I will derive SEDs with continuum and nebular components, and construct a detectability function that will allow me to understand if and under which conditions the light from the first galaxies could effectively appear to our telescopes. The additional critical step will be to include self-consistently the presence of lower-mass metal enriched PopII stars: their presence is expected to affect the overall galaxy emission, producing SEDs with mixed signatures. Through their study we could find out in which cases the contribution of the first stars is relevant and for how long it could be identified in observations before being completely wiped out by that of the PopII population. Once all the PopIII and PopIII+PopII galaxy models and mock SEDs are available, I plan to use a methodology analogue to the one we used in the `PISN-explorer` for local stars (see Chapter 8) in order to efficiently and meticulously investigate large samples of JWST data from ongoing and upcoming surveys, and unveil among them the hidden signatures of the first stars in distant galaxies.

Only with these kind of multiple efforts in predicting the properties of the different galaxies inhabiting the early Universe, it will be possible to fully exploit the unprecedented datasets provided by JWST that will be available in the forthcoming years.

Bibliography

Abohalima A., Frebel A., 2018, ApJS, 238, 36

Agertz O., Kravtsov A. V., Leitner S. N., Gnedin N. Y., 2013, ApJ, 770, 25

Aguado D. S., et al., 2023, arXiv e-prints, p. arXiv:2301.03604

Allende Prieto C., Beers T. C., Wilhelm R., Newberg H. J., Rockosi C. M., Yanny B., Lee Y. S., 2006, ApJ, 636, 804

Angel P. W., Poole G. B., Ludlow A. D., Duffy A. R., Geil P. M., Mutch S. J., Mesinger A., Wyithe J. S. B., 2016, MNRAS, 459, 2106

Aoki W., Tominaga N., Beers T. C., Honda S., Lee Y. S., 2014, Science, 345, 912

Baes M., Camps P., 2015, Astronomy and Computing, 12, 33

Barkana R., Loeb A., 2001, Phys. Rep., 349, 125

Behrens C., Pallottini A., Ferrara A., Gallerani S., Vallini L., 2018, MNRAS, 477, 552

Behroozi P. S., Wechsler R. H., Wu H.-Y., 2013a, ApJ, 762, 109

Behroozi P. S., Wechsler R. H., Wu H.-Y., 2013b, ApJ, 762, 109

Behroozi P. S., Wechsler R. H., Conroy C., 2013c, ApJ, 770, 57

Belokurov V., et al., 2007, ApJ, 654, 897

Bertelli G., Bressan A., Chiosi C., Fagotto F., Nasi E., 1994, A&AS, 106, 275

Bisigello L., et al., 2016, ApJS, 227, 19

Bond J. R., Cole S., Efstathiou G., Kaiser N., 1991, ApJ, 379, 440

Boquien M., Burgarella D., Roehlly Y., Buat V., Ciesla L., Corre D., Inoue A. K., Salas H., 2019, A&A, 622, A103

Bothwell M. S., et al., 2010, MNRAS, 405, 219

Bouché N., et al., 2007, ApJ, 671, 303

Bournaud F., Duc P. A., 2006, A&A, 456, 481

Bouwens R. J., et al., 2012, ApJ, 752, L5

Bouwens R. J., Illingworth G. D., Oesch P. A., Maseda M., Ribeiro B., Stefanon M., Lam D., 2017, arXiv e-prints, p. arXiv:1711.02090

Bouwens R. J., et al., 2021, AJ, 162, 47

Bouwens R. J., et al., 2022, ApJ, 931, 160

Brauher J. R., Dale D. A., Helou G., 2008, ApJS, 178, 280

Brodie J. P., Romanowsky A. J., Strader J., Forbes D. A., 2011, AJ, 142, 199

Bromm V., 2013, Reports on Progress in Physics, 76, 112901

Bromm V., Loeb A., 2003, Nature, 425, 812

Bromm V., Yoshida N., 2011a, ARA&A, 49, 373

Bromm V., Yoshida N., 2011b, ARA&A, 49, 373

Bryan S. E., Kay S. T., Duffy A. R., Schaye J., Dalla Vecchia C., Booth C. M., 2013, MNRAS, 429, 3316

Caffau E., et al., 2022, MNRAS,

Carnall A. C., McLure R. J., Dunlop J. S., Davé R., 2018, MNRAS, 480, 4379

Carney B. W., Wright J. S., Sneden C., Laird J. B., Aguilar L. A., Latham D. W., 1997, AJ, 114, 363

Carniani S., et al., 2016, A&A, 591, A28

Carniani S., et al., 2017, A&A, 605, A42

Carniani S., et al., 2018, MNRAS, 478, 1170

Carroll S. M., Press W. H., Turner E. L., 1992, ARA&A, 30, 499

Cayrel R., et al., 2004a, A&A, 416, 1117

Cayrel R., et al., 2004b, A&A, 416, 1117

Cescutti G., et al., 2022, arXiv e-prints, p. arXiv:2211.06086

Ceverino D., Primack J., Dekel A., 2015, MNRAS, 453, 408

Chevallard J., Charlot S., 2016, MNRAS, 462, 1415

Ciardi B., Ferrara A., 2005, Space Sci. Rev., 116, 625

Cohen J. G., Huang W., 2009, ApJ, 701, 1053

Cormier D., et al., 2014, A&A, 564, A121

Correa C. A., Wyithe J. S. B., Schaye J., Duffy A. R., 2015, MNRAS, 450, 1514

Curti M., et al., 2023, MNRAS, 518, 425

Curtis-Lake E., et al., 2022, arXiv e-prints, p. arXiv:2212.04568

D'Odorico V., et al., 2018, ApJ, 863, L29

Daddi E., et al., 2010, ApJ, 713, 686

Dalton G., et al., 2016, in Evans C. J., Simard L., Takami H., eds, Society of Photo-Optical Instrumentation Engineers (SPIE) Conference Series Vol. 9908, Ground-based and Airborne Instrumentation for Astronomy VI. p. 99081G, doi:10.1117/12.2231078

Davé R., Finlator K., Oppenheimer B. D., 2011, MNRAS, 416, 1354

De Looze I., et al., 2014, A&A, 568, A62

De Silva G. M., et al., 2015, MNRAS, 449, 2604

Decataldo D., Pallottini A., Ferrara A., Vallini L., Gallerani S., 2019, MNRAS, 487, 3377

Dekel A., et al., 2009, Nature, 457, 451

Díaz-Santos T., et al., 2013, ApJ, 774, 68

Donnan C. T., et al., 2023, MNRAS, 518, 6011

Eisenstein D. J., Hut P., 1998, ApJ, 498, 137

Elahi P. J., Cañas R., Poulton R. J. J., Tobar R. J., Willis J. S., Lagos C. d. P., Power C., Robotham A. S. G., 2019, PASA, 36, e021

Fakhouri O., Ma C.-P., Boylan-Kolchin M., 2010, MNRAS, 406, 2267

Fan X., et al., 2006, AJ, 132, 117

Farrah D., et al., 2013, ApJ, 776, 38

Fensch J., et al., 2019, A&A, 628, A60

Ferland G. J., et al., 2013, Rev. Mexicana Astron. Astrofis., 49, 137

Ferland G. J., et al., 2017, Rev. Mexicana Astron. Astrofis., 53, 385

Ferrara A., Tolstoy E., 2000, MNRAS, 313, 291

Ferrara A., Vallini L., Pallottini A., Gallerani S., Carniani S., Kohandel M., Decataldo D., Behrens C., 2019, MNRAS, 489, 1

Ferrara A., Pallottini A., Dayal P., 2022a, arXiv e-prints, p. arXiv:2208.00720

Ferrara A., et al., 2022b, MNRAS, 512, 58

Finkelstein S. L., 2016, PASA, 33, e037

Finkelstein S. L., et al., 2017, The Cosmic Evolution Early Release Science (CEERS) Survey, JWST Proposal ID 1345. Cycle 0 Early Release Science

Fiore F., Ferrara A., Bischetti M., Feruglio C., Travascio A., 2023, ApJ, 943, L27

Fulbright J. P., et al., 2010, ApJ, 724, L104

Gaia Collaboration et al., 2018, A&A, 616, A12

Gallazzi A., Charlot S., Brinchmann J., White S. D. M., Tremonti C. A., 2005, MNRAS, 362, 41

Gallerani S., et al., 2010, A&A, 523, A85

Galli D., Palla F., 1998, A&A, 335, 403

Garaldi E., Kannan R., Smith A., Springel V., Pakmor R., Vogelsberger M., Hernquist L., 2022, MNRAS, 512, 4909

García Pérez A. E., et al., 2016, AJ, 151, 144

Gardner J. P., et al., 2006, Space Sci. Rev., 123, 485

Gelli V., Salvadori S., Pallottini A., Ferrara A., 2020, MNRAS, 498, 4134

Gelli V., Salvadori S., Ferrara A., Pallottini A., Carniani S., 2021, ApJ, 913, L25

Gelli V., Salvadori S., Ferrara A., Pallottini A., Carniani S., 2023, arXiv e-prints, p. arXiv:2303.13574

Giardino G., et al., 2016, in Skillen I., Balcells M., Trager S., eds, Astronomical Society of the Pacific Conference Series Vol. 507, Multi-Object Spectroscopy in the Next Decade: Big Questions, Large Surveys, and Wide Fields. p. 305

Gilmore G., et al., 2012, The Messenger, 147, 25

Gilmore G., et al., 2022, A&A, 666, A120

Gnedin N. Y., 2010, ApJ, 721, L79

Gnedin N. Y., Kaurov A. A., 2014, ApJ, 793, 30

González V., Labbé I., Bouwens R. J., Illingworth G., Franx M., Kriek M., Brammer G. B., 2010, ApJ, 713, 115

Graciá-Carpio J., et al., 2011, ApJ, 728, L7

Grassi T., Bovino S., Schleicher D. R. G., Prieto J., Seifried D., Simoncini E., Gianturco F. A., 2014, MNRAS, 439, 2386

Graziani L., Salvadori S., Schneider R., Kawata D., de Bennassuti M., Maselli A., 2015, MNRAS, 449, 3137

Habing H. J., 1968, Bull. Astron. Inst. Netherlands, 19, 421

Hahn O., Abel T., 2011, MNRAS, 415, 2101

Heger A., Woosley S. E., 2002, ApJ, 567, 532

Heiderman A., Evans Neal J. I., Allen L. E., Huard T., Heyer M., 2010, ApJ, 723, 1019

Herrera-Camus R., et al., 2018, ApJ, 861, 95

Hirano S., Hosokawa T., Yoshida N., Umeda H., Omukai K., Chiaki G., Yorke H. W., 2014, ApJ, 781, 60

Hirano S., Hosokawa T., Yoshida N., Omukai K., Yorke H. W., 2015, MNRAS, 448, 568

Hirashita H., Ferrara A., 2002, MNRAS, 337, 921

Hockney R. W., Eastwood J. W., 1988, Computer simulation using particles

Hsiao T., et al., 2023, in American Astronomical Society Meeting Abstracts. p. 153.05

Inoue S., Dekel A., Mandelker N., Ceverino D., Bournaud F., Primack J., 2016, MNRAS, 456, 2052

Ivans I. I., Sneden C., James C. R., Preston G. W., Fulbright J. P., Höflich P. A., Carney B. W., Wheeler J. C., 2003, ApJ, 592, 906

Jaacks J., Thompson R., Finkelstein S. L., Bromm V., 2018, MNRAS, 475, 4396

Jakobsen P., et al., 2022, A&A, 661, A80

Jiang L., et al., 2013, ApJ, 773, 153

Johnson J. L., Dalla Vecchia C., Khochfar S., 2013, MNRAS, 428, 1857

Johnson B. D., Leja J., Conroy C., Speagle J. S., 2021, ApJS, 254, 22

Joshi G. D., Pillepich A., Nelson D., Zinger E., Marinacci F., Springel V., Vogelsberger M., Hernquist L., 2021, MNRAS, 508, 1652

Karlsson T., Johnson J. L., Bromm V., 2008, ApJ, 679, 6

Katz H., Kimm T., Sijacki D., Haehnelt M. G., 2017, MNRAS, 468, 4831

Kennicutt Robert C. J., 1998, ApJ, 498, 541

Kennicutt R. C., Evans N. J., 2012, ARA&A, 50, 531

Khokhlov A., 1998, Journal of Computational Physics, 143, 519

Kirby E. N., Cohen J. G., Guhathakurta P., Cheng L., Bullock J. S., Gallazzi A., 2013, ApJ, 779, 102

Knollmann S. R., Knebe A., 2009, ApJS, 182, 608

Kohandel M., Pallottini A., Ferrara A., Zanella A., Behrens C., Carniani S., Gallerani S., Vallini L., 2019, MNRAS, 487, 3007

Kohandel M., Pallottini A., Ferrara A., Carniani S., Gallerani S., Vallini L., Zanella A., Behrens C., 2020, MNRAS, 499, 1250

Kravtsov A. V., Klypin A. A., Khokhlov A. M., 1997, ApJS, 111, 73

Kroupa P., 2001, MNRAS, 322, 231

Krumholz M. R., McKee C. F., Tumlinson J., 2009, ApJ, 693, 216

Labbe I., et al., 2022, arXiv e-prints, p. arXiv:2207.12446

Laporte N., et al., 2017, ApJ, 837, L21

Larson P. L., 1998, Gaia, 15, 389

Leitherer C., et al., 1999, ApJS, 123, 3

Leja J., Johnson B. D., Conroy C., van Dokkum P. G., Byler N., 2017, ApJ, 837, 170

Leung T. K. D., Pallottini A., Ferrara A., Mac Low M.-M., 2020, ApJ, 895, 24

Limongi M., Chieffi A., 2018, VizieR Online Data Catalog, p. J/ApJS/237/13

Liu B., Bromm V., 2020, MNRAS, 497, 2839

Longair M. S., 2007, Galaxy formation. Springer Science & Business Media

Looser T. J., et al., 2023, arXiv e-prints, p. arXiv:2302.14155

Lupi A., Bovino S., 2020, MNRAS, 492, 2818

Ma X., et al., 2018, MNRAS, 478, 1694

Madau P., Dickinson M., 2014, ARA&A, 52, 415

Madden S. C., et al., 2013, PASP, 125, 600

Maio U., Dolag K., Ciardi B., Tornatore L., 2007, MNRAS, 379, 963

Maio U., Ciardi B., Dolag K., Tornatore L., Khochfar S., 2010, MNRAS, 407, 1003

Majewski S. R., et al., 2017, AJ, 154, 94

Mannucci F., Cresci G., Maiolino R., Marconi A., Gnerucci A., 2010, MNRAS, 408, 2115

Marconi A., et al., 2022, in Evans C. J., Bryant J. J., Motohara K., eds, Society of Photo-Optical Instrumentation Engineers (SPIE) Conference Series Vol. 12184, Ground-based and Airborne Instrumentation for Astronomy IX. p. 1218424, doi:10.1117/12.2628689

Markov V., Carniani S., Vallini L., Ferrara A., Pallottini A., Maiolino R., Gallerani S., Pentericci L., 2022, A&A, 663, A172

Martel H., Shapiro P. R., 1998, MNRAS, 297, 467

Matthee J., Mackenzie R., Simcoe R. A., Kashino D., Lilly S. J., Bordoloi R., Eilers A.-C., 2022, arXiv e-prints, p. arXiv:2211.08255

McConnachie A. W., 2012, AJ, 144, 4

Mo H. J., White S. D. M., 2002, MNRAS, 336, 112

Mo H., Van den Bosch F., White S., 2010, Galaxy formation and evolution. Cambridge University Press

Moore B., 1994, Nature, 370, 629

Mori M., Umemura M., 2006, Nature, 440, 644

Moster B. P., Naab T., White S. D. M., 2013, MNRAS, 428, 3121

Moster B. P., Naab T., White S. D. M., 2018, MNRAS, 477, 1822

Murray N., 2011, ApJ, 729, 133

Naidu R. P., et al., 2022a, arXiv e-prints, p. arXiv:2208.02794

Naidu R. P., et al., 2022b, ApJ, 940, L14

Nakajima K., Maiolino R., 2022, MNRAS, 513, 5134

Navarro J. F., Frenk C. S., White S. D. M., 1997, ApJ, 490, 493

Norris M. A., et al., 2014, MNRAS, 443, 1151

O'Shea B. W., Wise J. H., Xu H., Norman M. L., 2015, ApJ, 807, L12

Ocvirk P., et al., 2020, MNRAS, 496, 4087

Padmanabhan T., 1993, Structure formation in the universe. Cambridge university press

Pallottini A., Ferrara A., Gallerani S., Salvadori S., D'Odorico V., 2014, MNRAS, 440, 2498

Pallottini A., Ferrara A., Gallerani S., Vallini L., Maiolino R., Salvadori S., 2017a, MNRAS, 465, 2540

Pallottini A., Ferrara A., Bovino S., Vallini L., Gallerani S., Maiolino R., Salvadori S., 2017b, MNRAS, 471, 4128

Pallottini A., et al., 2019, MNRAS, 487, 1689

Pallottini A., et al., 2022, MNRAS, 513, 5621

Parkin T. J., et al., 2013, ApJ, 776, 65

Pavesi R., Riechers D. A., Faisst A. L., Stacey G. J., Capak P. L., 2019, ApJ, 882, 168

Planck Collaboration et al., 2014, A&A, 571, A16

Planck Collaboration et al., 2016, A&A, 596, A108

Pontzen A., Governato F., 2012, MNRAS, 421, 3464

Press W. H., Schechter P., 1974, ApJ, 187, 425

Richings A. J., Schaye J., Oppenheimer B. D., 2014, MNRAS, 442, 2780

Ricotti M., Gnedin N. Y., 2005, ApJ, 629, 259

Rieke M. J., Kelly D., Horner S., 2005, in Heaney J. B., Burriesci L. G., eds, Society of Photo-Optical Instrumentation Engineers (SPIE) Conference Series Vol. 5904, Cryogenic Optical Systems and Instruments XI. pp 1–8, doi:10.1117/12.615554

Rieke M., et al., 2019, BAAS, 51, 45

Rizzo F., Kohandel M., Pallottini A., Zanella A., Ferrara A., Vallini L., Toft S., 2022, A&A, 667, A5

Roederer I. U., Preston G. W., Thompson I. B., Shectman S. A., Sneden C., Burley G. S., Kelson D. D., 2014, AJ, 147, 136

Rosdahl J., Schaye J., Dubois Y., Kimm T., Teyssier R., 2017, MNRAS, 466, 11

Rosdahl J., et al., 2018, MNRAS, 479, 994

Salvadori S., Ferrara A., 2009, MNRAS, 395, L6

Salvadori S., Ferrara A., 2012, MNRAS, 421, L29

Salvadori S., Ferrara A., Schneider R., 2008, MNRAS, 386, 348

Salvadori S., Ferrara A., Schneider R., Scannapieco E., Kawata D., 2010, MNRAS, 401, L5

Salvadori S., Tolstoy E., Ferrara A., Zaroubi S., 2014, MNRAS, 437, L26

Salvadori S., Skúladóttir Á., Tolstoy E., 2015, MNRAS, 454, 1320

Salvadori S., Bonifacio P., Caffau E., Korotin S., Andreevsky S., Spite M., Skúladóttir Á., 2019, MNRAS, 487, 4261

Santini P., et al., 2021, A&A, 652, A30

Sargsyan L., et al., 2012, ApJ, 755, 171

Schaerer D., et al., 2020, A&A, 643, A3

Shetrone M. D., Côté P., Sargent W. L. W., 2001, ApJ, 548, 592

Shibuya T., Ouchi M., Harikane Y., 2015, ApJS, 219, 15

Simon J. D., 2019, arXiv e-prints, p. arXiv:1901.05465

Springel V., 2005, MNRAS, 364, 1105

Springel V., White S. D. M., Tormen G., Kauffmann G., 2001, MNRAS, 328, 726

Springel V., et al., 2018, MNRAS, 475, 676

Stark D. P., Schenker M. A., Ellis R., Robertson B., McLure R., Dunlop J., 2013, ApJ, 763, 129

Starkenburg E., Oman K. A., Navarro J. F., Crain R. A., Fattahi A., Frenk C. S., Sawala T., Schaye J., 2017a, MNRAS, 465, 2212

Starkenburg E., Oman K. A., Navarro J. F., Crain R. A., Fattahi A., Frenk C. S., Sawala T., Schaye J., 2017b, MNRAS, 465, 2212

Starkenburg E., et al., 2017c, MNRAS, 471, 2587

Stecher T. P., Williams D. A., 1967, ApJ, 149, L29

Susa H., Hasegawa K., Tominaga N., 2014, ApJ, 792, 32

Tacchella S., Bose S., Conroy C., Eisenstein D. J., Johnson B. D., 2018, ApJ, 868, 92

Tacchella S., et al., 2023, arXiv e-prints, p. arXiv:2302.07234

Tacconi L. J., et al., 2010, Nature, 463, 781

Takahashi K., Yoshida T., Umeda H., 2018, ApJ, 857, 111

Tegmark M., Silk J., Rees M. J., Blanchard A., Abel T., Palla F., 1997, ApJ, 474, 1

Teyssier R., 2002, A&A, 385, 337

Tolstoy E., Hill V., Tosi M., 2009, ARA&A, 47, 371

Toro E. F., 2013, Riemann solvers and numerical methods for fluid dynamics: a practical introduction. Springer Science & Business Media

Trebitsch M., Blaizot J., Rosdahl J., Devriendt J., Slyz A., 2017, MNRAS, 470, 224

Treu T., et al., 2022, ApJ, 935, 110

Tumlinson J., 2010, ApJ, 708, 1398

Vallini L., Gallerani S., Ferrara A., Pallottini A., Yue B., 2015, ApJ, 813, 36

Vallini L., Ferrara A., Pallottini A., Gallerani S., 2017, MNRAS, 467, 1300

Vallini L., Pallottini A., Ferrara A., Gallerani S., Sobacchi E., Behrens C., 2018, MNRAS, 473, 271

Vallini L., Ferrara A., Pallottini A., Carniani S., Gallerani S., 2020, MNRAS, 495, L22

Vallini L., Ferrara A., Pallottini A., Carniani S., Gallerani S., 2021, MNRAS, 505, 5543

Vanzella E., et al., 2017, MNRAS, 467, 4304

Vanzella E., et al., 2019, MNRAS, 483, 3618

Vrug A., ter Braak C., Dicks C., Robinson B., Hyman J., Higdon D., 2009, International Journal of Nonlinear Sciences & Numerical Simulation, 10, 273:290

Wadsley J. W., Stadel J., Quinn T., 2004, New Astronomy, 9, 137

Walker M. G., Peñarrubia J., 2011, ApJ, 742, 20

Weingartner J. C., Draine B. T., 2001, ApJ, 548, 296

Weisz D. R., Dolphin A. E., Skillman E. D., Holtzman J., Gilbert K. M., Dalcanton J. J., Williams B. F., 2014, ApJ, 789, 147

Williams C. C., et al., 2018, ApJS, 236, 33

Wise J. H., Abel T., Turk M. J., Norman M. L., Smith B. D., 2012a, MNRAS, 427, 311

Wise J. H., Turk M. J., Norman M. L., Abel T., 2012b, ApJ, 745, 50

Wise J. H., Demchenko V. G., Halicek M. T., Norman M. L., Turk M. J., Abel T., Smith B. D., 2014, MNRAS, 442, 2560

Woosley S. E., Weaver T. A., 1995a, ApJS, 101, 181

Woosley S. E., Weaver T. A., 1995b, ApJS, 101, 181

Xing Q.-F., Zhao G., Aoki W., Honda S., Li H.-N., Ishigaki M. N., Matsuno T., 2019, Nature Astronomy, 3, 631

Xu H., Wise J. H., Norman M. L., Ahn K., O'Shea B. W., 2016, ApJ, 833, 84

Yue B., Ferrara A., Xu Y., 2016, MNRAS, 463, 1968

Ziparo F., Ferrara A., Sommovigo L., Kohandel M., 2023, MNRAS, 520, 2445

de Bennassuti M., Salvadori S., Schneider R., Valiante R., Omukai K., 2017, MNRAS, 465, 926

de Jong R. S., et al., 2019, The Messenger, 175, 3